Dissertation

Experimental investigation of injection cooling for water as the working fluid of high temperature heat pumps and theoretical study of industrial drying processes

ausgeführt zum Zwecke der Erlangung des akademischen Grades eines Doktors der technischen Wissenschaften unter der Leitung von

Ao.Univ.Prof. Dipl.-Ing. Dr.techn. Karl PONWEISER

Institut für Energietechnik und Thermodynamik / E302

eingereicht an der Technischen Universität Wien

Fakultät für Maschinenwesen und Betriebswissenschaften

von

Dipl.-Ing. Stefan FALKNER

0826830

Seibersdorf 15, 4131 Kirchberg/D.

Gutachter:

Univ.Prof. Dipl.-Ing. Dr.techn. Tobias PRÖLL
Institut für Verfahrens- und Energietechnik / H89300, BOKU Wien

Ao.Univ.Prof. Dipl.-Ing. Dr.techn. Andreas WERNER
Institut für Energietechnik und Thermodynamik / E302, TU Wien

Wien, 19.12.2018   **eigenhändige Unterschrift**

Für Viktoria

Abstract

This work is intended to investigate and advance industrial high temperature heat pumps in order to increase the supply temperature and to expand the field of application, especially in concern of industrial drying processes.

Drying processes are energy-intensive and the most important process steps in various branches of industry. About 85 % of all drying processes are operated by fossil-fired, convective exhaust air dryers. The use of high temperature heat pumps recovering thermal energy from the exhaust air offers opportunities as a substitute for fossil energy supply.

Since the compressor and the working fluid play the central roles in concern of elevated temperatures, the focus was on these two components as parts of high temperature heat pumps. General theoretical investigations have shown that water as refrigerant causes high compressor discharge temperatures but suits well for higher heat source temperatures and in the second stage of a cascaded heat pump cycle. Direct injection cooling offers chances to reduce the elevated thermal loads but also increases the risk of hydrolock. An injection system was developed and tested successfully. As a subsequent experimental step, an existing reciprocating compressor test bench was adapted and operated with the injection system. A certain temperature decrease of the discharged vapour could be achieved. The considered compressor was rather insensitive to liquid drops in the cylinder space.

In order to investigate the drying behaviour of clay bricks in a chamber dryer, an open and easily expandable drying library has been developed. The modelling approaches and the descriptive mathematical formulations were implemented in the modelling language Modelica and validated using measurement data from drying tests performed on a small-scale laboratory container. All the substantial properties and processes were reproduced with sufficient accuracy. The models are forming the basis to investigate drying processes in conjunction with the energy supply by high temperature heat pumps, to assess the process quality, and to extend their field of application.

Kurzfassung

Diese Arbeit beschäftigt sich mit der Untersuchung und Weiterentwicklung industrieller Hochtemperatur Wärmepumpen, mit der Absicht die Wärmeabgabetemperatur zu steigern und den Anwendungsbereich, insbesondere in Bezug auf die industrielle Trocknung, zu erweitern.

Trocknungsprozesse sind in hohem Maß energieintensiv und zählen in verschiedenen Industriezweigen zu den wichtigsten Prozessschritten. Rund 85 % aller Trocknungsprozesse werden mit fossil befeuerten konvektiven Ablufttrocknern betrieben. Die Wärmerückgewinnung aus der Abluft unter Verwendung von Hochtemperatur Wärmepumpen bietet sich als Substitut der fossilen Energiebereitstellung an.

Da der Verdichter sowie das Arbeitsmedium die zentrale Rolle, im Zusammenhang mit erhöhten Temperaturen, einnehmen, wurde der Fokus auf diese beiden Komponenten der Wärmepumpe gelegt. Theoretische Untersuchungen haben gezeigt, dass Wasser als Kältemittel hohe Verdichterendtemperaturen verursacht, jedoch für höhere Wärmequellentemperaturen und in der zweiten Stufe eines Kaskadenzyklus gut geeignet ist. Direkte Zylindereinspritzung bietet Möglichkeiten, die hohe thermische Belastung zu reduzieren, erhöht aber auch die Gefahr von Wasserschlag. Ein Einspritzsystem wurde entwickelt und erfolgreich getestet. In einem weiteren Versuchsaufbau wurde ein vorhandener Kolbenverdichterprüfstand adaptiert und mit dem Einspritzsystem betrieben. Ein Temperaturabfall des verdichteten Arbeitsmediums konnte erreicht werden. Der betrachtete Kompressor erwies sich als weitgehend unempfindlich gegenüber Flüssigkeiten im Zylinderraum.

Um das Trocknungsverhalten von Tonziegeln in einem Kammertrockner zu untersuchen, wurde eine offene und leicht erweiterbare Trocknungsbibliothek entwickelt. Die Modellierungsansätze und daraus resultierenden mathematischen Formulierungen wurden in der Modellierungssprache Modelica implementiert und anhand von Messdaten aus Trocknungsexperimenten validiert. Alle wesentlichen Eigenschaften und Prozesse wurden mit ausreichender Genauigkeit reproduziert. Die Bibliothek bildet die Grundlage, für die Untersuchung von Trocknungsprozessen in Verbindung mit Hochtemperatur Wärmepumpen zur Energiebereitstellung, um Aussagen zur Prozessqualität treffen und den Anwendungsbereich erweitern zu können.

Danksagung

Zuallererst möchte ich mich in aller Form bei Ao.Univ.Prof. Dipl.-Ing. Dr.techn. Karl Ponweiser für die vorbildliche wissenschaftliche Betreuung, die konstruktive Zusammenarbeit und die wertvollen fachlichen Ratschläge sehr herzlich bedanken.

Meine Tätigkeit am Institut für Energietechnik und Thermodynamik wurde durch Karl Ponweiser und Univ.Prof. Dipl.-Ing. Dr.techn. Markus Haider ermöglicht, wodurch auch der Grundstein für die vorliegende Arbeit gelegt wurde, vielen Dank dafür. Aber auch allen anderen Mitarbeitern des Institutes, insbesondere Dominik, Esmaeil, Gregor, Johannes, Stylianos, Thomas, Wolfgang sei an dieser Stelle für die zahlreichen sehr unterhaltsamen Diskurse und das hervorragende Arbeitsklima gedankt.

Außerdem bedanke ich mich bei Ao.Univ.Prof. Dipl.-Ing. Dr.techn. Andreas Werner und Univ.Prof. Dipl.-Ing. Dr.techn. Tobias Pröll für die Begutachtung dieser Arbeit.

Dem gesamten DryPump Projektkonsortium möchte ich für die ebenfalls recht konstruktive Zusammenarbeit danken. Sie alle sind für den überaus positiven Abschluss des Projekts, dessen Ergebnisse auch Basis für diese Arbeit waren, mitverantwortlich. Besonders hervorheben möchte ich die Mitarbeiterinnen und Mitarbeiter der Firmen sowie Institutionen AIT, AMT, LMF und Wienerberger AG.

Meinen Kollegen und Freunden Dipl.-Ing. Dr.rer.nat. Georg Brunauer, Dipl.-Ing. Dr.techn. Markus Zöchbauer und Dipl.-Ing. Dr.techn. Thomas Keplinger möchte ich recht herzlich danken. Sie haben einen wertvollen Beitrag zur Konzeptionierung und zum Aufbau des Einspritzsystems geleistet.

Ein großer Dank geht an meine Eltern Christine und Bernhard für ihre bedingungslose Unterstützung, die sie mir in jeglicher Art und Weise während des gesamten Studiums gegeben haben.

Zum Schluss möchte ich meiner Freundin Viktoria danken, die durch ihre unglaublich hilfreiche Unterstützung, ihr Verständnis und ihre liebevollen Aufmunterungen einen wesentlichen Anteil an der Fertigstellung dieser Arbeit hat.

Preface

A major part of this thesis yields from my work in the Austrian research funding framework *Energieforschung 1. Ausschreibung* project *DryPump No. 848 912*. The project's content and thus that of the thesis are partly based on the results of the Austrian research funding framework *e!Mission.at 4. Ausschreibung* project *SteamUp No. 843 872*. The objectives, the teams, and the main results of the mentioned projects should briefly be outlined in advance, since there are several references to involved organisations, test set-ups, etc. in course of the thesis.

The aim of the SteamUp project was to technically scope to what extent water is suitable for the use in high temperature heat pumps (HTHPs) as a refrigerant with a condensation temperature up to 200 °C in order to utilise industrial low temperature waste heat (60 to 90 °C) in the future. With a HTHP using water as a refrigerant, it is possible to develop new applications for industrial heat pumps. The focus was placed on the development of a novel compressor concept for the use in selected industrial processes, since it plays the key role in context to an elevated operation temperature.

The project team was formed by employees of the Austrian Institute of Technology GmbH[1] (AIT), the Institut für Energietechnik und Thermodynamik[2] (IET), and Leobersdorfer Maschinenfabrik[3] (LMF).

Three processes were identified in which the use of a HTHP is eligible. The most promising application in a practicable performance class and a reasonable coefficient of performance (*COP*) was a sterilisation process using an autoclave. It has also been found out that the compression of water vapour in a reciprocating compressor is feasible as part of a compression heat pump process. The high thermal load can be reduced by the direct injection of liquid water into the cylinder. Then the temperature would be in normal range, hence, an increased duration of life for the gland packing, piston, and rider rings could be ensured. However, the performance

---

[1] The Energy Department of the AIT, with a team of around 130 employees, develops sustainable energy systems by applying interdisciplinary approaches. The examinations range from individual components to energy concepts for buildings, cities, and entire regions. https://www.ait.ac.at/

[2] The IET is part of the Faculty for Mechanical Engineering and Industrial Management of TU Wien. Within this faculty IET is the centre of competence for the mechanical and process engineering aspects of energy technology. Details to organisation, teaching, research, and industry cooperation can be found on the following homepage: https://www.iet.tuwien.ac.at/

[3] LMF is the leading Austrian manufacturer of high pressure reciprocating compressor systems, which are developed and produced at the headquarters in Leobersdorf (Lower Austria). https://www.lmf.at/home/

of direct injection and the indemnification of the cylinder, piston rod, crank mechanism, etc. need to be investigated and tested further. The question concerning the heat pump's economic efficiency remains unclear. As a result, it's theoretically feasible to realise a HTHP with water as the working fluid [1].

DryPump is intended to solve major industrial research questions in context of using compression heat pumps for industrial drying at a temperature range from 60 to 95 °C evaporator temperature and up to 170 °C condenser temperature. For this purpose the temperature resistance of critical materials, safe start-up and shut-down, and direct injection for cooling the hot gas are investigated under real operating conditions using appropriate compressor concepts of relevant size. Concepts for the process integration were developed. The theoretical results obtained from the SteamUp project are now used to design a test bench.

Several different processes with the required supply air temperatures in the range from 80 to 170 °C could have already been identified for the project partners Wienerberger AG and Agrana in preliminary investigations. By integrating a compression heat pump, the vapour of the exhaust air can be used as the energy source and the drying process can be operated as a closed air loop. The water vapour in the air is condensed. Subsequently, the sensible and latent energy from the wet exhaust air, together with the mechanical compressor energy, are reintroduced into the circuit air stream to elevate its temperature.

The project team was formed by employees of the AIT, Wienerberger AG[4], AGRANA Research & Innovation Center GmbH[5] (Agrana), AMT Kältetechnik GmbH[6] (AMT), Bitzer Kühlmaschinenbau GmbH[7], the IET, and the Institut für Ziegelforschung Essen e.V.[8] (IZF). LMF acts as subcontractor.

The following technical goals and highlights were achieved in the DryPump project:

- Development of technically feasible concepts and their economic evaluation when using compression heat pump technologies for industrial drying of selected processes

- Evaluation of the sealant and lubricant properties and the operation mode for the safe start-up and shut-down of screw-type compressors, with a refrigeration capacity of approximately 350 kW, at an evaporator temperature from 60 to 95 °C and condensation temperature up to 125 °C

---

[4]Wienerberger was founded in 1819 as an Austrian brick manufacturer and is the world's largest producer of hollow bricks. Wienerberger AG is also the number one producer of facing bricks in Europe and the USA and the market leader for tiles in Europe. The company has presence in approximately 30 countries worldwide. https://wienerberger.at/

[5]The Agrana Research & Innovation Center GmbH, is AGRANA's research and development company for starch, bioethanol, sugar, and fruit. http://www.agrana-research.com/start/

[6]AMT Kältetechnik GmbH is a Styrian company specialised in the field of consulting, planning, engineering, installation, and service of refrigeration systems. http://www.amt-kaelte.com/

[7]BITZER was founded in 1934 in Sindelfingen (Germany) and is today one of the world's largest manufacturers of refrigerant compressors. https://www.bitzer.de/

[8]The IZF was founded in 1952 as a research centre for the brick industry. The activities have been related to applied research and development, consulting, and services in the coarse-ceramic industry. http://www.izf.de/

- Evaluation of direct cylinder injection for cooling the hot gas and the phenomenological investigation of the spray drop vaporisation when using water as the working fluid (R718)

- Optimisation of the discontinuous, heat pump driven, brick drying process' operating conditions, at constant brick quality and the aim of minimising the total energy input including auxiliary devices

- Bricks were dried with a heat pump for the first time, according to the consortium's knowledge. The tests showed very good agreement with the theoretical investigations.

- A concept to provide a live steam temperature of up to 170 °C for industrial drying under the usage of a compression heat pump in various continuously operated drying plants

- Proposals to answer the technological challenges in conjunction with industrial drying using compression heat pumps, such as high evaporator and condenser temperature and direct water injection for cooling the hot gas

Concerning the technical requirements of the operating parameters, the considered drying processes of Wienerberger AG and Agrana are phenomenological representatives for other industries, such as for the energy-intensive paper industry or the production of veneer boards. Thus, the results contribute significantly to offer heat pump solutions in conjunction with drying processes for a wide range of user groups in the medium-term [2].

The publications resulting from the DryPump project are briefly summarised as [3], [4], [5], [6], and [7].

Contents

Nomenclature

Initialisms

ACU	Air Circulating Unit
BDC	Bottom Dead Centre
CAD	Computer-Aided Design
CFC	ChloroFluoroCarbons
CP	Critical Point
CV	Control Volume
DP	Drying Period
FV	Finite Volume
GWP	Global Warming Potential
HDEV	HochDruckEinspritzVentil
HTHP	High Temperature Heat Pump
HCFC	HydroChloroFluoroCarbons
HFC	HydroFluoroCarbons
NMR	Nuclear Magnetic Resonance
ODP	Ozone Depletion Potential
PEEK	PolyEther Ether Ketone
PTFE	PolyTetraFluoroEthylene
SG	Safety Group
TDC	Top Dead Centre
WB	Wet-Bulb

Roman symbols

Sign	Unit	Description
a	$\frac{\mathrm{m}^2}{\mathrm{s}}$	Thermal diffusivity
A	m^2	Cross section
A	m^2	Area
A	$\frac{\mathrm{m}^2}{\mathrm{g}}$	Specific surface
B	m	Width
B	1	Adjusted heat transfer number
c	$\frac{\mathrm{J}}{\mathrm{kg\,K}}$	Specific heat capacity
c	$\frac{\mathrm{mol}}{\mathrm{m}^3}$	Concentration
C	m^3	Constant
C	$\frac{\mathrm{m}^2}{\mathrm{s}}$	Constant
C	$\frac{\mathrm{J}}{\mathrm{kg}}$	Heat capacity
c	1	Coefficient
COP	1	Coefficient Of Performance
CV	1	Cumulative Volume
D	m	Diameter
D	$\frac{\mathrm{m}^2}{\mathrm{s}}$	Diffusion coefficient
f	Hz	Frequency
F	N	Force
g	$\frac{\mathrm{m}}{\mathrm{s}^2}$	Gravitational acceleration
h	$\frac{\mathrm{J}}{\mathrm{kg}}$	Specific enthalpy
h	m	Height
$\dot{H}$	W	Enthalpy flow rate
H	m	Height
i	1	Discretisation index
j	$\frac{\mathrm{mol}}{\mathrm{m}^2\,\mathrm{s}}$	Diffusive molar flux
k	$\frac{\mathrm{K}}{\mathrm{s}}$	Change of temperature
k	1	Exponent
k	$\frac{\mathrm{W}}{\mathrm{m}^2\,\mathrm{K}}$	Heat transmission coefficient
k	1	Polytropic index

k	$\frac{\mathrm{m^2}}{\mathrm{Pa\,s}}$	Transport coefficient
kA	$\frac{\mathrm{W}}{\mathrm{K}}$	Thermal conductance
L	m	Length
L	m	Characteristic length
$\dot{m}$	$\frac{\mathrm{kg}}{\mathrm{s}}$	Mass flow rate
m	kg	Mass
m	1	Exponent
M	$\frac{\mathrm{kg}}{\mathrm{mol}}$	Molar mass
$\dot{n}$	$\frac{\mathrm{mol}}{\mathrm{s}}$	Molar flow rate
n	1	Exponent
n	mol	Amount of substance
n	1	Number of
n	$\frac{1}{\mathrm{s}}$	Rotational speed
N	1	Total number of
p	Pa	Pressure
p	Pa	Partial pressure
p	1	Dimensionless pressure
P	W	Power
$\dot{Q}$	W	Heat flow rate
r	m	Radius
R	$\frac{\mathrm{J}}{\mathrm{kg\,K}}$	Specific gas constant
$\Re$	$\frac{\mathrm{J}}{\mathrm{mol\,K}}$	Molar gas constant
s	m	Length
s	$\frac{\mathrm{J}}{\mathrm{kg\,K}}$	Specific entropy
s	m	Wall thickness
S	$\frac{\mathrm{kg}}{\mathrm{m^3\,s}}$	Source
S		General source
SEC	$\frac{\mathrm{kWh}}{\mathrm{kg}}$	Specific Energy Consumption
SMD	m	Sauter Mean Diameter
$SMER$	$\frac{\mathrm{kg}}{\mathrm{kWh}}$	Specific Moisture Extraction Ratio
t	s	Time
t	s	Duration
T	K	Thermodynamic temperature

$\boldsymbol{u}$	$\frac{\text{m}}{\text{s}}$	Velocity
u	$\frac{\text{m}}{\text{s}}$	Velocity
u	$\frac{\text{J}}{\text{kg}}$	Specific internal energy
U	J	Internal energy
v	$\frac{\text{m}^3}{\text{kg}}$	Specific volume
$\dot{V}$	$\frac{\text{m}^3}{\text{s}}$	Volume flow rate
V	m^3	Volume
VE	1	Volumetric efficiency
VHC	$\frac{\text{J}}{\text{m}^3}$	Volumetric heating capacity
w	$\frac{\text{J}}{\text{kg}}$	Specific work
w	$\frac{\text{m}}{\text{s}}$	Velocity in z-direction
W	J	Work
x	$\frac{\text{mol}}{\text{mol}}$	Mole fraction
x	m	Coordinate
X	$\frac{\text{kg}}{\text{kg}}$	Mass of water referred to the mass of dry air
y	$\frac{\text{kg}}{\text{kg}}$	Mass of water referred to the mass of the dry product
z	m	Coordinate

Greek symbols

Sign	Unit	Description
α	$\frac{\text{W}}{\text{m}^2\,\text{K}}$	Heat transfer coefficient
β	$\frac{\text{m}}{\text{s}}$	Mass transfer coefficient
γ	1	Linear shrinkage coefficient
Γ	$\frac{\text{kg}}{\text{m}\,\text{s}}$	Diffusion coefficient
Γ		General diffusion coefficient
δ	m	Boundary layer thickness
ϵ		General density
ϵ	1	Porosity
ϵ	1	Emission coefficient
ζ	1	Exergy efficiency
η	Pa s	Dynamic viscosity

η	1	Efficiency
$\varTheta$	rad	Contact angle
ϑ	°C	Temperature
κ	1	Isentropic exponent
κ	$\frac{\mathrm{m}^2}{\mathrm{s}}$	Moisture diffusion coefficient
λ	$\frac{\mathrm{W}}{\mathrm{m\,K}}$	Thermal conductivity
μ	1	Diffusion resistance
ν	$\frac{\mathrm{m}^2}{\mathrm{s}}$	Kinematic viscosity
ξ	$\frac{\mathrm{kg}}{\mathrm{kg}}$	Mass fraction
$\varPi$	1	Compression ratio
ρ	$\frac{\mathrm{kg}}{\mathrm{m}^3}$	Density
σ	$\frac{\mathrm{N}}{\mathrm{m}}$	Surface tension
σ	$\frac{\mathrm{W}}{\mathrm{m}^2\,\mathrm{K}^4}$	Stefan–Boltzmann constant
τ	1	Tortuosity
ϕ		General variable
φ	1	Relative humidity
χ	$\frac{\mathrm{m}}{\mathrm{m}}$	Linear relative shrinkage
ψ	$\frac{\mathrm{m}^3}{\mathrm{m}^3}$	Volumetric moisture content

Indices

Sign	Description
$-$	Before
$+$	After
1, 2, 3, …	Numeration
$1 + X$	Referred to the mass of dry air
air	Air
amb	Ambient
$brick$	Brick
c	Capillary
c	Concentration
C	Cold

C	Core
Car	Carnot
$centre$	Centre
ch	Chamber
$cond$	Conductive
$conv$	Convective
$crit$	Critical
CV	Control volume
D	Drop
del	Delay
dim	Dimensionless
$disch$	Discharge
dry	Dry
eff	Effective
el	Electrical
eq	Equilibrium
f	Friction
fan	Fan
$final$	Final
H	Hot
HE	Heat exchanger
i	Counter index
in	In
ind	Indicated
ini	Initial
inj	Inject
j	Dimension index
$leak$	Leakage
$loop$	Loop
$loss$	Loss
m	Molar
max	Maximum
mea	Measurement

min	Minimum
out	Out
p	Isobaric
p	Related to pressure
p	Porous
pc	Phase change
plate	Plate
rad	Radiation
ref	Reference
s	Isentropic
sat	Saturation
SE	Shrinking end
sh	Shelf
sh	Superheat
sim	Simulation
sink	Sink
source	Source
spec	Specific
stroke	Stroke
suc	Suction
surf	Surface
test	Test
th	Thermal
tot	Total
tr	Triple point
v	Vaporisation
vap	Vapour
w	Water
wall	Wall
WB	Wet-Bulb
wet	Wet
y	Related to y
δ	Related to boundary layer thickness

ϑ	Related to temperature
ψ	Related to volumetric moisture content

Dimensionless numbers

Sign	Description
$Bi = {\alpha\,L}/{\lambda}$	Biot number
$Le = {a}/{D}$	Lewis number
$Nu = {\alpha\,L}/{\lambda}$	Nußelt number
$Oh = {\eta}/{(L\,\rho\,\sigma)^{0.5}}$	Ohnesorge number
$Pr = {\nu}/{a}$	Prandtl number
$Re = {u\,L}/{\nu}$	Reynolds number
$Sc = {\nu}/{D}$	Schmidt number
$Sh = {\beta\,L}/{D}$	Sherwood number
$St = {c\,(\vartheta - \vartheta_{pc})}/{\Delta h_{pc}}$	Stefan number
$We = {\rho\,u^2\,L}/{\sigma}$	Weber number

Introduction

According to Statistik Austria, the industrial sector was responsible for around $30\,\%$ of Austria's final energy consumption in 2016. That's equivalent to $329\,\mathrm{PJ/a}$, whereof approximately $75\,\%$ were used to provide industrial process heat. The industry is one of the main producers of climate-related emissions, since around $50\,\%$ of the industry's energy demand is covered by fossil fuels [1, 8]. Considering industrial sectors of a typical industrialised country like Canada in 2002, where drying accounts as essential part of the production chain, industrial energy is consumed primarily in the paper and pulp ($30\,\%$), mining ($15.5\,\%$), and chemical industry ($7.4\,\%$). Depending on the industry sector and used technology, drying can represent a major fraction of the energy use. The energy for drying accounts for up to $70\,\%$ of the total energy in manufacturing wood products, about $50\,\%$ of textile, $27\,\%$ of paper, and $33\,\%$ of pulp production [9]. In Austria, the paper industry accounts for $21\,\%$ of the industrial sector's total energy consumption [8].

In 1982, drying was estimated to account for at least $10\,\%$ of industrial energy demand in typical industrialised regions like the U.K. and Europe [10]. More recent estimates suggest that drying processes account for up to $25\,\%$ of the total industrial energy demand in advanced countries worldwide [2].

However, dryers are major energy consumers, because of the requirement to provide the latent heat of evaporation for all the moisture that is removed. The relative energy demand is rising, not at least due to the appearance of many new drying requiring products on the market [10]. Drying processes are among the most important process steps in various branches of the industry. Water is removed from a product to prevent rot, increase shelf life, minimise transport costs, or as a part of the production chain and requirement for further processing [5].

The energetically ideal drying process takes place at ambient conditions. Considering pure convective drying, the product's temperature drops below ambient temperature as a result of the evaporation process at the product's surface. This effect is often referred to as evaporative cooling. As the drying progresses, the drying product's temperature rises and approaches ambient temperature. At the end of the drying process, the drying product, the drying air, and the evaporated water are reaching ambient temperature again. All that results in a slow, gentle, and energy efficient drying. Nowadays the requirements on the producing industry are increasing, e.g. the production process as well as the drying process have to be fast and flexible. Starting again with the drying air and the drying product at ambient conditions, the air has to be heated

under supply of external energy to decrease the process duration. The temperature of the whole system is elevated for this reason. The drying air, the drying product, and the evaporated water are leaving the dryer with significantly higher temperature compared to the ambient temperature.

About 85 % of all drying processes are operated by fossil-fired, convective exhaust air dryers. 99 % of these systems dissipate the exhaust air including the water vapour to the environment without further use of its energy potential [2, 4]. Hence, dryers tend to have pretty low thermal efficiency, often below 50 % [10]. Considering the ideal drying process, there is a huge necessity and potential for improving efficiency and reducing energy consumption.

There are essentially three spheres of activity, in order to improve the energy efficiency of drying processes: the drying product, the energy supply for the drying process, and the drying plant. Some improvements are obvious such as, thermal insulation reduces heat losses of the drying plant by radiation, conduction, and convection. The waste heat recovery seems to be more complex and offers large saving potential of thermal energy. The hot exhaust air continues to be used directly by heat exchange to preheat the drying air. In addition, compression heat pumps are also used for waste heat recovery. Industrial drying processes can be performed more efficiently by integrating heat pumps. Heat pumps are using waste heat as a heat source to provide thermal energy at a higher temperature level by adding mechanical compressor energy [5].

In the past, heat pumps have already been used in drying processes. The main applications were the drying of food and timber. Due to the heat pump's limited operation temperature, the heat pump drying was limited to these fields.

In the future, the heat pump's operation temperature should be increased by the development of high temperature heat pumps (HTHPs). Fallow waste heat potentials of a higher temperature range can then be re-used. The application fields can be extended to numerous other drying processes, such as in the paper and pulp, petrochemical, and non-metallic mineral industry. The temperature required in most industrial drying processes ranges from 100 to 200 °C [2].

The compressor and the working fluid play the central roles as part of the HTHP. A primary goal of this work is to perform investigations on a novel reciprocating compressor concept for the use in selected industrial processes in context to an elevated thermal load, when using water as the working fluid. Therefore the direct injection of liquid water into the cylinder for cooling the hot gas and the associated risk on damaging the compressor should be analysed.

The described intents concern the energy supply for the drying process to increase efficiency and expand the application field of HTHP. As mentioned before, the drying product and the drying plant offer further prospects. Specifically, the drying behaviour of clay bricks in chamber dryers should be investigated, since drying is an important and the most energy consuming process in the production chain of clay bricks [11]. Subsequently, another main goal of this work is, to investigate and mathematically describe the processes in the drying material and the dryer as its surrounding environment, during the drying process. Models for simulative description should be developed and implemented in a suitable simulation environment.

The models are forming the basis for the simulation of drying processes. In future, the

models should be used as sub-models for the optimisation of overall processes and for finding proper controlling strategies. Therefore, Modelica (cf. Chapter 2.3.3) was chosen as the modelling language, since it suits ideally for the simulation of the dynamic behaviour of multi-domain systems.

Chapter 1

Experimental investigation of injection cooling for water as the working fluid of high temperature heat pumps

As already outlined in the general Introduction, industrial drying processes can be performed more efficiently by the integration of heat pumps. HTHPs need to be advanced further in order to increase the supply temperature and to expand the field of application.

First some important fundamentals according to, HTHPs, the considered reciprocating compressor type, and alternative injection applications are presented. Subsequently, general theoretical investigations on the use of water as a working fluid, and in particular, as an application under the usage of a reciprocating compressor with direct injection cooling are following. Finally, the set-up and results from the experimental investigations on the developed injection system and the reciprocating compressor test bench are presented. The chapter concludes with a summary and outlook. At this point it should be noted, unless otherwise stated, hereinafter a subcritical operated vapour compression heat pump is considered if there's talk about a heat pump.

1.1 Introduction

Industrial HTHPs are applied to provide industrial process heat. Waste heat of low temperature can be brought to a higher temperature level and is returned to a given process under supply of external energy. The variety of heat pumps with high thermal output ranging from 20 kW to 20 MW and elevated supply temperature has grown steadily in recent years [12]. The required thermal output as well as the occurring temperatures and nature of the heat source and sink are

from great importance to select the working fluid, size, and type of used aggregates. The heat pump system has to work reliably and efficiently under the given circumstances.

The compressor as the most complex component of a compression heat pump plays a key role in terms of the achievable temperature and thermal output. It's charged with the system's highest occurring temperature. With conventional compression, this temperature can be far beyond the condenser temperature respectively the sink temperature and could lead to wear rates of unacceptable levels for various components. Compressors of the reciprocating type are often used. Those are well suited for higher pressure ratios as well as for higher flow rates, which together corresponds to increased thermal outputs. For increased flow rates other types of compressors are used more frequently, namely the screw and turbo compressors [13]. However, applying several reciprocating compressor in parallel also results in higher flow rates. In addition, any requirement of oil-free compression will rule out most of the screw type compressors [14]. High pressure ratios respectively increased temperature shifts, generally have a negative effect on the system's efficiency for all compressor types [15].

The selection of the working fluid is also closely related to the given operation conditions. A high enthalpy of vaporisation and a high critical temperature are important for efficient use of subcritically operated heat pumps. Further, a variety of other requirements apply on the working fluid [15]. An innovative approach to advance HTHPs is the development and investigation of a heat pump with water as refrigerant or working fluid. Water is a natural refrigerant, it's completely neutral in regard to harmful effects on humans, animals, and the environment. The global warming potential equals zero and so does the ozone depletion potential. It's non-toxic, non-combustible, and non-explosive. That compares with some technical challenges caused by the thermodynamic properties of water: very high compressor discharge temperatures and thus extreme thermal loads to the components used in the compressor, high pressure ratios, and a large specific volume and consequently large volume flows [1].

It's examined theoretically which operation conditions are advantageous for an efficient use of water as a working fluid. A novel reciprocating compressor concept with liquid direct injection is developed and investigated experimentally in order to reduce the compressor discharge temperature and to control the increased thermal load. These measures represent opportunities to increase the achievable supply temperatures and significantly expand the field of application of HTHPs in the drying industry and in other industry branches as well.

1.2 High temperature heat pumps

1.2.1 Basic working principles and thermodynamic fundamentals

A heat pump is a device that transfers thermal energy from a heat source at low temperature (cold side) to a heat sink at higher temperature (hot side) under supply of electrical energy. The basic scheme of a compression heat pump is shown in Fig. 1.1 and consists of a compressor, a condenser, an expansion valve, and an evaporator [15].
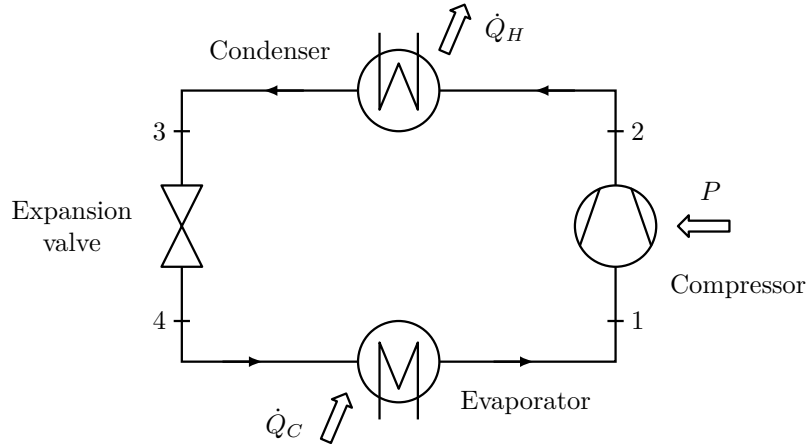
Figure 1.1: Basic scheme of a compression heat pump, adapted from [15]

The working fluid (refrigerant) vapour at low pressure level (state 1) is taken to the higher pressure level (state 2) by the compressor under supply of mechanical power P. The temperature also rises. In the condenser, the refrigerant's sensible heat and latent enthalpy of vaporisation, represented by $\dot{Q}_H$, is transferred to the heat sink until state 3 is reached. The condensed refrigerant is brought to the lower pressure level (state 4) by the expansion valve before it enters the evaporator. In the evaporator, the working fluid is vaporised by absorbing the heat flow rate of the heat source $\dot{Q}_C$. When entering the compressor, the refrigerant circuit closes and the compression starts again. This process is referred to as an thermodynamic cycle running anticlockwise.

The source's thermal energy arises at low temperature on the system's low pressure side, the thermal energy transferred to the sink arises at high temperature on the high pressure side. Thermal energy is "pumped" from a low to a high temperature level. This process doesn't violate the second law of thermodynamics, since energy has to be supplied for compression [15].

The idealised compression heat pump process is conveniently illustrated in the T, s-chart as shown in Fig. 1.2 and consists of the following sub-processes:

- 1 - 2: Polytropic compression of vapour, often assumed as isentropic compression (1 - 2s)

- 2 - 3: Isobaric remove of vapour superheat and condensation

- 3 - 4: Isenthalpic expansion (throttling) to the saturated region

- 4 - 1: Isobaric vaporisation

The real heat pump process differs lightly from the course shown in Fig. 1.2, e.g. due to pressure losses in the heat exchangers or non-isenthalpic expansion due to thermal losses [15].

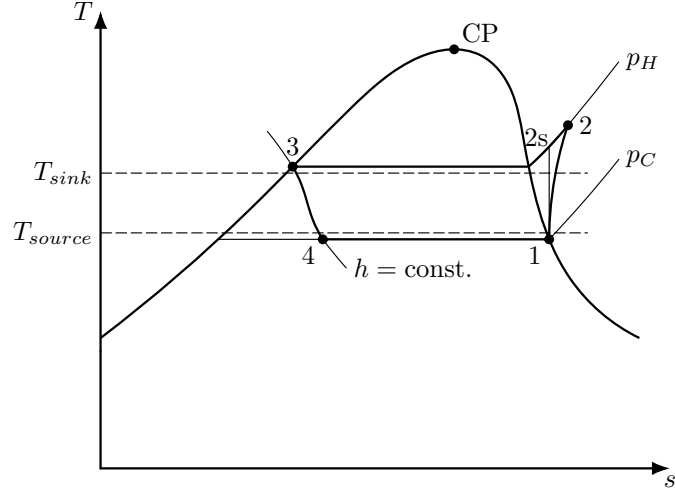The power input through compression P, the heat flow rate supplied by the heat source $\dot{Q}_C$,

Figure 1.2: Theoretical heat pump cycle in T, s-chart, adapted from [15]

and the heat flow rate delivered to the heat sink $\dot{Q}_H$ can be determined as follows [16]:

$$P = \dot{m}\left(h_2 - h_1\right) = \frac{\dot{m}}{\eta_s} \int_1^2 v \, \mathrm{d}p \tag{1.1}$$

$$\dot{Q}_H = -\dot{m}\left(h_3 - h_2\right) = -\dot{m} \int_2^3 T \, \mathrm{d}s \tag{1.2}$$

$$\dot{Q}_C = \dot{m}\left(h_1 - h_4\right) = \dot{m} \int_4^1 T \, \mathrm{d}s \tag{1.3}$$

$\dot{m}$ denotes the refrigerant mass flow rate, h the specific enthalpy, v the specific volume at a certain thermodynamic state, and η_s the compressor's isentropic efficiency (cf. Eq. 1.16).

The most common indicator to compare the performance of heat pump systems is the coefficient of performance COP. Which is defined as usable thermal energy flow delivered per power input. In general, heat pumps have a COP of 4 to 6.

$$COP = \frac{\dot{Q}_H}{P} \tag{1.4}$$

The ideal heat pump cycle is the reversed Carnot cycle, which can be used as the standard cycle. Its coefficient of performance COP_{Car} represents the maximum theoretical achievable value and is given by:

$$COP_{Car} = \frac{T_H}{T_H - T_C} = \frac{1}{\eta_{Car}} \geq COP \tag{1.5}$$

as the reciprocal value of the Carnot efficiency η_{Car}. Where T_C and T_H denote the saturation

temperatures corresponding to the evaporator's pressure level p_C and the condenser's pressure level p_H. This performance value serves as a second law standard. The comparison to actual cycles results in the exergy (second-law) efficiency ζ [17]:

$$\zeta = \frac{COP}{COP_{Car}} \tag{1.6}$$

Refrigerant

The selection of a refrigerant as working fluid for mechanical vapour compression heat pumps or refrigerators depends on its thermodynamic properties, environmental impact, and the given process parameters. The following requirements apply: high critical temperature, high enthalpy of vaporisation, high volumetric heating capacity, high heat transfer coefficients in the apparatus (condenser, evaporator), low final compressor discharge temperature, pressures above atmospheric pressure (but as low as possible on the suction side), thermal stability, low flammability, good lubricating properties, compatible with materials of construction and lubricant, and advantageous chemical and toxic properties [12, 15, 18].

To quantify the capability of a refrigerant at given process parameters, the volumetric heating capacity VHC is defined as:

$$VHC = \frac{h_2 - h_3}{v_1} \tag{1.7}$$

With h as the refrigerant's specific enthalpy and v as the specific volume when entering the compressor (indices according to Fig. 1.2). VHC depends on the refrigerant's thermodynamic properties at the chosen pressure levels. High values of VHC allow the operation of compression heat pumps or refrigerators with a relatively low volume flow rate, which leads to a compact design of the equipment [15].

Refrigerants can be classified by their chemical composition: chlorofluorocarbons (CFCs), hydrochlorofluorocarbons (HCFCs), hydrofluorocarbons (HFCs), and inorganic natural refrigerants. In the past, CFCs, HCFCs, and HFCs have been extensively used due to their excellent thermodynamic properties. However, the disadvantage of these synthetic refrigerants is their strong negative environmental impact. Consequently, extensive research activities have been initiated to find new, more environmental-friendly refrigerants.

The impact of refrigerants on ozone destruction is estimated by the ozone depletion potential (ODP), which is the ratio of the destructive potential of the given fluid and the depletion caused by an equal amount of the reference substance R11. The global worming potential (GWP) quantifies the ability to absorb infrared radiation relative to carbon dioxide [19].

In ASHRAE[1] Standard 34 refrigerants are also classified according to their toxicity (A, B) and flammability (1-3) in six safety groups (SGs) [12, 19].

---

[1]The American Society of Heating, Refrigerating and Air-Conditioning Engineers (ASHRAE) is a global professional association with the mission to advance the art and sciences of heating, ventilating, air conditioning, and refrigerating to serve humanity and promote a sustainable world. https://www.ashrae.org/

Compressor

The refrigerant vapour at evaporator pressure level is taken to the condenser pressure level by the compressor. The ratio of these pressure levels is called compression ratio Π:

$$\Pi = \frac{p_H}{p_C} \tag{1.8}$$

According to Eq. 1.1, the compression ratio determines the required compression power and further affects the COP (cf. Eq. 1.4). High compression ratios have a negative effect on the heat pump's performance. Furthermore, the condenser pressure should be chosen moderately, since the enthalpy of vaporisation decreases with increasing pressure (cf. Fig. 1.2) and the requirements on material strength increase [15].

Different types of compressors are used in mechanical vapour compression heat pumps: scroll and rotary vane compressors in small and medium heat pumps up to 100 kW thermal output, reciprocating compressors up to 500 kW, screw compressors from 50 kW up to around 5 MW, and turbo compressors in large systems above 2 MW, as well as oil-free turbo compressors above 250 kW. For industrial heat pumps, the majority of compressors is of the reciprocating, screw, scroll, or rotary vane type. Compressors are available with variable-speed control to run the power unit according to heating load [19, 20].

Evaporator and condenser

Heat pumps can be classified according to the heat source and sink type. Possible combinations are air-air, air-water, or water-water. Hence, the heat exchanger's design strongly depends on the type of application.

If the refrigerant exchanges heat with water, different types of heat exchangers are used. Plate and frame heat exchangers are often employed. The heat is transferred by corrugated metal plates. Tube in tube heat exchangers are also used, shaped by two coaxial tubes with the inner one corrugated to increase the heat transfer area and to force turbulence. Shell and tube heat exchangers are used as well.

Air heat exchangers are basically constituted by finned tube bundles. The refrigerant flows in tubes and air is blown by fans. This is the most common type for low capacity heat exchangers. More complex devices are employed for larger units. However, they are working on the same operation principle [20].

The design of the heat exchangers plays a significant role in the heat pump's overall efficiency. The heat exchange areas and the corresponding temperature difference directly affect the operating pressures and further the energy required to provide the same heating load. A larger heat exchange area causes lower temperature difference and the system becomes more efficient [17], since the exergy losses due to the heat transfer fall with decreasing temperature gradient in the heat exchanger [16].

Liquid receiver and expansion valve

The liquid receiver (not shown in Fig. 1.1) is placed at the condenser outlet to store high pressure liquid leaving the condenser. Its purpose is to collect fluid when load fluctuations occur. It's sized to contain the whole refrigerant charge during the power-off periods.

The expansion valve is a metering device that feeds working fluid to the evaporator, irreversibly taking the refrigerant from the condenser pressure to the evaporator pressure [20].

1.2.2 Temperature limitations

The aim of HTHPs is to provide process heat at elevated temperatures. In case of subcritically operated heat pumps, a condenser temperature rise is associated with increasing the condenser pressure.

The majority of heat pump compressors is lubricated with oil, thus the refrigerant in the compressor contains oil. The oil chemically changes and contaminates the refrigerant, at temperatures ranging from 160 to 200 °C. Usually there's no oxygen in the system, hence the oil doesn't burn. Some refrigerants decompose at elevated temperatures. Specifically, ammonia is sensitive to decomposed oil contamination, in the presence of some metals. Also, the properties of the reciprocating compressor's valve material can change, making them more susceptible to failure [17]. Increased temperature and pressure will also influence the compressor material's duration of life. In case of reciprocating compressors, the piston rings for sealing the cylinder space to the ambient are critical components. Those are charged with the highest occurring gas temperature and additionally rub on the cylinder wall [13].

The thermal limit of application in terms of process performance is determined by the refrigerant's critical temperature. Depending on the refrigerant, a gap of 10 to 15 K from the condenser temperature should be maintained [12]. As mentioned in the previous chapter, the enthalpy of vaporisation decreases with increasing condenser temperature and pressure, what negatively influences the COP.

The supercritical or transcritical heat pump cycle is basically possible. The operation with carbon dioxide as the refrigerant (R744) is known. Its appliance is limited, since the pressurised fluid must experience very large temperature differences in the supercritical region. In order to operate efficiently, the difference of the sink's inlet and outlet temperature has to be large too. These operation conditions are rarely required in industrial processes [1]. For example, the process is used for hot air supply [21].

1.2.3 Process enhancements

As already mentioned, an increase of the temperature lift and an increase of the condenser temperature lead to different technological problems. In addition, they have negative impact on the process performance. There are different possibilities to improve the process efficiency and to

lower the compressor discharge temperature in conjunction with these enhanced requirements. Some of them are introduced in the following.

Internal heat exchanger

The application of an internal heat exchanger improves the process efficiency, in certain cases. It subcools the refrigerant leaving the condenser by superheating the vapour before entering the compressor. As a result of the subcooling, the amount of heat absorbed from the heat source increases without significant increase of the compression work. The amount of heat absorbed by the heat sink increases, compared to the conventional process [15]. Notice, the superheating leads to a higher compressor discharge temperature, which may cause problems [17]. The usage of an internal heat exchanger is not necessarily related to enhanced operation requirements, but is often implemented to heat pumps as a simple installation to increase efficiency and should therefore briefly be mentioned for reasons of completeness.

Multi-stage operation

The cycle efficiency is significantly reduced with an increase of the pressure ratio [17], the COP decreases and the process becomes uneconomic. In this case, multi-stage operation makes sense, since the pressure ratio of a certain stage assumes more favourable values again [15].

The compressor discharge temperature due to high compression ratios can be lowered by substituting the single-stage compressor, in the conventional scheme from Fig. 1.1, by a two-stage compressor with an interstage cooler. The heat absorbed by the heat sink is reduced and the sum of the compression works of the two stages can be smaller than the work of the single-stage compressor. Generally, this solves the compressor discharge temperature problem but does not lead to an improvement of cycle performance. The COP can even be reduced due to the decreased thermal energy delivered to the sink. The expansion still takes place from high to low pressure level so that the expansion losses are the same, compared to the conventional process [17].

Larger temperature shifts can also be obtained by a two-stage heat pump cycle using different refrigerants. It's also known as the two cascaded heat pump cycle. Doing so, it is possible to select the most appropriate refrigerant for each temperature level. The disadvantage of the cascaded cycles is that an additional heat exchanger is required between the condenser of the low temperature cascade cycle and the evaporator of the high temperature cascade cycle [17]. An additional heat exchanger is always related to additional exergy losses.

Another way to meet high pressure ratios, hence large temperature differences between thermal source and sink, is injecting vapour into the compressor at an intermediate pressure. Fig. 1.3 shows the scheme of such an application and Fig. 1.4 illustrates the changes in state in the p, h-chart. After the condenser (state 5), the refrigerant is sent to the first expansion valve, at its exit (state 6) vapour and liquid are separated at an intermediate pressure. The liquid with state 7 goes to the second expansion valve before entering the evaporator. The vapour with state 9
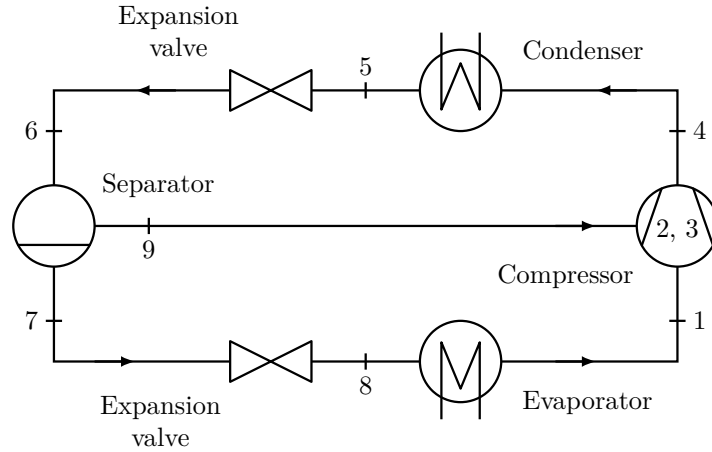
Figure 1.3: Scheme of a heat pump cycle with vapour/liquid separation and vapour injection to the compressor, causing an intermediate cooling

is forwarded to the compressor's intake of the second stage, where it mixes with superheated vapour from the end of the first stage (state 2) to state 3. Vapour injection causes intermediate cooling which lowers the compression work [20]. Notice, the mass flow rate through the first stage is lower than through the second stage.
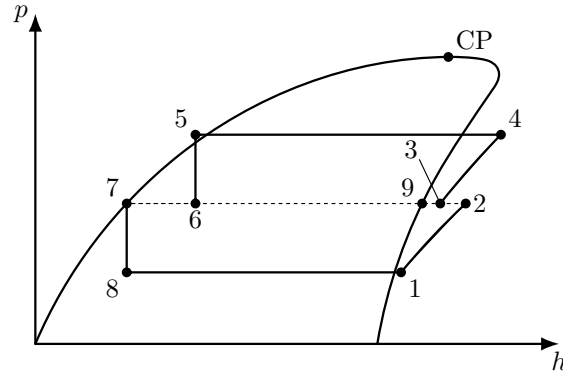

Figure 1.4: p, h-chart of a heat pump cycle with vapour/liquid separation and vapour injection to the compressor, causing an intermediate cooling, adapted from [20]

The two-stage heat pump cycle with an interstage flash cooler is a quite similar process. The high pressure liquid from the condenser is expanded to the intermediate pressure. The flash gas is directly removed by the second stage compressor together with the vapour coming from the discharge of the first stage compressor. The remaining liquid is further expanded to the evaporator pressure level. The irreversible expansion process is taken over smaller pressure differences, so that the losses are significantly reduced [17]. That also applies for the process described before. The main difference between these cycles is that the compressor stages are

clearly separated and the discharge of the first stage enters the flash cooler. Hence, the suction state of the second stage (state 3 according to Fig. 1.4) lies on the dew line.

Another cycle using injection technology is sketched in Fig. 1.5. The corresponding p, h-chart is shown in Fig. 1.6. Refrigerant exiting from the condenser with state 5 can take two different
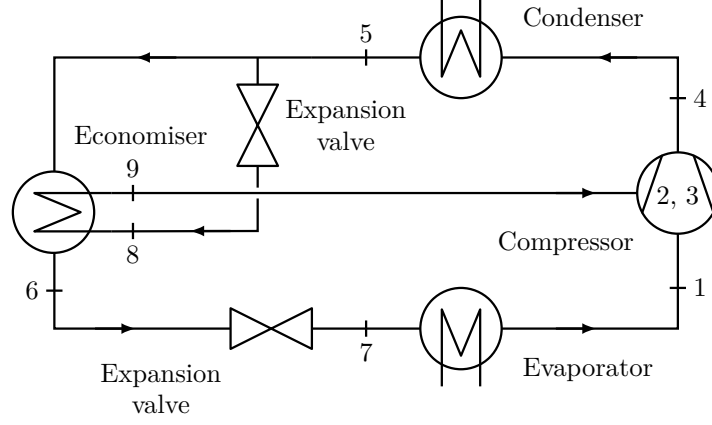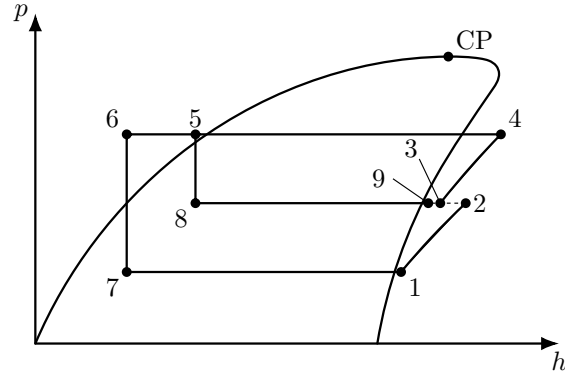
Figure 1.5: Scheme of a heat pump cycle with an economiser and vapour injection to the compressor, causing an intermediate cooling, adapted from [20]

ways. A certain amount of refrigerant (primary fluid) flows to the first expansion valve, after passing through the economiser (state 6), and goes to the evaporator (state 7). In the economiser the primary fluid transfers heat to another amount of secondary fluid flowing along path 5-8-9. This secondary fluid is expanded from state 5 to an intermediate pressure (state 8) by a second valve and reaches the compressor as superheated vapour with state 9. Primary fluid is further subcooled and secondary fluid heats up and mixes with vapour from the first compression stage (state 2) to state 3 [20].

Figure 1.6: p, h-chart of a heat pump cycle with an economiser and vapour injection to the compressor, causing an intermediate cooling, adapted from [20]

Such injection systems are implemented in scroll compressors. Qin et al. [22] and Kim et al. [23] are investigating scroll compressors with injection systems under the usage of an

economiser. In [22] the experimental results have shown that the thermal output of an air source heat pump system was raised up by 28.6 % compared with the conventional system. The research proves that refrigerant injection can improve the thermal output especially for high pressure ratios. Injection cooling is also employed in screw compressor with a COP increase by about 20 % [20].

In addition scroll compressors which can bear liquids exist on the market, thus allowing saturated vapour injection, so-called wet vapour injection. The use of wet vapour injection is also aimed at limiting the compressor discharge temperature [20]. There are many scientific papers, as [24] and [25], related to this topic.

Suction injection cooling

Suction injection cooling can usually be employed in scroll compressors and is an effective technology to decrease the compressor discharge temperature. A certain amount of the subcooled refrigerant coming from the condenser is expanded to the low temperature two-phase fluid. Then, it flows into the suction pipe and mixes with the superheated vapour from the evaporator to reduce the suction temperature. The compressor discharge temperature decreases. Furthermore, the refrigerant's specific volume decreases with the decreasing suction temperature, which leads to the increase of the compressor mass flow rate. If the injection mass flow rate is rather high, the compressor will also inhale liquid fluid which can further cool the compression process [26]. Wet vapour compression takes place.

Supercritical process

A supercritical respectively transcritical mechanical vapour compression heat pump consists of similar components as the subcritical cycle (cf. Fig. 1.1). The most significant difference is the replacement of the two-phase condenser by a gas cooler. As shown in Fig. 1.7, a single-phase, sensible cooling process takes place in the refrigerant supercritical region (path 2-3), with large temperature glide transfering thermal energy to the heat sink. The refrigerant is neither gas nor liquid, its temperatures and pressures are independent properties, thus an additional control device is needed. However, the evaporator still absorbs thermal energy from the heat source by vaporisation at constant pressure and temperature [19].

As mentioned in Chapter 1.2.2, the operation with carbon dioxide as the refrigerant (R744) is known. Compared to conventional refrigerants, its remarkably low critical temperature of $\vartheta_{crit} = 31.1\,°C$ allows CO_2 heat pumps to work above the critical pressure $p_{crit} = 73.8\,bar$ [19].

Rotary and reciprocating compressors are used [20]. Vapour injection systems in case of rotary compressors and internal heat exchangers can also be employed [19]. Chung et al. [27] are presenting results from experimental performance investigations of a twin-rotary compressor using flash tank vapour injection for interstage cooling. The thermal output and COP improvements of the system were 9.2 % and 7.1 % compared to the non-injection system, at the operation temperatures $-15\,°C$ outdoor and $20\,°C$ indoor.
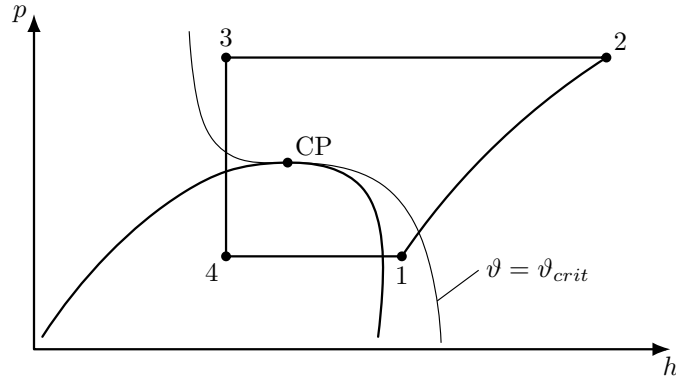
Figure 1.7: p, h-chart of a supercritical vapour compression heat pump cycle, adapted from [19]

Supercritical CO_2 cycles claim higher pressure differences between compressor discharge and suction, resulting in elevated expansion losses. Hence, expansion work recovery is more beneficial to improve efficiency in such systems. The expansion work is used to reduce the energy consumption of the compressor [19].

1.2.4 State of the art and research

Industrial HTHPs

The variety of heat pumps with high thermal output of 20 kW to 20 MW and raised supply temperature has grown steadily in the recent years. The temperatures of typical heat sources range from 17 to 65 °C and the determined COP values are between 2.4 and 5.8 with a temperature shift of 95 to 40 K. R245fa, R717 (ammonia), R744 (supercritical carbon dioxide), R134a, and R1234ze(E) are mainly used as refrigerants. The compressors installed in HTHPs are single- or twin-screw, two-stage turbo, and several parallel reciprocating compressors. Internal heat exchangers are applied to ensure sufficient overheating of the refrigerant before entering the compressor. Parallel compressors are used to achieve higher thermal outputs. Economisers, two-stage compressors, or intermediate injection lead to an increase of performance. Two-stage cycles as cascade are implemented on a large scale [12]. Tab. 1.1 summarises a selection of marketable HTHPs with a sink temperature equal or greater than 100 °C. The Norwegian company Vicking Heating Engines AS represents the industrial benchmark with the HeatBooster and a supply temperatures up to 150 °C [28]. The vapour compression heat pump system with an internal heat exchanger was developed by Viking Heat Engines AS in collaboration with AVL Schrick[2]. It's equipped with a proven reciprocating machine technology designed for 40 000 operating hours at temperatures up to 200 °C before half life maintenance. The system was successfully tested with HFO-1336mzz(Z) and R245fa as the working fluid [29].

---

[2]https://www.avl-schrick.com/

Table 1.1: Selection of industrial HTHPs, adapted from [12, 28]

Manufacturer	Product	Refrigerant	ϑ_{max} °C	$\dot{Q}_H$ kW	Compressor
Kobelco[a]	SGH 165	R134a/R245fa mix	165	70 to 660	Twin-screw
Kobelco	SGH 120	R245fa	120	70 to 370	Twin-screw
Vicking Heating Engines AS[b]	HeatBooster	R245fa or R1336mzz(Z)	150	28 to 188	Recip.
Ochsner[c]	IWWDSS R2R3b	R134a/ÖKO1[d] cascade	130	170 to 750	Screw
Ochsner	IWWDS ER3b	ÖKO1	130	170 to 750	Screw
Mayekawa[e]	Eco Sirocco	R744	120	65 to 90	Screw
Hybrid Energy[f]	Hybrid HP	R717/R718	120	250 to 2500	Recip.
Combitherm[g]	HWW 245fa	R245fa	120	62 to 252	Recip.

[a] http://www.kobelco.co.jp/english/
[b] http://www.vikingheatengines.com/heatbooster/
[c] https://www.ochsner.com/en/
[d] contains R245fa [12]
[e] http://www.mayekawa.com/
[f] https://www.hybridenergy.no/
[g] https://www.combitherm.de/

Ochsner provides HTHPs with screw compressors and condenser temperatures up to 130 °C. Waste heat of 35 to 55 °C is used as heat source for a single-stage cycles or 8 to 25 °C for a two-stage cascade cycles. The thermal output ranges from 170 to 750 kW. Higher thermal outputs can also be achieved by connecting several machines [28].

The Japanese company Kobe Steel developed the SGH 120 heat pump, which generates steam at 120 °C with a mass flow rate of 0.51 t/h and a COP of 3.5 from a waste hot water source with a temperature of 65 °C. It's equipped with a two-stage screw compressor using R245fa as refrigerant. The SGH 165 consists of a single-stage compressor heat pump with a R134a/R245fa mixture as refrigerant and a steam compressor. It generates superheated steam with 165 °C by compressing the 110 °C dry saturated steam coming from the heat pump unit. The mass flow rate of the supplied steam is 0.89 t/h and the COP reaches 2.5 when absorbing waste heat of a hot water source of 70 °C [21].

The transcritical CO_2 heat pump Eco Sirocco offered by Mayekawa supplies hot air. Inlet air is heated from 20 to 120 °C at a thermal output of about 90 kW and a COP of 2.9, when using water of 25 °C as the heat source. Heating air from 30 to 100 °C reaches 100 kW thermal output under a COP of 3.43 [12].

State of research

There are a few experimental research activities in which a sink respectively supply temperature higher than 120 °C was reached so far.

Chamoun et al. [30] have shown the technical feasibility of a condenser temperature up to 145 °C with water as the working fluid. Therefore, a twin-screw air compressor was adapted. Liquid water is injected to the suction chamber before compression to avoid excessive superheating. The presented heat pump test bench shows high performance, highly depending on the heat source temperature. The heat pump is able to shift a heat source temperature ranging from 85 to 95 °C to a condenser temperature of 145 °C with a corresponding COP between 4.5 and 5.5.

The highest supply temperature of 155 °C was achieved at a test bench with a single-stage HTHP using an internal heat exchanger and R1336mzz-Z as the refrigerant [12]. The system was operated at condenser temperatures ranging from 75 to 160 °C. The latter temperature was reached with a gross temperature shift of 45 K and a COP of 2.67. The results are promising, since the test bench was made up of marketable components, with minimal modifications at the compressor [31].

Refrigerants for HTHPs

Nowadays R134a and R245fa are widely used in HTHPs. However, the European F-gas regulation [32] states that only refrigerants with a GWP lower than 150 may be used in all new heat pumps by 2022. Tab. 1.2 shows properties of the newly developed HFO refrigerants R1336mzz(Z), R1233zd(E), R1234ze(Z), R1234ze(E), and R1234yf for the use in HTHP. Properties for the low GWP natural refrigerants like R718 (water), R744 (carbon dioxide), R717 (ammonia), R600 (butane), and R601 (pentane) are also shown. Essential criteria for the application in HTHPs are the thermodynamic suitability, the environmental impact, and the safety classification [12].

R134a is used in the first stage in case of two-stage HTHPs because of the low critical temperature. R1234yf and R1234ze(E) are shown as candidates of the substitute refrigerant of R134a, due to their similar critical temperature [33].

R1233zd(E) is shown as candidate of the substitute refrigerant of R245fa due to the similar critical temperature [33]. Also, R1234ze(Z) is considered as a promising substitute [12].

The refrigerant R1336mzz-Z is from high interest. The advantages of R1336mmz-Z are: the very high critical temperature of 171.3 °C, a low GWP of 2, an ODP of 0, and good safety properties (safety group A1 which indicates lower toxicity and no flammability). Furthermore, R1336mzz-Z is thermally stable up to 250 °C in the presence of metals commonly used in equipment constructions [34] and, as already proven, it allows condenser temperatures up to about 160 °C [31]. It is considered as a substitute for R123 and R245fa.

As R600 and R601 are highly flammable (safety group A3), these refrigerants are not used in large installations. R717 is toxic and highly flammable, but due to its high volumetric heating capacity it is successfully used in large machines up to 90 °C supply temperature. R744 is used in supercritical cycles [12]. R718 as a refrigerant is discussed in more detail in Chapter 1.5.1.

Table 1.2: Properties of refrigerants for HTHPs, adapted from [12]

Refrigerant	Chemical formula	ϑ_{crit} °C	p_{crit} bar	ODP	GWP	SG
R245fa	$C_3H_3F_5$	154	36.5	0	858	B1
R134a	$C_2H_2F_4$	101.1	40.6	0	1430	A1
R1336mzz-Z	$C_4H_2F_6$	171.3	29	0	2	A1
R1233zd(E)	$C_3ClF_3H_2$	166.5	36.2	0	1	A1
R1234ze(Z)	$C_3H_2F_4$	150.1	35.3	0	<1	A2
R1234ze(E)	$C_3H_2F_4$	109.4	36.4	0	7	A2L
R1234yf	$C_3H_2F_4$	94.7	33.8	0	4	A2L
R718	H_2O	373.9	220.6	0	0	A1
R601	C_5H_{12}	196.6	33.7	0	20	A3
R600	C_4H_{10}	152	38	0	20	A3
R717	NH_3	132.3	113.3	0	0	B2L
R744	CO_2	31.1	73.8	0	1	A1

1.3 Reciprocating compressors

1.3.1 Basic working principles and thermodynamic fundamentals

The basic reciprocating compression element is a single cylinder compressing on one side of the piston. Rotary motion provided to the compressor shaft is converted to reciprocating motion by use of a crankshaft and a connection rod. Heavy duty machines are additionally equipped with a piston rod and a cross head. Piston rings are sealing the cylinder space to the ambient. Spring-loaded suction and discharge valves are used that open automatically when the proper pressure difference exists across the valve. The suction valves opens when the pressure in the cylinder is slightly below the suction pressure. Discharge valves open when the pressure in the cylinder is slightly above the discharge pressure. Fig. 1.8 shows the basic element with the piston at the top dead centre (TDC) and the p,V-chart (indicator card) of the ideal reciprocating cycle. The compression starts at state 1, where both valves are closed. The piston moves to the left, reducing the gas volume resulting in the rise of pressure. Compression ends at state 2, where the pressure inside the cylinder has reached the discharge pressure. The discharge valves opens just beyond state 2. Compressed gas is flowing out through the discharge valves to the plenum. After the piston reaches the bottom dead centre (BDC), the discharge valves closes. The clearance volume is filled with gas at discharge pressure (state 3). During the expansion stroke both valves remain closed and the remaining gas in the clearance space increases in volume. The pressure decreases. This continues until the pressure inside the cylinder drops below the suction pressure at state 4. The inlet valves opens, and gas flows into the cylinder until the end of the reverse

stroke at state 1. The inlet valves closes and the cycle starts again with the next revolution of the crankshaft [35].
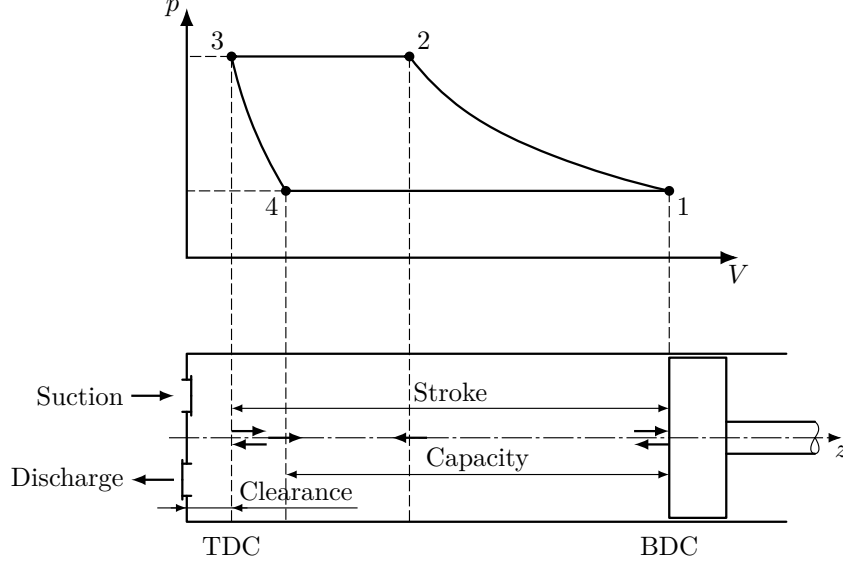

Figure 1.8: Basic reciprocating compressor element and the p,V-chart (indicator card) of the ideal reciprocating cycle, adapted from [35]

The volumetric efficiency VE gives information about the quality of the compression process. It is defined as the ratio of the so-called capacity $(V_1 - V_4)$ and the stroke volume $(V_1 - V_3)$:

$$VE = \frac{V_1 - V_4}{V_1 - V_3} = \frac{\dot{m}\, v_{suc}}{n\, (V_1 - V_3)} \tag{1.9}$$

Where n denotes the rotational speed, $\dot{m}$ the delivery mass flow rate and v_{suc} the specific volume of the suction gas. VE is reduced due to increasing pressure ratio Π and increasing clearance volume V_3. The larger Π is, the larger is the gas volume V_4 after the expansion of the mass trapped in the clearance volume V_3. Consequently the actual capacity $(V_1 - V_4)$ decreases as the mass sucked does [20]. Normal clearance will vary between 4 and 16 % for most standard cylinders [35].

The work to be provided for a single cycle is called indicated work W_{ind} and corresponds to the spanned area in the p,V-chart. The p,V-chart can be determined experimentally [13]:

$$W_{ind} = \oint V\, \mathrm{d}p = -\oint p\, \mathrm{d}V = -\oint p\, A\, \mathrm{d}z = -\oint F\, \mathrm{d}z \tag{1.10}$$

$$P_{ind} = n\, W_{ind} = \dot{m}\, w_{ind} \tag{1.11}$$

Where P_{ind} denotes the indicated power, w_{ind} the specific indicated work, F the force on the piston, and A the net cylinder area.

For reversible compression cycles it can be shown that:

$$w_{ind} = \int_1^2 v \, \mathrm{d}p \tag{1.12}$$

Hence, just the compression sub-process from state 1 to state 2 has to be considered, when discussing the specific indicated work. The optimum compression process concerning the indicated work is the reversible isothermal compression. Assuming the ideal gas, the specific indicated work can be determined by

$$w_{ind} = R\,T_1 \ln\left(\frac{p_2}{p_1}\right) \tag{1.13}$$

with R as the fluid's specific gas constant. This assumption requires ideal cooling and slow compression. In real compressors, heat removal is very limited, so that isentropic (reversible, adiabatic) compression is more appropriate than isothermal compression to describe the process. The specific indicated work and the discharge temperature are increased.

$$w_{ind} = \frac{\kappa}{\kappa - 1}\,R\,T_1 \left(\left(\frac{p_2}{p_1}\right)^{\frac{\kappa-1}{\kappa}} - 1\right) \tag{1.14}$$

$$T_2 = T_1 \left(\frac{p_2}{p_1}\right)^{\frac{\kappa-1}{\kappa}} \tag{1.15}$$

κ denotes the isentropic exponent. However, adiabatic compression is never obtained exactly, since some heat is always removed or added. Therefore, compression takes place along a polytropic change in state. The isentropic exponent in Eq. 1.14 and Eq. 1.15 is replaced by the polytropic index k. k is determined experimentally for a given type of machine and may be lower or higher than the isentropic exponent κ [35]. If k is smaller than κ, the cooling of the cylinder space is more intense. As the rotational speed increases, the time for heat transfer becomes smaller and the actual process approaches the isentropic process $(k \rightarrow \kappa)$ [13].

During the compression process several phenomena are causing irreversibilities. Among them are friction losses in the mechanical compressor's components, fluid friction losses, fluid leaks towards the suction valve, and a very significant due to pressure losses in suction and discharge valves. In addition, the model assumption of an ideal gas is just sufficiently accurate for moderate pressures. That leads to the introduction of the isentropic efficiency. It's defined as the ratio of the ideal enthalpy change of the isentropic compression and the enthalpy change of the actual compression [20]:

$$\eta_s = \frac{h_{2s} - h_1}{h_2 - h_1} \tag{1.16}$$

1.3.2 Concepts to decrease the compressor discharge temperature

As outlined in the previous chapter, optimal compression concerning energy consumption claims an isothermal process. Furthermore, the permissible compressor discharge temperature is limited for different reasons. Limitations regarding the heat pump process have already been discussed in Chapter 1.2.2. Oil accumulations can cause fires or explosions in downstream sections of oil-lubricated air compressors. In gas compressors, unwanted chemical reactions or lubrication problems limit the discharge temperature. For non-lubricated compressors with self-lubricating sealing elements, the wear rate increases with increasing temperature to unacceptable levels [13]. Therefore, different cooling possibilities should be presented.

The cylinder design specifies the available area for the heat exchange between gas and cylinder. Typical machines with increased heat transfer area include a small diameter cylinder with a long stroke or a large diameter cylinder with a short stroke [36]. However, it's not always possible to realise such a design. In addition, forced cooling through the cylinder barrel and heads is most common for heavy duty compressors. The cylinders and cylinder heads are surrounded by water jackets. Thermal energy is removed by the flowing water and the heat transfer from the metal to the water is much more efficient than the heat transfer from metal to the surrounding air [14].

The internal cooling of reciprocating compressor parts is a promising technology to reduce the temperature. In case of a double-acting cylinder, the piston and the piston rod as well are thermally stressed due to their direct contact with the working fluid and due to friction at the sealing gaps. A two-phase coolant is contained within the hollow piston and the piston rod. Owing to the reciprocating motion, both phases are generally intermixed and the fluid flows back and forth between both ends of the cavity. Thereby, thermal energy is absorbed from warmer parts and released at the colder oil-lubricated cross head [37].

A very effective technique to approach an isothermal process is to apply multi-stage compression with intercoolers and an aftercooler. Fig. 1.9 illustrates idealised multi-stage compression and idealised single-stage compression with equal total compression ratios in the p, v-chart, starting with state 1 and finishing with state 3. The grey area represents the energy savings due to the multi-stage operation with intercooling. Fig. 1.10 shows the processes in the T, s-chart. The grey area represents the decrease of the thermal energy removed from the system by the intercoolers, hence, it also represents the energy savings. After each intercooler, the fluid's temperature again equals the suction temperature. Assuming an infinite number of compression stages, the process will approach isothermal compression. But there is a limitation in the number of stages. The additional required equipment for each stage causes additional costs and increases the size of the system. Furthermore, each intercooler introduces additional pressure losses [13].

All the presented concepts have one thing in common. Considering the cylinder space, they are kind of a dry cooling mechanism. Machines that involve direct contact of the compressed gas with liquids try to benefit from the liquid as an external agent to absorb the heat of compression.

Representatives of this group are liquid piston and liquid ring compressors. In case of the liquid piston compressor, a so-called liquid piston directly compresses the gas and is used as a
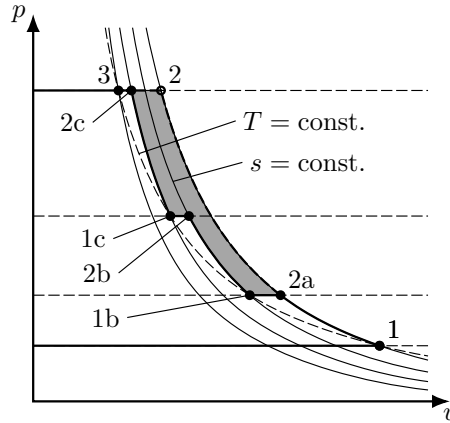
Figure 1.9: Comparison of idealised multi-stage and idealised single-stage compression with equal total compression ratios in the p, v-chart

medium to carry thermal energy out of the cylinder. For example, the liquid piston is controlled by switching the inlet and outlet of the hydraulic valve between two cylinders. In this arrangement, one liquid piston is emptying while the other is filling. However, liquid piston compressors have certain drawbacks. First, at high pressures gas can be solved in the liquid and possibly cause cavitation in low pressure areas of the system. Second, the liquid can leave the cylinder when discharging the gas through valves [36].

Another option of a liquid cooling mechanism to decrease the compressor discharge temperature is the injection of wet vapour or a liquid directly into the cylinder or into the suction pipe. The injection applications discussed in Chapter 1.2.3 are all in conjunction with rotary compressors. Considering reciprocating compressors with injection cooling, special attention must be paid to prevent damage by hydrostatic lock. Hydrolock occurs when the volume of a liquid is greater than the clearance volume of the cylinder. The piston cannot complete its stroke, since liquids are almost incompressible. Consequently, mechanical failure can occur [38].

The development of an reciprocating air compressor using direct water injection to achieve quasi-isothermal compression is presenter in [39] and [40]. Water is sprayed in the cylinder in high quantity that is sufficient to achieve cooling without significant vaporisation. The cylinder with a diameter of $385\,\mathrm{mm}$ and a stroke of $400\,\mathrm{mm}$ was equipped with 360 nozzles and a novel discharge valve to provide inherent safety features. The tests have been done at rotational speed up to $380/\mathrm{min}$ and pressure ratios up to 25. It was shown that the transient air temperatures can be maintained below $100\,^{\circ}\mathrm{C}$ compared to an adiabatic discharge temperature of about $500\,^{\circ}\mathrm{C}$.

Another investigation concerning the effectiveness of the internal water spray cooling in reciprocating air compressors is shown in [41]. The application is based on the concept of suction injection cooling. Water is sprayed into the suction pipe, where the drops and the suction air are mixed before entering the cylinder. Sensible heat and latent heat are transferred between drops and the air. It was indicated that the lower the mean drop diameter, and the longer the
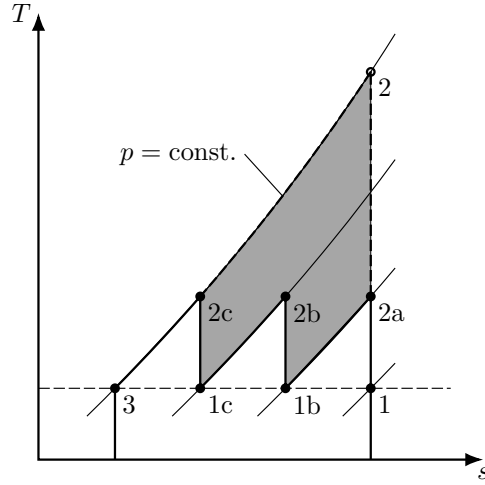
Figure 1.10: Comparison of idealised multi-stage and idealised single-stage compression with equal total compression ratios in the T, s-chart, adapted from [13]

suspending period of the drop, the better the cooling effectiveness is. Compared to the reference case with a pressure ratio of 8, a decrease in the discharge temperature of $28 \, \mathrm{K}$ was achieved. However, deposition of drops in the suction pipe, plenum, and suction valve aren't avoidable. Water accumulations cannot be excluded.

Friedl et al. [42] planned to apply the concept of suction injection cooling on a heat pump cycle with a reciprocating compressor. The refrigerant itself serves as the injected medium (cf. Chapter. 1.2.3). Initial numerical studies and experimental tests have shown that the drops generated by the nozzle would be to large (up to $120 \, \mu\mathrm{m}$) to pass their way into the cylinder space without deposition, especially through the suction valve. Operation without risking a compressor failure was not possible under the circumstances. The reciprocating compressor seems to be disadvantageous for suction injection cooling, especially because of the tight path through the suction valve [43].

1.4 Supplementary applications of injection cooling

Applications of injection cooling in compressors have been discussed so far. More specifically, this has just concerned the sub-category of positive displacement compressors. Injection cooling is also applied in turbo compressors for the compression of water vapour, air, and other gases [44]. Apart from the compressor technology, there are other fields of application too. Some of them should briefly be outlined.

Water injection at internal combustion engines reduces, the combustion temperature, $\mathrm{NO_x}$ and soot emissions, and tends to reduce fuel consumption [45]. In this context, there are numerous scientific papers in which different types of engines and injection options are investigated: water

injection to the intake manifold of a naturally aspirated petrol direct injection engine [46], fuel water injection through one and the same nozzle hole or through separate nozzle holes of a large size diesel direct injection engine [47], or direct water injection in a turbocharged diesel engine [48].

In the so-called wet gas turbine cycle, water or steam is injected in different parts of gas turbine, e. g. before the compressor inlet, between compressor stages, or directly into the combustor [49]. In doing so, the advances are the same as with the injection cooling in internal combustion engines. Injection cooling is applied extensively to stationary gas turbines. The application for aero engines, in which fuel consumption plays a key role, is very limited [50, 51].

Injection coolers are also used in steam generators to control the temperature of the working fluid. The steam temperature should be kept constant before it enters the superheater or the steam turbine. The advantage of the injection cooler lies in its simple design and, compared to heat exchangers, in its higher control rate. Usually, injection coolers are placed between the superheaters. Injection immediately upstream of the high pressure or medium pressure turbine is generally avoided to prevent the risk of turbine blade damage due to injection water drops [52].

1.5 Theoretical investigations

The use of water as a refrigerant in HTHPs creates opportunities as well as technical challenges. General investigations are presented in this regard. In particular, the aspects and additional challenges of using reciprocating compressors in conjunction with injection cooling are clarified. The compressor is the heat pump's most complex component and therefore demands the central part of the investigations.

1.5.1 Water as the working fluid

Water (R718) is a natural refrigerant, hence it does not have to be produced synthetically. It's completely neutral in regard to harmful effects on humans, animals, and the environment. The GWP equals zero and so does the ODP. It's non-toxic, non-combustible, and non-explosive. Furthermore, it shows a high enthalpy of vaporisation, good heat transfer properties, good chemical and thermal stability. It's cheap and available in sufficient quantity. That's important in concern of large heat pumps. In particular, the high critical temperature should be mentioned, since this is an important property of refrigerants for subcritical operated HTHPs. The critical temperature of organic working fluids is much lower (cf. Tab. 1.2) [1, 12, 53].

That compares with some disadvantageous properties. Due to the low volumetric heating capacity VHC, high volume flow rates and thus large compressors are required for higher thermal outputs. The claimed temperature shifts of the heat pump process with the corresponding compression ratios Π result in very high compressor discharge temperature causing extreme thermal loads to components used in the compressor. Furthermore, conventional lubricants are not soluble in water and corrosion of machine components by dissolved gases, such as oxygen and carbon

dioxide, is possible. In addition, the vapour pressure of water is lower than the atmospheric pressure for temperature ranges below 100 °C. Depending on the temperature level of the heat source, vaporisation in partial vacuum is required. This partial vacuum implies challenges for the compressor design, especially for sealing the affected zones from the environment [1, 53].

At first glance, water appears rather unsuitable for efficient use as a refrigerant in HTHPs, in particular due to the low volumetric heating capacity and the high required compression ratio. There are some technical problems to cope with, such as the risk of corrosion and high thermal loads on the compressor components. The usage of austenitic stainless steels for the components in contact with water vapour contains the corrosion effects. Theoretical investigations are carried out to examine other negative aspects. An idealised heat pump process, according to the T, s-chart illustrated in Fig. 1.2, with a temperature shift of $(\vartheta_H - \vartheta_C) = 50\,\text{K}$ and an isentropic efficiency $\eta_s = 0.8$ is examined for different refrigerants. Depending on the refrigerant, the considered condenser temperature ϑ_H ranges from 60 °C to $(\vartheta_{crit} - 10\,\text{K})$.

Compression ratio

Fig. 1.11 shows the dependency of the compression ratio Π on the condenser temperature ϑ_H for different refrigerants and the introduced operation case. All the illustrated trends are
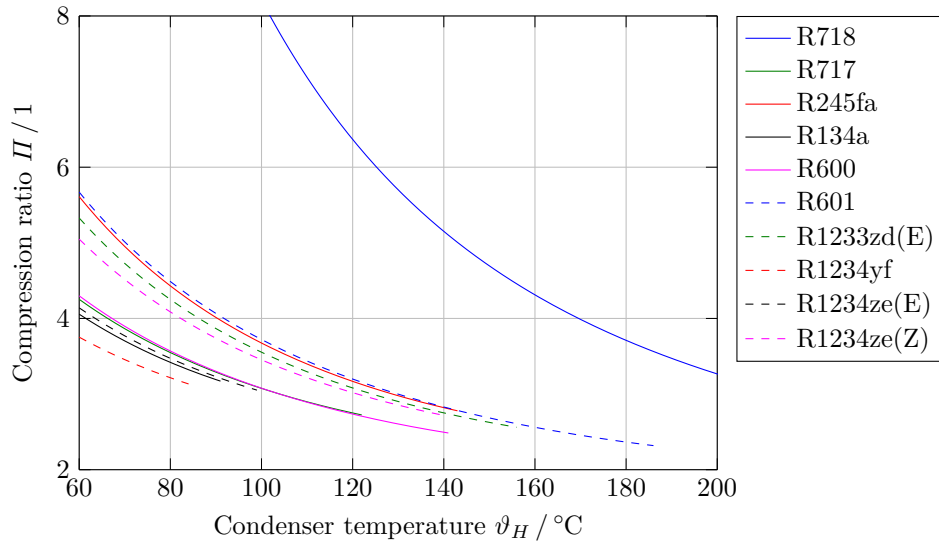
Figure 1.11: Required compression ratio for a temperature shift of $(\vartheta_H - \vartheta_C) = 50\,\text{K}$ of different refrigerants with a maximum condenser temperature of $(\vartheta_{crit} - 10\,\text{K})$

showing the same behaviour. The compression ratio decreases with rising condenser temperature. Aside from water, these graphs are close together at a similar range of values. Water shows an acceptable compression ratio of 4 at a condenser temperature of about 170 °C. As described in Chapter 1.2.1, high compression ratios are associated with increased compressor work and have

negative impact on the COP and should therefore be kept low. With regard to the compression ratio, the application range of water as the refrigerant can be interpreted as shifted to higher temperature conditions.

Coefficient of performance

Further investigations reveal that water has an acceptable theoretical COP at low condenser temperature and an excellent COP for elevated condenser temperatures (cf. Fig. 1.12). This characteristic can be explained by the distinctive two-phase region of water, which corresponds to a high enthalpy of vaporisation. High enthalpy of vaporisation positively effects the COP. The typical course of the COP has a maximum at a certain condenser temperature and drops significantly for higher ones. As the condenser temperatures gets closer to the critical temperature, the enthalpy of vaporisation approaches to zero. The trend for water does not drop in the illustrated temperature range, since there is still a significant distance to the critical temperature of 373.9 °C.
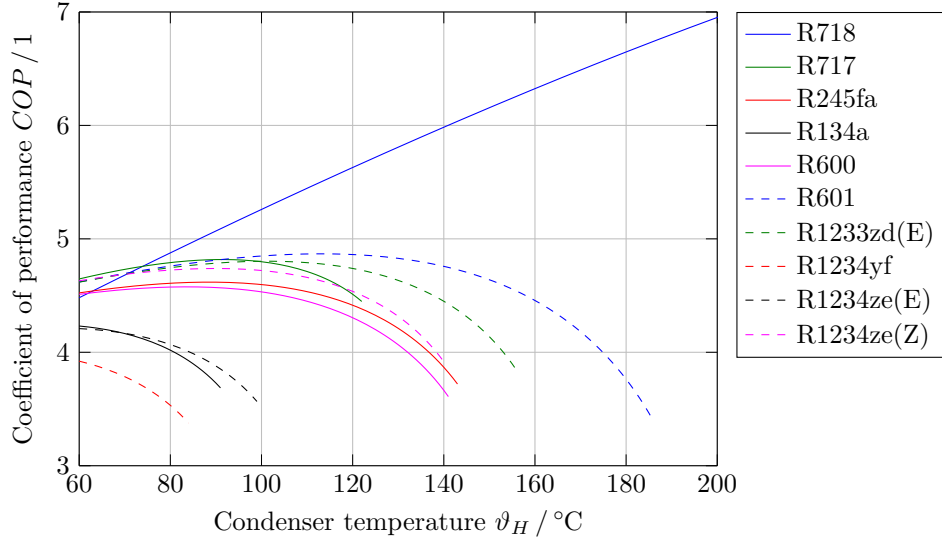
Figure 1.12: Theoretical COP of a heat pump process with a temperature shift of $(\vartheta_H - \vartheta_C) = 50\,\text{K}$ and an isentropic efficiency $\eta_s = 0.8$ for different refrigerants with a maximum condenser temperature of $(\vartheta_{crit} - 10\,\text{K})$

Volumetric heating capacity

Fig. 1.13 compares different refrigerants in terms of their volumetric heating capacity over the condenser temperature. The VHC addresses the required suction volume flow rate at a given thermal output. Low volumetric heating capacities necessarily lead for high thermal output to large compressors, which are difficult to design and consequently are causing high costs. The

practical limit is around 0.5 to $1\,\mathrm{MJ/m^3}$ for efficient compressors [12]. For the considered case, this corresponds to a condenser temperature of 120 to $140\,^{\circ}\mathrm{C}$ and an evaporator temperature of 70 to $90\,^{\circ}\mathrm{C}$.

This characteristic of steam is well known from its clockwise Rankine cycle. The low pressure part of the steam turbine, often expanding the steam till partial vacuum, has large dimensions compared to the high and medium-pressure part.
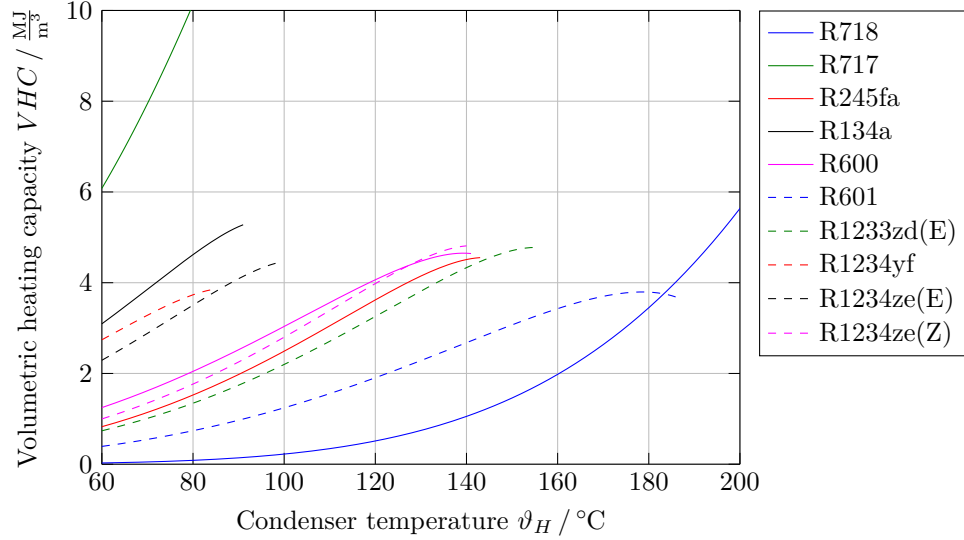
Figure 1.13: Theoretical VHC of a heat pump process with a temperature shift of $(\vartheta_H - \vartheta_C) = 50\,\mathrm{K}$ and an isentropic efficiency $\eta_s = 0.8$ for different refrigerants with a maximum condenser temperature of $(\vartheta_{crit} - 10\,\mathrm{K})$

The suitability of common refrigerants used in HTHPs has been considered for a given operation range in the basis of their Π, theoretical COP, and VHC. The change of the thermodynamic properties with increasing temperature and the high ϑ_{crit} leads to advantageous values of the mentioned quantities for water. It's shown that water becomes increasingly attractive, as the condenser temperature approaches $200\,^{\circ}\mathrm{C}$. In addition, the fact that the evaporator is operating in partial vacuum for temperatures below $100\,^{\circ}\mathrm{C}$ has certain disadvantages. As a result, it is suggested that water is suitable as a refrigerant for the use at elevated heat source temperatures and in the second stage of a cascaded heat pump cycle.

Compressor discharge temperature

The compressor discharge temperature is significantly higher when compressing water vapour, compared to common refrigerants. A single-stage isentropic compression process with a compression ratio of 5 starting at the dew line is used to approach the situation. R134a is used as the representative of conventional refrigerants. The changes in state are shown in Fig. 1.14 as ϑ, s-charts for R134a on the left and for R718 on the right. It can be observed that the temperature differ-

ence $\Delta\vartheta_s$ and the corresponding superheating $\Delta\vartheta_{sh}$ of the working fluid R718 ($\Delta\vartheta_s = 172.6\,\mathrm{K}$ and $\Delta\vartheta_{sh} = 120.4\,\mathrm{K}$) is much higher than for R134a ($\Delta\vartheta_s = 50.6\,\mathrm{K}$ and $\Delta\vartheta_{sh} = 8.5\,\mathrm{K}$). The isentropic compression process ends at high temperature levels, due to the slightly decreasing dew line and the steeply increasing isobars in the superheated area of water. With R134a, the course of the dew line decreases much steeper. This results in lower levels of superheating during and after the compression. Notice, the scaling of the specific entropy s is stretched for R134a compared to R718. With the same scaling, the dew line of R134a would appear even steeper as shown in Fig. 1.14 and the effect would be displayed even more pronounced.

For the sake of completeness, so-called overhanging refrigerants have an overhanging two-phase region. Isentropic compression of non-superheated suction vapour ends in the two-phase region, thus, without superheating and may cause compressor damage. As a consequence, suction vapour superheating can be necessary [54].
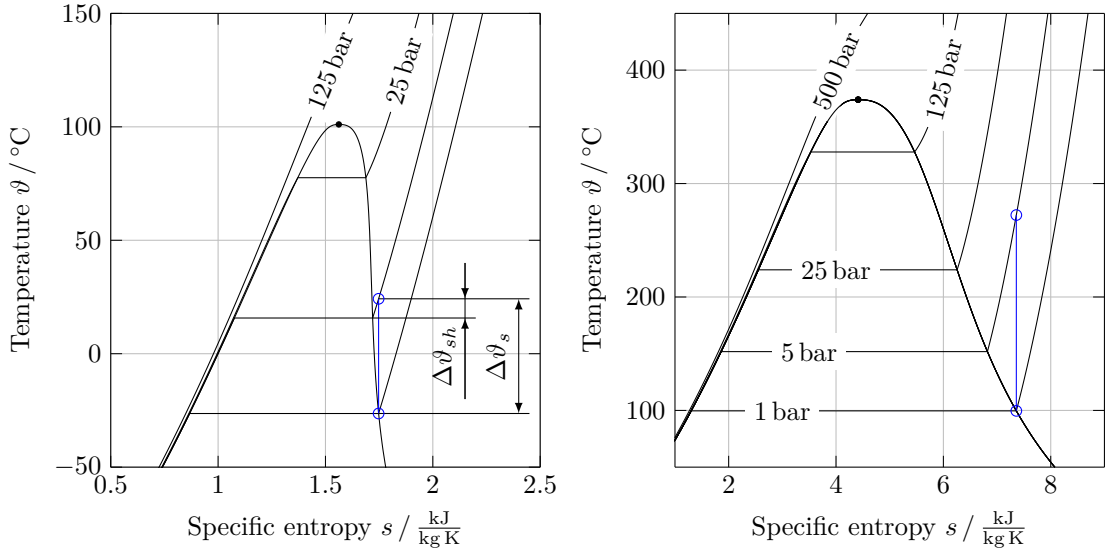
Figure 1.14: Comparison of the superheating caused through isentropic compression of R134a (left) and R718 (right)

The design of the compressor and the selection of materials is critical in concern of the higher appearing thermal load. Different cooling concepts to reduce the compressor discharge temperature and to increase process efficiency have already been introduced in Chapters 1.2.3 and Chapter 1.3.2 and will further be discussed in Chapter 1.5.2 in terms of the considered reciprocating compressor.

As a result, elevated condenser temperatures can be achieved through the usage of water as the refrigerant in HTHPs. Water suits as refrigerant at higher heat source temperatures and in the second stage of a cascaded heat pump cycle. In addition, using water as a refrigerant results in the possibility to operate heat pumps as an open processes.

Open cycles

The major difference to conventional cycles is that open cycles are using the process fluid as the heat pump's working fluid. So-called vapour recompression heat pumps are similar to conventional vapour compression heat pumps. The cycle misses an evaporator, and the compressor takes the working fluid as a vapour directly from the process. Most reported studies concern the application of vapour recompression systems for waste water treatment, for seawater desalination, or for heat pump assisted distillation columns. In most cases, water is used as the working fluid and oil-lubricated compressors cannot be applied due to the required vapour quality [17].

Another open cycle is the direct integration of a heat pump for process steam supply (e. g. in the food and paper industry). Treated process feed water can directly be vaporised, compressed and used as process steam. As a result, the condenser is eliminated and the investment for the heat pump system is significantly reduced [1].

1.5.2 Reciprocating compressor with injection cooling

In order to reduce the compressor discharge temperature, a possibility for cooling has to be provided. On the one hand, this is necessary to limit the thermal load for the materials, and on the other hand, to reduce the required work for compression. As described in Chapter 1.3.1, the optimum in terms of efficiency would be an isothermal compression. But, with the real medium the minimum compressor discharge and suction temperature have to be higher than the medium's saturation temperature to prevent condensation.

Different cooling concepts were presented, as injection of vapour or liquids into the suction pipe or directly into the cylinder and multi-stage compression with intercooling by external heat exchangers. Even though the intermediate cooling is easier to realise, the process with injection cooling performs energetically better. It benefits from the lower transient temperature during the compression stroke. That has a positive effect on the required indicated work. Further, there are no heat losses via the external cooler to the ambient. But there is an increased mass flow rate in the condenser through the vaporised amount of injected water, hence, the thermal output is increased as well. The reduced temperatures during compression also have a positive effect on the piston rings' duration of life. Those are the critical components since they are charged with the highest occurring gas temperature and additionally rub on the cylinder wall [13]. The negative aspect is that injected liquid water can accumulate in the cylinder space, what especially is critical for reciprocating compressors. There's an increased risk of hydrolock and consequently of mechanical failure. At the end of compression all injected liquid water has to be vaporised and the compressor discharge has to be superheated. Hence, the injected quantity and the spray drop diameter have to be chosen appropriately, to reduce the risk of hydrolock. That's essential for both of the mentioned injection methods. However, the investigations on suction injection cooling of Yang, Zhou, and Sun [41] and Koller and Friedl [43] have shown, deposition of drops and water accumulations in the suction pipe, plenum, and suction valve aren't avoidable

especially because of the tight paths through the suction valve. It seems that direct injection is more appropriate, since the liquid vapour mixture does not have to pass manifolds and the intake valve.

The risk of hydrolock is always given, if a liquid is present in the cylinder space. Unlike gases, liquids are almost incompressible. The common countermeasures to avoid hydrolock are: to keep the water inlet temperature of the cooling jacket above the working fluid's saturation temperature at suction pressure, to avoid long and poorly insulated piping, the use of trace heating, to rinse the system with e. g. nitrogen before and after regular operation [1], greater clearance volume, horizontal piston movement with discharge downwards, and the usage of separators between the stages.

The selection of materials for the piston and rider rings is from great importance. Pistons rings are used to seal the cylinder space to the ambient and can be oil lubricated or non-lubricated. If the working fluid cannot be brought into contact with oil for safety (increased temperatures) or hygienic (open cycles) reasons, non-lubricated compressors are required [13]. Usually, two or three diagonally cut rings are used. The rider rings support the weight of the piston and piston rod [35]. Most compressor units are equipped with teflon (PTFE) or other high performance polymer piston rings, where no lubrication is required. PTFE can be used for a maximum gas temperature of about 230 °C. Polyether ether ketone (PEEK) is used up to a maximum durable temperature of 250 °C. The material is advantageous through its mechanical stability, hardness, chemical stability, and good dynamic friction behaviour. Carbon fibre materials can even be used at higher temperatures. However, they are very brittle and do not suit for large pistons. Furthermore, they are much more expensive than polymer rings [1].

The impact of direct water injection on different process variables and process efficiency at elevated condenser temperatures will be investigated in the following chapter. It has to be ensured that neither the process with interstage cooling nor the process with injection cooling exceeds a compressor discharge temperature of 250 °C. An estimation of the required injection mass is made, in order to adjust superheating during compression to a desired value. Furthermore, it's investigated which diameters of the injected drops are permissible to ensure complete vaporisation until the end of the compression stroke, and thus minimise the risk of hydrolock.

Modelling and theoretical investigation of the heat pump cycle and the reciprocating compression cycle with direct injection cooling

The heat pump cycle as shown in Fig. 1.15 is considered in detail, to confirm the outlined statements regarding the evaluation of the different cooling concepts. Special attention is paid to the compression process. The two-stage reciprocation compression process can optionally be operated with interstage cooling or injection cooling. The cylinder geometry corresponds to the parameters from Tab. 1.7. Stage 1 and 2 are designed with a cylinder diameter of 100 mm and 65 mm. The clearance volumes referred to the stroke volumes are 0.1933 and 0.4482. The stroke respectively the piston displacement is 100 mm for both stages. The isentropic efficiencies of

$\eta_s = 0.864$ and $\eta_s = 0.813$ result from the suction and discharge temperatures for the medium water, which are also indicated in Tab. 1.7. The evaporator pressure of $p_C = 1.75\,\text{bar}$ with
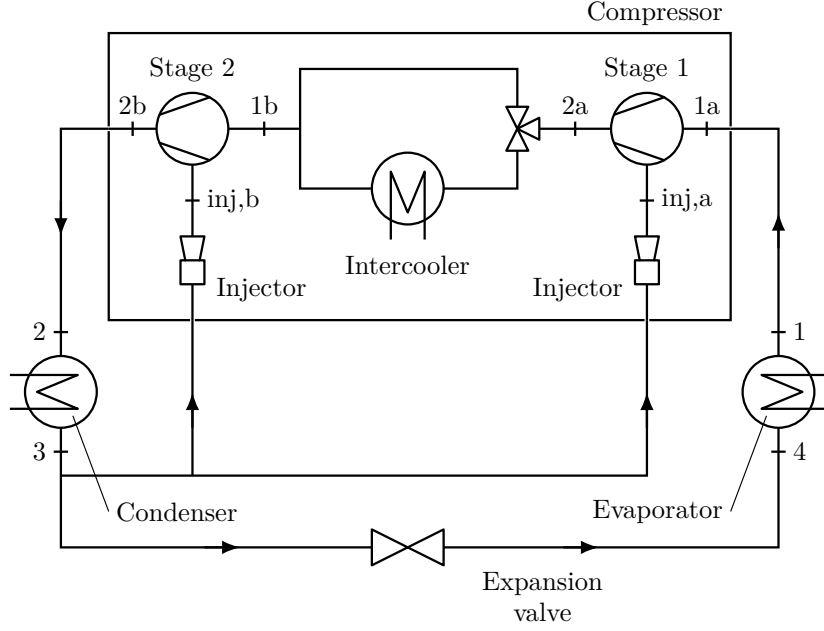

Figure 1.15: Scheme of a heat pump cycle with two-stage compression and optional interstage cooling or injection cooling

the corresponding saturated steam temperature of $\vartheta_C = 116\,°\text{C}$ and the condenser pressure of $p_H = 8.12\,\text{bar}$ with the corresponding saturated steam temperature of $\vartheta_H = 171.4\,°\text{C}$ are selected as boundary conditions. That expresses a temperature shift of $55.4\,\text{K}$. As already discussed, water performs well as a refrigerant in this operating range. A subcooling of $4\,\text{K}$ is present for the condenser outlet (state 3). In case of injection operation, fluid with the subcooled state 3 is injected directly to the cylinder space. Such a basic design requires a minimum of additional equipment and no appreciable additional external energy. However, the mass flow through the evaporator is reduced by the injected mass rates. An additional boundary condition of $4\,\text{K}$ superheating applies for the evaporator outlet (state 1), for the suction of stage 2 (state 1b), and, in case of the injection cooling operated process, for the discharge of stage 2 (state 2b).

Tab. 1.3 summarises the idealised sub-processes of the cycle with interstage cooling and the cycle with injection cooling. The compression process is assumed as irreversible and free from leakage in both cases. Suction and discharge states are coupled via the isentropic efficiencies, the injection quantities, and thermodynamic properties thereof. The sub-processes are shown in Fig. 1.16 as a ϑ, s-chart. It can clearly be seen that the compressor discharge temperatures in the process with injection cooling are significantly lower than in the conventional compression process. For the conventional process the large superheatings are reduced by the intercooler and the condenser. The outlet temperatures in the process with injection are adjusted by the

injection quantity. Thus, the temperature in the cylinder space is already reduced during the compression processes itself. Further, it can be seen that different intermediate pressures occur for the different operation types. The increase of pressure can be explained by the additional mass injected and vaporised after the suction process has already finished.

Table 1.3: Sub-processes of the idealised heat pump cycle with two-stage compression and optional interstage cooling or injection cooling

1 - 2:	Two-stage compression	
	Cycle with interstage cooling	
	1a - 2a:	Irreversible compression
	2a - 1b:	Isobaric intercooling
	1b - 2b:	Irreversible compression
	Cycle with injction cooling	
	1a - 2a:	Irreversible compression with injection cooling
	1b - 2b:	Irreversible compression with injection cooling
2 - 3:	Isobaric desuperheating, condensation, and subcooling	
3 - 4:	Isenthalpic expansion	
4 - 1:	Isobaric vaporisation and superheating	
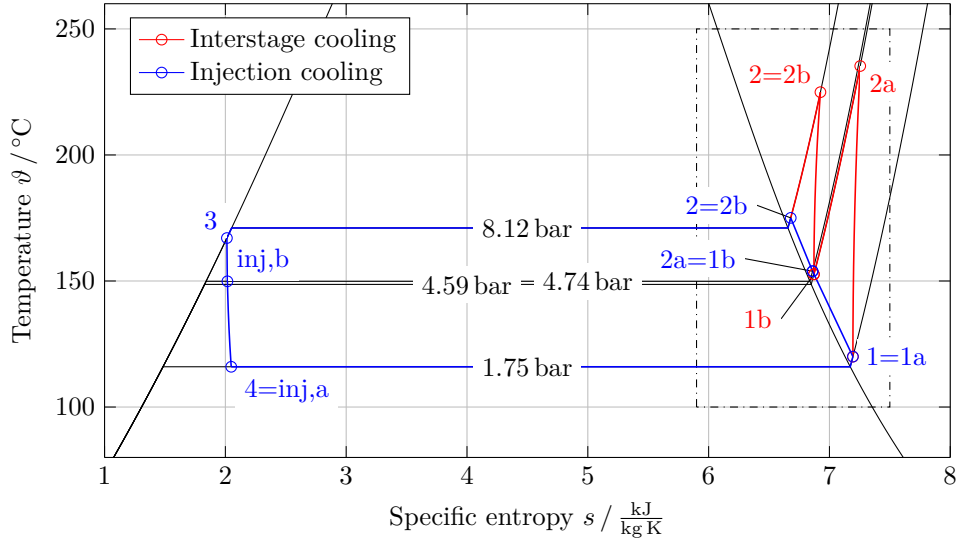
Figure 1.16: ϑ, s-chart of the idealised heat pump process with two-stage compression and optional interstage cooling or injection cooling

The heat pump process with its sub-processes has been considered so far. However, in order to predict the resulting mass flow, the already mentioned intermediate pressure, the required injection quantity, etc. the compression process has to be considered in detail. Tab. 1.4 summarises the

idealised sub-processes of the reciprocating compression process with injection cooling. Fig. 1.17 shows the sub-processes for both cooling concepts in the ϑ, s-chart. By now the clearance volume of the cylinder space is from importance. The working fluid's mass remaining in the clearance volume at the end of the compression stroke (state ch,2) is isentropically expanded till a certain piston position. As soon as the cylinder pressure has slightly decreased below the suction pressure (state ch,3), steam of state 1 is sucked in and mixed isobarically. Consequently, not the entire stroke volume is available as suction volume. At the BDC state ch,1 got reached, the direction of the piston movement changes and the compression stroke begins. 3 different model approaches are implemented, in case of compression with injection cooling. M1 equates an injection at BDC with instantaneous vaporisation, M2 an injection at BDC with delayed vaporisation, and M3 a later injection with instantaneous vaporisation. The injection itself is modelled as an isenthalpic expansion. For delayed injection as in M3, state inj,a and state inj,b aren't according to Fig. 1.17, since the cylinder pressure has already increased. However, the specific enthalpy in the energy balance isn't changing, since an isenthalpic expansion is assumed. The simulation results according to the injection cooling process shown in Fig. 1.17 were obtained under the usage of model M1. The results from model M2 and M3 show almost the same appearance, since most of the states are given as boundary conditions.

Table 1.4: Sub-processes of the idealised reciprocating compression cycle with injection cooling

ch,3 - ch,1:	Isobaric suction of state 1
ch,1 - ch,2:	Irreversible compression with injection cooling
	3 - inj: Isenthalpic expansion
	M1 - Injection at BDC and instantaneous vaporisation
	(1) Isobaric mixing of ch,1 and inj
	(2) Compression to ch,2
	M2 - Injection at BDC and vaporisation at the end of compression
	(1) Compression of ch,1 and compression of inj
	(2) Isobaric mixing with inj to ch,2
	M3 - Injection just before discharge and instantaneous vaporisation
	(1) Compress of ch,1
	(2) Isobaric mixing with inj to ch,2
ch,2:	Isobaric discharge
ch,3 - ch,1:	Isentropic expansion

Tab. 1.5 summarises the most important results which cannot be found directly in the ϑ, s-chart. The stated masses, works, and heat refer to a complete compression cycle respectively one total revolution of the crankshaft. As already mentioned, the intermediate pressure for the injection cooling processes increases slightly. The discharge mass increases due to the additionally injected mass. However, the mass remaining in the clearance volume also increases and the
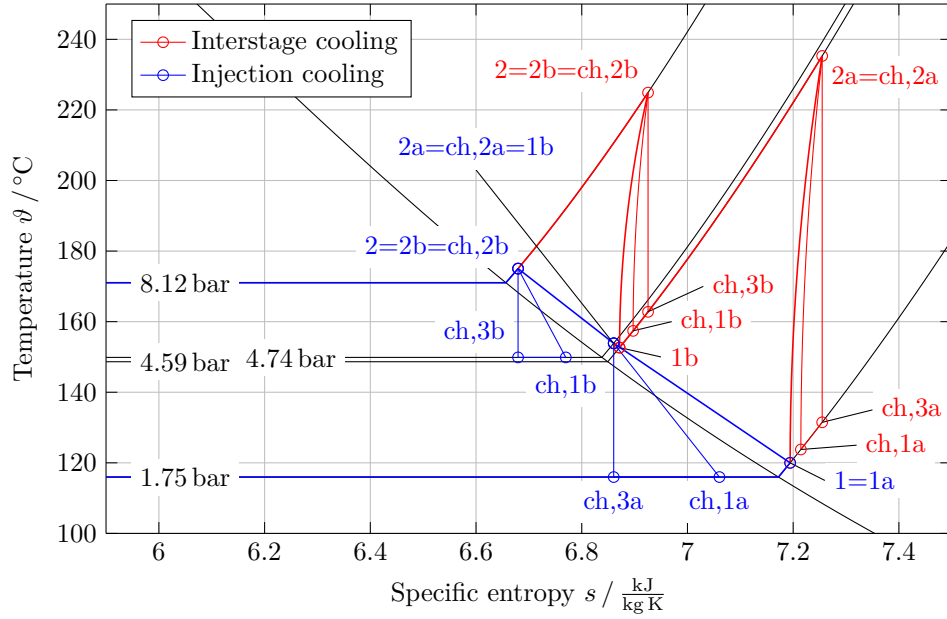
Figure 1.17: ϑ, s-chart of the idealised two-stage reciprocating compression cycle with optional interstage cooling or injection cooling

volume after expansion increases. Consequently the suction mass decreases as the volumetric efficiency does, since it relates to the suction sub-process. That applies to both compressor stages. The determined injection mass is given with approximately 50 mg per revolution for stage 1 and with approximately 32 mg per revolution for stage 2. Referred to the suction mass that corresponds to an injection ratio of about 9 % and 5 %. The area beneath the line connecting state 2 and 3 in the ϑ, s-chart Fig. 1.16 corresponds to the mass flow related heat transferred to the sink by the condenser. This area is visibly larger for the process with intercooling due to its large superheating compared to that of the injection cooling processes. However, a higher thermal output results in all three cases of injection cooling, since the discharge mass flows are higher. It should be noted that the thermal output for M1 is lower than for M2 and M3. That results from the lower discharge flow rate. The transferred specific heat is the same in all three injection cases, since state 2 and state 3 are specified as boundary conditions of 4 K superheating and 4 K subcooling. For all three injection models the required indicated compression work is lower than for the process with interstage cooling, even though the increased flow rate. The work required for model M1 is particularly low. Model M1 assumes that the entire injected water mass vaporises instantaneously at BDC. Hence, during the compression stroke the temperature level within the cylinder space is lower than for the other two models. That approaches an isothermal compression best, which represents the optimum compression process in terms of energy consumption. Hence, M1 performs the best with a COP of about 6.6, although the slightly lower thermal output compared to M2 and M3. That equates a COP increase of 10 %

compared to the process with interstage cooling. In addition, mass flow rates, thermal outputs, and the required power for a compressor rotational speed of 800/min are listed in the bottom section of Tab. 1.5.

Table 1.5: Simulation results of the interstage cooling cycle and the injection cooling cycle with the different modelling approaches

Variable	Interst.	Inj. M1	Inj. M2	Inj. M3	Unit
Intermediate pressure	4.59	4.745	4.759	4.758	bar
Suction mass	609.1	569.3	568.4	568.5	mg
Discharge mass	609.1	648.3	652.9	652.6	mg
Thermal output	1.333	1.344	1.354	1.353	kJ
Coefficient of performance	5.998	6.594	6.287	6.31	1
Stage 1					
Injection mass	0	47.81	51.99	51.59	mg
Injection ratio	0	83.97	91.47	90.75	$\frac{\text{g}}{\text{kg}}$
Indicated work	136.1	124.5	133.1	132.3	J
Volumetric efficiency	78.9	73.75	73.63	73.64	10^{-2}
Stage 2					
Injection mass	0	31.13	32.53	32.49	mg
Injection ratio	0	50.44	52.43	52.4	$\frac{\text{g}}{\text{kg}}$
Indicated work	86.25	79.3	82.19	82.12	J
Volumetric efficiency	75.42	74.08	74.27	74.25	10^{-2}
Rotational speed $n = 800/\text{min}$					
Suction mass flow rate	29.23	27.33	27.28	27.29	$\frac{\text{kg}}{\text{h}}$
Discharge mass flow rate	29.23	31.12	31.34	31.32	$\frac{\text{kg}}{\text{h}}$
Thermal output	17.78	17.92	18.05	18.04	kW
Indicated power	2.964	2.717	2.87	2.859	kW

If the compressor would be designed as a single-stage compressor without injection cooling, an outlet temperature of 375 °C, an overheating of 203.6 K, and a COP of 4.95 would result. The isentropic efficiency therefore was chosen as 0.65, since an increased pressure ratio has negative effects on it [20]. In contrast, there's a COP of 6.6 for the model M1. As a result, the two-stage compression with direct injection cooling suggests a theoretically possible COP increase of 33 %. Further, the compressor discharge temperature of about 375 °C for the single-stage process and of about 235 °C for the two-stage process can be reduced to a desired value.

Theoretical investigations on drop vaporisation

The investigations so far indicate how the injection cooling influences the reciprocating compression and heat pump process. Ideal drop vaporisation has been assumed. However, it's still not clear which conditions have to be fulfilled in order to vaporise the injected water during the compression to achieve the desired cooling effect.

Finely atomised water is injected into the cylinder to cool the water vapour during the compression stroke. The finer the atomisation, the larger is the surface of the atomised water for heat transfer compared to its volume. Thus, the liquid vaporises faster. In other words, for a given drop size, there's a minimum vaporisation duration to achieve complete vaporisation. For this purpose, the vaporisation process of a single water drop at its surface is examined as shown in Fig. 1.18. The drop is assumed to be perfectly spherical symmetric with the diameter D and
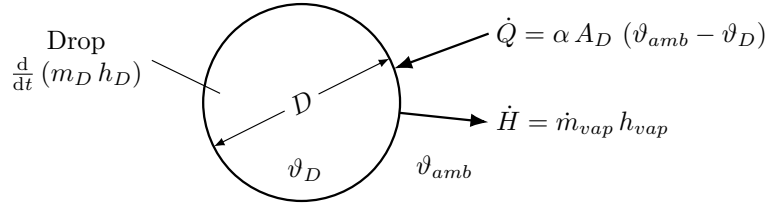
Figure 1.18: Mass and energy balance of a single vaporising drop

consists of saturated liquid water corresponding to the conditions on the boiling curve with the temperature $\vartheta_D = \vartheta_{sat}(p)$. There are no temperature or pressure gradients inside the drop, since saturation prevails. Hence, the lumped parameter model can be applied. The increased pressure inside the drop due to surface tension is neglected. The pressure p and consequently the drop temperature $\vartheta_D = \vartheta_{sat}(p)$ and the ambient steam temperature ϑ_{amb} are rising during the compression stroke. However, a constant temperature difference between the drop and the surrounding steam $\Delta\vartheta = (\vartheta_{amb} - \vartheta_D) = \text{const.}$ is assumed to ensure heat transfer to the drop. Further, it is assumed that the latent fraction of $\dot{Q}$ used for vaporisation is much larger than the sensible fraction for increasing the drop temperature, to guarantee saturated conditions at any point in time.

The change in time of the drop mass m_D equates the mass flow rate $\dot{m}_{vap}$ of the leaving vapour:

$$\frac{\mathrm{d}m_D}{\mathrm{d}t} = -\dot{m}_{vap} \tag{1.17}$$

Assuming a localised liquid incompressible drop the energy balance can be written as:

$$\frac{\mathrm{d}}{\mathrm{d}t}(m_D\, h_D) = \alpha\, A_D\, \Delta\vartheta - \dot{m}_{vap}\, h_{vap} \tag{1.18}$$

With h_D as the specific enthalpy of the drop corresponding to the conditions on the boiling curve, h_{vap} as the specific enthalpy of the leaving vapour corresponding to the conditions on the dew curve, α as the heat transfer coefficient, and $A_D = A_D(t) = \pi D^2(t)$ as the time dependent

spherical surface. The convective heat flow rate $\dot{Q}$ is described by the boundary layer theory (cf. Chapter 2.2.4) and can also be expressed by the theory of similarity [55]:

$$Nu = \frac{\alpha\,D}{\lambda_{vap}} \tag{1.19}$$

Where Nu denotes the dimensionless Nußelt number, λ_{vap} the thermal conductivity of the boundary layer, and D the characteristic length of the geometry. There's also an empiric expression for the Nußelt number depending on the Reynolds number Re and the Prandtl number Pr, if the drop-vapour relative velocity is non-zero. It was obtained from experiments of vaporising single-component drops at atmospheric pressure and moderate ambient temperatures with low transfer rates and is valid for $2 \leq Re \leq 200$:

$$Nu = 2 + 0.6\,Re^{0.5}\,Pr^{0.33} \tag{1.20}$$

The expression reduces to $Nu = 2$ for zero convection. For forced convection with high transfer rates, the correlation was extended by introducing the adjusted heat transfer number

$$B = \frac{c_{p,vap}\,\Delta\vartheta}{\Delta h_v} \tag{1.21}$$

for the assumption that the sensible heat fraction of $\dot{Q}$ is vanishingly low compared to the latent heat fraction for vaporisation. Where $c_{p,vap}$ denotes the isobaric specific heat capacity of the boundary layer and Δh_v the fluid's specific enthalpy of vaporisation. Two different Nußelt correlations for high transfer rates are finally given as [56]:

$$Nu = \left(2 + 0.6\,Re^{0.5}\,Pr^{0.33}\right)\frac{\ln\left(1 + B\right)}{B} \tag{1.22}$$

$$Nu = 2\,\frac{\ln\left(1 + B\right)}{B} + 0.6\,Re^{0.5}\,Pr^{0.33}\left(1 + B\right)^{-0.7} \tag{1.23}$$

However, it's not trivial to estimate the Nußelt number for the complex flow conditions at the drop surface due to the injection and the moving piston. In addition, the pressure in the cylinder changes. Nu is assumed to be constant for further investigations.

The dependence of the spherical drop mass in time can be described as follows:

$$m_D\left(t\right) = \rho_D\left(t\right)\,V_D\left(t\right) = \frac{\rho_D\left(t\right)\,\pi}{6}\,D^3\left(t\right) \tag{1.24}$$

With ρ_D as the drop's density and V_D as the drop volume. Inserting Eq. 1.17, Eq. 1.19, and Eq.1.24 to Eq. 1.18 with the specific enthalpy of vaporisation as $\Delta h_v = (h_{vap} - h_D)$ leads to:

$$-\frac{\mathrm{d}}{\mathrm{d}t}\left(\rho_D\,D^3\,\Delta h_v\right) = 6\,Nu\,\lambda_{vap}\,D\,\Delta\vartheta \tag{1.25}$$

For now, the pressure p is assumed to be constant. Thus, the temperatures and consequently the fluid properties remain constant as well. That leads to the non-linear differential equation of first order

$$D\left(t\right)\frac{\mathrm{d}D}{\mathrm{d}t} = -\frac{2\,Nu\,\lambda_{vap}\,\Delta\vartheta}{\Delta h_v\,\rho_D} = -C = \text{const.} \tag{1.26}$$

with the initial condition $D\left(0\right) = D_{ini}$. As a result, a solution can be found analytically as the case structure:

$$D\left(t\right) = \begin{cases} \pm\left(D_{ini}^2 - 2\,C\,t\right)^{0.5} & \text{if } D_{ini}^2 \geq 2\,C\,t \\ 0 & \text{if } D_{ini}^2 < 2\,C\,t \end{cases} \tag{1.27}$$

from the physical point of view only the positive solution is meaningful.

However, the fluid properties are changing in time, if the system's pressure p changes. The increase of p from suction pressure p_{suc} to discharge pressure p_{disch} is assumed to be linear. p_{disch} is reached at t_{dich} and remains constant thereafter:

$$p\left(t\right) = \begin{cases} p_{suc} + \frac{p_{disch}-p_{suc}}{t_{dich}}\,t & \text{if } 0 \leq t \leq t_{dich} \\ p_{disch} & \text{if } t > t_{dich} \end{cases} \tag{1.28}$$

Consequently, Eq. 1.25 with the given initial condition $D\left(0\right) = D_{ini}$ has to be solved numerically. The initial value problem was implemented and integrated over time using modelling language Modelica [57] and the modelling and simulation environment Dymola [58]. These tools are presented in detail in Chapter 2.3.3.

In the following, the results of the analytic solution for $p = p_{suc} = 1.75$ bar (solid lines) and $p = p_{disch} = 4.6$ bar (dashed lines) as well as of the numerical solution for non-constant pressure (chain dotted lines) are illustrated as a parameter variation in Fig 1.19. The compressor's rotational speed was chosen, as in the previous chapter, with $n = 800/\text{min}$. Liquid water is injected at BDC right after the suction process has finished. The maximum available time for vaporisation was chosen with the duration of a half revolution of the crankshaft $t_{max} = 1/(2\,n) = 37.5$ ms respectively the duration of the compression stroke. If the vaporisation has already been completed upon reaching discharge pressure would even be better, in order to reduce the probability of water accumulation in the cylinder or discharge valve and consequently of hydrolock. $t_{disch} = 1/(4\,n) = 18.75$ ms was estimated as the duration of a quarter revolution of the crankshaft. Two different parameter variations were performed. The chart on the left shows the results for different initial drop diameters D_{ini} with constant $\Delta\vartheta\,Nu$. For the results on the right, $\Delta\vartheta\,Nu$ was varied with $D_{ini} = 15\,\mu\text{m}$. In general, small initial diameters and increasing heat transfer conditions have a positive effect on the duration to complete vaporisation. The differences in the analytical solutions are caused by the pressure dependency of the fluid properties. In particular, the enthalpy of vaporisation decreases with increasing pressure. At higher pressures less thermal energy has to be supplied to vaporise the same amount of liquid water as at lower pressure. In other words, the vaporisation is completed earlier. The duration of
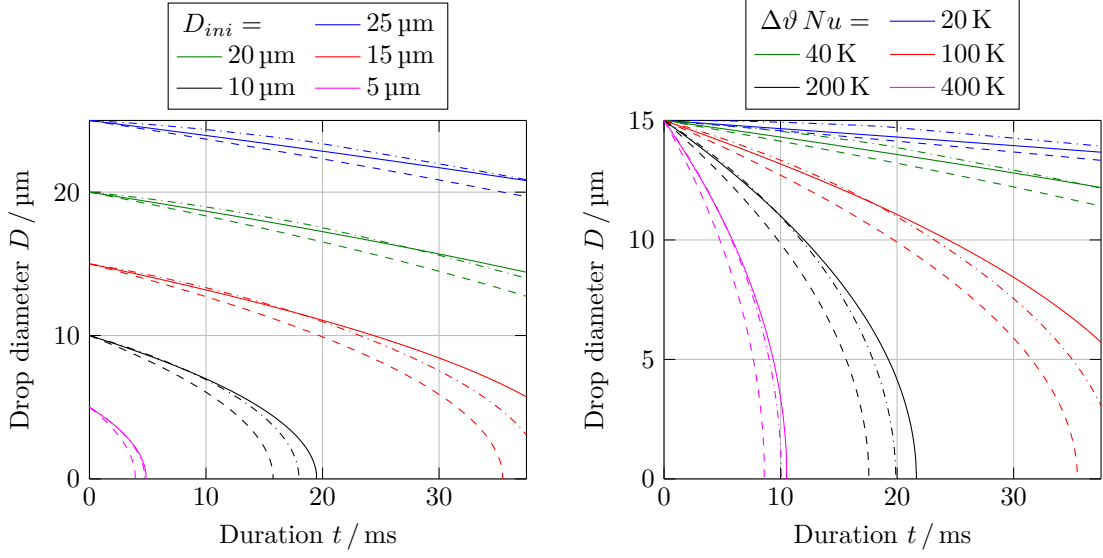
Figure 1.19: Dependence of the drop vaporisation on the initial drop diameter with $\Delta\vartheta\,Nu = 100\,\mathrm{K}$, the present temperature difference and the Nußelt number with $D_{ini} = 15\,\mu\mathrm{m}$

vaporisation for the numerical solutions lies just between the two analytical solutions. However, at the beginning of the simulation the increasing pressure seems to have a negative effect on the vaporisation rate.

As a result, it seems that drops with $D_{ini} < 15\,\mu\mathrm{m}$ vaporise sufficiently fast under advantageous heat transfer conditions for a compressor rotational speed $n = 800/\mathrm{min}$ to provide the desired cooling effect and reduce the risk on machine failure.

For the sake of completeness, the prior taken assumption of neglecting the surface tension should be discussed. The vapour pressure of liquids depends on the prevailing temperature as well as on external forces. Tensile or compressive forces caused by the surface tension can be considered as external forces. Compressive forces arise with convex curving of the surface (drops). Tensile forces are caused by concavely curved surfaces (capillary water). Tab. 2.1 summarises the relationship between drop or capillary radius and the pressure or drag caused by the surface tension. A vapour pressure increase occurs in drops. In capillary water a vapour pressure reduction results. However, that only becomes important when the drop or capillary radius is very small. In particular, the vapour pressure increase becomes significant at drop radiuses of less than $0.01\,\mu\mathrm{m}$ [59]. The assumption to neglect the effects of surface tension is permissible for the examined diameter's order of magnitude. The effect of lowering the vapour pressure in conjunction with capillary water will be discussed at Chapter 2.2.2 in detail.

Drop formation and additional requirements on the injection cooling

In advance, it should be outlined that injectors or atomisers generally do not produce drops of uniform size but a drop size distribution which can be illustrated in a so-called histogram. Different characteristic drop diameters or parameters derived thereof are often used to specify the spray quality. For calculations concerning the heat and mass transfer the so-called Sauter mean diameter SMD is preferably chosen [60]:

$$SMD = \frac{\sum\limits_{i=1}^{N} n_i \, D_i^3}{\sum\limits_{i=1}^{N} n_i \, D_i^2} \tag{1.29}$$

Where n_i denotes the number of drops in the corresponding drop size interval D_i. The actual poly-disperse distribution is replaced by the same number of drops with the same volume surface ratio but mono-disperse size [56].

There are different drop formation mechanisms, depending on the design and operating conditions of injectors. It can roughly be distinguished between dripping, the liquid jet breakup, the liquid sheet breakup, and the atomisation of liquids by gases. A relatively simple drop formation process is dripping from a capillary or from a solid horizontal surface in an acceleration field. If the outlet velocity from the capillary respectively borehole increases, the liquid leaves as a cylindrical shaped continuous body. Different forces affecting the jet's surface lead to interference and oscillations in the liquid. These interferences increase under favourable conditions, the jet gets instable and breaks up into drops. That's referred to as the liquid jet breakup. Different formation regimes with decreasing spray size can be distinguished by continuously increasing the outlet velocity. Another drop formation mechanisms is the liquid sheet breakup. Many technical atomisation processes rely on the breakup of the fluid as conical or flat shaped sheets. First, a fluid sheet is formed, which then breaks up to drops. In addition, liquid drops can be accelerated and disaggregated when a gas encounters their surface with sufficient relative velocity. They are affected by aerodynamic effects. There's talk of atomisation of liquids by gases [60].

The breakup of the liquid and the resulting spray properties depend on a variety of influences, such as flow effects inside the injector, the jet velocity profile and the turbulence at the injector outlet, as well as the physical and thermodynamic properties of the liquid and the surrounding gas. Some influences such as turbulence, inertia, surface tension, and viscosity can be characterised by considering various dimensionless numbers as the Reynolds number Re, the Weber number We, and the Ohnesorge number Oh. It was attempted to combine the breakup affecting forces to find empiric relations about the drop size distribution or a mean drop diameter under the usage of these dimensionless numbers. However, descriptive equations were only found in special cases so far. Hence, experimental investigations are still required to be able to make clear statements for a given application cases [60].

Apart from the achievable drop diameter, there are additional requirements on the injection

system, the injector, and the resulting spray as well, in conjunction with the injection cooling for reciprocating compressors. The spray's angle and penetration length should be large for good spread of the cooling drops in the cylinder space. But not too wide and not too deep to avoid being sprayed directly on the cylinder wall or the piston crown. Otherwise, a coherent liquid film with a minor cooling effect may be formed. Which also increases the probability of liquid water accumulation in the cylinder space. Furthermore, high injection frequencies given by the compressor's rotational speed have to be possible. In the previous considered application case the rotational speed was given as $n = 800/\mathrm{min} = 13.3/\mathrm{s}$. In order to be able to precisely specify the injection timing and the injection quantity a short response time of the injector is required as well. In addition, a rapid opening of the injector is important to ensure full flow in the shortest possible amount of time. The injection process usually starts at the earliest possible point in time just after closing the suction valve. The shorter the injection duration, the more time remains for the drop vaporisation. In the previous application case, an injection mass per revolution of about 50 mg was determined for stage 1 and about 30 mg for stage 2. An advantageous constructive design is also from importance, for simple integration into a conventional reciprocating compressor.

All these additional requirements and the demand of finest sprays are known too well in the automotive industry. Therefore it's obvious to use a marketable product from this industry branch.

1.6   Experimental investigations

An injection system was developed and intensively tested based on the findings of the theoretical investigations. It should meet all the requirements outlined in Chapter 1.5.2. Particular emphasis was placed on achieving the smallest possible drop diameter for rapid drop vaporisation. The determined drop diameter of about 15 µm origins from theoretical investigations. These investigations were carried out under some simplifications. In particular, the determination of the Nußelt number isn't trivial for the complex flow conditions at the liquid's drop surface due to the injection, the moving piston, and the changing cylinder pressure. In order to be able to make founded statements regarding the characteristic of drop vaporisation for hot gas cooling and the risk of machine damage, experimental investigations have to be carried out. An existing reciprocating compressor test bench was adapted for this purpose. The developed injection system was installed to the reciprocating compressor and tested while operating.

1.6.1   Injection system

The requirements on the injection system pose several technical challenges. Among other things, high injection frequencies with high precision in timing and quantity are of importance.

Injector

The central component of an injection system is the injector. Under the usage of simple nozzles it's not possible the achieve drop diameters of about $15\,\mu m$. With an axial hollow cone nozzle drops can be produced with diameters in the range of $50\,\mu m$ [1]. High pressure injectors of the fuel injection field are offered which fulfil the given requirements. Most of the injectors used in the automotive industry are equipped with solenoid technology [45]. However, these are much more difficult to control than the selected piezoelectrically activated high pressure injector HDEV4 [61] manufactured by Robert Bosch AG[3]. The most important technical features are summarised in Tab. 1.6.

Table 1.6: Technical features of the Bosch HDEV4 piezo injector for the medium petrol [61, 62]

Parameter	Value	Unit
Spray angle	85 ± 5	°
Drop size SMD	10 to 15	µm
Penetration	<30	mm
System pressure	200	bar
Needle lift	≤35	µm
Duration till fully lifted	180	µs
Interval duration	≥50	µs
Injection duration	70 to 5000	µs
Injection quantity	0.5 to 150	mg

The injector is actuated according to the piezoelectric principle. By supplying a voltage or electric charge to the multi-layer piezoelectric elements respectively piezo stack, the extent of the piezoelectric crystals change and drive the injector needle [45, 62]. The injector operates at a pressure of $200\,bar$, generates drops of a diameter $<15\,\mu m$ with a spray penetration length of $<30\,mm$, and has a wide range in terms of injection quantity. However, the manufacturer's information in Tab. 1.6 refers to the use of the medium petrol.

Liquid water should serve as the medium in this application which shows other fluid properties compared to petrol. As already mentioned, there are empirical relations to estimate the drop size distribution or a mean drop diameter for a given atomiser, but only for special cases. There are many unpredictable influences affecting the atomisation process. Hence, experimental investigations are required to be able to make clear statements for the given application case, before the injector can be used at the reciprocating compressor test bench. In addition, the absence of lubricating behaviour of water could cause problems. The upcoming tests will also determine, if the injector's duration of life decreases dramatically due to the change in the treated media.

---

[3]https://www.bosch.com/products-and-services/mobility/

High pressure pump

The rest of the injection system can be designed, since the injector has been selected as the system's central component. The injector requires an operating pressure of 200 bar. This is far above the condenser pressure. The minimum system as shown in Fig. 1.15 cannot be implemented under the circumstances. An additional high pressure pump is required. A pneumatically operated hydraulic pump was chosen, with a double-acting piston, a maximum operating pressure of 215 bar, and a bladder accumulator to provide a stable operation pressure.

It should be mentioned that the additional energy to power the high pressure pump has a negative impact on the heat pump's COP. However, the main focus of the investigation is the evaluation of the injection system and its cooling effect.

Control system and amplifier

The control system consists of a real-time aware microcontroller with a clock rate of 16 MHz, a locator providing the TDC position, and a specially developed signal amplifier. The amplifier is equipped with 4 channels, hence, a maximum of 4 injectors can be used.

The typical signal sequence of the locator mounted on the compressor's flywheel is shown in Fig. 1.20. Based on this signal, the microcontroller calculates the start and end time of injection for each compressor stage. It generates the control signal as a simple rectangular function. This signal is boosted by the amplifier circuit to actuate the injector. The resulting control voltage deviates slightly from the perfect rectangular function, due to the capacitive resistance of the piezoelectric elements and the technically limited amperage.
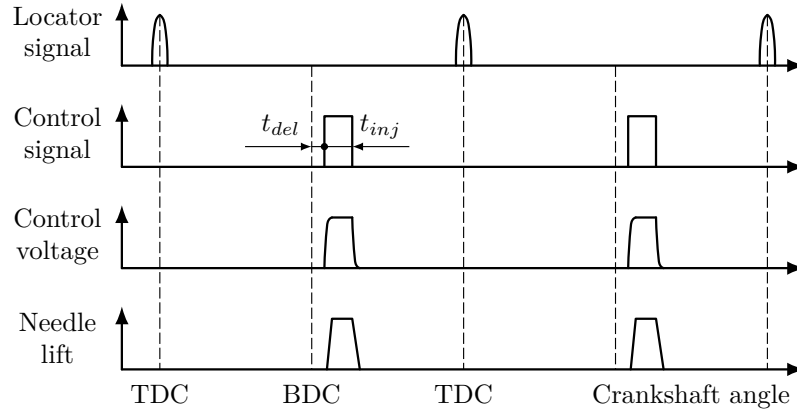
Figure 1.20: Evolution of the locating signal, the control signal, the control voltage, and the needle lift over the crankshaft angle

The delay of the injection start time to the BDC t_{del} and the injection duration t_{inj} can be specified by the user via a serial interface for each compressor stage. The injection parameter set and the compressor rotational speed are logged to a text file during the operation.

The control program has to operate efficiently, in order to be able to precisely specify the injection timing. It works as a loop, hence the same code is repeated over and over. The loop duration t_{loop} is an important quantity to assess the code efficiency. It specifies the smallest possible resolution of the time scale. It was attempt to keep the loop duration as short as possible when the piston is moving from the BDC to the TDC. Thus, the injection start time and end time can be specified very precisely. The loop duration in the mentioned section was reduced from initially 120 µs to 12 µs by optimising the control program code. In other words, it can be injected in 12 µs packages instead of 120 µs packages. The effects on the injection mass trend are shown in Fig. 1.23 and will be discussed in the following chapter. The increase in code efficiency was achieved by shifting various calculation procedures as well as the read-in and read-out via the serial interface to a defined point in time respectively piston position, namely immediately after reaching the TDC. There are no specific requirements regarding efficiency after this piston position.

Determination of the injection mass

The injection system in the first experimental set-up was essentially built of a reservoir filled with distilled water, the high pressure pump, the injector with its fixture, the control system, and amplifier.
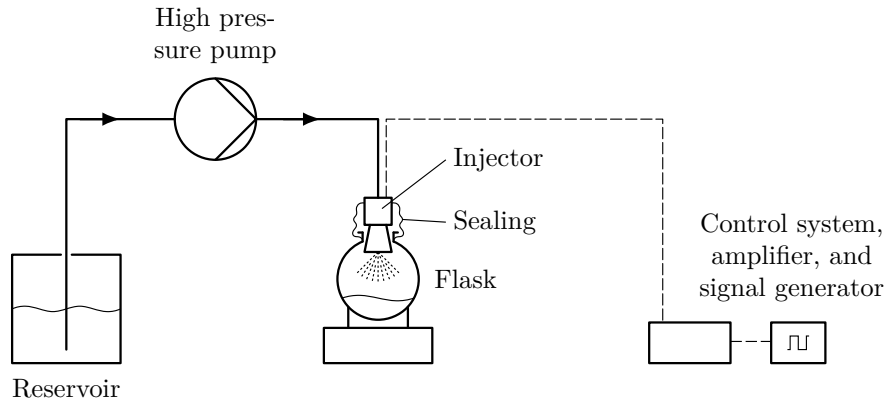
Figure 1.21: Experimental set-up for the injection mass determination

As shown in Fig. 1.21, water was injected into the flask. A sealing connected the injector and the flask to trap all the water. The flask was weighted before and after a certain number of injections of a given injection duration t_{inj}. As a result, the mass per injection m_{inj} could be determined. The used scales had a maximum relative measurement error of 2 %. Since there was no locator in this set-up, the controller's input signal had to be provided by a function generator. Hence the code could be kept as unchanged as possible. Just the number of injections had to be counted in order to stop when reaching the chosen number of injections. However, the loop duration wasn't changed noticeably.

The experiment was carried out at an ambient temperature of about 19 °C and an injection frequency of 15 Hz for different injection pressures and injection durations. The results are graphically summarised in Fig. 1.22 for the permissible range of injection duration according to Tab. 1.6.
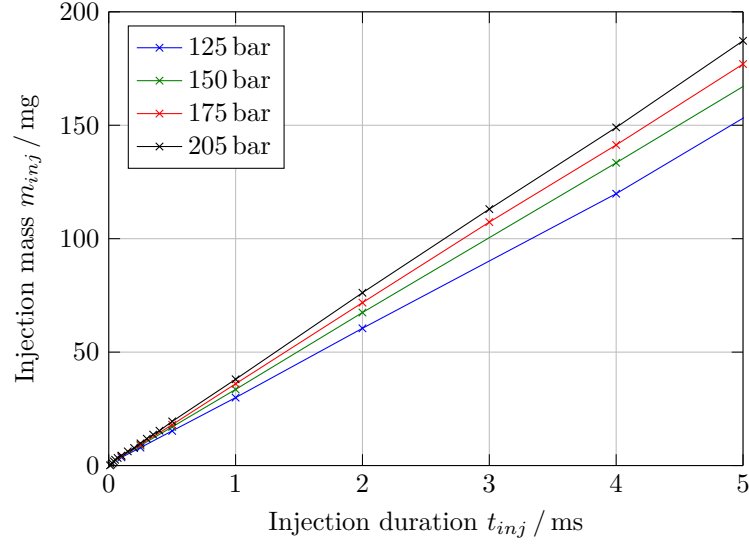
Figure 1.22: The mass per injection depending on the injection duration for different injection pressures

As expected, the injection mass increases with increasing injection pressure for a given injection duration. In the theoretical investigations from Chapter 1.5.2 an injection mass of 50 mg per injection was demanded. In case of an injection pressure of 205 bar that corresponds to an injection duration of 1.3 ms. The crankshaft angle changes approximately 6.2° for a rotational speed of 800/min. The time and crankshaft angel available for vaporisation are reduced by the stated values.

Fig. 1.23 shows the injection mass trend of three test sections with water and the characteristic trend for the original medium petrol [62]. Excepting the green curve, the trends for water show no significant difference compared to the trend for petrol.

The chart on the right side illustrates the opening effect respectively the influence of the needle lift. The curves increase progressively and from a certain point in time they change linearly. Full needle lift got reached at the discontinuity. According to Breitbach et al. [62], the injector has fully opened after 180 μs (blue curve). In the executed tests the complete needle lift was already reached after 50 μs. That leads back to the specially developed signal amplifier.

The green curve is shown to illustrate the influence of the loop duration. It was determined under the usage of the non-optimised control program with a loop duration of $t_{loop} = 120$ μs. The loop duration expresses the smallest possible resolution of the time scale and corresponds to $\Delta m_{inj} = 4.7$ mg packages which can be injected. The red curve was recorded after the
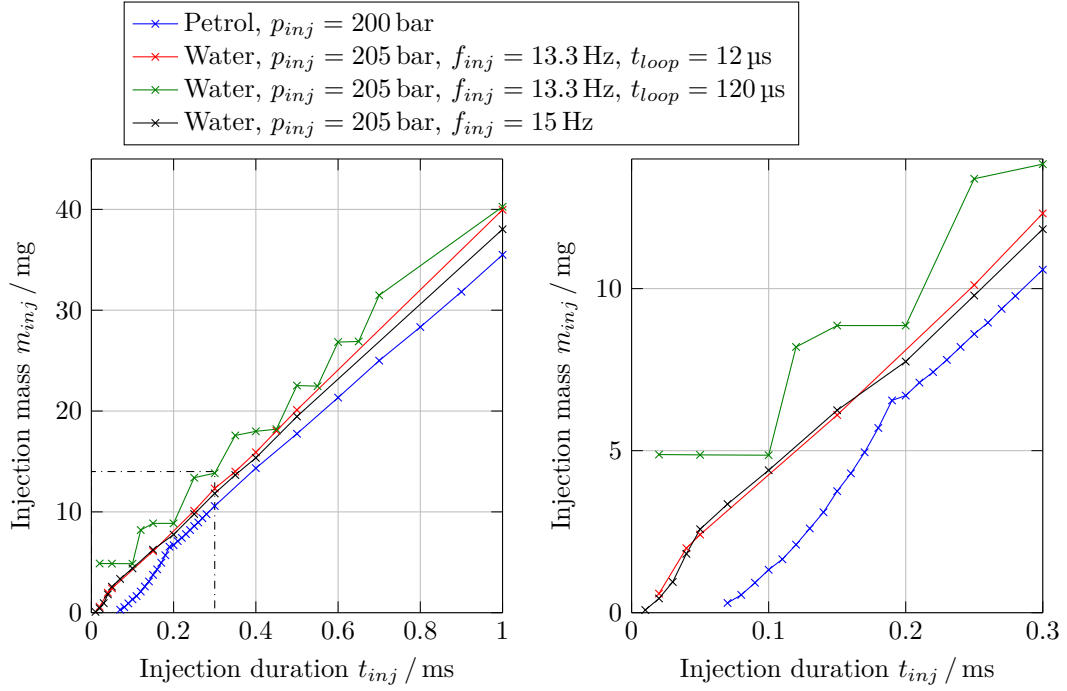
Figure 1.23: The effect of the injector needle lift and the control programs loop duration on the injection mass. Data series of petrol are according to [62].

code optimisation for a loop duration of $t_{loop} = 12\,\mu s$ and a corresponding mass resolution of $\Delta m_{inj} = 0.47\,mg$. With the optimised control program $\Delta m_{inj} = 0.47\,mg$ packages can be inject.

During the tests water was expanded from 205 bar operation pressure to ambient pressure. The counter pressure in the reciprocating compresser corresponds to the suction pressure of the cylinder stage when injecting at BDC. The suction pressure of the second stage equates approximately 4.2 bar (cf. Tab. 1.7). However, the pressure differences are almost the same. Hence, it can be assumed that the counter pressure does not have a significant impact on the injected mass.

In conclusion, the set up injection system has passed the first functional tests and fulfils the requirements with regard to the water injection mass, injection mass flow rate, and accuracy.

Determination of the SMD and drop size distribution

The actual achievable drop diameter and the drop distribution have to be determined experimentally for the medium water, since many external and unpredictable influences affect the atomisation system.

The used measurement system bases on the laser diffraction technique to determine the size of the spray's drops. A laser beam penetrates the spray while the intensity of the scattered light is detected. The measured data are analysed to determine the size of the drops which

46

have caused the diffraction pattern. The drops are assumed to be ideally spherical shaped and can be detected of a size ranging from 0.1 to 3000 µm [60]. The most important results are the distribution of the spray volume over the drop diameter and the Sauter mean diameter SMD.

Fig. 1.24 shows the scheme of the experimental set-up to examining the generated spray. The injection system has not changed compared to the previous attempt system. The flask for collecting the spray water was replaced by the optical measuring device. 10 spray events with a certain injection duration, frequency, and pressure were detected, averaged and evaluated for each experiment. The experiments were carried out at an ambient temperature of about 19 °C.
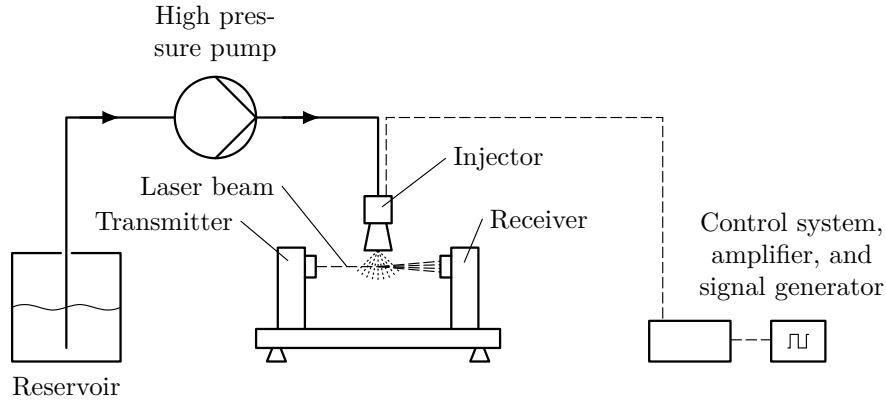
Figure 1.24: Experimental set-up to evaluate the generated water spray

The results of the first parameter variation are shown in Fig. 1.25. The injection pressure and the injection duration were varied at a constant injection frequency of 15 Hz and a measuring distance of the laser beam from the injector needle of 40 mm. The series of experiments for 205 bar represents the reference process and therefore shows finer resolution.

The SMD varies slightly with changing injection duration, but remains to a large extent below 20 µm for a pressure of 205 bar. As the injection pressure decreases, the recorded curve shows a similar shape but shifted to higher SMD values. A $SMD < 15$ µm cannot be generated over the entire injection duration spectrum for 205 bar and the medium water. According to the manufacturer the SMD varies between 10 and 15 µm when using the original medium petrol (cf. Tab. 1.6). Fig. 1.26 illustrates the spray volume distribution. The cumulative spray volume CV is plotted over the drop diameter D for an injection duration of 0.5 ms. According to the previous statements about the pressure dependence, the 205 bar experiment holds the largest volume fraction at small diameters.

Another parameter variation was carried out to investigate the characteristic for different injection frequencies. The injection pressure was kept constant at 205 bar bar and the injector distance from the laser beam was 40 mm. In Fig. 1.27 and Fig. 1.28 the reference case and the curves for increased and lowered injection frequencies are shown. The spray quality does not dependent on the injection frequency.

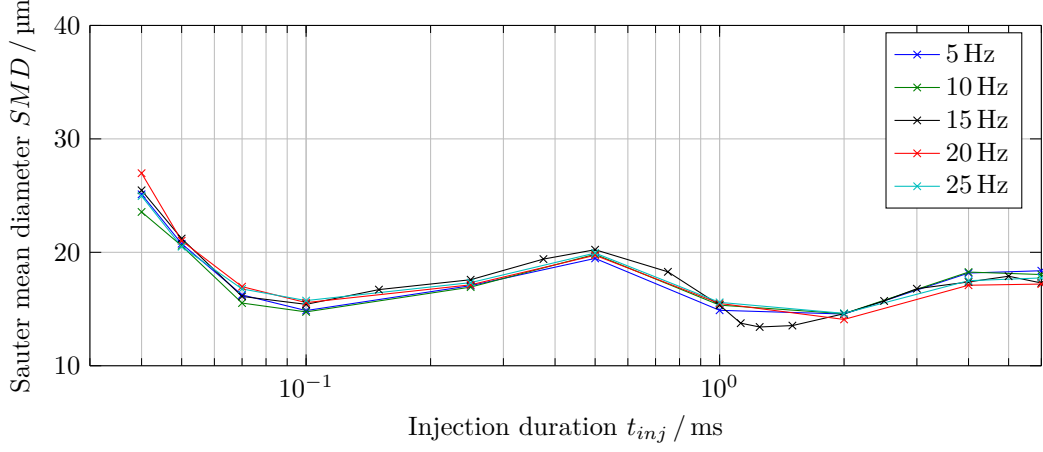Further, the distance of the laser beam from the injector was varied. The tests were carried
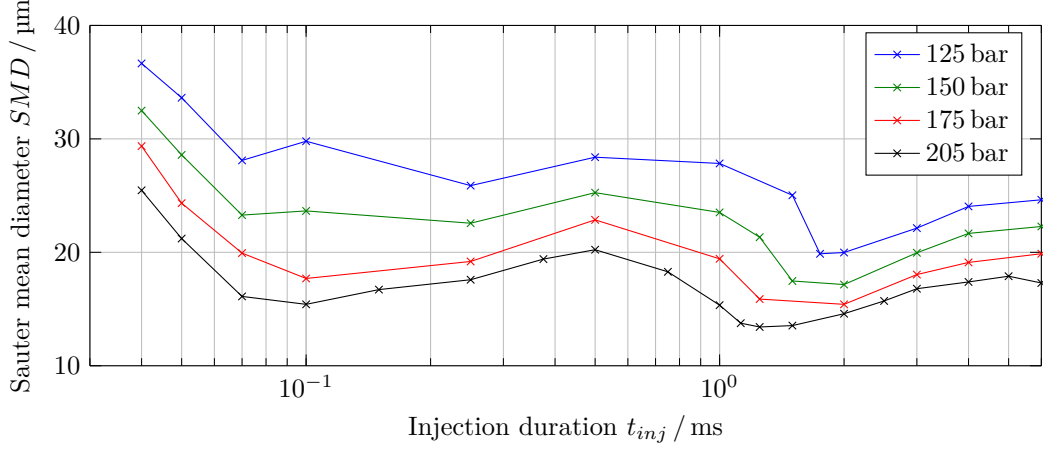
Figure 1.25: The dependency of the SMD on the injection duration t_{inj} and pressures p_{inj} at constant injection frequency $f_{inj} = 15\,\text{Hz}$ and a measuring distance of the laser beam from the injector of $40\,\text{mm}$
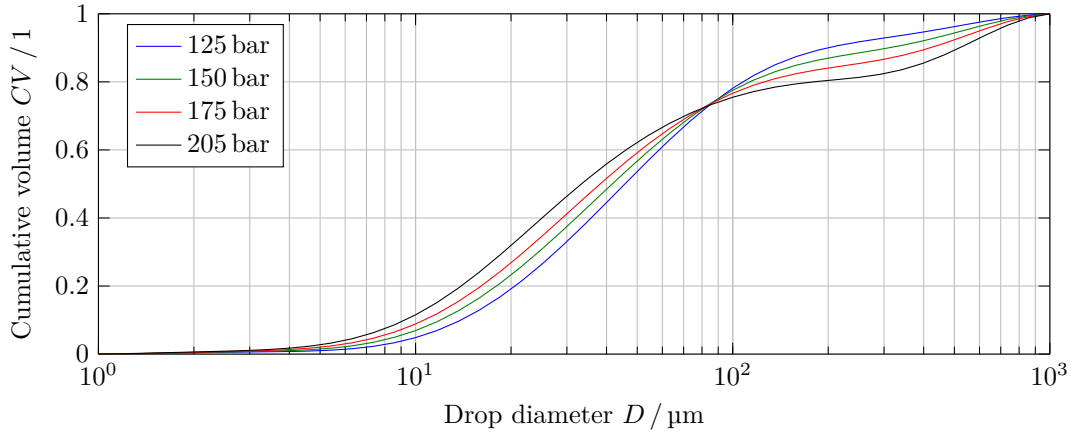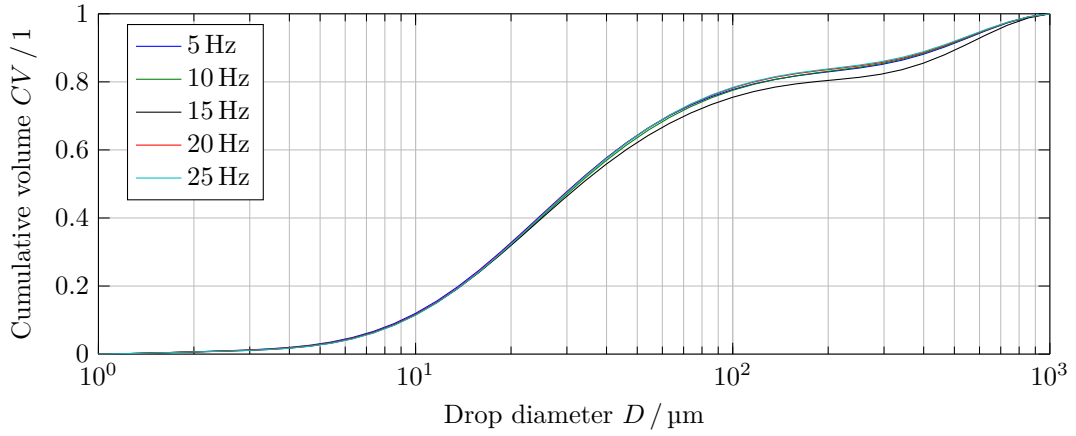

Figure 1.26: The cumulative volume over the drop diameter D for different injection pressures p_{inj} at constant injection frequency $f_{inj} = 15\,\text{Hz}$, injection duration $t_{inj} = 0.5\,\text{ms}$, and a measuring distance of the laser beam from the injector of $40\,\text{mm}$

out at $205\,\text{bar}$ and an injection frequency of $15\,\text{Hz}$ for different injection durations. The curves for the distances 60 and $80\,\text{mm}$ show similar appearance to the reference case. When measuring with the laser closer to the injector ($20\,\text{mm}$) the spray seems to be from poor quality. The spray is not fully developed at this distance. Parts of the spray are shaped as ligaments. The optical measuring method uses the laser diffraction technique and requires ideal spherical drops. Hence, the requirements for a correct measurement are therefore not given. In addition, there's also the mentioned drop formation mechanism namely the atomisation of liquids by gases till a certain distance from the nozzle is reached.

Figure 1.27: The dependency of the SMD on the injection duration t_{inj} and frequencies f_{inj} at constant injection pressure $p_{inj} = 205\,\text{bar}$ and a measuring distance of the laser beam from the injector of $40\,\text{mm}$

Figure 1.28: The cumulative volume over the drop diameter D for different injection frequencies f_{inj} at constant injection pressure $p_{inj} = 205\,\text{bar}$, injection duration $t_{inj} = 0.5\,\text{ms}$, and a measuring distance of the laser beam from the injector of $40\,\text{mm}$

According to Tab. 1.6 the penetration length of the petrol spray is $< 30\,\text{mm}$. But measurements were carried out at distances of 40, 60, and 80 mm. It should be mentioned that injecting to the ambient as in the tests, does not represent the regime in the cylinder space. There's higher pressure in the cylinder which increases after the injection. Further, the fluid is discharged from the cylinder by the piston movement with each revolution. During the suction process fresh gas enters the cylinder. The regime in the cylinder is "reset" with each revolution. However, the periodic spray impulses to the ambient are forming a flow profile which appears with greater penetration length in the tests. Eddies with reversal direction were recognised at the boundary
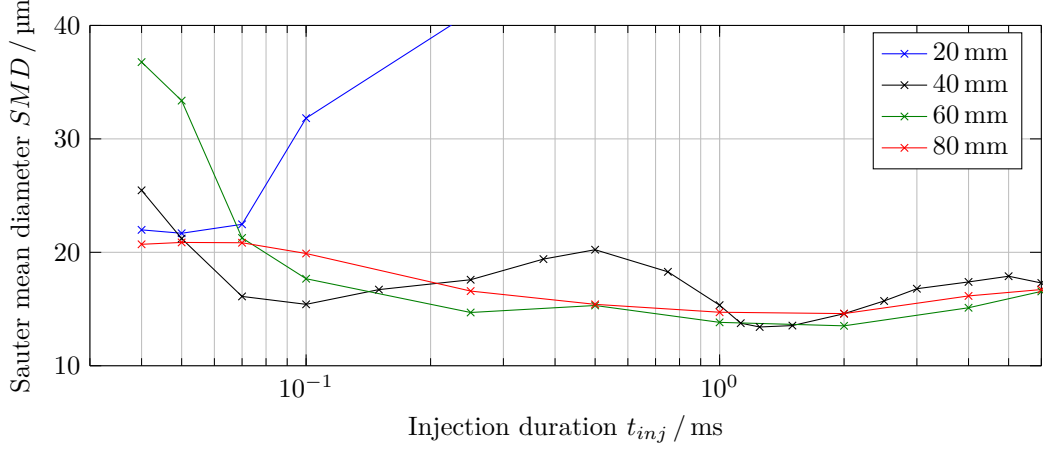
Figure 1.29: The dependency of the SMD on the injection duration t_{inj} and spray length at constant injection pressure $p_{inj} = 205$ bar and injection frequency $f_{inj} = 15$ Hz
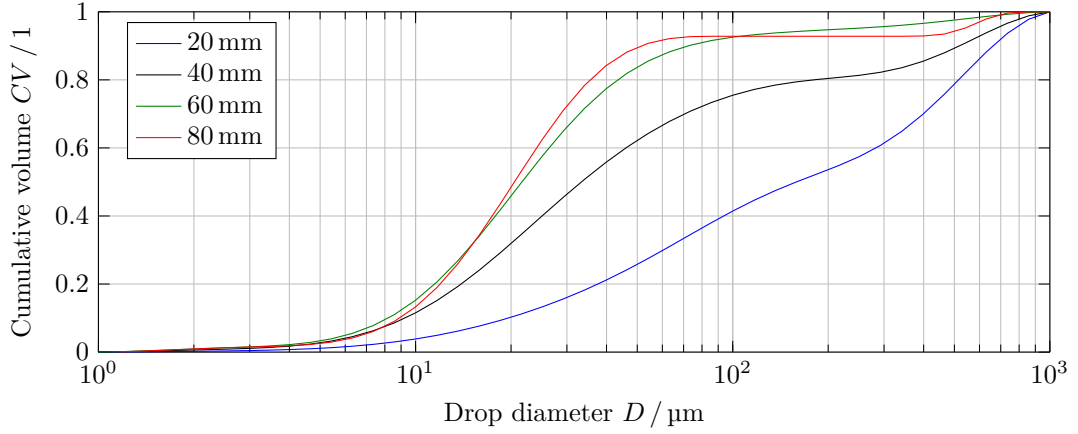
Figure 1.30: The cumulative volume over the drop diameter D for different spray lengths at constant injection pressure $p_{inj} = 205$ bar, injection frequency $f_{inj} = 15$ Hz, and injection duration $t_{inj} = 0.5$ ms

areas of the spray cone. An observation of the real regime is required in order to be able to make clear statements about the influence of the medium water on the penetration length. However, that would have caused too much effort for the tests in advance. It cannot be excluded that parts of the spray collide with the cylinder wall or the piston crown.

It should also be noted that the injection process is performed at higher temperature levels when considering the compressor's cylinder. Due to the low injection mass flow rate the injected liquid prevails at the temperature of the injector's mounting position, namely the cylinder head. Usually, this temperature exceeds the saturation temperature at suction pressure. The

injection results in an expansion to the two-phase region (cf. Fig. 1.16). That is referred to as flash vaporisation. At some fuel injecting nozzles the size and inertia of the drops are reduced by flashing [56]. That would therefore have positive effects on the achievable SMD and the penetration length.

1.6.2   Test bench reciprocating compressor

The experimental set-up including a two-stage reciprocating compressor can be operated conventionally using an intercooler or with direct water injection into the cylinder for hot gas cooling. As outlined in Chapter 1.5.1, water suits as refrigerant at higher heat source temperatures and in the second stage of a cascaded heat pump cycle. The function of a reciprocating compressor for water as the working fluid is evaluated for temperatures up to $120\,^\circ$C source side and up to $170\,^\circ$C sink side according to Tab. 1.7 and Fig. 1.16. That requires a suction pressure of about 1.75 bar and a maximum discharge pressure of about 8.2 bar as the operation boundary conditions of the vapour compressor.

Experimental set-up

An existing reciprocating compressor test bench was expanded at the production site of the manufacturer LMF. The developed injection system was installed to the reciprocating compressor as schematically shown in Fig. 1.31. Additional aggregates are illustrated as well, e.g. units to provide the working fluid and to preheat and rinse the system.

The steam station for providing the working fluid is essentially built of the water treatment, the steam generator, and the expansion valve E1. Feed water is pressed through the water treatment with a pressure of about 5 bar and brought to a water hardness $< 1\,^\circ$dH. Subsequently, the liquid water is vaporised by the electric steam generator to wet steam with $95\,\%$ vapour quality and passed to a buffer tank. After the expansion valve E1 superheated steam is present at compressor suction pressure. The electrical steam generator with a thermal output of $45\,$kW offers a maximum steam mass flow rate of $60\,$kg/h. The piping between E1 and the compressor suction of stage 1 is partly equipped with trace heating to be able to adjust the suction temperature and to compensate heat losses to the environment.

The two compressor stages are arranged in horizontal opposed construction and the manufacturer's design parameters are summarised in Tab. 1.7. The water vapour is stage by stage brought from the suction pressure of about 1.75 bar to the final pressure 8.12 bar. The mechanical drive (crankshaft, cross head, etc.) is oil-lubricated. The cylinder walls respectively sliding surfaces are from non-lubricated design, because of the low solubility of oil in the working fluid water and the possible decomposition of oil at elevated temperatures. The PEEK piston and rider rings are critical components concerning the operation temperature. It's limited to $250\,^\circ$C. As shown in Tab. 1.7, the design temperatures of the conventional process are lower than this temperature limit.
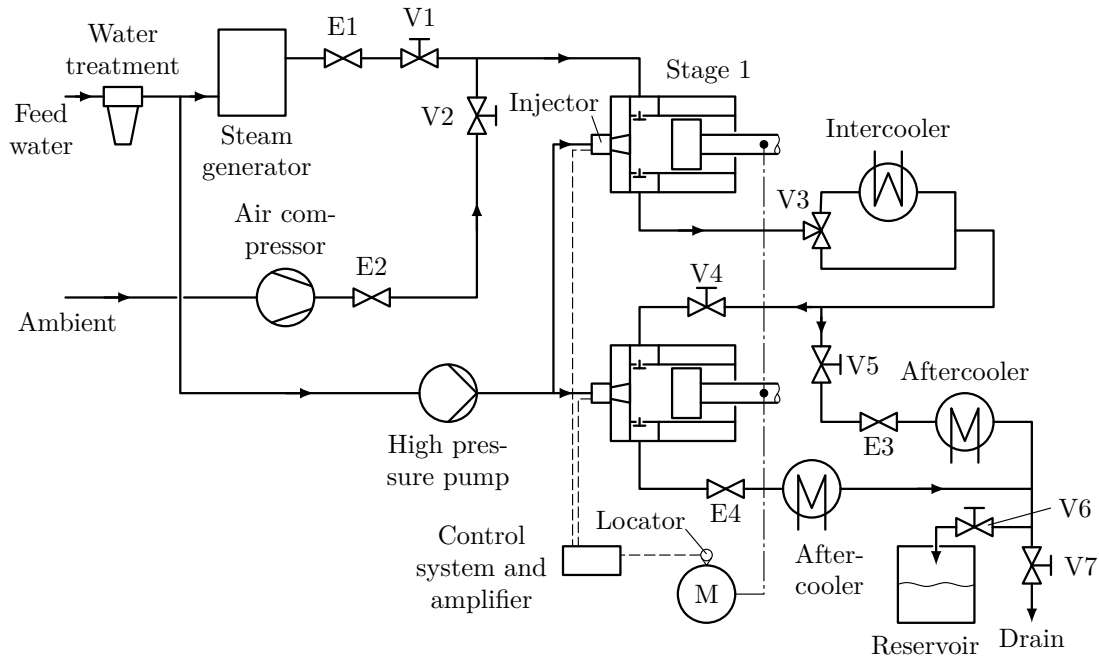
Figure 1.31: Schematic view of the reciprocating compressor test bench including injection system and additional units

Each compressor stage is designed with the suction port at the top and the with discharge downwards. This arrangement reduces the risk of a hydrolock. The piping between the compressor stages are equipped with a trace heating as well. There's an alternative fluid route through the intercooler if cooling is required.

The compression process can be operated conventionally with intercooling or with injection cooling. The injection system was already introduced in Chapter 1.6.1. A certain fraction of the treated water mass is sucked by the pneumatically driven high pressure pump and pressurised to 205 bar. The injection water flows through the illustrated pipes to the compressor stages and is preheated by a trace heating before it reaches the injectors. At both cylinder heads an injector is mounted. It directly axial concentrical injects into the cylinder space. The piston position and the rotational speed are determined by an inductive proximity sensor (locator) which is mounted on the flywheel of the mechanical drive. This sensor provides the information for the injection control and amplifier when the piston runs through TDC. Thus, the crank angle relative to the TDC can be determined where the injection has to be performed with a given injection duration. The electric motor's rotational speed can be adjusted by a frequency converter.

Different operation modes are possible. The vapour provided by the steam station is guided to the compressor stage 1 via the partly heated suction pipe (V1 opened, V2 closed). After the compression stroke, the working fluid passes through the heated bypass. Then it's expanded to ambient pressure by the throttle E3, condensed in the aftercooler, and finally goes down the

Table 1.7: Design parameter of the two-stage reciprocating compressor according to the manufacturer LMF

Parameter	Value		Unit
Rotational speed	800		$\frac{1}{\min}$
Mass flow rate	15.7		$\frac{\text{kg}}{\text{h}}$
	Stage 1	Stage 2	
Diameter	0.1	0.065	m
Stroke	0.1	0.1	m
Clearance	0.1933	0.4482	1
Suction pressure	1.746	4.185	bar
Discharge pressure	4.311	8.12	bar
Compression ratio	2.47	1.94	1
Suction temperature	120	145	°C
Discharge temperature	227.1	228.7	°C

drain (V4 closed, V5 opened). That is an open single-stage process. Notice, the suction and discharge valves of stage 2 have to be removed to operate idle for the single-stage mode.

During the two-stage mode, the working fluid passes through the steam station and stage 1 as well. Afterwards it flows to stage 2 (V4 opened, V5 closed). The trace heating is again used to set the inlet temperature of stage 2. The suction and discharge valve have to be inserted. The steam is further compressed in stage 2 and expanded to ambient pressure by the throttle E4, condensed in the aftercooler, and finally goes down the drain.

All system components have to be brought to the required operating temperature before water vapour can be sent through the system. Hence, condensation effects are avoided. Otherwise, there is a risk of water accumulation and hydrolock in the cylinder spaces. For this purpose, ambient air is precompressed by an air compressor and guided to the partly heated suction pipe (V1 closed, V2 opened). The trace heating further heats the air and compensates thermal losses to the environment. The precompressed air is further compressed by the stages before it's expanded to ambient pressure and discharged through the drain.

This operation mode is also used to rinse the system with air after regular tests with steam. Condensation and accumulation of water can occur and cause problems when restarting the system without rinsing after the latest test series. In addition, the ferritic steel used would be prone to corrosion. The use of expensive austenitic stainless steel was omitted in the design of the compressor and most parts of the piping.

Sensing elements and quality of measurement data

The Temperature was measured at 14 positions, the pressure relative to the ambient 8 times, once the absolute ambient pressure, and once the mass flow rate. All these quantities were logged in intervals of 30 s. Tab. 1.8 summarises the specification, measuring range, and accuracy of the installed sensors.

Table 1.8: Specification and accuracy of the installed sensors

Quantity	Range	Unit	Accuracy	Sensor type
Temperature	-50 to 400	°C	$\pm\left(0.3 + 0.005\,\vartheta/{}^{\circ}\mathrm{C}\right)$ K	Pt100 Class B
Temperature	-40 to 1000	°C	$\pm\max\left(1.5,\,0.004\,\vartheta/{}^{\circ}\mathrm{C}\right)$ K	Thermocouple Type K1
Abs. pressure	0 to 2.5	bar	$\pm 0.0137\,\mathrm{bar}$	Transmitter
Rel. pressure	-1 to 1.5	bar	$\pm 0.0137\,\mathrm{bar}$	Transmitter
Rel. pressure	0 to 10	bar	$\pm 0.045\,\mathrm{bar}$	Transmitter
Mass flow rate	12 to 28	$\frac{\mathrm{kg}}{\mathrm{h}}$	$\pm 0.017\,\dot{m}$	Vortex

The relative pressure and the temperature were measured at each stage just before the suction, just after the discharge, in the suction plenum, and in the discharge plenum. Class B Pt100 sensors as well as relative pressure transmitters with a measuring range of 10 bar were used (excepting the stage 1 suction plenum transmitter with a measuring range from -1 to 1.5 bar). Another Pt100 sensor was attached to the merge after the intercooler and bypass as well as after the merge of the aftercoolers (cf. Fig. 1.31). Furthermore, the temperature of the cylinder heads close to the cylinder chamber was measured by Pt100 sensors. Thermocouples were provided for measuring the temperature of the preheated injection water after the trace heating respectively before the injector inlet at each stage. A measuring section was installed to the non-heated part of the suction pipe of stage 1 to determine the suction mass flow rate.

The Pt100 resistance thermometers were gauged with a calibration furnace. For this purpose, the corresponding amperages were determined by repeated application of different temperature loads. Hence, a regression or calibration line was determined. Just marginal deviations from the theoretical curve were detected for all the considered sensors.

Three different transmitters were installed to measure the mentioned pressures. Their measuring ranges and accuracies are summarised in Tab. 1.8. The measurement error of the resulting absolute pressure is composed additively according to the error propagation. It's the sum of the error from the absolute pressure sensor for the ambient pressure and the error from the respective relative pressure transmitter.

A vortex flowmeter with a maximum relative measuring error of $\pm 1.7\,\%$ was used to determine the suction mass flow rate. Due to the measuring principle, a minimum flow rate of the medium is required which corresponds to a minimum Reynolds number of 20 000 for gaseous fluids. The relative error increases significantly and cannot be quantified for lower Reynolds numbers. The

maximum velocity is limited with $46\,\mathrm{m/s}$. That results in a permissible measuring range of $11\,\mathrm{kg/h} < \dot{m} < 29\,\mathrm{kg/h}$ for a given fluid temperature of $130\,^{\circ}\mathrm{C}$ and an absolute pressure of $1.8\,\mathrm{bar}$.

There also was the possibility to determine the discharge mass flow rate if steady-state operation was the case. By opening V6 and closing V7 condensate can be collected in the reservoir for a certain period of time. By subsequent weighing the mass flow rate can be determined.

As already mentioned, the compressor rotational speed and the injection parameter set have been recorded by the injection control log.

Indicator bores were placed to the cylinders. The transient pressure evolution in each cylinder space was recorded over the crankshaft angle respectively piston position. According to the calibration report, the used sensors do not exceed a measurement error of $0.07\,\mathrm{bar}$ between 0 and $9.4\,\mathrm{bar}$. The signal from these pressure sensors and of the locator were recorded with a sampling rate of $10\,\mathrm{kHz}$. Hence, just a short sequence of a few seconds could be recorded as otherwise huge mounds of data would be generated.

The ambient temperature was manually documented during the tests at periodic intervals.

For the sake of completeness, various other sensors were used for machine monitoring and trace heating control. Sensors including analogue or digital displays were also installed for observation but not recorded.

Simulation

A model was implemented in Modelica [57] to determine the theoretically expected discharge temperature under the usage of measurement data from experimental tests as boundary conditions. The compression process combined with the theoretical descriptions of the injection cooling are formulated as a mathematical system for steady-state operation. The indicated power P_{ind} can be written as:

$$P_{ind} = \dot{m}_{disch}\left(h_{disch,s} - h_{suc}\right)\frac{1}{\eta_s} \tag{1.30}$$

with $h_{disch,s} = h\left(p_{disch}, s_{suc}\right)$ as the discharge specific enthalpy after isentropic compression. The heat losses to the environment are rather high compared to the indicated power. Subsequent tests have shown that they cannot be neglected. The heat losses are formulated as dependent on the suction and discharge temperature:

$$\dot{Q}_{loss} = kA\left(\frac{\vartheta_{suc} + \vartheta_{disch}}{2} - \vartheta_{amb}\right) \tag{1.31}$$

kA denotes the thermal conductance of the compressor stage in regard to the heat losses to the environment. The mass and energy balances can be written as:

$$0 = \dot{m}_{suc} - \dot{m}_{disch} + \dot{m}_{inj} \tag{1.32}$$

$$0 = \dot{m}_{suc}\,h_{suc} - \dot{m}_{disch}\,h_{disch} + \dot{m}_{inj}\,h_{inj} + P_{ind} - \dot{Q}_{loss} \tag{1.33}$$

under the assumption of neglectable low leakage. The tests V15, V24, and V26 of conventional operation without injection cooling are presented in the later part of the results. Those were used to validate the model. The thermal conductance kA of stage 1 was found as 2.83 W/K. The isentropic efficiency η_s can be determined from the indicator card and is summarised in Tab. 1.10 for the different tests. An η_s of 0.76 was chosen for the simulation. If these parameters are known, the theoretically expected discharge state for the process with injection cooling can be determined. The results are also summarised in Tab. 1.10.

Results

Tab. 1.9 shows an overview of the target parameters of selected stationary operating conditions which were approached on the test bench in single-stage operation. The single-stage compression from 1.8 to 4.2 bar was applied under variation of the compressor rotational speed, the injection duration, the crankshaft position when injecting, and the injection duration.

Table 1.9: Target parameters of selected stationary operation conditions

Test no.	n	p_{suc}	ϑ_{suc}	p_{disch}	t_{inj}	Pos.
	$\frac{1}{\min}$	bar	°C	bar	µs	
V15	800	1.8	132	4.2	0	-
V18	800	1.8	132	4.2	100	BDC
V19	800	1.8	132	4.2	200	BDC
V22	800	1.8	132	4.2	200	BDC+90°
V24	600	1.8	132	4.2	0	-
V25	600	1.8	132	4.2	200	BDC
V26	500	1.8	132	4.2	0	-
V27	500	1.8	132	4.2	200	BDC
V29	800	1.8	132	4.2	400	BDC

Fig. 1.32 summarises the results of different tests with equal compressor rotational speed n of approximately 800/min in the ϑ, s-chart. The changes in state of the individual experiments are shown in different colours. V15 origins from the conventional process without injection cooling and represents the reference case. The working fluid's state 1 was measured in the suction pipe 200 mm upstream to the suction plenum just before it enters the cylinder block. An isobaric heating of the working fluid arises on it's way to the plenum and suction valve (state 2). The cylinder block material of higher temperature lifts the fluid temperature by waste heat from the compression process. The compression process from state 2 to state 3 follows. State 3 was recorded in the plenum of the discharge. With isentropic compression the change in state would follow vertically upwards in the ϑ, s-chart and with non-isotropic adiabatic compression including entropy production to the top right. The process appears with entropy decrease for the given compressor. Hence, the waste heat flow to the environment is relatively large compared to the
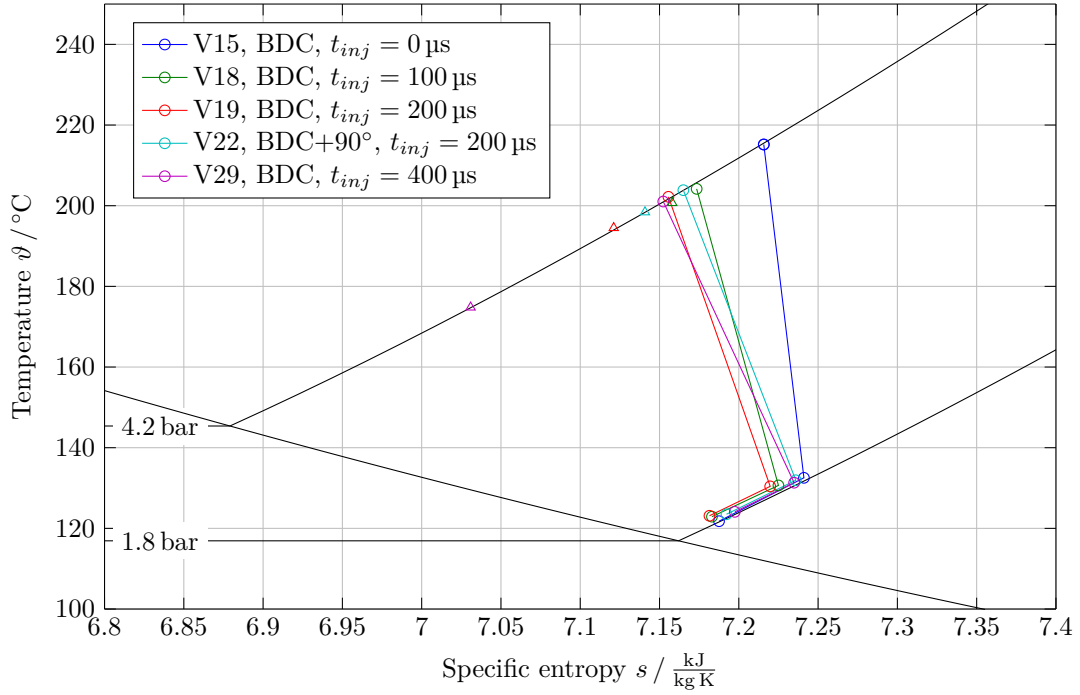
Figure 1.32: Experimental results of single-stage tests with a compressor rotational speed $n = 800/\text{min}$

power indicated to the fluid. V18 illustrates the first usable test with injection cooling. It was performed with injection of $100\,\mu\text{s}$ at BDC. A significant decrease in temperature of about $11\,\text{K}$ was observed compared to the reference test V15. The triangle of the same colour indicates the theoretic thermodynamic state in which the fluid was expected according to the simulation under ideal vaporisation. The measured and simulated results differ about $1.9\,\text{K}$. The injection quantity was increased in the next step. For V22 the injection timing was changed too. It was injected a quarter crankshaft revolution after BDC, hence, to higher cylinder pressure and with less time to vaporise the liquid drops. Contrary to expectations, the discharge temperature did not drop more sharply with increasing the injection quantity. A cooling effect ranging from 10 to $15\,\text{K}$ can be observed for all the tests. Also V22 with less time available for vaporisation offers a similar result. The results from the simulation deviate from the actually measured values especially for V29 with $400\,\mu\text{s}$ injection duration. As a result, total vaporisation of the injected fluid cannot be assumed for the prevailing circumstances.

As a consequence, the compressor rotational speed was lowered while maintaining the compression ratio. Thus, more time is available for drop vaporisation. An increasing cooling effect was expected. Fig. 1.33 summarises test results at varied rotational speed. For a certain rotational speed, the test without injection cooling is indicated by a solid line and the process with injection cooling by a dashed line. V15 and V19 operating at 800/min are known from Fig. 1.32.
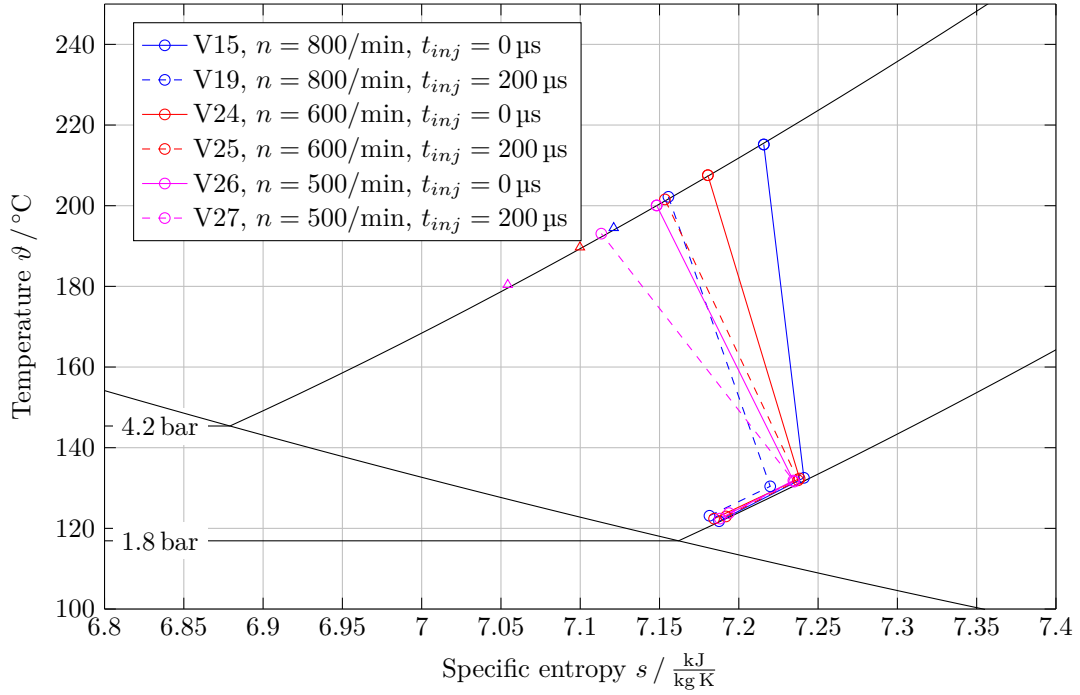
Figure 1.33: Experimental results of single-stage tests for differing compressor rotational speed

Lowering the rotational speed generally leads to lower discharge temperatures. At 600/min a discharge temperature decrease of 6 K and at 500/min a reduction of 7 K can be observed due to injection cooling. Therefore, it cannot be assumed that a rotational speed reduction is accompanied by the vaporisation of a higher amounts of water. The speed reduction was limited by 500/min due to the frequency converter settings of the main motor.

Table 1.10: Summary of measurement data and simulation results

Test no.	n	$\dot{m}_{vort}$	$\dot{m}_{scales}$	ϑ_{amb}	ϑ_{suc}	η_s	$\vartheta_{disch,mea}$	$\vartheta_{disch,sim}$
	$\frac{1}{\min}$	$\frac{\text{kg}}{\text{h}}$	$\frac{\text{kg}}{\text{h}}$	°C	°C	1	°C	°C
V15	797	24.56	24.56	26	132.53	0.77	215.17	216
V18	793.65	24.45	23.65	27	130.65	0.76	204.18	202.1
V19	794.7	23.38	23.38	28	130.42	0.74	202.2	194.5
V22	793.65	23.84	23.79	27	131.93	0.77	203.85	198.4
V24	594.65	18.24	17.20	27	132.35	0.77	207.56	207.2
V25	594.65	17.97	16.57	28.5	131.92	0.76	201.56	189.7
V26	500.00	14.372	13.818	25.5	131.86	0.76	200.07	198.2
V27	500.00	13.419	13.375	27	131.59	0.74	193.07	180.4
V29	791.55	21.22	21.72	29	131.32	0.68	201.04	174.8

58

Tab. 1.10 lists further measurement data and simulation results. Considering the compression process as a polytropic change in state for the ideal gas, the polytropic index k can be determined by transposing Eq. 1.15 and using the measurement data as boundary conditions. For the given tests of conventional operation V15, V24, and V26 with the rotational speeds 800, 600, and 500/min the corresponding polytropic indices of 1.285, 1.255, and 1.23 can be found. The isentropic exponent is $\kappa = 1.33$ [16] for water as an angled triatomic molecule. According to the statements from Chapter 1.3.1, the cooling of the fluid is more intense if k is smaller than κ. In other words, it's a slow-running machine. The slower the machine runs the smaller k gets. $\dot{Q}_{loss}$ cannot be neglected in the simulative calculations.

In addition, a p,V-chart respectively indicator card was recorded for each test. The evolution of the pressure in the cylinder space is drawn over the piston stroke or crankshaft angle. On the left side of Fig 1.34, the indicator card of the conventional process is shown for $n = 500/min$ (V26). The graph on the right side origins from a test with injection at BDC (V27). The charts were recorded with a sampling rate of $10\,\text{kHz}$.

Starting at the discharge pressure or dimensionless pressure of $p_{dim} = 1$ (TDC), the piston moves towards BDC and expands the clearance mass. The suction valve begins to open when the cylinder pressure drops slightly below suction pressure or $p_{dim} = 0$. A corrugated pressure curve can be observed during the suction process which reflects the typical chattering of the suction valve. If BDC got reached, the piston changes its moving direction, the suction valve closes, and the compression process begins. The discharge valve begins to open when reaching the discharge pressure. During the discharge the concerned valve is chattering too. The right chart shows higher pressure when discharging. That indicates an increased discharge resistance, e. g. due to the presence of liquids. Further, the suction pressure was reached at a larger cylinder volume. The effect can be explained by the expansion of an increased clearance mass due to the injected mass.

Two important quantities can be determined from the indicator card. The required indicated power P_{ind} results from the pressure acting on the piston crown and corresponds to the area spanned in the p,V-chart. It can be determined by solving the closed line integral:

$$P_{ind} = n \oint V \, \mathrm{d}p = -n \oint p \, \mathrm{d}V \tag{1.34}$$

The isentropic efficiency follows as:

$$\eta_s = \frac{P_{ind,s}}{P_{ind}} = \frac{\dot{m}_{disch}\left(h_{disch,s} - h_{suc}\right)}{P_{ind}} \tag{1.35}$$

with $h_{disch,s} = h\left(p_{disch}, s\left(p_{suc}, h_{suc}\right)\right)$ as the discharge specific enthalpy in case of isentropic compression. The determined isentropic efficiencies range from 0.74 to 0.77 with exception of V29. An η_s of 0.76 was used for the validation and simulation process. The maximum difference in the efficiencies is $3\,\%$. According to Eq. 1.35 the isentropic efficiency is directly proportional

59

$p_{dim} = \dfrac{p(t) - p_{suc}}{p_{disch} - p_{suc}} \,/\, 1$

$\eta_s = 0.76$

$P_{ind} = 901.3\,\text{W}$

$\eta_s = 0.74$

$P_{ind} = 860.9\,\text{W}$

$\dfrac{V(t)}{V_{stroke}} \,/\, 1$

$\dfrac{V(t)}{V_{stroke}} \,/\, 1$
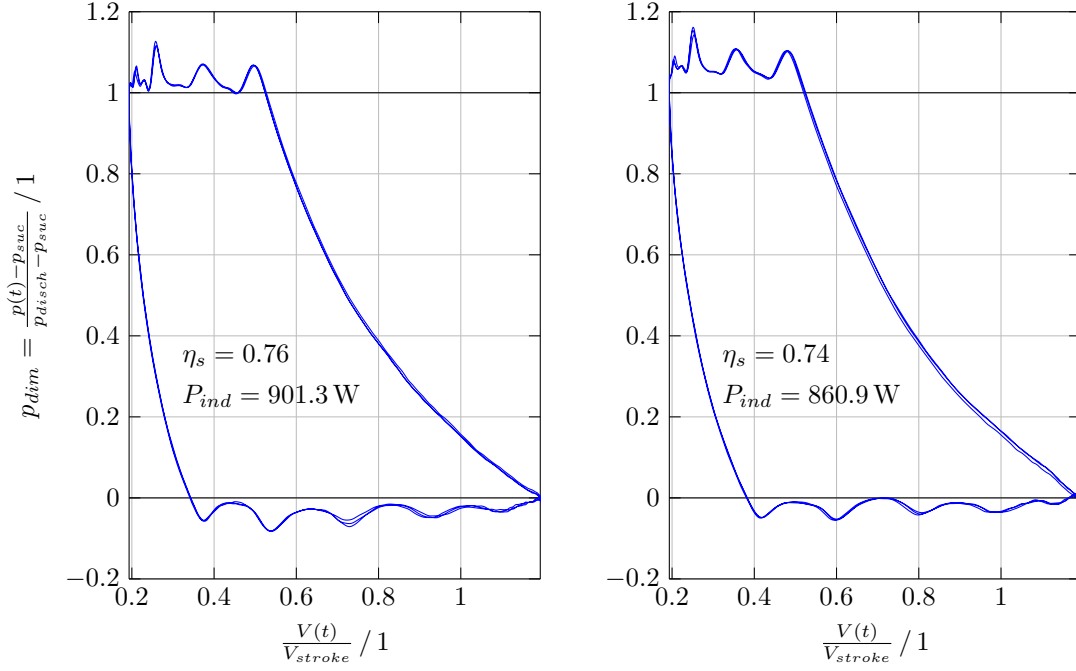
Figure 1.34: The indicator card of the conventional compression process on the left and the process with injection at BDC on the right for 500/min rotational speed

to the mass flow rate. Considering that the mass measurement is associated with $\pm 1.7\,\%$ relative error the deviation of $3\,\%$ can result just from the measurement error. V29 is considered as untrustworthy due to the large differences in mass flow and efficiency compared to other tests at the same rotational speed.

Two-stage operation

Based on the findings from the single-stage test series the planned two-stage tests were completely waived, since no essential increase in knowledge was expected.

Discussion

There could be several reasons why the cooling effect found in the perfect vaporisation model did not arise to the expected extent. The drops that were generated are too big and do not vaporise in time. In other words the time available is too short. The theoretical investigations on drop vaporisation origin from an energy balance at the drop surface. These investigations were carried out under some simplifications. In particular, the determination of the Nußelt number isn't trivial for the complex flow conditions at the liquid's drop surface due to the injection, the moving piston, and the changing cylinder pressure. In addition, the manufacturer of the used

HDEV4 high pressure injector specifies an SMD between 10 and 15 μm for the medium petrol. The investigations at the injector test bench with the medium water revealed a SMD of <20 μm at a comparable injection pressure.

Another reason could be that the penetration length of the spray with water is different compared to that specified by the manufacturer for petrol of 30 mm. Considering a drop of a larger diameter and a higher density medium is generated, it takes longer to decrease the momentum and the penetration length increases. That could result in being sprayed directly on the cylinder walls or on the piston crown. The drops are forming a coherent liquid film with a minor cooling effect. The cooling effect of the magnitude of 10 K more or less independent of the injection quantity indicates the film formation on the cylinder wall. In the best case it's transported to the discharge by the piston rings or past the piston rings and does not lead to hydrolock.

It's not possible to determine the actually vaporised amount of water, since a mixed temperature was measured in the discharge plenum. There are superheated steam and liquid drops close to the saturation temperature at discharge pressure.

The used compressor is rather insensitive to liquid drops in the cylinder space or a liquid film on the cylinder walls, since obviously not the entire injected amount of water is vaporised. This water has to leave the cylinder space as liquid. In some cases, the compressor's acoustics had changed for a few seconds during injection and a slight knocking was heard. This could indicate slight water accumulation in the cylinder.

Nevertheless, the compression of water vapour from 1.8 to 4.2 bar corresponds to a temperature shift from 116.9 °C evaporator temperature to 145.4 °C condenser temperature for single-stage compression. Thus, the safe operation of a reciprocating compressor with water as the working fluid for increased evaporator and condenser temperatures has been demonstrated.

1.7 Summary and outlook

The aim of this chapter was to investigate and advance industrial HTHPs in order to increase the supply temperature and to expand the field of application. Since the compressor and the working fluid play the central roles in this concern, the focus was placed on these two components as parts of HTHPs.

Industrial HTHPs are applied to provide industrial process heat. Waste heat of low temperature can be brought to a higher temperature level and is returned to a given process under supply of external energy. The current industrial benchmark is represented with a supply temperature up to 150 °C under the usage of a reciprocating compressor and the synthetic refrigerant HFO-1336mzz(Z). The highest achieved supply temperature in the research field is 155 °C, under the usage of HFO-1336mzz(Z) as well.

First some important fundamentals according to HTHPs and the considered reciprocating compressor type were presented. Special attention was paid on outlining different thermal limi-

tations, the cooling possibilities, as well as increasing the process efficiency.

The majority of heat pump compressors is oil-lubricated. The oil chemically changes and contaminates the refrigerant at temperatures ranging from 160 to 200 °C. Some refrigerants decompose at elevated temperatures. Increased temperature and pressure will also influence the compressor material's duration of life. In case of reciprocating compressors the piston rings are charged with the highest occurring gas temperature. The thermal limit in terms of process performance is determined by the refrigerant's critical temperature. The enthalpy of vaporisation decreases with increasing condenser temperature and pressure and negatively influences the COP.

There are different possibilities to increase the heat pump process' efficiency. In various cases that is realised by a cooling system and accompanied by a reduction of the compressor discharge temperature. Multi-stage operation also makes sense especially if elevated temperature lifts require high pressure ratios. On the one hand, a two-stage heat pump also known as two cascaded heat pump cycle can be used. Or on the other hand, multi-stage compression with external intercoolers or injection cooling with working fluid in gaseous or liquid state can be performed.

The possibilities of injection cooling are proven for rotary compressors. With reciprocating compressors there's just little experience in research. Alternative fields with experience in injection cooling application were briefly outlined, such as the automotive industry, gas turbines, and steam power plants.

General theoretical investigations on the use of water as a working fluid, and in particular, as an application under the usage of a reciprocating compressor with direct injection cooling were following.

Water (R718) as a natural refrigerant does not have to be produced synthetically. It's completely neutral in regard to harmful effects on humans, animals, and the environment. The GWP equals zero and so does the ODP. It's non-toxic, non-combustible, and non-explosive. Furthermore, it shows a high critical temperature, high enthalpy of vaporisation, and good chemical and thermal stability. That compares with some disadvantageous properties. Due to the low volumetric heating capacity VHC, high volume flow rates and thus large compressors are required for higher thermal outputs. Furthermore, conventional lubricants are not soluble in water and corrosion of machine components by dissolved gases is possible. In addition, the vapour pressure of water is lower than the atmospheric pressure for a temperature below 100 °C. Operation in partial vacuum would be required. This partial vacuum implies challenges for the compressor design, especially for sealing the affected zones from the environment. Incoming air regards the heat exchanger performance and places an additional load to the compressor. Hence, a significant amount of non-condensable gas in the system results in a loss of cycle performance.

It was found that elevated condenser temperatures can be achieved through the usage of water as the refrigerant. Water suits at higher heat source temperatures and in the second stage of a cascaded heat pump cycle. In addition, using water as a refrigerant results in the possibility

to operate heat pumps as an open processes. The theoretical investigations have shown that a theoretical COP of about 6.6 can be achieved under the appliance of direct injection cooling and water as the working fluid. That expresses an increase of 10 % compared to the process with interstage cooling and an increase of 33 % compared to the single stage operation. Furthermore, the compressor discharge temperature can be reduced significantly to a desired value.

The investigations on drop vaporisation have indicated that drops with a diameter $< 15\,\mu m$ vaporise sufficiently fast under advantageous heat transfer conditions for the introduced application case. The determined drop diameter originated from theoretical investigations and were carried out under several simplifications.

However, experimental investigations were carried out to evaluate the hot gas cooling with liquid water injection. In the first experimental step, an injection system was developed and successfully tested. The injection system has passed the first functional tests and has fulfilled the requirements with regard to the injection mass, injection mass flow rate, and accuracy. A SMD of $< 20\,\mu m$ at 205 bar injection pressure was achieved for the medium water.

As the next experimental step, an existing reciprocating compressor test bench was adapted and operated with the injection system. A cooling effect due the liquid injection ranging from 6 to 15 K was observed for all the tests compared to the conventional processes. There could be several reasons why the cooling effect did not arise to the expected extent. The generated drops were too big and did not vaporise in time. Another reason could be that the penetration length of the water spray was different to the specified for petrol by the manufacturer. Possibly the drops were sprayed directly on the cylinder walls or on the piston crown. The cooling effect of the magnitude of 10 K more or less independent from the injection quantity indicates the film formation on the cylinder wall. Further, the used compressor was rather insensitive to liquid drops in the cylinder space or a liquid film on the cylinder walls, since obviously not the entire injected amount of water was vaporised.

Further investigation concerning this topic would certainly make sense, since water as a refrigerant offers remarkably properties. In addition, the theoretical investigations for elevated temperature levels promise excellent efficiency.

The next step would be the investigation of the original regime in combination with the injection cooling in the cylinder space. For this purpose, a possibility of optical accessibility has to be created. Then, the spray in the cylinder can be examined during the compression process by a high speed camera and the already used laser diffraction device. Statements about water accumulation and the actual penetration depth are possible. Furthermore, there's the possibility of large scale simulative investigations with more complex modelling.

Alternative atomisers originating from the automotive industry can be considered. There's a chance for the appearance of even more suitable products on the market in the next few years. Not least due to the very intensive and successful development of the injector technology in the past years.

As a further step, the compression process can be considered as decoupled from the heat pump process. The manufacturer LMF of the compressor used at the test bench suggest opportunities in conjunction with the compression of air, methane, and butane, among other things. The injection of water for cooling with subsequent condensation and separation from the working fluid offers a way to increase efficiency.

Chapter 2

Theoretical study of industrial drying processes

As already outlined in the general Introduction, there's a huge necessity and potential for improving efficiency and reducing energy consumption concerning industrial drying processes. The aim of this chapter is to investigate the drying behaviour of clay bricks in chamber dryers as a specific application case.

First it's stated why drying is such an essential and energy consuming process in the production chain of clay bricks, followed by some important fundamentals. The commonly used dryer types in the brick and tile industry and the facilities for the drying energy supply are presented. Bricks are usually manufactured of clay. The most important properties of clay in conjunction with drying are discussed. In order to be able to investigate the drying behaviour, the transport processes within the drying product and at the drying product's surface have to be describable. Practical and permissible modelling assumptions of the thermodynamic processes, the mathematical derivation and formulation are presented. Subsequently, a model for chamber dryers and the drying kinetics of the drying material are introduced. The models were implemented to a suitable simulation environment and validated with measurement data. The chapter concludes with a summary and outlook.

2.1   Introduction

The production of clay bricks can roughly be divided into the following sections: raw material processing, shaping, drying, firing, stacking, and packaging.

For the production of ceramic bricks, mainly clays and clay materials are used as raw material. The clay is usually mined from the company's own quarries. Specific substances are often added to achieve special properties. For the production of highly heat insulating bricks, organic or inorganic pore-forming agents are added to the processed material to increase the pore volume.

All species are crushed, mixed, and homogenised in dry or wet state. Mixing water is required to provide the material's plasticity for shaping, hence it's intended to enable the free movement of the solid particles along each other. To produce green bodies of low texture, the water content must be as high as possible, but due to the required energy amount for the moisture removal, it should be kept as low as possible. The content of mixing water ranges between 15 and 35 % (mass of water referred to the mass of the dry product).

A continuous bar is shaped via extruding the mixed material and periodically cut at the green bodies height. For the most brick products the shaping process has finished with the cutting. The production of roof tiles requires subsequent steps.

The water content required for shaping has to be removed in course of the drying process, before the bricks are fired. Sending a wet green body to the kiln, would already destroy the product at the beginning of the firing process. The temperature of the bricks' inner sections remains below the boiling temperature as long as there's still a significant amount of liquid water in the product. The surface would be exposed to the kiln temperature. That would result in high thermal stress and subsequent cracking. Furthermore, the freshly shaped green bodies are less resistant to mechanical stress. During the drying process, the product's volume decreases slightly, which is due to an effect called shrinkage, and the mechanical resistance increases.

After the drying process, the moisture content prevails below the allowed kiln-entrance moisture content. The bricks are usually carried through a tunnel kiln, in which the firing process is performed in oxidising atmosphere at a temperature ranging between 900 and 1200 °C. The door-to-door time has to be chosen with regard to the required dwell time for the chemical processes.

Then, the material is cooled to the exit temperature. The bricks are stacked and packed before they are distributed [11].

Nowadays the drying air is heated directly by gas burners or indirectly by heat exchangers, in contrast to the formerly customary outdoor drying. Fossil-fired, convective exhaust air dryers are mainly used and the drying duration is less. These systems dissipate the exhaust air including the water vapour to the environment. It cannot longer be used energetically [4]. The duration of the drying process ranges between a few hours and several days, depending on the material's composition, preparation, geometric dimensions, and the drying method [63].

The drying process is the most energy-intensive section of the production chain [4], since a phase change of water is needed. Hence, the minimum theoretically required thermal energy equates the energy to evaporate the attached water. For convective drying, the enthalpy of vaporisation $\Delta h_v \approx 2500\,\text{kJ/kg} = 0.6944\,\text{kWh/kg}$ [64] acts as a thermodynamic barrier.

In real operated dryers, additional energy is required to overcome heat and mass transfer resistances, product-specific moisture bonding effects, conductive losses, leakages, and for powering additional components. The electrical energy requirement arises in particular through the ventilation of the drying air. It has an impact on the uniformity and magnitude of the heat

and mass transfer [11]. The total supplied energy is commonly denoted as the specific energy consumption SEC (cf. Chapter 2.2.1). The energy needed for drying clay bricks using fossil-fired dryers is ranging from 1 to 2 kWh/kg [3]. Defining the dryer's efficiency as $\eta = {\Delta h_v}/{SEC}$ leads to a corresponding efficiency η ranging from 0.35 to 0.7. Hence, there's huge necessity and potential for improving efficiency and reducing energy consumption.

2.2 Fundamentals

2.2.1 Variety of dryers and usage in the brick and tile industry

Drying is an important step of the production chain in several industry branches. Due to the diverse use and the very long history of drying, the range of dryers and drying technologies is very wide. Therefore, a simple classification of dryers into a few generic types isn't possible. But they all have one thing in common. As an intermediate or the final production step as well, moisture should be removed from the drying material in compliance with the required quality criteria. However, a selection of the most common classification possibilities should be presented first [65, 66]:

- Temperature and pressure level in the dryer: ambient conditions, above or beneath ambient temperature, vacuum or excess pressure

- The method of heating the material to be dried: convective, conductive, or radiative

- Operation mode: continuous or discontinuous (batch)

- The method of moving the wet material through the dryer: trucks, hot cylinders, conveyor belt, fluid bed, spray

- Heating medium: fossil fuel, electricity, heat recovery

- Shape of the dryer: tunnel, chamber, drum

- Mechanical aid, to improve drying

- The method of circulating the drying medium

- The nature of the wet material and the manner of its introduction into the dryer

- Required duration for drying

The variety of dryers used in the brick and tile industry for modelled ceramics is limited. The majority of drying plants that are used are, tunnel, chamber, and impingement dryers of the following conceptions or modifications thereof. All of them are convective dryers. Thermal energy is supplied by heated air or other gases, flowing over the surface of a solid. The heat for evaporation is transferred by convection to the exposed surface of the material and the evaporated

moisture is carried away by the drying medium [67]. Other types don't play a significant role in the brick and tile industry.

Chamber dryer
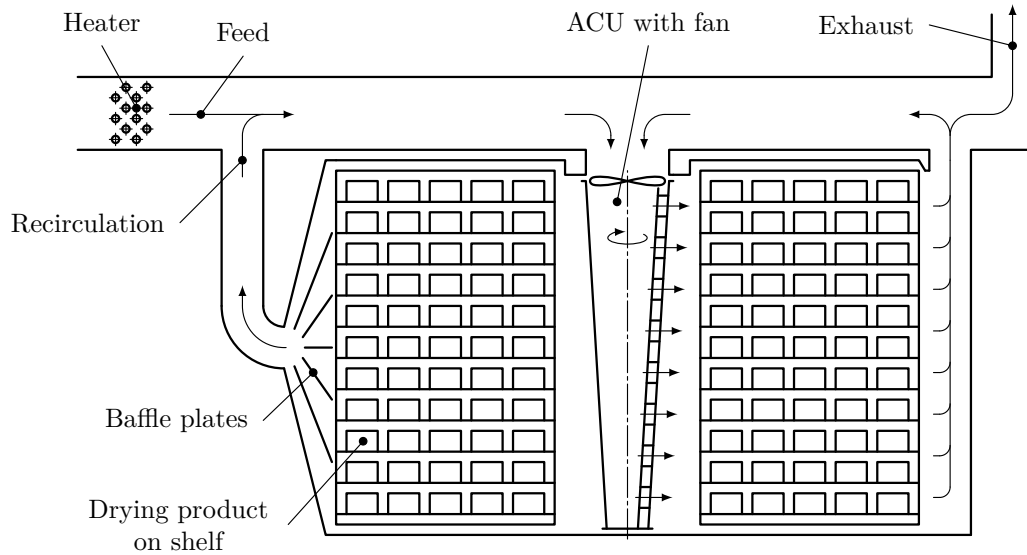
Figure 2.1: A typical configuration of a chamber dryer, enhanced by an air circulation unit

A typical configuration of a discontinuous or batch dryer is shown in Fig. 2.1. The wet material is placed on shelves, which are set in the dryer room. The feed air flow supplied to the dryer prevails generally between 90 °C and 150 °C. The feed flow mixes with recirculating air from the chamber. Modern chamber dryers are often equipped with rotating air circulation units (ACUs). They are designed to improve the mixing of fresh hot air and recirculating air and ensure uniform temperature distribution and air flow through the dryer chamber. These dryers are available for drying of various types of ceramics, as drying conditions, duration, temperature, air mass flow rate can easily be changed and controlled [67]. Usually several chamber dryers are operating at the same time, where each chamber works in batches. If the chambers are properly connected, the all-over process can be seen as approximately continuous. However, the use of chamber dryers is always advantageous, if the drying product is very sensitive regarding to the drying parameters and if the treated product is changed frequently [63].

In addition to fans and ACUs more primitive installations can also improve the result and efficiency of drying. Baffle plates for deflecting, branching, or merging of air streams, act more or less as channels providing parallel, uniform flow [68]. Another measure concerns the arrangement or loading of the dryer. If the clearance among the bricks isn't sufficient, it results in non-uniform drying and drifting the air flow between trucks and the wall of the chamber. The bricks on the trucks should be arranged in an appropriate way [67].

For example, Beckmann et al. [69] performed an improvement of the drying process of roof tiles in an industrial chamber dryer by applying these steps. As a result, they achieved a more uniform drying and a significant reduction of the drying duration.

Other apparatus for treating the drying medium can also be installed if necessary, such as chillers for vapour condensation or cyclone separators for removing particles.

Tunnel dryer

In contrast to chamber dryers, a typical continuous type of ceramic drying is the tunnel dryer which simplest configuration, operated as counter-current, is shown in Fig. 2.2. The wet material put on trucks is moved through the tunnel, starting the drying process in a humid atmosphere at rather low temperature and ending it as dry material under dry and hot air conditions. In doing so, the drying medium of about $70\,^{\circ}\mathrm{C}$ up to $200\,^{\circ}\mathrm{C}$ is provided by a heater to the tunnel's part with dry climate [63]. Depending on the dryer's design, the feed air can also be supplied as co-current or cross-current to the trucks' moving direction [66].
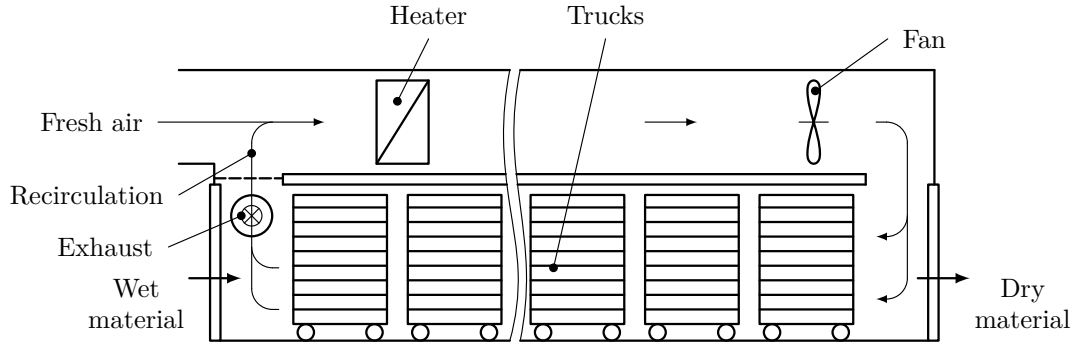
Figure 2.2: Configuration of a typical tunnel dryer operating in counter-current mode, adapted from [67]

Modern continuous dryers are often provided with up to ten tracks. Moving fans between these tracks ensure high flow velocity and proper mixing of the drying air causing an efficient and homogeneous drying process. Another rise of flow velocity and limited climate control is possible by recirculation and removing partial air streams at certain locations along the path through the tunnel and adding them again at other positions.

Continuous dryer concepts are used for mass-production and require a large amount of installation space. Since the dryer's length in conjunction to the trucks' feed rate expresses the drying duration, such applications are inflexible in operation. Delays or interruptions are causing further deregulations. A drying product that is insensitive with regard to susceptibility to cracking and a reasonable constant production rate are required [63].

Impingement dryer

Impingement dryers for hollow bricks and thin-walled products are used increasingly. The drying material is conveyed on bands through a tunnel. Thus, the process is also operated continuously. The green bodies are transported past slot nozzles, from which they are blown at with high velocity. Heat and mass transfer are increased. In case of large-sized hollow products, that also leads to an improved and even through-flow of the body. Consequently, the drying process performs remarkable fast [63, 66]. It's possible to control the climate and flow rate of air at each optimum state in some zones, separated in the dryer [67]. A maximum in flexibility can be reached through this drying concept, even when changing the product [63].

Supply of thermal energy

One of the drying medium's main tasks in convective drying is the mass and energy transport. In most applications thermal energy provided by different energy sources is transported to the drying product by the drying medium as an intermediate energy carrier.

The drying thermal energy often origins from other processes accruing there as waste heat. Brickworks usually operate drying plants in connection to the kiln to increase efficiency. The air heated in the tunnel kiln's cooling zone is supplied partly or entirely to the dryers. In addition, the enthalpy of the kiln's exhaust gases also can be displaced to the dryers, using heat exchangers for heating up air streams. Also air that is used to cool the tunnel roof can be supplied to the dryers. Many brickworks are capable to cover the total demand of thermal energy for drying in this way alone. However, a major disadvantage of this kind of energy supply is the high inflexibility since it's governed by the kiln's production rate. The energy supply for drying can be made more flexible by partly decoupling the kiln process. The additional required thermal energy is then usually supplied by gas burners or heat exchangers fed by steam or hot water. These apparatus are simple to control [63].

For small quantities infrared and microwave heating systems are used. Materials are heated directly by infrared irradiation of lamps, rods, or plates. When wet materials are heated in the first drying period by infrared radiation, the surface temperature increases to a temperature higher than the wet-bulb temperature (cf. Chapter 2.2.3) and the drying rate rises. The drying operation must be performed carefully as a rapid drying rate may result in a product's lack of quality. However, the power control of infrared sources is relatively simple to handle. Such applications are often combined as infrared convective heating systems [67].

Microwave systems for industrial heating are operated at frequencies covering two bands which are effective for heating of water. Microwaves are generated in a magnetron, which is introduced into an applicator where the wet materials are heated via transmission through a wave guide. Wet materials are heated internally because microwave energy can penetrate the inside of the body. Only wet materials are heated selectively and rapid heating is possible. The operation and control processes are easy, and drying is possible in any atmosphere including a vacuum. In the drying of thick ceramics by microwave heating, the material internal temperature may rise to a

temperature higher than the surface temperature. This results in explosive expansion due to the internal vapour pressure. Therefore, the microwave power should be controlled appropriately to prevent overheating the inside of the body [67].

The disadvantage of electric heating systems is that they are costly to operate. In both cases and in contrast to the energy supply by heat pumps, the whole thermal energy for heating has to be provided electrically. In addition, there is a high economic outlay for the installation, in case of microwave heating systems [70].

Heat pumps are another option to provide thermal energy for drying electrically. Any convective dryer can be fitted with a heat pump. Furthermore chamber dryers are the most commonly reported dryers used in conjunction with heat pumps. Heat pump dryers are known to be energy efficient, due to the principal advantages of the ability to recover energy from the exhaust gas. Many researchers have demonstrated, as in [71] and [72], the importance of producing a range of precise drying conditions to dry a wide range of products and improve their quality [67]. Real systems are implemented in the wood, food, and pharmaceutical industry so far [19, 73, 74].

As mentioned in the Preface of this work, one of the DryPump project's main goals was, to investigate and reasonably expand the application range of heat pump systems in the drying industry, including the brick and tile industry. As part of the project, a test bench in form of a drying container was set up and equipped with a compression heat pump. Drying tests on clay bricks were carried out. Therefore, the possibility of energy supply by heat pumps with respect to drying processes should be outlined concisely in the current chapter. The drying container itself will be described in course of the modelling process at the following Chapter 2.3.1.

The basic component of the compressor heat pump system comprises an expansion valve, two heat exchangers as evaporator and condenser, and a compressor [67]. The schematic diagram of the implementation of a basic heat pump system to a certain drying process is shown in Fig. 2.3. The hot drying air passes through the dryer and receives moisture from the bricks. The wet air
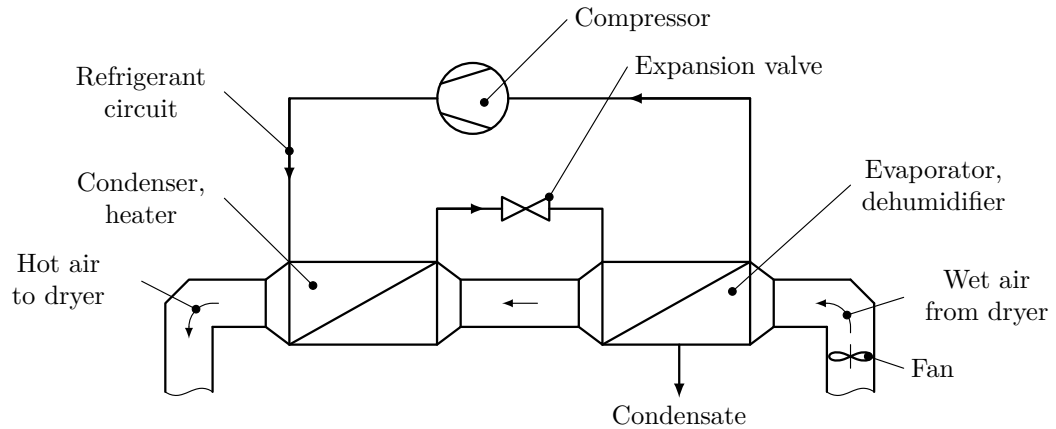
Figure 2.3: Thermal energy supply of a compression heat pump drying system, adapted from [67]

driven by a fan is transported to the evaporator where the dehumidification process takes place. The air is first cooled sensibly to its dew point. Further cooling results in condensation of water from the air. After that, the cooled and dehumidified air is sensible heated again at the heat pump's condenser to the desired temperature. The latent enthalpy of vaporisation of the vapour in the air is transferred by the evaporator for vaporising the refrigerant. The gaseous refrigerant is then taken to the higher pressure level by the compressor, the temperature also rises. After that, the refrigerant is driven through the condenser, where its enthalpy of vaporisation is used to heat the air flow. The condensed refrigerant is brought to the lower pressure level by the expansion valve before it enters the evaporator again [67]. The heat pump process regarding to the refrigerant circuit was described in detail at Chapter 1.2.1.

In addition to the heat pump process' coefficient of performance COP, the specific energy consumption SEC, defined as

$$SEC = \frac{\int P_{el}\,\mathrm{d}t}{\int \dot{m}_{vap}\,\mathrm{d}t} \tag{2.1}$$

is commonly used to quantify and compare energy efficiencies of different dryer types. Where P_{el} corresponds to the consumed electrical energy and $\dot{m}_{vap}$ to the evaporated water. Alternatively, another parameter the specific moisture extraction rate $SMER$ as the reciprocal of SEC, can also be used as a performance indicator of dryers [67].

2.2.2 Clay and clay minerals

Clay is the main and most important component of the raw material used for the production of clay bricks. It's a composition of clay minerals, other minerals, and organic matter and is giving the plastic and shapeable attributes to the raw material. As a weathered product of rocks with high feldspar content like granite its chemical formation, mineralogical structure, and grain size composition are high dependent on the mining location. Drying behaviour, plasticity, and the required amount of tempering water are mainly influenced by the grain size distribution. In general, greater fractions of grains smaller than $2\,\mu\text{m}$ lead to higher plasticity of the raw material [75].

Structure and plasticity of clay minerals

Clay minerals are part of the layer silicate minerals group. The basic modules are $[\text{SiO}_4]$-tetrahedrons and $[\text{Me(O,OH)}_6]$-octahedrons, where Me represents a metal like Al or Mg in common cases. The tetrahedral layer is formed by hexagonal rings, where the tetrahedrons' free tops are facing the same direction. The octahedral layer is connected to the tetrahedral layer by sharing the tetrahedrons' top oxygen ions. The remaining oxygen ions of the octahedral layers are ligated to protons, forming hydroxide ions OH^-. Several of these double layers are connected by dipole-dipole interaction, hydrogen bond, and van der Waals interaction. This group of silicate minerals is called double layer minerals (stratification T-O...T-O) with kaolin clay as the main representative. Fig. 2.4 shows the structure of a double layer clay mineral.

O

T

O

O O
⊘ OH
● Al
• Si
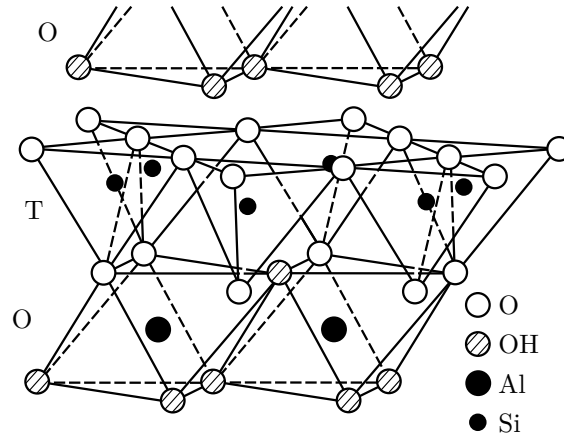
Figure 2.4: Structure of a double layer clay mineral, adapted from [76]

If there is another tetrahedral layer connected to the octahedral layer (stratification T-O-T...T-O-T), the formation is part of the three layer minerals (Montmorillonite and Illite). Fig. 2.5 shows the structure of such a three layer mineral.

T

O

T

O O
⊘ OH
● Al, Mg, Fe
• Si
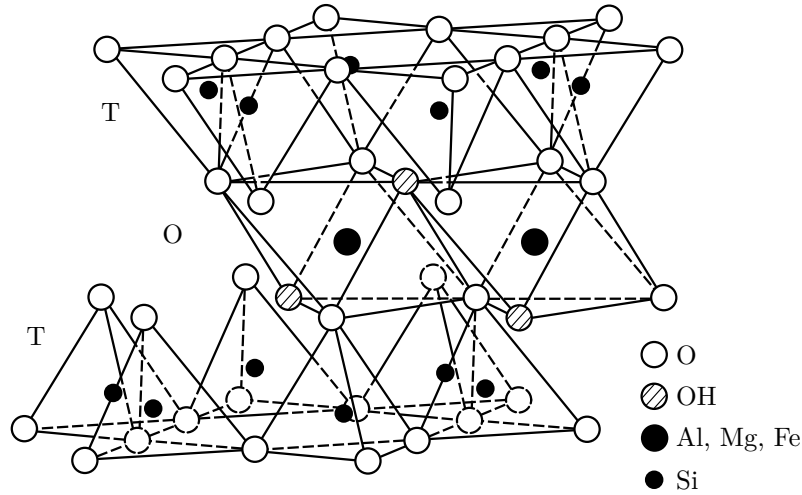
Figure 2.5: Structure of a three layer clay mineral, adapted from [76]

In most cases the Me cation occurs as Al^{3+} or Mg^{2+}. But the high diversity of clay minerals is based on the exchange of several cations. The Al^{3+} or Mg^{2+} cations of the octahedral layer and also the Si of the tetrahedrons can be replaced by other appropriate elements. Negative excess charge can occur and can be balanced by additional cations between the layers. H_2O molecules as interlayer water and hydroxides as intermediate layers are also possible. This fact causes another rise of clay mineral variety [76, 77].

Layer silicate minerals offer a large specific surface where negative electrical charges can occur. Therefore Salmang and Scholze [77] explain several causes in detail. In wet suspensions or so-

called ceramic creams these charged particles are surrounded by ions and polar molecules like water molecules. On a solid particle's surface hydrated cations are bonded firmly by adsorption, consequently the concentration of cations is increased [77]. Due to the electrostatic effect between the dipole structure of water and the mineral's surface an adhesive cover of water follows till a certain distance. Close-by layers are stiff tightened while water molecules and hydrated cations are getting moveable with increasing distance to the negatively charged solid particle. Such a set-up of fixed and of moveable layers is called diffuse double layer. Fig. 2.6 illustrates the model of the diffuse double layer at the surface of a circular clay particle. Actually clay minerals are shaped flat [78].

Negative charged particle

Suspension

Polar water molecules
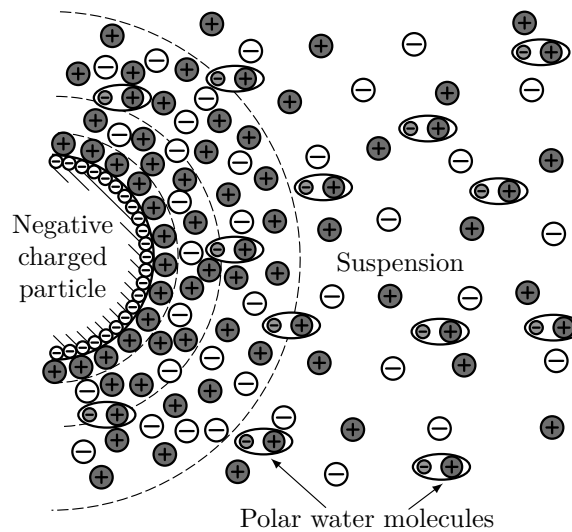
Figure 2.6: Diffuse electrical double layer, adapted from [77]

The diffuse attached cover water alleviates the particles' movement along each other in large measure. Hence it's essentially responsible for the plastic characteristic of clay. Another consequence is the clay's shrink and swell capacity if its water content changes [79].

Bonding between water and solid material

Depending on the nature of bonding, it can be distinguished between adhering, swelling, and capillary related interstitial liquids. Chemical bonding would be another type, but in this case the removing of chemical bonded moisture isn't part of the drying process.

Adhering liquid is covering the outer surface of the lump-sized material as a continuous water film. That equates a free water surface, where the vapour pressure depending on temperature equals the saturation vapour pressure.

Swelling water is part of the solid phase, like the above mentioned interlayer water, while adhering moisture and water in capillary tubes are coating the grains' surfaces. It's responsible for volume changes of the solid bodies in porous media [70]. Because of the higher bonding quality,

this kind of water remains in the compound during the drying process until the temperature is rising. Depending on the clay's composition the amount of swelling water and also the shrink and swell capacity vary. Hence, high fractions of swell-able clay minerals are disadvantageous for the drying behaviour [79].

Capillary related interstitial liquid is described as water in the caverns and channels of porous media. The vapour pressure of water in macropore media with a pore radius greater than $1\,\mu m$ remains at the temperature dependent saturation value, like for adhering water. In fine-pored media with a pore radius lower than $0.1\,\mu m$ vapour pressure is significant lower (capillary condensation) [63, 70]. For the drying process that leads to the following consequences. The vapour pressure for drying products with high moisture content is equal to the saturated vapour pressure. While drying, the water is driven to the body's surface due to capillary forces. First the larger capillaries get cleared, the moisture content decreases but the fine pores are still filled. Hence, the vapour pressure for small moisture contents is lower compared to high moisture contents. The connection between vapour pressure and moisture content is caused through forces to the liquid phase impressed through bonds to the solid phase. With other words, a liquid's vapour pressure is also influenced by external forces and not only by its own temperature [59]. Materials are called hygroscopic if they are able to bind water with a simultaneous significant lowering of vapour pressure [67].

The two main phenomena of interaction between liquid and solid phases are surface tension and adsorption. Drag and pressure forces through surface tension can also be seen as external forces. These forces are the main reason for the above described capillary effects and also for causing moisture transport through porous media. But this will be discussed in detail in Chapter 2.2.4. Another reason for the appearance of external forces is the van der Waals interaction between molecules of the liquid and solid phase, which are also most significant at low moisture contents. This type of bond is called adsorption [59].

Nevertheless, for the sake of completeness it's mentioned that vapour pressure drop can also appear in chemical solutions and through chemical absorption.

All the specified types of bond between liquid and solid material with responsibility for lowering the vapour pressure are summarised as sorption. In most cases, it's not possible to distinguish strictly between these types of bonding [59].

If a wet solid is exposed to a continuous and constant supply of fresh air, it continues to lose moisture until the vapour pressure of the moisture in the solid is equal to the partial pressure of the vapour in the air. The solid and the surrounding air are in equilibrium. This moisture content of the solid is called the equilibrium moisture content under the prevailing conditions [67].

The trends of equilibrium moisture content over relative humidity at a certain temperature are called equilibrium moisture isotherm. Those are determined in experiments, where two different curves can be found. If equilibrium was reached while drying, the corresponding moisture content is higher than the moisture constant that can be found while humidification, under the same surrounding air conditions (hysteresis) [59].

Fig. 2.7 shows the equilibrium moisture isotherms for different clays and temperatures. Two typically distinct areas can be identified. For low values of relative humidity pure adsorption takes action. At high relative humidity capillary condensation is responsible [70].
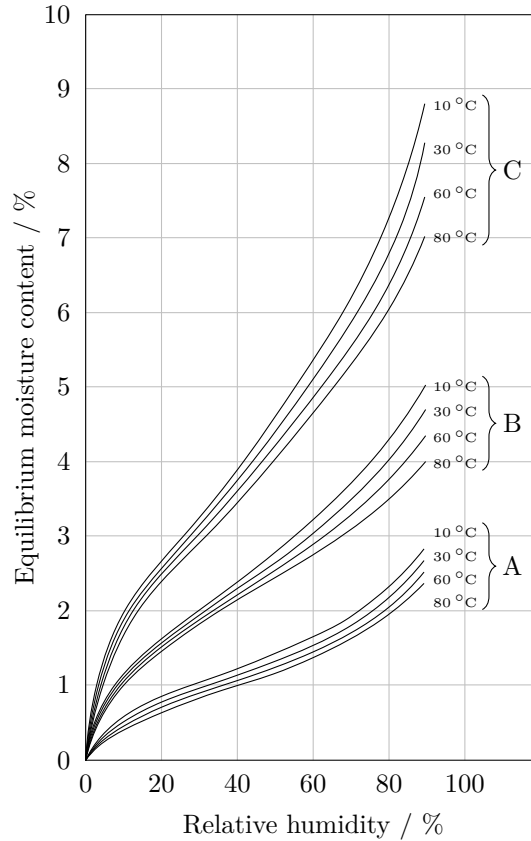
Figure 2.7: Equilibrium moisture isotherms for different clays: Clay A with low to clay C with high swell-ability, adapted from [80]

Each type of bond is reducing the molecule's degree of mobility and can be seen as energy loss of the bonded liquid phase. The energy loss appears as released thermal energy. In general it's called bond enthalpy and more specific for adsorptive and capillary bond it's called heat of wetting.

While drying, liquid water is evaporated and exits the drying product. Therefore the enthalpy of vaporisation and additionally the bonding enthalpy have to be provided. But that is just the case for very low water contents, where the drying product shows hygroscopic behaviour. At higher moisture contents the bonding enthalpy is insignificantly small.

In the energy balance of dryers the bonding enthalpy usually can be neglected. But if the drying process starts at the hygroscopic part with low moisture content, and it has to be dried till very low moisture content, the bonding energy also has to be part of the energy balance [59, 63].

Shrink swell behaviour

While drying or wetting of different compounds, the solid particles are moving relatively under the effect of inner forces to each other. Such behaviour is called shrinking or swelling.

Shrinking is the tightening of an almost dimensionally stable body. The body's volume consists of solid, liquid, and gaseous volume. In general the solid matter isn't changing its volume while drying. Thus, it can be assumed that the body's change of volume is equal to the change of liquid volume less the generated hollow volume. Matter is shrinking in an ideal way, if its volume is decreasing in the same amount as the liquid volume does. Such behaviour can be observed while drying of peat, pasta, and ceramic bodies of high water content, if they can shrink unhindered.

Fig. 2.8 shows three types of different shrinking curves. Clay and kaolin are shrinking at high water contents. Others, like wood and coal aren't shrinking at high water contents but start to shrink after falling below a certain water content limit. Peat and pasta are changing their length and volume constantly over the whole water content range. For goods with explicitly orientated inner connections the shrinkages deviate towards individual spatial directions. This anisotropic behaviour is known from goods with fibrous structure, wood, paper, gels, and pastes.

Aside from the moisture removal the amount of shrinkage is also depending on the circumstances while drying. Unhindered shrinking is given when neither drag or pressure forces are influencing the drying body. This is only the case if the product dries very slowly, since there is no nameable moisture gradient arising through the body's volume. Also external forces have to be absent. If moisture is removed from the layers close to the surface, these regions are forced to shrink. The inner layers initially hold the starting moisture content, hence, their volume remains the same. Mechanical stresses between the layers are the consequences. Also outer forces can be the reason for hindered shrinkage. If a plastic body is shrinking on a rough or adhesive surface the amount of shrinkage is less due to frictional and adhesive forces [63].

As already mentioned ideal shrinkage is the case, if the drying product's volume decreases in the same amount as the liquid volume does. The following equations are corresponding to the curves in Fig. 2.8 and represent such behaviour for a body's length L, surface A, and volume V.

$$L = L_{dry} \left(1 + \gamma\, y\right) \tag{2.2}$$

$$A = A_{dry} \left(1 + \gamma\, y\right)^2 \tag{2.3}$$

$$V = V_{dry} \left(1 + \gamma\, y\right)^3 \tag{2.4}$$

$$\chi = \frac{L_{ini} - L}{L_{ini}} \tag{2.5}$$

Where γ denotes the linear shrinkage coefficient, y the water content as the containing mass of water referred to the mass of the completely dry product, χ the linear relative shrinkage, and e. g. L_{ini} the initial length. The linear shrinkage coefficient for clays ranges from 0.48 to 0.7 [81, 82].
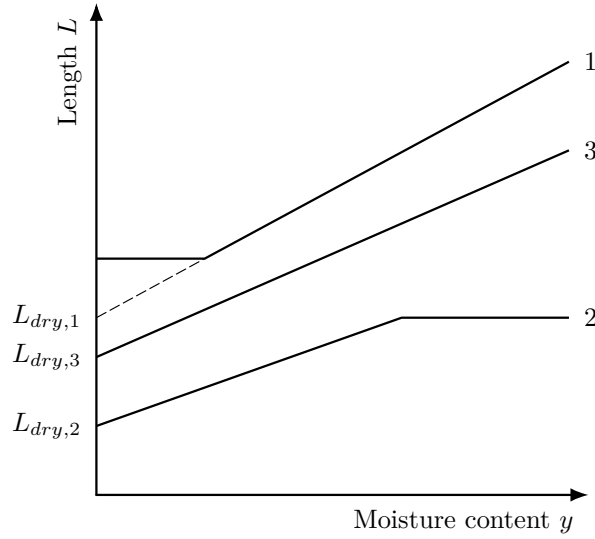
Figure 2.8: Typical shrinking curves for 1 clay and kaolin, 2 wood and coal, 3 peat and pasta, adapted from [63]

These coefficients appear to be independent of external drying conditions if these are mild [65]. Common values for the linear relative shrinkage χ of clays range from 0.03 to 0.11 [75].

Fig. 2.9 illustrates the shrinking pattern of clay. It's representing a certain depth of a brick's wall or the whole brick under mild drying conditions with negligible moisture gradients. Throughout the raw material processing, clay is provided with relatively high water content to ensure proper plasticity for shaping. The extruded green body contains as much moisture, so that the clay particles are totally surrounded by water. At the beginning of convective drying water starts to evaporate at the brick's surface. The volume of contraction equates the outgoing shrinkage water. Clay particles are moving closer together. Hence the shrinking process also starts at the brick's surface. Due to capillary effects water flows from inner sections to the brick's surface. The surface stays fully covered by water. With further water release the particles are moving closer and closer, the shrinking process shifts to inner cross sections. If the clay's particles have moved as close, so that they are touching each other, the evaporating water volume cannot be compensated by shrinkage. This so-called shrinking end is indicated by the vertical dashed line in Fig. 2.9. With ongoing drying, gaseous pores will be developed. The evaporating water has to be replaced by vapour or entering drying air. The point in time when the first gaseous pores are formed can be observed at the brick's surface. Light reflections turn from dark to bright. After that, water is still carried to the brick's surface due to capillary effects. The capillaries of bigger size are filled first by air. Smaller ones are still flooded. So that just as before, the brick's surface can be seen as free water surface, even if it's not fully connected [75].

Tests of drying thin-walled cylinders of clay have shown that if the moisture content variations through the material are negligible, shrinkage ends abruptly. Otherwise, when moisture gradients
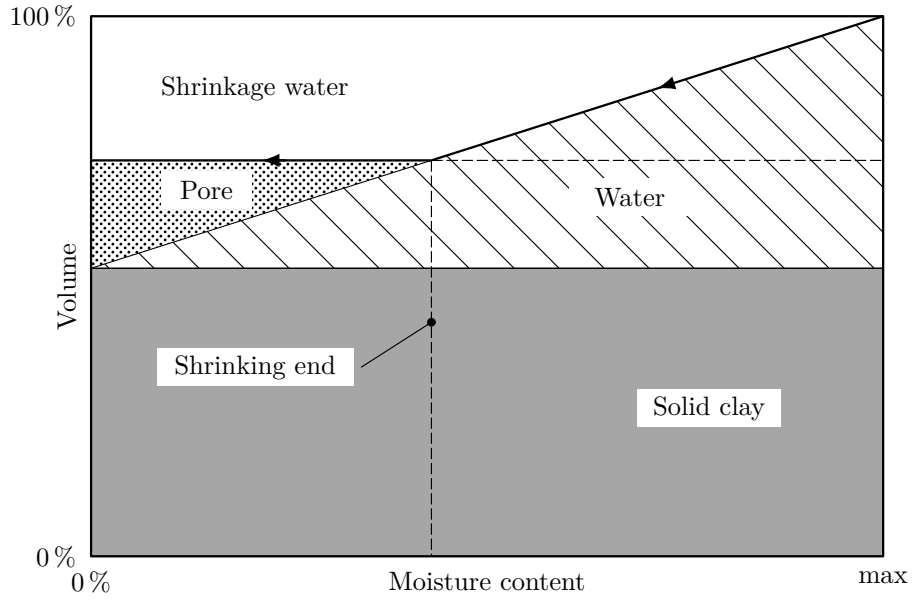
Figure 2.9: Shrinking pattern of clay, adapted from [67]

are present, the shrinking end is more sluggish [65]. Thus the shrinkage behaviour highly depends on the drying product's geometry and also on the drying conditions. Moisture gradients or shrinkage gradients which are responsible for inner mechanical stress, often cause surface cracks. On the other hand shrinkage and also the compound's stability will increase with continuing drying or decreasing water content. Especially for very low water contents when there is just adsorptive water bonding present [70].

Surface cracks are unrecoverable damages and have to be avoided through the whole production chain. Keey [65], Lykov and Pezold [81] are dealing with this major issue by focusing on the drying process. Musielak and Śliwa [83] are introducing two numeric models to predict surface cracks.

2.2.3 The drying process

Bricks are usually dried convective with hot air. The air cools down during the drying and picks up the evaporated water from the surface. Coupled heat and mass transfer occurs across the boundary layer. The drying product's moisture content decreases. Depending on the dried material, three periods of drying may be distinguished, as the drying rate's typical curve shows in Fig. 2.10. The drying process starts with a constant drying rate. This is the first drying period (DP). In the second DP the drying rate decreases. In case of capillary-porous materials it is followed by a stage due to hygroscopic effects as third DP.
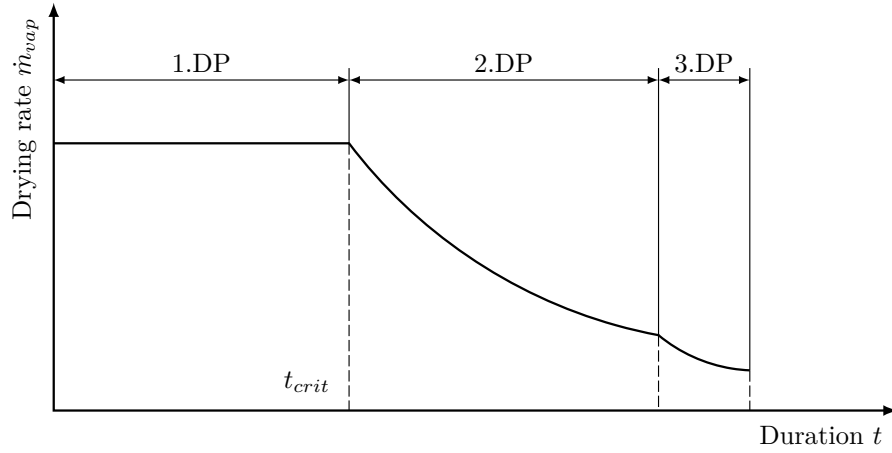
Figure 2.10: Drying rate of a capillary-porous material with hygroscopic behaviour, adapted from [75]

First drying period

While liquid water is present at the exchange surface, the drying rate only depends on the surrounding air conditions, such as temperature, relative humidity, velocity, and flow configuration. If these parameters are kept constant the drying product attains a certain constant temperature, after a short transient starting section. The drying rate also remains constant. This stage is commonly referred to in literature as the constant drying rate stage or first drying period [84].

The heat flow supplied by the drying medium is entirely used for transforming the liquid water into vapour. The position where evaporation takes place, the so-called drying interface, is located at the surface [75, 84]. No energy transfer occurs within the product during this period, as it acts like an adiabatic wall. The product's temperature remains constant. This steady-state adiabatic temperature is called cooling limit or wet-bulb temperature and depends on the surrounding air conditions [55]. According to Krischer and Kast [59], the drying product's temperature varies from the wet-bulb temperature. However, the difference can be neglected. In addition, it can be assumed that bonding between water and clay particles can also be neglected for this drying period. The transferred thermal energy is entirely used to evaporate the liquid water [75].

Evaporation takes place at the brick's surface and leads to shrinkage. First the removed water is compensated by tightening the clay particles, while moisture from inner sections is also transported to the surface due to capillary effects. If the particles have moved as close together, so that they are touching each other, shrinkage has ended. As the drying process progresses, evaporating water is simply replaced by surrounding air, starting in capillaries of bigger size on the product's surface. As mentioned in previous statements, the brick's surface can still be seen as free water surface, surrounded by saturated air. The vapour pressure depending on temperature equals the saturation vapour pressure. This is an important issue to be able to

describe the heat and mass transfer, since the driving forces are linked together.

With continued drying, the exposed surface is still supplied with liquid water from the inside of the product by capillary effects. The liquid migrates from regions with high moisture content towards regions with low moisture content. The constant drying rate period lasts as long as the surface is supplied with liquid water. Its duration $t = t_{crit}$ depends highly on the drying conditions and on the medium properties [84]. The phenomenon of capillary transport is an important topic in context of drying porous media and will be treated in a specific Chapter 2.2.4.

Fig. 2.11 shows the characteristic time dependent moisture distributions of a capillary-porous, non-hygroscopic sufficiently large plate, dried from both sides. Only the distribution of the moisture content changes during the first drying period, starting with even distribution $y(z, t = 0) = y_{ini}$. Moisture gradients can be seen as the driving force of transport. Compared to inner layers, the water content at the product's surface decreases more intense. The moisture gradient at the surface is growing with progressed drying. When $t = t_{cirt}$ got reached, the surface dried up [59].
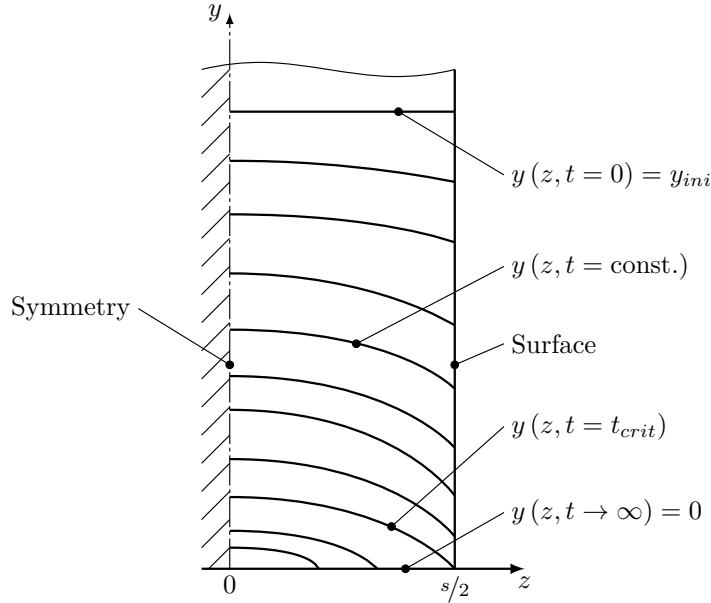
Figure 2.11: Moisture distribution at different times of a capillary-porous, non-hygroscopic material, dried from both sides, adapted from [59]

Second drying period

If the capillary forces aren't sufficient to carry enough moisture to the surface, the second drying period or decreasing rate stage begins. The drying rate falls steadily (cf. Fig. 2.10). The drying interface migrates towards inner sections, hence, evaporation takes place beneath the surface and the vapour diffuses through the air-filled pores. As a result, a diffusion resistance in the dry

layer prevails in addition to the mass transfer resistance at the surface. The drying behaviour is also influenced by the diffusion conditions of the dry layer. With continued drying, the drying interface migrates further to inner sections. At the same time moisture from the wet core is still carried against the interface's moving direction due to the capillary effect.

Thermal energy is transferred by convection to the drying product and transported through the dry layer by conduction. The drying rate is reduced and the heat flow supplied to the medium is temporarily greater than required for evaporation. The excess energy is used to heat up the product, the surface at first, followed by the inner part.

The dried pores in vicinity of the wet core are filled with saturated air. The drying interface is located where the prevailing saturation vapour pressure corresponds to the current layer temperature. The temperature and the water vapour pressure are clearly linked at the drying interface, hence, the mass transfer during the second drying period can also be described.

The drying interface is moving toward the product's core until it reaches the product's centre or if in case of one-side drying the opposite side. Then the drying process has finished.

Bonding energies are playing only a minor role during the second drying period, since the bonded water is extracted only within the third drying period. As already mentioned in Chapter 2.2.2, bonding energies can be neglected if the drying process was started at high moisture content. Additionally, the drying process often has finished before hygroscopic effects rise up. In the brick and tile industry the process is often stopped at water contents y ranging from 0.5% to 3.0%. Thus, the hygroscopic properties of the raw materials don't have to be taken into account in the mathematical formulations [75].

In context to this work, it's assumed that the drying process only consists of the first and second drying period. The only hygroscopic effect taken into account is that drying can be carried out until the equilibrium moisture content, corresponding to the surrounding air conditions, is reached.

The described modelling approach is often referred to as the wet core model. It is assumed that dry and wet zones within the product are stacked in series. Not many works have focused on the second drying period. For the sake of completeness, it should be mentioned that an alternative approach also exists in the literature. Schlünder [85] elucidated the first drying period by the so-called wet surface model and also applied it for the second drying period. He claims that the product's surface remains partly wet during the second drying period, due to the capillary transport through particular thin pores. The dry and wet zones are arranged in parallel.

The h_{1+X},X-chart

The h_{1+X},X-chart is a convenient tool to demonstrate the changes in state of wet air. As shown in Fig. 2.12, the specific enthalpy referred to the mass of dry air h_{1+X} is drawn versus the humidity X in an oblique-angle system of coordinates. The isotherms $\vartheta = $ const. and lines of constant relative humidity $\varphi = $ const. are also shown. Two main regions can be distinct. The

unsaturated and the oversaturated region separated by the saturation line $\varphi = 1$. Baehr and Kabelac [16] are describing in detail how the thermodynamic properties are linked and how the chart is constructed.
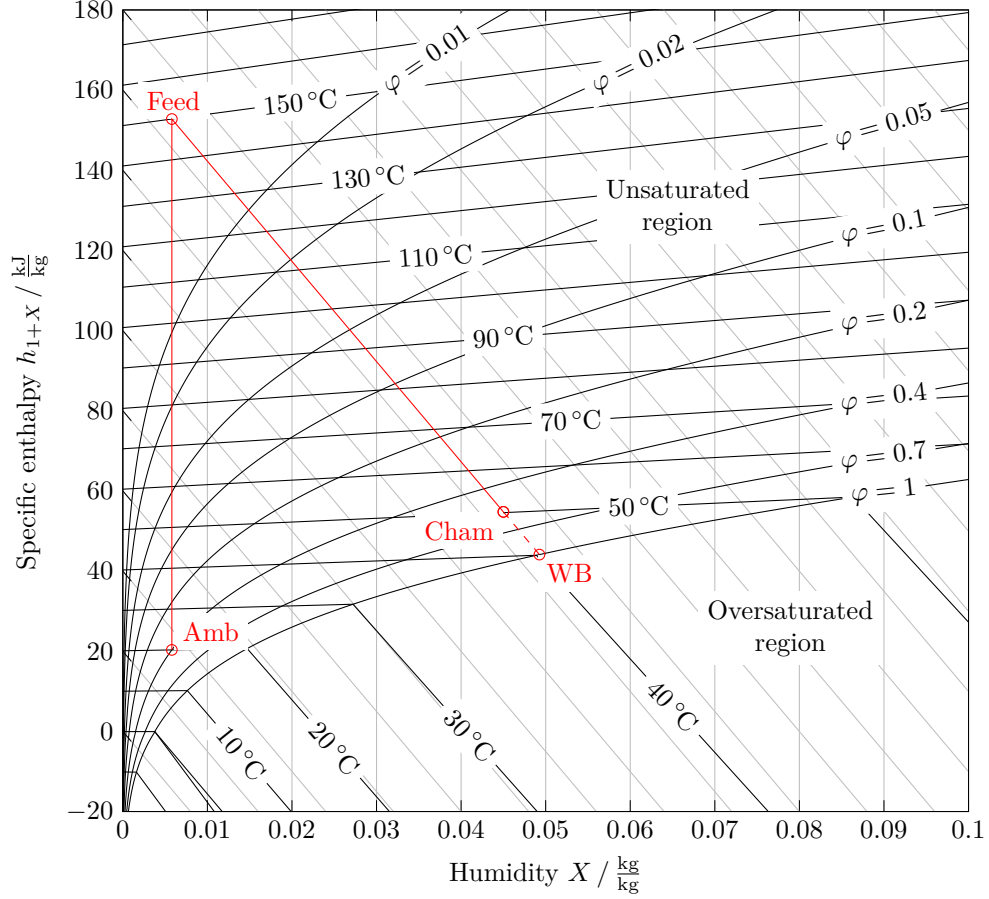
Figure 2.12: Changes in state of wet air on its way through a chamber dryer during the first drying period, shown in the h_{1+X},X-chart

The red path plotted in Fig. 2.12 indicates the changes in state of a typical drying process during the first drying period in a chamber dryer. Ambient air ($\vartheta = 20\,°C$, $\varphi = 0.4$) is heated up to a feed temperature of $\vartheta = 150\,°C$. The humidity X remains constant, the relative humidity φ drops. Then it enters the chamber. There neither are thermal losses nor leakages through the dryer walls. Accordingly, a chamber climate is developed which lies on the same isenthalpic line as the feed air flow climate does. The distance from the saturation line mainly depends on the drying rate and the feed mass flow rate. For the shown case a temperature of $\vartheta \approx 40\,°C$ and a relative humidity of $\varphi \approx 0.55$ are attained. As described in the previous chapter, the drying product's temperature attains the wet-bulb (WB) temperature $\vartheta \approx 40\,°C$, indicated by the circle on the saturation line with $\varphi = 1$.

83

Furthermore, it can be noted that the chamber climate is displayed by a single circle. The air volume in chamber dryers is mixed ideally and fulfils the basic requirements of the ideal stirred tank reactor [11]. Apparatus such as ACUs shown in Fig. 2.1 are responsible for uniform mixing. When modelling a chamber dryer, the following assumptions are often taken:

- The feed air flow entering the chamber is mixed immediately and uniformly.

- Hence, the same drying climate prevails at all locations within the dryer volume.

- The exhaust air conditions are equal to the state of the dryer atmosphere.

- All surfaces of the drying product are exposed to the same heat and mass transfer conditions.

2.2.4 Heat and mass transfer during drying processes

The heat and mass transfer processes, within the drying product and at the drying product's surface during the first and second drying period, are summarised in the current chapter. Practical and permissible modelling assumptions of the thermodynamic processes and the mathematical derivation and formulation are presented.

A general aspect should be mentioned first. Most drying products in the brick and tile industry are approximately plate-shaped or composed of single plates, such as hollow bricks [75]. Their extension in direction of the wall thickness is small compared to its dimension in the other directions. In conjunction with the previously introduced modelling of the chamber dryer as an ideal stirred tank reactor, the consideration of the drying product as a one-dimensional symmetrical plate is permitted. These are two important and useful simplifications. Consequently, the effort in the model equations' numerical treatment and the computational complexity while solving transient problems can be kept manageably.

Heat and mass transfer at the drying product's surface

As the labelling of convective dryers reveals, heat and mass transfer at the brick's surface are forced by convection. In a flowing fluid, energy and mass are also transported by the macroscopic movement of the fluid, not only through conduction and diffusion. Hence, convective transfer combines mass transport through diffusion, heat transport through conduction and transport of enthalpy through the flowing fluid itself.

The energy transport can be described by the boundary layer theory for one-dimensional problems. An imaginary fixed layer at the brick's surface is passed by a heat flow through conduction due to a temperature gradient and also through energy as enthalpy due to the fluid movement. Fig. 2.13 illustrates this so-called thermal boundary layer with the thickness δ_{th} and the summarised heat flow rate $\dot{Q}$. This heat flow rate is depending in a complex way on the boundary layer's temperature and flow field. The determination would encounter high difficulties.

Therefore, the equation

$$\dot{Q} = -\alpha\, A\, (\vartheta_\delta - \vartheta_{surf}) \tag{2.6}$$

defines the heat transfer coefficient α, as an empiric parameter. Where A denotes the involved surface, ϑ_δ the fluid's temperature at the boundary layer's (imaginary) surface $z = \delta_{th}$, and ϑ_{surf} the fluid's temperature at the solid wall's surface $z = 0$.

When fluid particles make contact with a solid surface, they assume zero velocity. Hence, the energy balance at the wall or at the drying product's surface can be written as Fourier's law of thermal conduction:

$$\dot{Q} = -\lambda\, A\, \left.\frac{\partial \vartheta}{\partial z}\right|_{z=0} \tag{2.7}$$

Where $\lambda = \lambda\,(\vartheta_{surf})$ denotes the fluid's thermal conductivity at the solid surface's temperature. If α is known, an approximation for δ_{th} can be made by linearising the temperature gradient [55, 86]:

$$\left.\frac{\partial \vartheta}{\partial z}\right|_{z=0} \approx \frac{\vartheta_\delta - \vartheta_{surf}}{\delta_{th}} \tag{2.8}$$

$$\delta_{th} \approx \frac{\lambda}{\alpha} \tag{2.9}$$

An alternative approach for the heat transfer problem can be made by using the theory of similarity. The number of affecting variables will be reduced through dimensionless correlations. The Nußelt number Nu is defined as

$$Nu = \frac{\alpha\, L}{\lambda} \tag{2.10}$$

and represents the forced heat transfer. Where L is the geometry's characteristic length corresponding to the considered heat transfer problem. Empiric Nußelt correlations for different heat transfer problems are often described as a function of the Reynolds number Re and the Prandtl number Pr:

$$Nu = c\, Re^n\, Pr^m \tag{2.11}$$

Where the coefficient c characterises the body's geometry and the exponents n and m the fluid flow's type [55].

The forced mass transfer can also be introduced by the boundary layer theory for one-dimensional problems. In analogy to the heat transfer, the convective mass transfer coefficient β_{conv} is defined by the following equation:

$$\dot{n}_{vap,surf} = A\, \beta_{conv}\, \Delta c_{vap} \tag{2.12}$$

$\dot{n}_{vap,surf}$ denotes the molar flow rate entering the concentration boundary layer with the thickness δ_c and Δc_{vap} the difference in vapour concentration between the boundary layer's surfaces. It
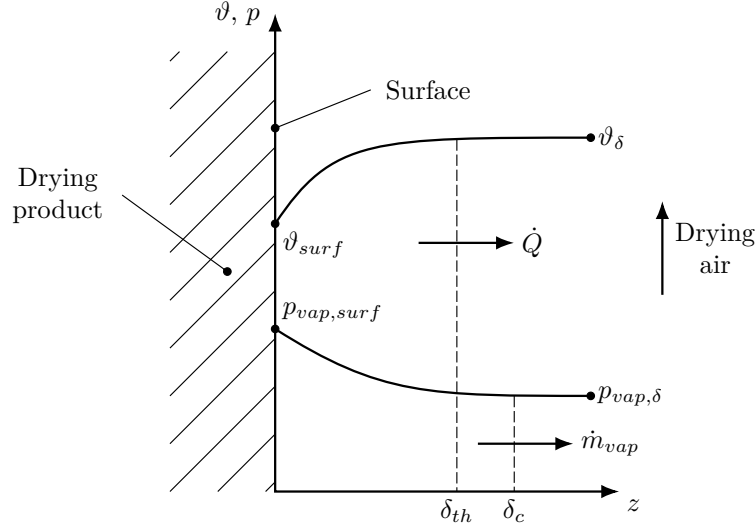
Figure 2.13: The thermal and concentration boundary layer at the drying product's surface

also can be written by definition, as a combination of diffusive and convective flows:

$$\dot{n}_{vap,surf} = \underbrace{A\,j_{vap,surf}}_{\text{Diffusion}} + \underbrace{x_{vap,surf}\,\dot{n}_{surf}}_{\text{Convection}} \tag{2.13}$$

Where $j_{vap,surf}$ is the diffusive molar flux of vapour, $x_{vap,surf}$ the mole fraction of vapour, and $\dot{n}_{surf}$ the convective molar flow rate of dry air and vapour at the drying product's surface. The diffusive part, approached by Fick's first law of diffusion, is proportional to the concentration gradient at the solid surface, for vanishing small convection $\dot{n}_{surf} \to 0$. It's also proportional to the concentration difference Δc_{vap}, hence, the mass transfer coefficient β can be defined in an appropriate way as:

$$j_{vap,surf} = -\left(c\,D\,\frac{\partial x_{vap}}{\partial z}\right)_{surf} = \beta\,\Delta c_{vap} \tag{2.14}$$

$$\beta = \frac{-\left(c\,D\,\frac{\partial x_{vap}}{\partial z}\right)_{surf}}{\Delta c_{vap}} \tag{2.15}$$

Where D denotes the diffusion coefficient of vapour in air. Eq. 2.13 can now be written as:

$$\dot{n}_{vap,surf} = A\,\beta\,\Delta c_{vap} + x_{vap,surf}\,\dot{n}_{surf} \tag{2.16}$$

According to the film theory, concentration and velocity distribution are just changing in z-direction, but not in time or the remaining directions. A stationary flow in z-direction can be assumed:

$$\frac{\partial \dot{n}_{vap}}{\partial z} = 0 \tag{2.17}$$

86

That leads to the following consequences for the molar flow rate in Eq. 2.16 with $\beta = \beta\left(\dot{n}\right)$:

$$\dot{n}_{vap} = -A\,\beta\left(c_{vap,\delta} - c_{vap,surf}\right) + x_{vap}\,\dot{n} \tag{2.18}$$

The concentration distribution $c_{vap}\left(z\right)$ and also the molar flow rate $\dot{n}_{vap}$ are depending on the convective flow $\dot{n}$. Baehr and Stephan [55] show that for the mass transfer without convection $\dot{n} \rightarrow 0$, β is proportional to the diffusion coefficient D.

$$\beta = \frac{D}{\delta_c} \tag{2.19}$$

For $\dot{n} \neq 0$ the molar flow rate $\dot{n}_{vap}$ can be found as

$$\dot{n}_{vap} = -A\,\frac{\dot{n}}{\exp\left(\frac{\dot{n}}{c\,\beta}\right) - 1}\left(x_{vap,\delta} - x_{vap,surf}\right) + x_{vap,surf}\,\dot{n} \tag{2.20}$$

by applying Eq. 2.17 on Eq. 2.18, with $\beta = \beta\left(\dot{n} \rightarrow 0\right)$.

The drying process is attended by a special case of mass transfer, the so-called one-side mass transfer. By inserting $\dot{n}_{air} = 0$ or $\dot{n} = \dot{n}_{vap}$ to Eq. 2.20

$$\dot{n}_{vap} = A\,c\,\beta\,\ln\frac{1 - x_{vap,\delta}}{1 - x_{vap,surf}} \tag{2.21}$$

follows for the one-dimensional one-side convective mass transfer [55].

For drying processes, the vapour mass flow rate $\dot{m}_{vap}$, also called drying rate, is from higher interest than the molar flow rate $\dot{n}_{vap}$. With $\dot{n}_{vap} = \dot{m}_{vap}/M_{vap}$, $c = n/V = p/(\Re\,T)$, $x_{vap} = n_{vap}/n = p_{vap}/p$, and $R_{vap} = \Re/M_{vap}$ the mass flow rate $\dot{m}_{vap}$ follows as:

$$\dot{m}_{vap} = \frac{p}{R_{vap}\,T}\,A\,\beta\,\ln\frac{p - p_{vap,\delta}}{p - p_{vap,surf}} \tag{2.22}$$

Where $\Re = 8.314\,\mathrm{J/(mol\,K)}$ denotes the molar gas constant, T the layer's mean thermodynamic temperature, $R_{vap} = 461.4\,\mathrm{J/(kg\,K)}$ the specific gas constant, $M_{vap} = 18.02\,\mathrm{kg/kmol}$ the molar mass, and p_{vap} the partial pressure of vapour. For the first drying period, the vapour partial pressure at the drying product's surface $p_{vap,surf}$ equals the saturation vapour pressure, as mentioned in Chapter 2.2.3.

In analogy to the heat transfer, the dimensionless approach of the convective mass transfer can be expressed by the average Sherwood number Sh:

$$Sh = \frac{\beta\,L}{D} = c\,Re^{n}\,Sc^{m} \tag{2.23}$$

Dividing Eq. 2.23 by Eq. 2.11 leads to the so-called Lewis correlation. The mass transfer coefficient β can be explained by the heat transfer coefficient α. In context of drying processes they

are connected through this correlation.

$$\frac{Sh}{Nu} = \frac{\beta\,\lambda}{D\,\alpha} = \left(\frac{Sc}{Pr}\right)^m = \left(\frac{a}{D}\right)^m = Le^m \tag{2.24}$$

$$a = \frac{\lambda}{c_p\,\rho} \tag{2.25}$$

$$Pr = \frac{\nu}{a} \tag{2.26}$$

$$Sc = \frac{\nu}{D} \tag{2.27}$$

$$\frac{\alpha}{\beta} = \rho\,c_p \left(\frac{a}{D}\right)^{1-m} \tag{2.28}$$

Where Sc denotes the Schmidt number, a the thermal diffusivity, c_p the isobaric specific heat capacity, ρ the density, and ν the kinematic viscosity of the drying air. As mentioned earlier, the exponent m depends on the fluid flow's type, for laminar flow $m = 0.33$ and for turbulent flow $m = 0.42$. Eq. 2.28 is by definition just valid for vanishing convective flows $\dot{n} \to 0$. For finite values a correction as introduced by Eq. 2.20 has to be made [55].

The diffusion coefficient's D temperature dependence at $p = 1\,\mathrm{bar}$ for vapour in air can be determined by the following equation [59]:

$$D = 22.6 \times 10^{-6}\,\frac{\mathrm{m}^2}{\mathrm{s}} \left(\frac{T}{273\,\mathrm{K}}\right)^{1.81} \tag{2.29}$$

Heat transport through dry layers

The energy transport through the product's dry layer can be described by Fourier's law for one-dimensional conduction:

$$\dot{Q} = -\lambda\,A\,\frac{\partial\vartheta}{\partial z} \tag{2.30}$$

Where $\dot{Q}$ denotes the heat flow rate, A the involved surface, λ the heat conduction coefficient of the dry product, and $\partial\vartheta/\partial z$ the temperature gradient as the driving force of heat conduction.

The drying interface, located at the inner bound of the dry layer, is behaving like a heat sink. The predominant proportion of the incoming heat flow is used for evaporation. The drying interface is moving very slowly towards the brick's wall centre, its temperature also rises slowly. Hence, the actual unsteady process can be modelled as a quasi-stationary heat conduction problem [75].

For sufficiently slow processes the following assumption can be made:

$$\frac{\partial\dot{Q}}{\partial z} = 0 \tag{2.31}$$

Executing this assumption on Eq. 2.30 leads to a second order differential equation with the

boundary conditions corresponding to Fig. 2.14. The equation for one-dimensional stationary heat conduction can be found as a solution:

$$\frac{\partial \vartheta}{\partial z} = \frac{\vartheta_{surf} - \vartheta_C}{s_{dry}} \qquad (2.32)$$

$$\dot{Q} = -\frac{\lambda}{s_{dry}} A \left(\vartheta_{surf} - \vartheta_C \right) \qquad (2.33)$$
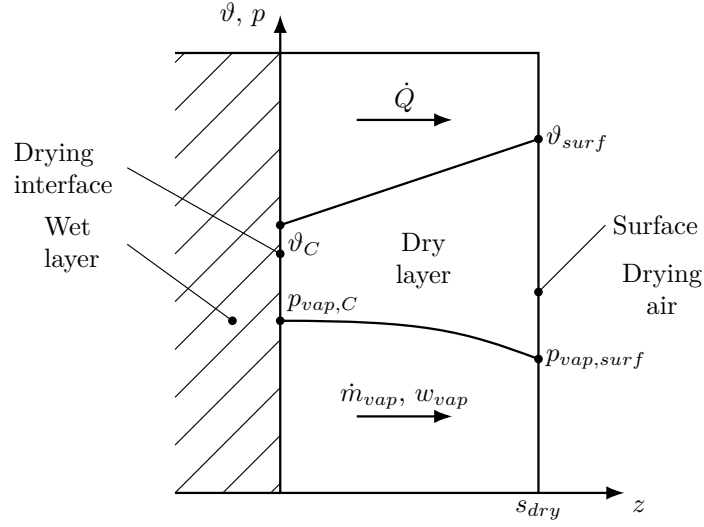
Figure 2.14: Heat and mass transport through the dry layer

Since the drying interface's temperature is rising very slowly during the second drying period, it can be assumed that the same applies for the wet core. In addition, the thermal conductivity of this region will be relatively high. As a result, the temperature of the wet region can be seen as even distributed. It equals the drying interface's temperature [75].

Vapour diffusion through dry layers

Mass is transported just in z-direction, hence a similar one-dimensional approach to Eq. 2.13, can be used for determining the diffusion problem. The molar flow rate of vapour $\dot{n}_{vap}$ can be written as

$$\dot{n}_{vap} = A c_{vap} w_{vap} = A \left(j_{vap} + c_{vap} \left(x_{vap} w_{vap} + x_{air} w_{air} \right) \right) \qquad (2.34)$$

where w_{vap} and w_{air} denote the velocities of the involved species, vapour and air, in z-direction. The diffusion problem linked to drying processes can again be seen as one-side diffusion with $w_{air} \to 0$. The molar flow rate of vapour is a multiple times higher compared the molar flow

rate of air. Using Fick's first law of diffusion leads to:

$$j_{vap} = -D\,\frac{\partial c_{vap}}{\partial z} = -c\,D\,\frac{\partial x_{vap}}{\partial z} \qquad (2.35)$$

$$\dot{n}_{vap} = -A\,c\,D\,\frac{1}{1-x_{vap}}\,\frac{\partial x_{vap}}{\partial z} \qquad (2.36)$$

Just for comparison, Eq. 2.36 written without the term $^1/_{(1-x_{vap})}$ describes equimolar diffusion. This term is called the Stefan correction. It's vanishing for small molar fractions of vapour x_{vap}.

The processes at the drying interface are changing very slowly, as argued in the previous chapter. The same applies for the drying rate. Hence, the same assumption of a quasi-stationary problem can be taken:

$$\frac{\partial \dot{n}_{vap}}{\partial z} = 0 \qquad (2.37)$$

Executing this assumption on Eq. 2.36 leads to a second order differential equation with the boundary conditions corresponding to Fig. 2.13 with the solution [55]:

$$\dot{n}_{vap} = -\frac{A\,D}{s_{dry}}\,\frac{p}{\Re\,T}\,\ln\frac{p - p_{vap,surf}}{p - p_{vap,C}} \qquad (2.38)$$

Again, the mass flow rate is more appropriate considering drying processes. With $\dot{n}_{vap} = {}^{\dot{m}_{vap}}/_{M_{vap}}$, and $R_{vap} = {}^{\Re}/_{M_{vap}}$ the mass flow rate $\dot{m}_{vap}$ follows as:

$$\dot{m}_{vap} = -\frac{A\,D}{s_{dry}}\,\frac{p}{R_{vap}\,T}\,\ln\frac{p - p_{vap,surf}}{p - p_{vap,C}} \qquad (2.39)$$

For the second drying period, the vapour partial pressure at the drying interface $p_{vap,C}$ equals the saturation vapour pressure, as mentioned in Chapter 2.2.3.

Eq. 2.29 describes the diffusion coefficient's temperature dependence for free diffusion of vapour in air. In porous media, this transport coefficient isn't only depending on temperature and pressure. The geometry, the porous structure and also the pore size distribution have an impact. For sufficiently large pores common molecular diffusion occurs. Just the reduced cross section caused by the solid particles and the increased intertwined diffusion path have to be taken into account. For non-free or hindered molecular diffusion the diffusion coefficient D in Eq. 2.39 has to be replaced by the lower effective diffusion coefficient D_{eff} defined by:

$$\mu = \frac{D}{D_{eff}} \qquad (2.40)$$

$$\mu = \frac{\tau_p}{\epsilon_p} \qquad (2.41)$$

Where μ denotes the dimensionless diffusion resistance with Eq. 2.41 as a first approximation, ϵ_p the porosity, and τ_p the tortuosity[1] [88]. Common values for μ of bricks range from 8 to 25 [11,

---

[1]Traditionally the length of the actual path line between two ports that the fluid particle travels divided by

89]. Finally the diffusion mass flow rate $\dot{m}_{vap}$ of vapour in porous media is:

$$\dot{m}_{vap} = -\frac{A\,D}{\mu\,s_{dry}}\,\frac{p}{R_{vap}\,T}\,\ln\frac{p - p_{vap,surf}}{p - p_{vap,C}} \tag{2.42}$$

But if the pore size is about the mean free path of the involved molecules, the gas molecules collide with the pore walls more frequent than with each other. Knudsen diffusion takes place [88]. The investigations of Telljohann [75] on pore size distributions for different clays have shown that the Knudsen diffusion plays only a minor role compared to the molecular diffusion. Typical pore size distributions are ranging from 3 nm to 200 μm [75].

Capillarity and moisture transport through wet porous media

Moisture is transported through the capillary pore structure. The movement is caused by the capillary effect, which should be described first. A vertical cylindrical-shaped capillary with the radius r_c is connected to a free water surface pressurised by the ambient pressure p_{amb}. Then the hydrostatic head rises by the so-called capillary head h_c. That requires depression in the raised concave surface (meniscus), the so-called capillary drag p_c. Gauge pressures are arising, if a liquids surface is curved convex to the outside (water drops).

$$p_c = h_c\,\rho\,g = \frac{2\,\sigma\,\cos\Theta}{r_c} \tag{2.43}$$

Where σ denotes the surface tension of water in air, Θ the contact angle at the concave interface, g the gravitational acceleration, and ρ the density of water.

Fig. 2.15 shows the pressure distribution of a model body made of capillaries of different sizes. According to Eq. 2.43, the capillary drag p_c increases with decreasing radius of the capillaries r_c. Tab. 2.1 is giving actual values of the capillary drag or pressure. As a result, if different-sized capillaries are connected to each other and evaporation takes place at the body's surface, thick capillaries are exhausted by thin ones at the beginning of the drying process [59].

Table 2.1: Drag and pressure of capillary tubes and drops [59]

Radius	Drag or pressure
m	bar
10^{-6}	1.5
10^{-7}	15
10^{-8}	150
10^{-9}	1500
10^{-10}	15 000

the length of a straight line between these ports. This path is taken by a diffusion motion and is independent of the net velocity [87].
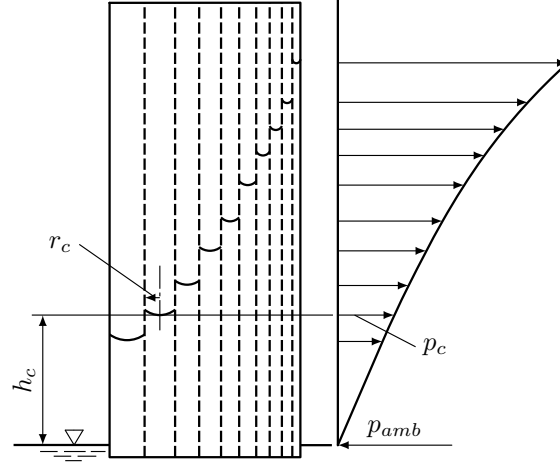
Figure 2.15: Pressure distribution of a model body composed of different-sized unresistant connected capillaries, adapted from [59]

The processes due to the capillary effects while drying can be described by a simple model of two unresistant connected capillaries, as shown in Fig. 2.16. Shrinkage is neglected and evaporation just takes place at the concave interface of the thin capillary. This assumption can be made, because the number of thin capillaries in drying products is markedly higher than the number of thick capillaries. In the first drying period, the beginning of drying, both capillaries have a flat water surface (Fig. 2.16.a). Evaporation takes place at the surface of capillary 1, the drying rate $\dot{m}_{vap}$ can be described by Eq. 2.22. The evaporated water will be replaced by water from capillary 2, its concave interface is moving inwards and the capillary gets filled by air from the outside. The driving pressure difference Δp_c can be calculated by:

$$\Delta p_c = 2\,\sigma \left(\frac{1}{r_{c,1}} - \frac{1}{r_{c,2}} \right) \tag{2.44}$$

For spherical meniscuses $\cos\Theta = 1$. On the other hand, a friction pressure loss Δp_f in capillary 1 due to the laminar flow arises. It can be described by the Hagen–Poiseuille law:

$$\Delta p_f = \frac{8\,\eta\,\dot{m}_{vap}}{\rho\,\pi\,r_{c,1}^4}\,s_2 \tag{2.45}$$

Where η denotes the dynamic viscosity of water and $\dot{m}_{vap}$ the moisture mass flow rate through capillary 1 or the evaporating mass flow rate. The pressure loss Δp_f is rising, with expanding the length of the fluid flow's path s_2 through capillary 1, while continuing the evaporation process. If a certain critical length $s_2 = s_{2,crit}$ is reached, Δp_c equals Δp_f and capillary 1 looses the ability to exhaust capillary 2 (Fig. 2.16.b). The end of the first drying period is reached.

$$\dot{m}_{vap}\,s_{2,crit} = \frac{\sigma}{4\,\eta} \left(\frac{1}{r_{c,1}} - \frac{1}{r_{c,2}} \right) r_{c,1}^4\,\pi\,\rho = \frac{\sigma\rho}{\eta}\,C_c \tag{2.46}$$

C_c is depending on the capillary system's structure. As mentioned in Chapter 2.2.3, the drying rate $\dot{m}_{vap}$ remains constant for constant drying conditions. The drying product's temperature is about the wet-bulb temperature. Hence, the moisture's surface tension σ, density ρ, and dynamic viscosity η also remain constant during the first drying period. Then the critical length $s_{2,crit}$ and subsequently the critical moisture content $y_{crit} = m_{w,crit}/m_{dry}$, where the first drying period ends, can be determined out of Eq. 2.46. This principle can be adapted for any capillary distribution, but only for constant drying conditions [59]. Metzger and Tsotsas [90] have shown, by advancing the model of two capillaries, how the pore size distribution influences the drying behaviour. In general, porous media with broad or binary pore size distribution, having micropores and macropores, will dry more easily with an extended first drying period, compared to porous media with a narrow pore size distribution.
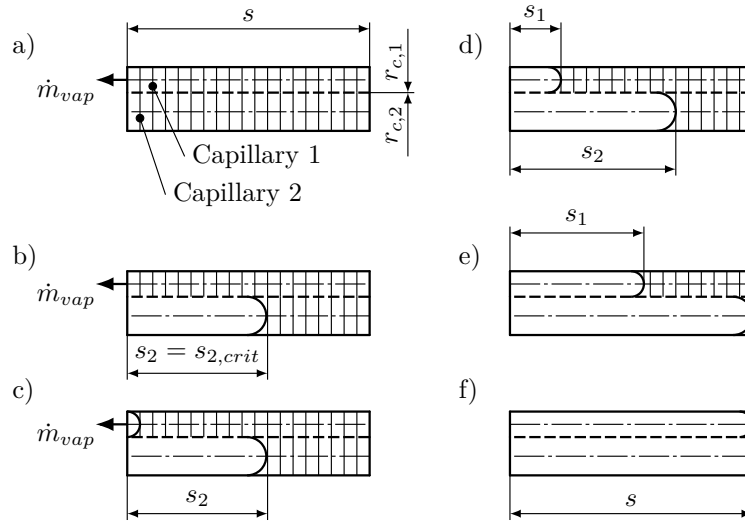
Figure 2.16: Moisture movement while drying in two connected capillaries of different sizes (a - f), adapted from [59]

When the first drying period has finished, Δp_c isn't longer greater than Δp_f. The meniscus of capillary 1 also has to move inwards (Fig. 2.16.c), the second drying period starts. The drying rate $\dot{m}_{vap}$ can be described by linking Eq. 2.22 for the mass transfer at the product's surface and Eq. 2.42 for the diffusion through the dried length s_1 of capillary 1 (Fig. 2.16.d). The additional vapour diffusion resistance with increasing diffusion length causes the drop of the drying rate $\dot{m}_{vap}$ during the second drying period. Under the assumption of a non-hygroscopic material, capillary 2 will dry up first (Fig. 2.16.e) and with ongoing evaporation capillary 1 follows (Fig. 2.16.f) [59].

Capillary moisture movement is caused by pressure gradients $\partial p/\partial z$, like all the other types of fluid flows. It occurs as long as the pressure distribution differs from the equilibrium pressure

distribution. Such an equalisation process is often described by the following approach:

$$\dot{m}_w = -k_p\,\rho_w\,A\,\frac{\partial p}{\partial z} \tag{2.47}$$

Where $\dot{m}$ means the moisture mass flow rate, k_p the transport coefficient related to pressure, and ρ the density of water. But in general neither the geometry of the pore system nor the forcing pressure gradients in the liquid can be measured directly. A straight usage of Eq. 2.47 isn't possible. But the moisture movement also can be related to the, easier to measure, volumetric moisture gradient $\partial\psi/\partial z$, with $\psi = V_w/V$. Thus, the moisture diffusion coefficient κ is introduced by the following approach:

$$\dot{m}_w = -\kappa\,\rho_w\,A\,\frac{\partial \psi}{\partial z} \tag{2.48}$$

The moisture diffusion coefficient κ isn't a constant parameter. It has to be determined experimentally and depends on the moisture's temperature ϑ and the volumetric moisture content ψ [59].

In contrast to the previous transport phenomena, a quasi-stationary process cannot be assumed in case of moisture transport through the porous medium ($\partial\dot{m}/\partial z \neq 0$). It has to be solved numerically as an initial value boundary value problem and will be demonstrated in detail at Chapter 2.3.2.

Investigations on the temperature dependence for a given moisture content ψ have shown, that κ is proportional to the quotient of the moisture's surface tension $\sigma(\vartheta)$ and it's dynamic viscosity $\eta(\vartheta)$ [70]:

$$\kappa \propto \frac{\sigma(\vartheta)}{\eta(\vartheta)} \tag{2.49}$$

Telljohann [75] shows that there is a sufficiently linear relation between σ/η and ϑ, for the temperature range from interest regarding to drying processes. With a given κ at a certain reference temperature ϑ_{ref}, the temperature dependence can be written as:

$$\frac{\kappa(\vartheta)}{\kappa(\vartheta_{ref})} = 1 + 0.0225\,\frac{\vartheta - \vartheta_{ref}}{°\mathrm{C}} \tag{2.50}$$

Furthermore, the moisture diffusion coefficient κ depends highly on the drying product's water content. In accordance to the remarks in Chapter 2.2.2: From the beginning of the drying process till the end of shrinkage, the pore volume is equal to and flooded by the water volume V_w. That is simultaneously the available amount of Volume for the capillary transport of moisture to the drying product's surface [91].

Here, the cross section of capillaries A_c which is allowing a fluid flow, related to the total cross section A equals the current water volume fraction ψ [92] (cf. the approximation of the diffusion resistance μ by Eq. 2.41):

$$\psi = \frac{A_c}{A} = \frac{V_w}{V} \tag{2.51}$$

The mass flow rate $\dot{m}$ of water flowing through the capillary cross section A_c with the mean velocity w is:

$$\dot{m}_w = w\,A_c\,\rho_w \tag{2.52}$$

By adjusting Eq. 2.45, Eq. 2.48, and Eq. 2.51 it can be shown that κ follows a squared relation with ψ, if the current water content ψ is greater than the limiting moisture content at the end of shrinkage ψ_{SE}.

$$\kappa \propto \psi^2 \text{ if } \psi \geq \psi_{SE} \tag{2.53}$$

If a reference moisture diffusion coefficient κ_{ref} at a certain reference moisture content $\psi_{ref} \geq \psi_{SE}$ is known, the following formulation can be made

$$\kappa = \kappa_{ref}\left(\frac{\psi}{\psi_{ref}}\right)^2 \text{ if } \psi \geq \psi_{SE} \tag{2.54}$$

to describe the dependence of the moisture diffusion coefficient κ on the volumetric moisture content $\psi \geq \psi_{SE}$. Usually κ_{ref} is determined at mass concentration of $y_{ref} = 0.25$ and a temperature $\vartheta = 25\,^\circ$C. Ordinary values range from $\kappa_{ref} = 8 \times 10^{-9}\,\mathrm{m^2/s}$ for clays with bad drying behaviour, to $\kappa_{ref} = 100 \times 10^{-9}\,\mathrm{m^2/s}$ for clays with good drying behaviour [75]. Low values of κ cause high moisture gradients and subsequently high susceptibility to cracking.

For lower moisture fractions $\psi < \psi_{SE}$ the volume loss is compensated by the penetration of air into the green brick, as described before. Thin capillaries exhaust thicker ones. With decreasing ψ the capillaries which still remain flooded are getting thinner and thinner. The flow resistance increases strongly, thus the moisture diffusion coefficient has to drop drastically. This behaviour can be described by the following approach [91], where k_ψ expresses the slop of the curve:

$$\kappa = \kappa_{ref}\left(\frac{\psi_{SE}}{\psi_{ref}}\right)^2 \times 10^{k_\psi(\psi-\psi_{SE})} \text{ if } \psi < \psi_{SE} \tag{2.55}$$

Fig. 2.17 compares the predicted result out of Eq. 2.54 and Eq. 2.55, to experimental data for typical clays. Two distinct ranges, separated at the limiting water content ψ_{SE}, can be identified.

There are several experimental methods to determine reference values κ_{ref}. Krischer and Kast [59] present two important destructive methods. A stationary one of long duration where the steady-state condition has to be fulfilled. The big advantage is its high precision. A transient method is also introduced. It reduces testing time significantly but increases inaccuracy. This technique will be discussed in detail as part of the validation calculation in Chapter 2.3.4. Zanden and Wit [93] are introducing a non-destructive method by measuring the mass of a drying brick at both outer ends. The method failed for low water concentrations. Heijden et al. [94] are using nuclear magnetic resonance (NMR) as another non-destructive method to measure moisture profiles during non-isothermal drying of fired-clay bricks.
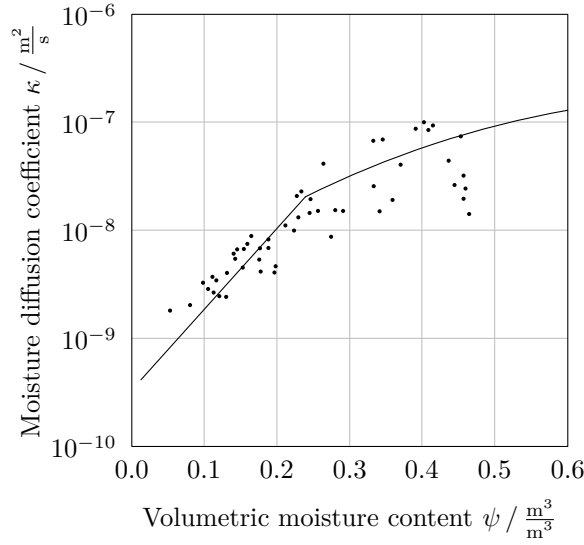
Figure 2.17: Comparison of calculated moisture diffusion coefficient (solid line) with experimental results of Krischer and Kast [59] and Telljohann, Junge, and Specht [91] of different clays at 25 °C, adapted from [91]

2.2.5 Complementary statements and literature

Yataganbaba and Kurtbaş [95] have analysed the Scopus[2] database to find the various trends in scientific studies in the field of drying brick and tile, for the years from 1980 to 2015. A significant growth in scientific production could be observed, particularly in the period from 2000 to 2015. The countries that became evident as most productive on a scientific bases are Germany, the United States, and China.

However, there are lots of scientific papers and comprehensive works to find. Alternative model approaches to describe the drying kinetics should be supplemented. Followed by papers in which the drying kinetic and the dryer itself are combined to form an overall model of different complexity.

Krischer and Kast [59] propose an empirical lumped model often called thin layer model. The wall's cross section is also separated by the drying interface in a dry and wet layer. Its position is provided as a function of the current moisture content and the critical moisture content when the second drying period begins has to be known. The empirical parameters depend on the drying conditions and have to be determined experimentally. Hence, the model is rather unsuitable for transient processes with changing drying conditions.

Vasić, Grbavčić, and Radojević [96, 97] introduce an effective diffusivity that represents an overall mass transport property of moisture, which includes all possible moisture transport mechanisms that are simultaneously controlling the moisture migration process in a material

---

[2]Scopus is the world's largest abstract and citation database of peer-reviewed research literature. With over 22 000 titles from more than 5000 international publishers. https://www.scopus.com/

during the whole drying process. Two approaches have been presented: the analytical solution of Crank [98] for one-dimensional diffusion in a plate sheet and the approach of Efremov [99] for describing the drying kinetics of porous material, based on the analytic solution of Fick's second low for one-dimensional diffusion. The effective diffusivity again depends on the drying air conditions such as velocity, temperature, and humidity.

Boukadida, Nasrallah, and Perre [100], Pakala and Plumb [101] are investigating the heat and mass transfer of porous media using a two-dimensional approach of the wet core model with moving drying interface.

Shokouhmand et al. [102] present the performance optimisation of a chamber dryer using a two-dimensional brick as porous media. The physical and turbulence model for the air flow was solved by a three-dimensional, stationary, and segregated solver.

There are also publications concerning the subject of tunnel dryers. Silva Almeida et al. [103] are simulating stationary drying processes of bricks in a cross-flow tunnel dryer using a three-dimensional tunnel model. Mabrouk, Khiari, and Sassi [104] are presenting transient simulations on drying granular products in a fixed bed tunnel dryer using a two-dimensional tunnel model. In both cases a thin layer model for the drying product was implemented.

The complexity of the single models has to be chosen appropriately. There is always a trade-off between accuracy, computational effort, and numerical stability. In case of the mentioned tunnel dryers, the tunnel volume was modelled by multi-dimensional approaches due to the large temperature and humidity gradients. For the drying product a simpler model approach was chosen.

The most important simplifications concerning this work are the one-dimensional symmetrical plate-shaped drying product and the ideal stirred tank reactor for the drying chamber.

2.3 Modelling, implementation, and validation of drying processes

One of the main tasks in this work is the modelling, implementation, and validation of a chamber dryer in its general structure and the drying kinetics of the contained drying product as well. All the substantial properties and processes have to be reproduced with sufficient accuracy under appropriate application of the previously discussed simplifications and modelling assumptions.

This chapter starts with the modelling of the drying chamber as the central part of the laboratory container, followed by supplementary aspects concerning the drying kinetics. After implementation in an proper simulation environment, the validation process is presented using measurement data from drying tests performed on the laboratory container.

The developed models are forming the basis for the simulation of drying processes. In future, the models will be used as sub-models for the optimisation of overall processes and for finding proper controlling strategies. Hence, it's important to focus on keeping the equation system's complexity low.

2.3.1 Modelling of the drying chamber

Laboratory container

First the laboratory container, set up as a test bench in course of the DryPump project, should briefly be introduced. Its drying chamber imitates the drying behaviour of a large-scale chamber dryer which has been modelled and implemented in its general structure. The measured data from the test series at the laboratory container are later used to validate the established models.
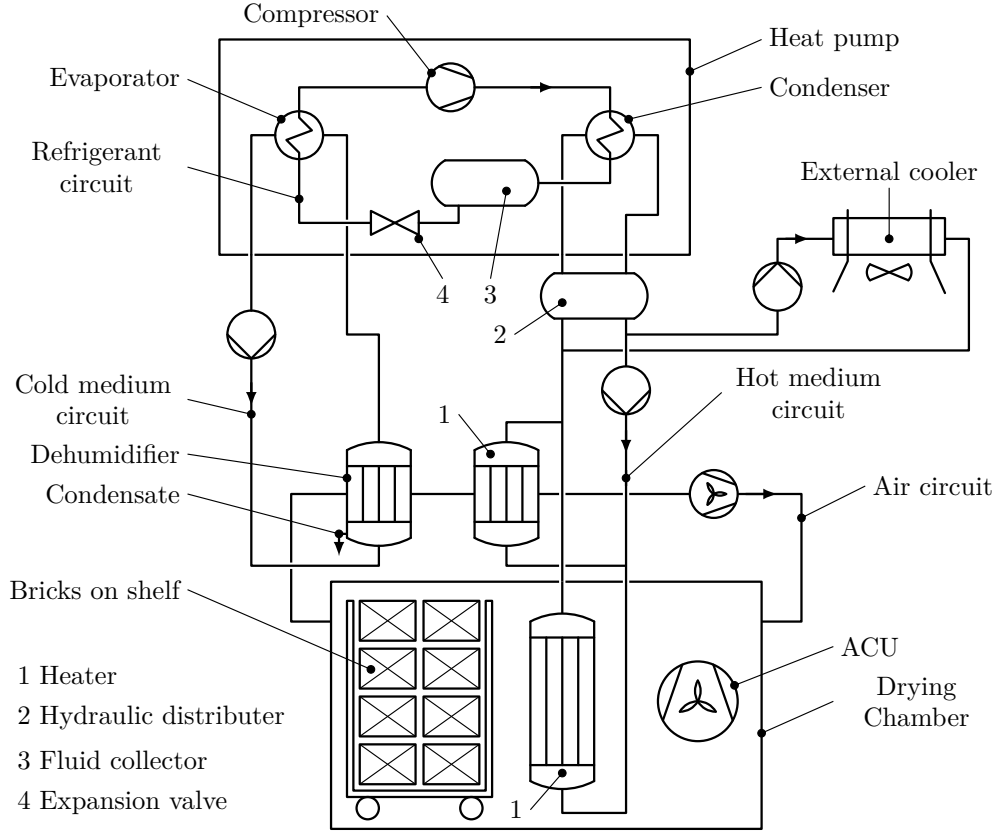
Figure 2.18: Schematic view of the experimental set-up of the closed-loop chamber dryer using a compression heat pump for providing the drying energy, adapted from [7]

Experiments were performed on a small-scale laboratory container set up by the project partners AIT, Wienerberger AG, and AMT on the production site of Wienerberger AG in Haiding (Austria). The container was equipped with an air circulation system including a dehumidifier and a heater, a drying chamber, and a compression heat pump as illustrated in Fig. 2.18. 24 wet bricks are arranged on a shelf. The hot supply air, circulated by the ACU, is further heated through a second heater inside the drying chamber and flows through the stack of bricks. To ensure fast and uniform drying, the shelf is placed on rails and moves periodically, thus reversing

the direction of the air flow through the bricks. The humid exhaust air from the drying chamber passes the dehumidifier, where the temperature of the air stream is lowered and the condensate is removed. Subsequently the dry air is heated before re-entering the drying chamber. The mass flow rate is adjusted by the fan of the air circuit. The thermal energy supplied to the drying process is provided by the heat pump. The heat pump, designed for a heating capacity of 50 kW consists of a speed-controlled reciprocating compressor, two plate heat exchangers (evaporator and condenser), and an expansion valve. Due to the used refrigerant R134a it can deliver a maximum temperature of 90 °C at the condenser. The typical operating temperature ranges from 50 to 60 °C. The heat pump cycle is connected to the drying process by two intermediate circuits filled with a water-glycol mixture [7]. The resulting advantage is a robust and flexible operation of the heat pump, in which the mass flow rates at its source and sink can be adapted to the required optimal operating conditions [4]. The hot medium circuit distributes the thermal energy from the heat pump condenser to the heaters, inside and outside of the drying chamber. Thus, the input of thermal energy is maximised at moderate temperature levels compared to a single heat exchanger. As a result, the temperature of the intermediate circuit required for heating the drying air can be lowered, decreasing the necessary temperature lift of the heat pump. Hence the system efficiency increases. Additionally, the hot medium circuit includes an external air cooler. The air cooler removes excess heat, controlling the temperature of the circuit and consequently that of the drying process [7]. As the heat pump carries mechanical energy into the system, an excess of energy would be existent. Less energy is removed from the drying chamber at the dehumidifier than is supplied at the heaters. If this excess energy would not be removed, or if it's not compensated by heat losses, the energy in the drying chamber would rise and result in disadvantageous operating conditions [3]. The cold medium circuit connects the evaporator of the heat pump to the dehumidifier of the air circuit.

The described experimental set-up was equipped with proper measuring and controlling instruments. As a result, some process parameters can be varied and all necessary physical quantities can be metrologically captured and logged. Hence, the sensitivity and efficiency of the drying process related to different process parameters can be investigated and the set of measured data can be used to validate the necessary components for simulating the process.

The processes concerning the drying medium along its way through the air circuit can be illustrated conveniently in the h_{1+X},X-chart. Fig. 2.19 shows two plots of idealised drying processes during the first drying period. The red path indicates the typical changes in state of the drying air at a natural gas heated chamber dryer and was already discussed in Chapter 2.2.3. The heat pump powered cycle is marked by the blue line starting at state 1. The heated drying medium is driven by a fan to the inlet of the chamber. Uniform adiabatic mixing of the feed flow with the humid air in the chamber would lead to state 2a. But the specific enthalpy of the established climate is higher, due to the internal heater. The shift of the specific enthalpy from state 2a to state 2 corresponds to the energy input of the internal heater. After leaving the chamber, the drying medium reaches the dehumidifier (source of the heat pump) where thermal
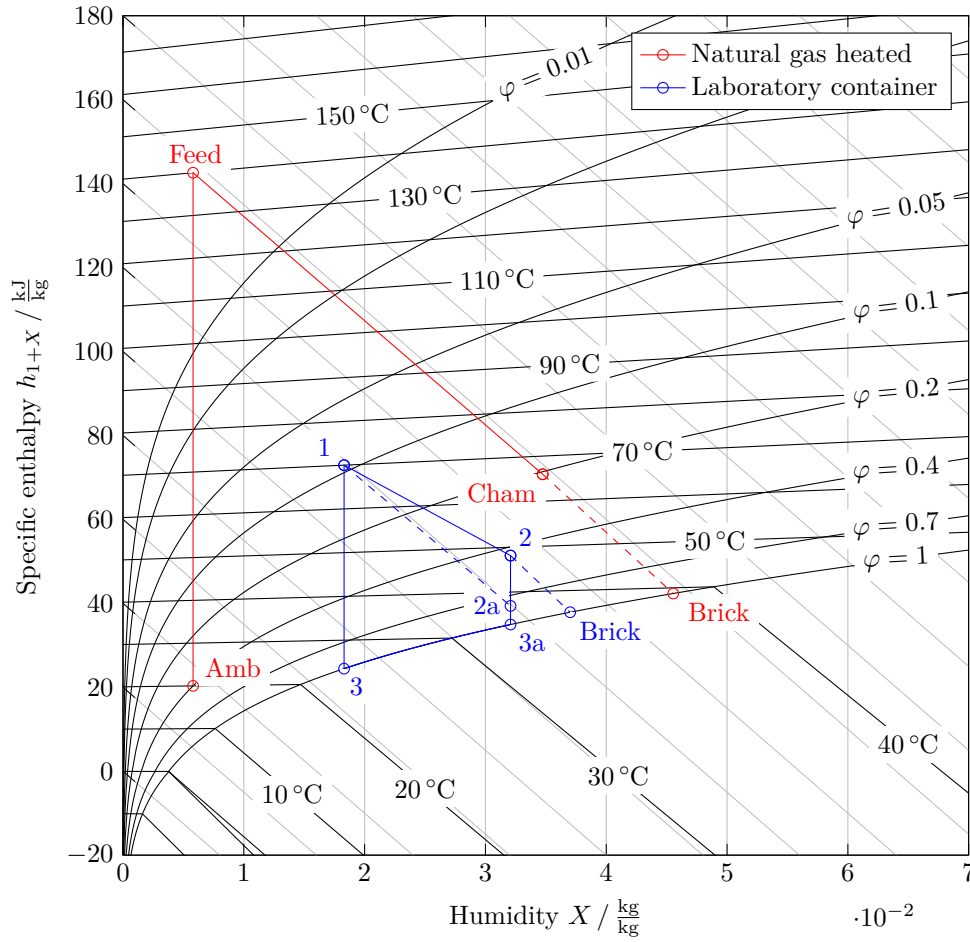
Figure 2.19: Changes in state during the first drying period of a natural gas heated ideal chamber dryer (red) and the heat pump powered ideal laboratory container (blue), shown in the h_{1+X},X-chart

energy is removed. First the temperature drops, the humidity X remains constant, and the relative humidity φ rises, until the air is saturated ($\varphi = 1$) at state 3a. With ongoing drain of thermal energy the temperature is further lowered along the saturation line under removing condensate. After that, the dry air with state 3 passes the heater (sink of the heat pump). The specific enthalpy is shifted with $X = $ const. to state 1 again.

Mass and energy balance of the drying chamber

In future, the chamber model will be used as a sub-model for optimisation of overall processes and for finding proper controlling strategies. It's important to focus on keeping the equation system's complexity low. The chamber's advantageously hydraulic design provides uniform conditions. As already mentioned in Chapter 2.2.3, the assumption of the ideal stirred tank reactor can be taken.

Heat and mass transfer are assumed to be averaged over time and position. Fig. 2.20 displays the schematic view and control volume of a drying chamber including the shelf and stack of brick with separate control volumes.
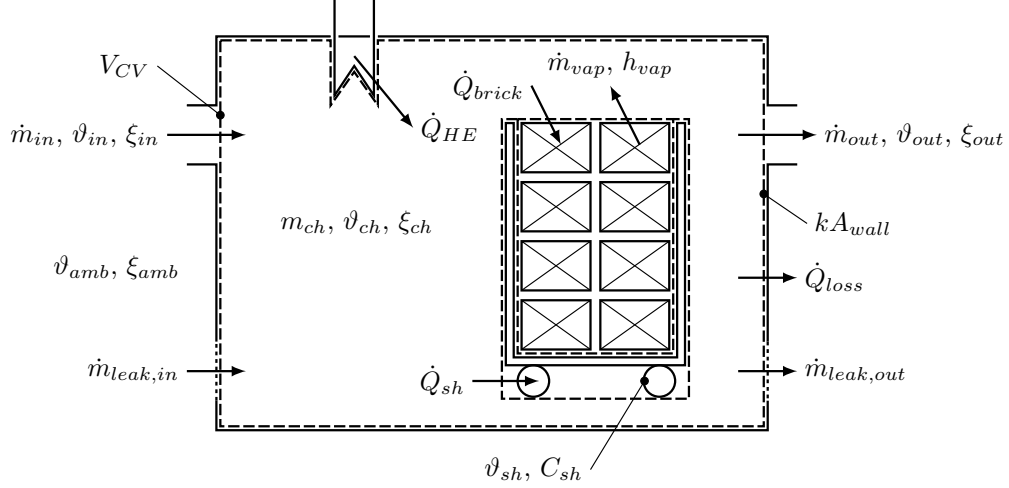
Figure 2.20: Mass and energy balance of the drying chamber

The mass balance of the drying medium can be written as:

$$\frac{\mathrm{d}m_{ch}}{\mathrm{d}t} = \dot{m}_{in} - \dot{m}_{out} + \dot{m}_{vap} \tag{2.56}$$

With $\dot{m}_{in}$ as the feed mass flow rate, $\dot{m}_{out}$ as the leaving mass flow rate, $\dot{m}_{vap}$ as the drying rate, and $m_{ch} = V_{CV}\,\rho_{ch}$ as the mass of wet air inside the approximately constant control volume CV ($V_{CV} \approx$ const. and $\rho_{ch} = \rho\left(\vartheta_{ch}, \xi_{ch}\right)$). The model validation in Chapter 2.3.4 has shown that a non-negligible leakage mass flow $\dot{m}_{leak}$ prevails. It is assumed that the incoming and the outgoing leakage are equal:

$$\dot{m}_{leak,in} = \dot{m}_{leak,out} = \dot{m}_{leak} \tag{2.57}$$

Considering the air circuit as a closed loop (excepting the condensate separation at the dehumidifier) the assumption is reasonable in order to fulfil mass conservation.

The mass balance of the species water in wet air is given as

$$\frac{\mathrm{d}\left(m_{ch}\,\xi_{ch}\right)}{\mathrm{d}t} = \dot{m}_{in}\,\xi_{in} - \dot{m}_{out}\,\xi_{out} + \dot{m}_{leak}\left(\xi_{amb} - \xi_{ch}\right) + \dot{m}_{vap} \tag{2.58}$$

with ξ as the mass fraction of the species water in the wet air and the assumption of the ideal stirred tank reactor:

$$\xi_{out} = \xi_{ch} \tag{2.59}$$

Conservation of energy leads to:

$$\frac{\mathrm{d}\,(m_{ch}\,u_{ch})}{\mathrm{d}t} = \dot{m}_{in}\,h_{in} - \dot{m}_{out}\,h_{out} + \dot{m}_{leak}\,(h_{amb} - h_{ch})$$
$$+ \dot{m}_{vap}\,h_{vap} - \dot{Q}_{brick} + \dot{Q}_{HE} - \dot{Q}_{loss} - \dot{Q}_{sh} \tag{2.60}$$

Again with the assumption of the ideal stirred tank reactor

$$\vartheta_{out} = \vartheta_{ch}, \tag{2.61}$$

$u_{ch} = u\,(\vartheta_{ch}, \xi_{ch})$ as the specific internal energy and $h_{ch} = h\,(\vartheta_{ch}, \xi_{ch})$ as the specific enthalpy of the wet air inside the chamber. $h_{in} = h\,(\vartheta_{in}, \xi_{in})$ denotes the specific enthalpy of the feed mass flow, $h_{out} = h_{ch} = h\,(\vartheta_{ch}, \xi_{ch})$ of the leaving mass flow, and $h_{amb} = h\,(\vartheta_{amb}, \xi_{amb})$ of the ambient air. $\dot{Q}_{brick}$ expresses the heat flow rate to the stack of bricks, $\dot{Q}_{HE}$ the energy input due to the internal heater, and $\dot{Q}_{sh}$ the heat exchange to the shelf. The energy loss due to conduction through the chamber walls $\dot{Q}_{loss}$, driven by the temperature difference between the chamber and the ambient air, is given as:

$$\dot{Q}_{loss} = kA_{wall}\,(\vartheta_{ch} - \vartheta_{amb}) \tag{2.62}$$

Where kA_{wall} denotes the thermal conductance through the chamber walls. The energy input of the ACU inside the chamber P_{fan} is negligibly small compared to the other energy flows.

Energy balance of the shelf

As indicated in Fig. 2.20 by $\dot{Q}_{sh}$, an energy transport between the shelf and the drying air arises. First, it should be outlined how this convective energy input influences the temperature distribution of the shelf. The dimensionless Biot number Bi plays a fundamental role in conduction problems that involve surface convection effects. It can be interpreted as the ratio between the energy input by convection and the transport due to conduction inside the body.

The shelf is shaped of steel plates with a maximum wall thickness of $s_{sh} = 4\,\mathrm{mm}$ and a thermal conductivity of $\lambda_{sh} = 45\,\mathrm{W/(m\,K)}$. The heat transfer coefficient due to convection is given with $\alpha_{sh} = 17\,\mathrm{W/(m^2\,K)}$. Then, the Biot number for the described problem can be determined as:

$$Bi = \frac{\alpha_{sh}\,\frac{s_{sh}}{2}}{\lambda_{sh}} = 7.56 \times 10^{-4} \tag{2.63}$$

If the condition $Bi < 0.1$ is fulfilled, heat conduction inside the body is much faster than convection at the surface, and temperature gradients inside are negligible. The lumped capacity method can be used [86], to formulate the energy balance of the shelf:

$$C_{sh}\frac{\mathrm{d}\vartheta_{sh}}{\mathrm{d}t} = \dot{Q}_{sh} = \alpha_{sh}\,A_{sh}\,(\vartheta_{ch} - \vartheta_{sh}) \tag{2.64}$$

$C_{sh} = c_{sh}\,\rho_{sh}\,V_{sh}$ denotes the heat capacity of the shelf's massive parts, which aren't in direct

contact to the drying product. And A_{sh} represents the shelf's total surface involved in the heat transfer.

To evaluate the shelf's thermal respond while heating the chamber, the differential Eq. 2.64 can be solved, considering a linear temperature rise of the drying air as the transient boundary condition given as:

$$\vartheta_{ch} = \vartheta_{ch,ini} + k_\vartheta \, t \tag{2.65}$$

As a solution

$$\vartheta_{ch} - \vartheta_{sh} = \left(\vartheta_{ch,ini} - \vartheta_{sh,ini} - k_\vartheta \, \frac{C_{sh}}{\alpha_{sh} \, A_{sh}} \right) \exp\left(-\frac{\alpha_{sh} \, A_{sh}}{C_{sh}} \, t \right) + k_\vartheta \, \frac{C_{sh}}{\alpha_{sh} \, A_{sh}} \tag{2.66}$$

can be found. The shelf is shaped of steel plates with the total volume $V_{sh} = {(A_{sh} \, s_{sh})}/{2}$, a specific heat capacity $c_{sh} = 490 \, \text{J/(kg K)}$, and a density $\rho_{sh} = 7800 \, \text{kg/m}^3$. According to the measurements on the laboratory container, presented in Chapter 2.3.4, the maximum change of the chamber's temperature is about $k_\vartheta \approx 10 \, \text{K/h}$. For $t \gg 1$ the exponential term of Eq. 2.66, representing the solution's homogeneous part, is losing on weight and a constant temperature difference will arise:

$$\vartheta_{ch} - \vartheta_{sh} = 1.2 \, \text{K} \tag{2.67}$$

For moderate heating rates with sufficient slow temperature changes, the following assumption can be made:

$$\vartheta_{sh} \approx \vartheta_{ch} \tag{2.68}$$

$\alpha = 17 \, \text{W/(m}^2 \, \text{K)}$ is a common value concerning the convective heat transfer conditions in conjunction to drying processes. For rising values of α the temperature difference determined in Eq. 2.67 would decrease. Bi out of Eq. 2.63 would increase slightly but still remain far below $Bi = 0.1$.

To investigate the energy transport between typical hollow bricks and perforated plates on which they are arranged on, the problem shown in Fig. 2.21 was solved for the first drying period under common drying conditions ($p = 1 \, \text{bar}$, $\vartheta_{ch} = 50 \, °\text{C}$, and $\varphi_{ch} = 0.45$).

During the first drying period, evaporation takes place at the product's surface. Hence, implementing the moisture transport through the brick's wet wall isn't from interest. The nodes drying rates and temperatures are independent in time and shrinkage is neglected. The discrete nodes are arranged as shown in Fig. 2.21 with the symmetry boundary conditions indicated by chain dotted lines. Mass and energy transfer due to convection with $\alpha = \text{const.}$ and $\beta = \text{const.}$ are possible at the uncovered surfaces. The partial covered surface is hindered concerning the mass transport, but energy transfer by conduction between the brick and the perforated plate is possible. Applying these assumptions and boundaries on Eq. 2.6, Eq. 2.22, and Eq. 2.30 leads
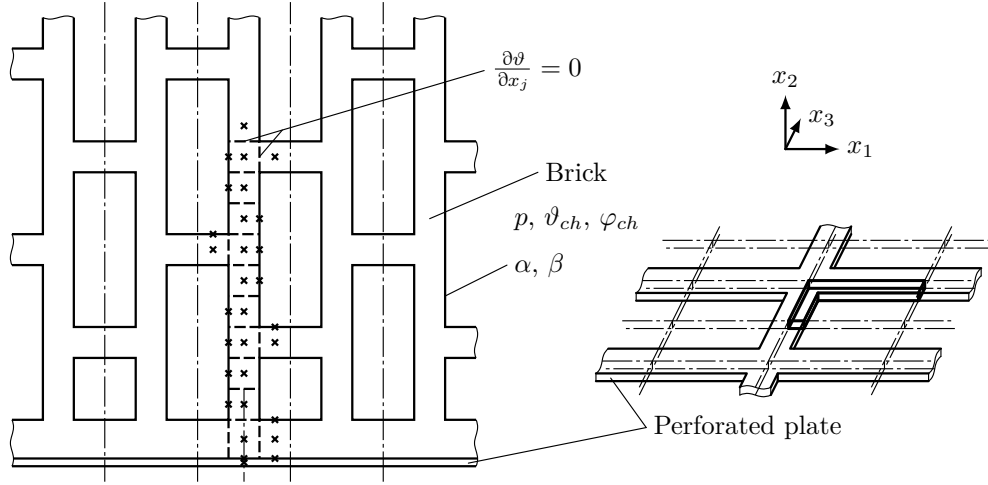
Figure 2.21: The effect caused by partial coverage of a brick's drying surface on its temperature distribution and on the covering perforated plate: schematic view, discretisation, and boundary conditions

to the set of governing transport equations

$$\dot{Q}_{conv,i,j} = \alpha \, A_j \left(\vartheta_{ch} - \vartheta_i \right) \tag{2.69}$$

$$\dot{m}_{vap,i,j} = A_j \, \beta \, \frac{2 \, p}{R_{vap} \left(T_{ch} + T_i \right)} \ln \frac{p - p_{vap} \left(\vartheta_{ch}, \varphi_{ch} \right)}{p - p_{vap,sat} \left(\vartheta_i \right)} \tag{2.70}$$

$$\dot{Q}_{cond,i,j} = -\lambda_i \, A_j \, \frac{\partial \vartheta_i}{\partial x_j} \tag{2.71}$$

with $j = 1 \ldots 3$ as index of the spatial directions, $i = 1 \ldots 28$ as index for the discrete nodes under the sign convention according to Fig. 2.20.

The results of the introduced problem are summarised in Fig. 2.22. The left chart shows the temperature distribution over the whole brick's width, the perforated plate and the surrounding drying air including the boundary layer. The right chart shows the distribution of the part influenced by the coverage more detailed.

The blue line indicates the wet-bulb temperature ϑ_{WB} corresponding to the drying climate and the green line equals the equilibrium temperature ϑ_{eq} which arises, if adiabatic drying is the case. Mass and energy transport at the surface are in equilibrium, no thermal energy is transported beyond the drying interface. ϑ_{WB} and ϑ_{eq} are almost equal, as claimed in Chapter 2.2.3. The disturbance in the temperature field appears due to the fact that the area involved in evaporation is reduced compared to the area involved to the energy input. As a result, the temperature of the regions close to the perforated plate rises, caused by excess of energy. After a depth of $\Delta x_2 \approx 35 \, \text{mm}$ there is no recognisable influence $\vartheta \approx \vartheta_{eq}$. The maximum temperature difference appears at the contact area with $\Delta \vartheta \approx 0.8 \, \text{K}$.
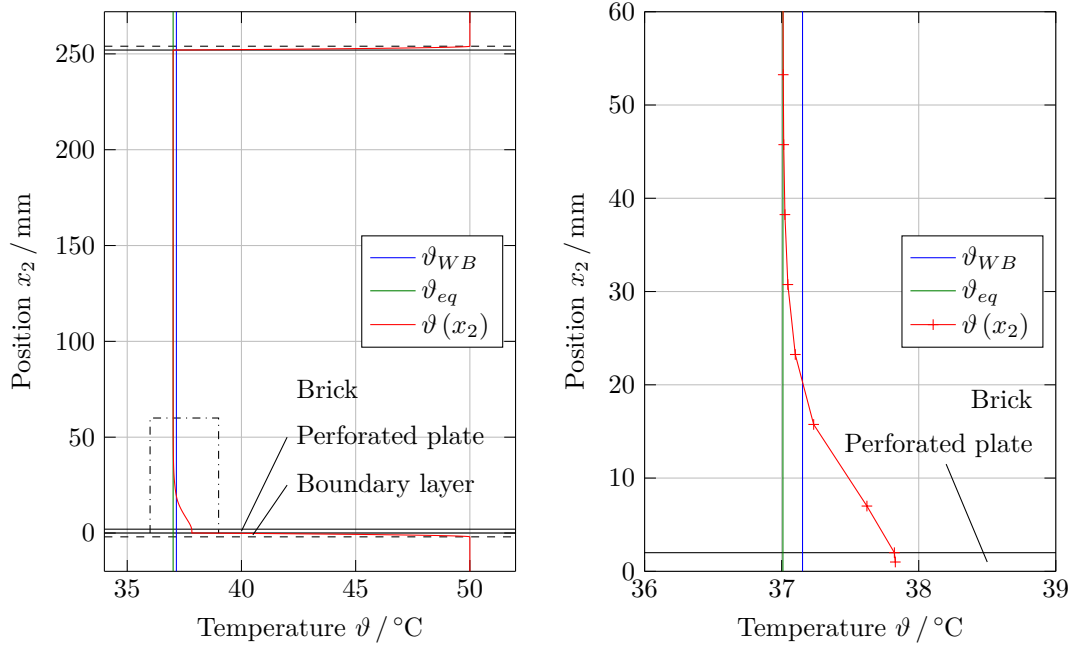
Figure 2.22: The effect caused by partial coverage of a brick's drying surface on its temperature distribution and on the covering perforated plate: results

The energy inputs caused through conduction and convection are difficult to distinguish. Due to the marginal effect of the coverage, it's assumed that there is no disturbance $\vartheta_{plate} = \vartheta_{brick}$ and the whole surface is available for the energy transfer by convection.

In case of a common hollow brick like the Wienerberger Porotherm 25-38, which was used for the tests at the laboratory container presented in Chapter 2.3.4, the ratio between the discussed surfaces is about:

$$\frac{A_{plate}}{A_{brick}} \, 100\,\% = 1.18\,\% \tag{2.72}$$

The covered surface A_{plate} is small compared to the brick's total surface A_{brick}. It's further assumed, that the brick's whole surface is involved in the mass transfer too.

The plate's thermal mass could be included in the brick's energy balance, since the plate's and brick's temperature are almost equal. The presented results are taken from considerations of the first drying period, where conditions remain constant. No statement concerning the change of the sensible energy content was made until now. With

$$\frac{C_{plate}}{C_{dry,brick}} \, 100\,\% = 1.56\,\% \tag{2.73}$$

it can be shown, that the perforated plate's heat capacity C_{plate} is very small compared to the complete dry brick's heat capacity $C_{dry,brick}$. Hence, C_{plate} will not be included in the energy balance. If the brick is still wet, C_{brick} is even higher compared to the presented case.

The first main conclusion of this chapter is, that the temperature of the shelf's massive parts can be set equal to the drying air's temperature $\vartheta_{sh} = \vartheta_{ch}$. And the second statement is that the perforated plate's temperature can be set equal to the brick's temperature $\vartheta_{plate} = \vartheta_{brick}$. The plates are supported by the shelf's massive components, hence they are linked conductive and differ in temperature. The available area for heat conduction is very small due to the geometric conditions. Energy transport between plates and the shelf's frame will be neglected.

Energy transport through thermal radiation

The aim of this chapter is to investigate the energy transport due to radiation between the chamber walls and the drying product. The example of the laboratory container's chamber loaded with 24 Wienerberger Porotherm 25-38 is used. According to Fig. 2.20, the stack of bricks can be seen as a perfect cuboid with an outer surface $A_{brick,rad} = 4.16\,\mathrm{m}^2$ and a surface temperature T_{brick}, which is entirely surrounded by the chamber walls with $A_{wall,rad} = 28.12\,\mathrm{m}^2$ and a surface temperature T_{wall}. The brick's temperature is taken from the results of the chapter before with $T_{brick} = (37 + 273.15)\,\mathrm{K}$. To estimate the chamber wall's temperature, the Biot number Bi can be used. Considering a thermally well insulated wall with $\lambda_{wall} \ll 1$ leads to:

$$Bi = \frac{\alpha_{wall}\, L_{char}}{\lambda_{wall}} \gg 1 \tag{2.74}$$

The energy flow caused by convection is dominant compared to the conductive energy flow through the wall. Hence, the temperature difference across the wall is much larger than that between the surface and the air [86]. It's assumed that $T_{wall} \approx T_{ch} = (50 + 273.15)\,\mathrm{K}$. The transfer between the shelf and the walls due to radiation is vanishingly small $(T_{sh} \approx T_{ch})$.

The energy transfer due to radiation of a grey body enclosed by another [55]:

$$\dot{Q}_{rad} = \frac{\sigma\, A_{brick,rad} \left(T_{wall}^4 - T_{brick}^4 \right)}{\frac{1}{\epsilon_{brick}} + \frac{A_{brick,rad}}{A_{wall,rad}} \left(\frac{1}{\epsilon_{wall}} - 1 \right)} = 350.2\,\mathrm{W} \tag{2.75}$$

Where $\sigma = 5.67 \times 10^{-8}\,\mathrm{W/(m^2\,K^4)}$ denotes the Stefan–Boltzmann constant, $\epsilon_{brick} = 0.93$ the brick's emission coefficients, and $\epsilon_{wall} = 0.8$ the wall's emission coefficients [55].

The energy transport due to convection of $n_{brick} = 24$ bricks, with $\alpha_{conv} = 17\,\mathrm{W/(m^2\,K)}$ and $A_{brick,conv} = 3.26\,\mathrm{m}^2$ per brick, can be determined by:

$$\dot{Q}_{conv} = \alpha_{conv}\, A_{brick,conv}\, n_{brick} \left(T_{ch} - T_{brick} \right) = 17.3\,\mathrm{kW} \tag{2.76}$$

The ratio between these energy flows is:

$$\frac{\dot{Q}_{rad}}{\dot{Q}_{conv}}\, 100\,\% = 2\,\% \tag{2.77}$$

The energy flow due to radiation is rather small compared to the convective flow. That is the case for the laboratory container's chamber. At real dryers of greater overall dimension the ratio is even smaller.

The determined values from the validation correspond anyway to an effective heat transfer α_{eff} averaged for the whole stack of bricks. The energy flows cannot be distinguished by measurement.

$$\dot{Q}_{tot} = \dot{Q}_{rad} + \dot{Q}_{conv} = \alpha_{eff}\, A_{brick,conv}\, (T_{ch} - T_{brick}) \tag{2.78}$$

2.3.2 Modelling of the drying kinetics

Most of the model equations have already been presented in Chapter 2.2.4. Some of the assumptions will be reviewed and specified for the given drying product. Furthermore, the balances of the drying product and the numerical treatment of the moisture diffusion through the wet region will be presented.

Proportion of energy flows

The Biot number Bi is a suitable dimensionless quantity, to assess the dominant heat flows and to estimate the temperature distribution. The drying product is a Wienerberger Porotherm 25-38 with a mean wall thickness of $s_{brick} = 8\,\mathrm{mm}$. Good heat transfer conditions with $\alpha = 30\,\mathrm{W/(m^2\,K)}$ are considered, which activate higher temperature gradients in the product's wall.

During the first drying period, evaporation takes place at the surface. It behaves like an adiabatic wall, the energy flow to the inside is zero. But, when starting a drying process the product has to be heated until the equilibrium temperature is reached. For estimating the temperature gradient, it is assumed that the whole energy input is converted to sensible energy. With the thermal conductivity for the wet material $\lambda_{wet} = 1.6\,\mathrm{W/(m\,K)}$ [105], the Biot number follows as:

$$Bi = \frac{\alpha\, \frac{s_{brick}}{2}}{\lambda_{wet}} = 0.075 \tag{2.79}$$

Even in case of elevated energy input, the condition $Bi < 0.1$ is fulfilled, heat conduction inside the body is much faster than convection at the surface. The temperature gradients inside are negligible and the lumped capacity method can be used [86] to describe the processes in the wet region. For the second drying period, the situation becomes even clearer. The energy transport to the wet core is reduced due to the resistance of the dry layer, the heat conduction through the wet core behaves unchanged.

The heat conductivity of the dry material ranges from $\lambda_{dry} = 0.8$ to $1.2\,\mathrm{W/(m\,K)}$ [75]. If the drying interface reaches the centre of brick's wall the Biot number becomes with $\lambda_{dry} = 1\,\mathrm{W/(m\,K)}$ to:

$$Bi = \frac{\alpha\, \frac{s_{brick}}{2}}{\lambda_{dry}} = 0.12 \tag{2.80}$$

It's close to the limiting value, but the lumped capacity model should not be used in this case.

The temperature difference across the wall should be taken into account.

In analogy to the thermal transport, the Biot number for mass transport can also be introduced. The convective transport at the surface is compared to the diffusive transport through the product.

$$Bi = \frac{\beta \frac{s_{brick}}{2}}{D_{eff}} = \frac{\mu \beta \frac{s_{brick}}{2}}{D} = 80 \tag{2.81}$$

With a diffusion coefficient $D = 2.95 \times 10^{-5}\,\mathrm{m^2/s}$ of vapour in air at $\vartheta = 43\,\mathrm{°C}$ (Eq. 2.29), a diffusion resistance $\mu = 20$, and a typical mass transfer coefficient $\beta = 0.029\,\mathrm{m/s}$ for turbulent flow (Eq. 2.28), the mass transport at the surface is dominant for $Bi \gg 1$. As a result, the lumped model isn't valid, a distributed parameter model should be used [86].

All model assumptions of Chapter 2.2.4 have been supported for the given case, so far. Now it should be verified, if the assumption of quasi-stationary heat conduction through the wall's dry section is valid.

The Stefan number St compares sensible and latent heat in conjunction with solidification processes. Quasi-stationary conduction can be considered, if $St < 1/7$ is the case [55]. The modified Stefan number for evaporation processes arises as:

$$St = \frac{c_{dry}\,\Delta\vartheta}{\Delta h_v\,\Delta y} \tag{2.82}$$

With the enthalpy of vaporisation $\Delta h_v \approx 2500\,\mathrm{kJ/kg}$ [64], the dry product's specific heat capacity $c_{dry} = 850\,\mathrm{J/(kg\,K)}$ [106], and a change of the moisture content $\Delta y = 0.2$ if the second drying period starts early, hence, is of long duration:

$$\Delta\vartheta_{max} = \frac{\Delta h_v\,\Delta y}{c_{dry}}\,St_{max} = 84\,\mathrm{K} \tag{2.83}$$

The maximum change in temperature within the second drying period is about $84\,\mathrm{K}$. Differentiation of Eq. 2.83 with respect to time t, delivers the following condition that has to be fulfilled:

$$\frac{\mathrm{d}\vartheta}{\mathrm{d}t} < -420.17\,\mathrm{K}\,\frac{\mathrm{d}y}{\mathrm{d}t} \tag{2.84}$$

The maximum change in temperature, to assume quasi-stationary heat conduction, depends on the drying rate at a certain point in time.

Mass and energy balance of the drying product

Most drying products in the brick and tile industry are approximately plate-shaped or composed of single plates, such as the considered hollow brick. The drying product is regarded as a one-dimensional symmetrical plate shown in Fig. 2.23.

The energy balance can be written as:

$$\frac{\mathrm{d}U_{brick}}{\mathrm{d}t} = \dot{Q}_{brick} - \dot{m}_{vap}\,h_{vap} \tag{2.85}$$
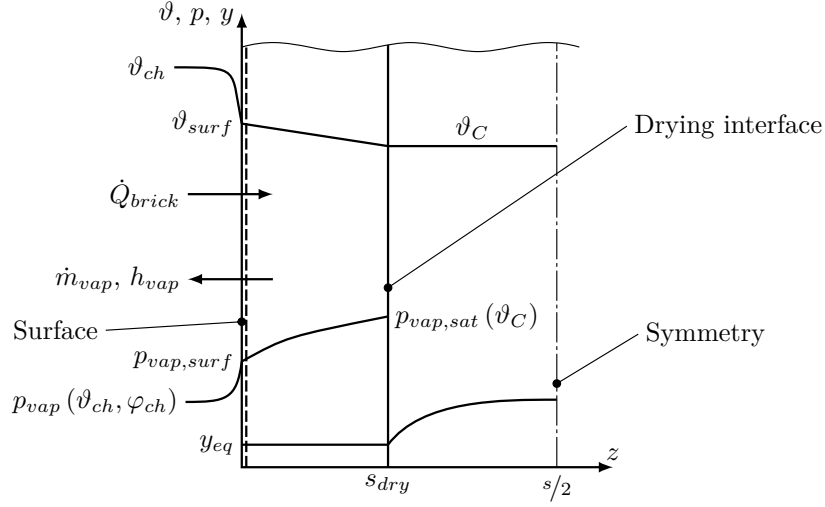
Figure 2.23: Mass and energy balance of the drying product and the distribution of the driving quantities

Where U_{brick} denotes the internal energy of the brick, $\dot{Q}_{brick}$ the heat flow rate between the brick and surrounding air, $\dot{m}_{vap}$ the vapour mass flow rate, and h_{vap} the vapour's specific enthalpy.

U_{brick} is composed of the internal energies of both dry layers and the internal energy of the wet core:

$$
\begin{aligned}
U_{brick} = {} & \frac{2\,s_{dry}}{s}\,m_{dry}\,(c_{dry} + c_w\,y_{eq})\,\frac{T_C - T_{ref} + T_{surf} - T_{ref}}{2} \\
& + \frac{s - 2\,s_{dry}}{s}\,m_{dry}\,(c_{dry} + c_w\,y_C)\,(T_C - T_{ref})
\end{aligned}
\tag{2.86}
$$

With T_C as the wet core's temperature, T_{surf} as the surface's temperature, $T_{ref} = T_{tr}$ as the reference temperature chosen as the triple point temperature, and y_C as the wet core's water content:

$$
y_C = \frac{1}{s/2 - s_{dry}}\int\limits_{s_{dry}}^{s/2} y\,\mathrm{d}z
\tag{2.87}
$$

Assuming quasi-stationary heat conduction, Eq. 2.6 and Eq. 2.33 can be combined to

$$
\dot{Q}_{brick} = \frac{A_{surf}}{\frac{1}{\alpha} + \frac{s_{dry}}{\lambda_{dry}}}\,(\vartheta_{ch} - \vartheta_C)
\tag{2.88}
$$

under the sign convention according to Fig. 2.20. A_{surf} includes the entire surface, also the surface of the opposite side.

Combining Eq. 2.22 and Eq. 2.42, under the sign convention according to Fig. 2.20, leads to:

$$\dot{m}_{vap} = \frac{A_{surf}}{\frac{1}{\beta} + \frac{\mu\, s_{dry}}{D}} \frac{p}{R_{vap}\, T_{surf}} \ln \frac{p - p_{vap}\left(\vartheta_{ch}, \varphi_{ch}\right)}{p - p_{vap,sat}\left(\vartheta_C\right)} \tag{2.89}$$

These are the transport equations according to the second drying period. During the first drying period the drying surface stays at the body's surface with $s_{dry} = 0$ and $\vartheta_C = \vartheta_{surf}$. The resistances due to the dry layer are vanishing.

Condensation, sorption, and shrinkage

Condensation or rather rising moisture content can also be investigated. This behaviour is observed mostly during the first drying period. Disadvantageous dryer operating or low brick temperatures in conjunction with high relative humidity inside the chamber especially at the beginning of drying are possible reasons. The following case structure has to be used for h_{vap}:

$$h_{vap} = \begin{cases} h_{vap}\left(\vartheta_{surf}\right) & \text{if } p_{vap,sat}\left(\vartheta_{surf}\right) \geq p_{vap}\left(\vartheta_{ch}, \varphi_{ch}\right) \\ h_{vap}\left(\vartheta_{ch}\right) & \text{if } p_{vap,sat}\left(\vartheta_{surf}\right) < p_{vap}\left(\vartheta_{ch}, \varphi_{ch}\right) \end{cases} \tag{2.90}$$

By definition $\dot{m}_{vap} > 0$ (cf. Eq. 2.89 and Fig. 2.23) for drying and $\dot{m}_{vap} < 0$ for condensation.

All the discussed types of bond between water and solid material are summarised under the term sorption. The only hygroscopic effect taken into account is that drying can be carried out until the equilibrium moisture content, corresponding to the surrounding air conditions, is reached $y_{final}\left(z\right) = y_{eq}\left(\vartheta_{ch}, \varphi_{ch}\right)$. This dependency can be provided by the equilibrium moisture isotherm. If $y = y_{eq}$ is reached at $z = {}^s\!/{}_2$ the drying process has finished and $\dot{m}_{vap} = 0$ (cf. Fig. 2.23). Bonding energies are neglected, since they play a minor role in industrial drying processes.

As shown in Chapter 2.2.2 shrinkage can be considered as ideal and linear. The drying product's volume decreases in the same amount as its liquid volume does. As a result, the volumetric water content ψ from Eq. 2.51 and the linear relative shrinkage χ from Eq. 2.5 are geometrically coupled. Shrinkage starts at a linear relative shrinkage $\chi_{ini} = 0$ and ends abruptly at $\chi = \chi_{SE}$. χ_{SE} denotes the linear relative shrinkage at shrinking end and has to be provided as an empiric parameter. The geometric dependency can be formulated for the changes of length, area, and volume:

$$L = L_{ini}\left(1 - \chi\right) \tag{2.91}$$

$$A = A_{ini}\left(1 - \chi\right)^2 \tag{2.92}$$

$$V = V_{ini}\left(1 - \chi\right)^3 \tag{2.93}$$

With $y = {}^{m_w}/_{m_{dry}}$, $\psi = {}^{V_w}/V$, and $\rho_w = {}^{m_w}/_{V_w}$ it can be shown that:

$$\psi \, \rho_w \, V = y \, m_{dry} \tag{2.94}$$

Following case structure can be found for the dependency between shrinkage χ and the volumetric water content ψ with ψ_{SE} as the volumetric water content at shrinking end, by applying $\Delta V = \Delta V_w = {}^{\Delta m_w}/_{\rho_w}$ while and $\Delta V = 0$ after shrinkage:

$$\chi = \begin{cases} 1 - \left(\frac{1-\psi_{ini}}{1-\psi} \right)^{\frac{1}{3}} & \text{if } \psi > \psi_{SE} \\ \chi_{SE} & \text{if } \psi \le \psi_{SE} \end{cases} \tag{2.95}$$

$$\psi_{SE} = 1 - \frac{1 - \psi_{ini}}{(1 - \chi_{SE})^3} \tag{2.96}$$

The water content related to the mass of dry product y with y_{SE} as the water content at shrinking end is a more appropriate quantity concerning drying processes:

$$\chi = \begin{cases} 1 - \left(1 - \frac{m_{dry}}{V_{ini} \, \rho_w} (y_{ini} - y) \right)^{\frac{1}{3}} & \text{if } y > y_{SE} \\ \chi_{SE} & \text{if } y \le y_{SE} \end{cases} \tag{2.97}$$

$$y_{SE} = y_{ini} - \left(1 - (1 - \chi_{SE})^3 \right) \frac{V_{ini} \, \rho_w}{m_{dry}} \tag{2.98}$$

Moisture transport in the wet part of the wall

The finite volume (FV) method will be used to derive the moisture transport by diffusion and should be introduced first. The FV method uses the integral form of the conservation equation. The considered region is subdivided into a finite number of non-overlapping control volumes (CVs), and the conservation equation is applied to each of these CVs. The centre of mass equates the so-called node, in which the variables are determined. Interpolation is used to express the variable value on the CV boundary, by taking the mean of the neighbouring nodes' values (CV centres). Surface and volume integrals are approximated using appropriate numerical quadrature equations. For each CV, an algebraic or differential equation is obtained, in which the node's variable and the neighbour nodes' variables appear. The FV method can be used in conjunction with any lattice type, hence it's suitable for complex geometries. The surfaces of the volume are given by the mesh, thus, they don't have to be referred to a coordinate system. The method is conservative by definition, as long as the surface integrals, representing the convective and diffusive flows, are determined consistently for both volumes sharing a surface. The disadvantage of the FV method compared to others is, that higher-order methods are more difficult to develop. That is due to the fact that the FV method requires three approximation levels: interpolation, differentiation, and integration [107].

The general differential equation of transport with ϕ as the dependent variable can be written as:

$$\frac{\mathrm{d}}{\mathrm{d}t}(\epsilon\,\phi) + \boldsymbol{\nabla}\cdot(\epsilon\,\boldsymbol{u}\,\phi + \boldsymbol{J}) = S \tag{2.99}$$

If ϵ is the density, then $\epsilon\phi$ denotes the amount of the corresponding extensive property contained in a unit volume. Using Fick's first law of diffusion to express the diffusive flux

$$\boldsymbol{J} = -\Gamma\,\boldsymbol{\nabla}\phi \tag{2.100}$$

leads to

$$\underbrace{\frac{\mathrm{d}}{\mathrm{d}t}(\epsilon\,\phi)}_{\text{Rate of change}} + \underbrace{\boldsymbol{\nabla}\cdot(\epsilon\,\boldsymbol{u}\,\phi)}_{\text{Convetion}} + \underbrace{\boldsymbol{\nabla}\cdot(-\Gamma\,\boldsymbol{\nabla}\phi)}_{\text{Diffusion}} = \underbrace{S}_{\text{Source}} \tag{2.101}$$

with Γ as the general diffusion coefficient and $\boldsymbol{u}$ as the velocity vector. A differential equation as a compilation of such terms is implying a balance of conservation, each term representing an influence on a unit-volume basis [108].

Eq. 2.48 would suggest the volumetric moisture content ψ as the dependent variable. Since ψ isn't a conservative quantity and the mass of moisture related to the mass of dry product y is a more appropriate quantity concerning drying processes, $\phi = y$ and $\epsilon = {}^{m_{dry}}/V$ are chosen. Conservation of $\phi = y$ or $\epsilon\,\phi = {}^{m_w}/V$ regarding the one-dimensional case leads to:

$$\frac{\mathrm{d}}{\mathrm{d}t}\left(\frac{m_{dry}}{V}\,y\right) + \frac{\partial}{\partial z}\left(\frac{m_{dry}}{V}\,w\,y\right) + \frac{\partial}{\partial z}\left(-\Gamma_y\,\frac{\partial y}{\partial z}\right) = S_y \tag{2.102}$$

Applying $\partial/\partial z$ on Eq. 2.94 with the assumption of ideal shrinkage

$$\frac{\partial V}{\partial z} = \begin{cases} \frac{\partial V_w}{\partial z} & \text{if } y > y_{SE} \\ 0 & \text{if } y \leq y_{SE} \end{cases} \tag{2.103}$$

delivers the following distinction of cases:

$$\frac{\partial \psi}{\partial z} = \begin{cases} \frac{m_{dry}}{\rho_w V}\,(1-\psi)\,\frac{\partial y}{\partial z} & \text{if } y > y_{SE} \\ \frac{m_{dry}}{\rho_w V}\,\frac{\partial y}{\partial z} & \text{if } y \leq y_{SE} \end{cases} \tag{2.104}$$

Differentiation with respect to the time t, again with the assumption of ideal shrinkage

$$\frac{\mathrm{d}V}{\mathrm{d}t} = \begin{cases} \frac{\mathrm{d}V_w}{\mathrm{d}t} & \text{if } y > y_{SE} \\ 0 & \text{if } y \leq y_{SE} \end{cases} \tag{2.105}$$

leads to:

$$\frac{\mathrm{d}}{\mathrm{d}t}\left(\frac{y}{V}\right) = \begin{cases} \frac{1-\psi}{V}\,\frac{\mathrm{d}y}{\mathrm{d}t} & \text{if } y > y_{SE} \\ \frac{1}{V}\,\frac{\mathrm{d}y}{\mathrm{d}t} & \text{if } y \leq y_{SE} \end{cases} \tag{2.106}$$

112

The diffusive mass flow is described by Eq. 2.48. Concerning this equation for the infinitesimal small volume ($dV = dA\,dz$) under the usage of Eq. 2.104 and subsequent identification of coefficients with Eq. 2.102 shows the relation for the diffusion coefficient:

$$\Gamma_y = \begin{cases} \kappa\,(1-\psi)\,\frac{m_{dry}}{V} & \text{if } y > y_{SE} \\ \kappa\,\frac{m_{dry}}{V} & \text{if } y \leq y_{SE} \end{cases} \tag{2.107}$$

Inserting to Eq. 2.102 with $m_{dry} = \text{const.}$, $V_{ini} = \text{const.}$, $w = 0$, $S_y = 0$, and Eq. 2.93 leads to the transport equation:

$$\frac{1-\psi}{(1-\chi)^3}\frac{dy}{dt} = \frac{\partial}{\partial z}\left(\kappa\,\frac{1-\psi}{(1-\chi)^3}\frac{\partial y}{\partial z}\right) \tag{2.108}$$

for $y > y_{SE}$ and

$$\frac{dy}{dt} = \frac{\partial}{\partial z}\left(\kappa\,\frac{\partial y}{\partial z}\right) \tag{2.109}$$

for $y \leq y_{SE}$.

The obtained differential Eq. 2.108 and Eq. 2.109 are describing the transport processes through the wet region shown in Fig. 2.23 during and after shrinkage. Evaporation takes place at the drying interface $z = s_{dry}$. Considering symmetry at the cross section centre, the drying rate $\dot{m}_{vap}/2$ expresses the boundary condition at the drying interface $z = s_{dry}$:

$$\dot{m}_w\left(z = s_{dry}, t\right) = -\frac{\dot{m}_{vap}}{2} \tag{2.110}$$

The drying interface is moving towards the cross section centre. A region is considered as dried up as soon as the equilibrium moisture content $y = y_{eq}$ is achieved.

The second boundary condition is the symmetry condition at the cross section centre:

$$\left.\frac{\partial y}{\partial z}\right|_{z=\frac{s}{2},t} = 0 \tag{2.111}$$

The initial condition is assumed to be even distributed:

$$y\left(t = 0, z\right) = y_{ini} \tag{2.112}$$

This initial value boundary value problem consists of the case structure Eq. 2.108 and Eq. 2.109 and the conditions Eq. 2.110, Eq. 2.111, and Eq. 2.112. It can be solved by applying the FV method. The considered region is discretised to n FVs with $1 \leq i \leq n$ to index the general FV. The so-called nodes in which the variables are determined, are located in the FVs centre. Only half of the brick wall's cross section is regarded, since the region of consideration is assumed to be symmetrical.

The moisture transport through the wet region is described by the case structure Eq. 2.108 and Eq. 2.109. The additional terms in Eq. 2.108 are accounting the difference in size of the
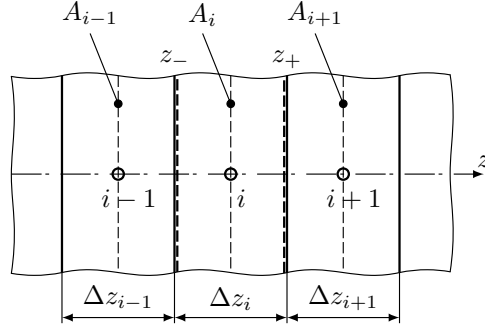
Figure 2.24: The general finite volume of the discretised region

neighbouring volumes, due to present moisture gradients. Lookahead: implementation and tests of the kinetics model have shown, that the shrinkage afflicted part's solution can be found until shrinkage ends. But, when $\chi = \chi_{SE}$ is reached at the surface, the equation system would change and numerical problems are arising. The solution for the shrinkage afflicted period differs marginal to the solution found, if neighbouring volumes are considered as equal-sized. Since the moisture diffusion coefficient κ during the shrinkage afflicted period is comparably large (all capillaries are flooded cf. Fig. 2.17), there are just small moisture gradients, hence, there is also just a small difference in the neighbouring volume's size. The differential Eq. 2.108 will be neglected and the FV method will be continued for the differential Eq. 2.109.

Integration of the differential Eq. 2.109 over the volume i with the neighbouring volumes $i-1$ and $i+1$ and the boundaries indicated by z_- and z_+

$$\int\limits_{z_-}^{z_+} \left(\frac{\mathrm{d}y}{\mathrm{d}t} \right) \mathrm{d}z = \int\limits_{z_-}^{z_+} \left(\frac{\partial}{\partial z} \left(\kappa \, \frac{\partial y}{\partial z} \right) \right) \mathrm{d}z \tag{2.113}$$

leads to:

$$\frac{\mathrm{d}y}{\mathrm{d}t} \bigg|_i \Delta z_i = \left(\kappa \, \frac{\partial y}{\partial z} \right)_{z_+} - \left(\kappa \, \frac{\partial y}{\partial z} \right)_{z_-} \tag{2.114}$$

The terms on the equation's right-hand side are expressing the diffusive flows over the volume's surfaces.

For the first drying period, moisture diffusion takes place in $1 \leq i \leq n$ with $i_{dry} = 0$. During the second drying period moisture diffusion happens to the volumes $(i_{dry} + 1) \leq i \leq n$. The volumes $1 \leq i \leq i_{dry}$ have dried up with the drying interface at $i = i_{dry}$.

For the general volume $(i_{dry} + 2) \leq i \leq (n-1)$ as shown in Fig. 2.24, the moisture gradients at the volume's boundaries can be expressed by finite differences. κ is high dependent on the moisture content, the mean moisture content of the neighbouring nodes is used for determination:

$$\left(\kappa \, \frac{\partial y}{\partial z} \right)_{z_-} = \frac{\kappa_i + \kappa_{i-1}}{2} \, \frac{2 \, (y_i - y_{i-1})}{\Delta z_i + \Delta z_{i-1}} \tag{2.115}$$

114

$$\left(\kappa \frac{\partial y}{\partial z}\right)_{z_+} = \frac{\kappa_{i+1} + \kappa_i}{2} \frac{2\left(y_{i+1} - y_i\right)}{\Delta z_{i+1} + \Delta z_i} \tag{2.116}$$

For $i = (i_{dry} + 1)$, evaporation takes place in this volume. The situation is shown in Fig. 2.25. Combining the equation of the diffusive mass flow rate Eq. 2.48 and Eq. 2.104 with the boundary condition Eq. 2.110 leads to the following expression:

$$\left(\kappa \frac{\partial y}{\partial z}\right)_{z_-} = \frac{\dot{m}_{vap}}{2\, m_{dry_{i_{dry}+1}}} \Delta z_{i_{dry}+1} \tag{2.117}$$

That's a boundary condition of the third type. $\dot{m}_{vap}$ is known through Eq. 2.89. The term representing the boundary to the wet core (between $(i_{dry} + 1)$ and $(i_{dry} + 2)$) can be expressed similarly to the general case:

$$\left(\kappa \frac{\partial y}{\partial z}\right)_{z_+} = \frac{\kappa_{i_{dry}+2} + \kappa_{i_{dry}+1}}{2} \frac{2\left(y_{i_{dry}+2} - y_{i_{dry}+1}\right)}{\Delta z_{i_{dry}+2} + \Delta z_{i_{dry}+1}} \tag{2.118}$$
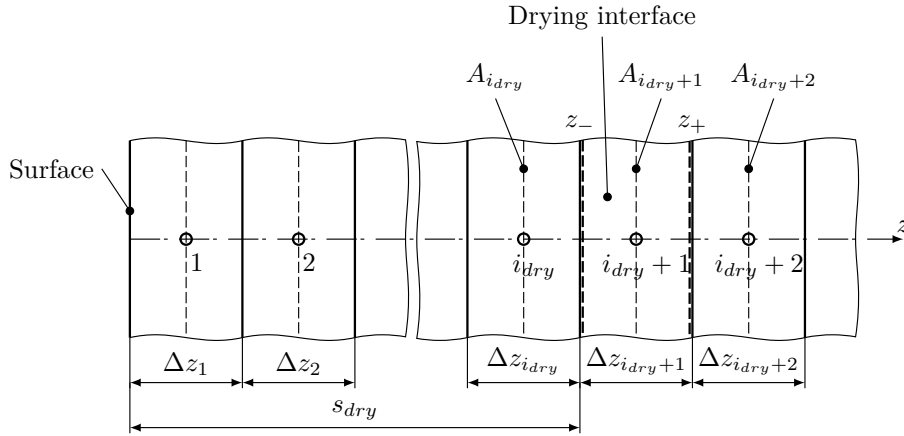
Figure 2.25: The finite volume containing the drying interface: boundary condition

The situation at the cross sections centre is shown in Fig. 2.26. For $i = n$ the term representing the left boundary z_- can again be written as in the general case:

$$\left(\kappa \frac{\partial y}{\partial z}\right)_{z_-} = \frac{\kappa_n + \kappa_{n-1}}{2} \frac{2\left(y_n - y_{n-1}\right)}{\Delta z_n + \Delta z_{n-1}} \tag{2.119}$$

The boundary at the wall's centre has to fulfil the condition of symmetry, Neumann, or the second type boundary condition:

$$\left(\kappa \frac{\partial y}{\partial z}\right)_{z_+} = 0 \tag{2.120}$$
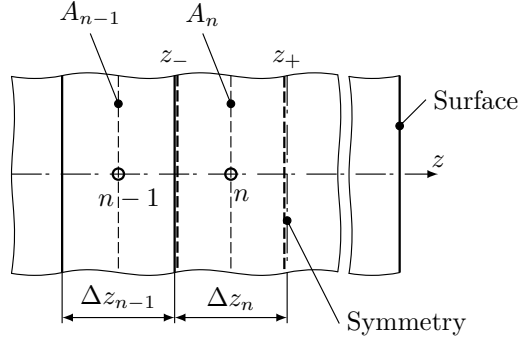
Figure 2.26: The finite volume at the centre of the product's wall: boundary condition

Differences in geometry just appear at the beginning of drying, caused through shrinkage. As already mentioned, for small water content differences between the neighbouring finite volumes, the assumptions $\Delta z_{i-1} = \Delta z_i = \Delta z_{i+1}$ can be taken.

By inserting the terms representing the left and right boundary in Eq. 2.114 and subsequent re-sorting, the following set of differential equations for the three different cases is given. For $i = (i_{dry} + 1)$:

$$\frac{\mathrm{d}y}{\mathrm{d}t}\bigg|_{i_{dry}+1} = \frac{\kappa_{i_{dry}+2} + \kappa_{i_{dry}+1}}{2\,\Delta z_{i_{dry}+1}^2}\, y_{i_{dry}+2} - \frac{\kappa_{i_{dry}+2} + \kappa_{i_{dry}+1}}{2\,\Delta z_{i_{dry}+1}^2}\, y_{i_{dry}+1} - \frac{\dot{m}_{vap}}{2\,m_{dry,i_{dry}+1}} \tag{2.121}$$

For $(i_{dry} + 2) \leq i \leq (n - 1)$:

$$\frac{\mathrm{d}y}{\mathrm{d}t}\bigg|_{i} = \frac{\kappa_{i+1} + \kappa_i}{2\,\Delta z_i^2}\, y_{i+1} - \frac{\kappa_{i+1} + 2\,\kappa_i + \kappa_{i-1}}{2\,\Delta z_i^2}\, y_i + \frac{\kappa_i + \kappa_{i-1}}{2\,\Delta z_i^2}\, y_{i-1} \tag{2.122}$$

For $i = n$:

$$\frac{\mathrm{d}y}{\mathrm{d}t}\bigg|_{n} = -\frac{\kappa_n + \kappa_{n-1}}{2\,\Delta z_n^2}\, y_n + \frac{\kappa_n + \kappa_{n-1}}{2\,\Delta z_n^2}\, y_{n-1} \tag{2.123}$$

With the moisture diffusion coefficient κ from Eq. 2.50, Eq. 2.54, and Eq. 2.55.

The time integration step would follow at this point. Therefore Patankar [108] explains the implicit, explicit, and Crank-Nicolson method. He also points out the advantages and disadvantages in terms of stability, accuracy, and complexity. In this work, the model equations are implemented by using the suitable object-oriented modelling language Modelica and the modelling and simulation environment Dymola. It's the solver's tasks to sort and integrate the system of equations. Only the initial conditions of the differential equations' variables have to be provided.

2.3.3 Implementation using Modelica

The presented equation system can conveniently be attributed to two main objects, the drying chamber and the drying kinetics. Those should be implemented in a suitable simulation environment. The mathematical formulation is given as a discrete, differential, algebraic equation system. Discrete denotes that several equations can change in course of the simulation due to the occurrence of events. Shrinkage, the first and the second drying period require different sets of the model equations. The used solver has to be able to sort and to integrate such a system. During the simulation, it's necessary to determine the point in time at which the event happens and the system of equations changes. The object-oriented modelling language Modelica and the modelling and simulation environment Dymola are capable instruments to meet these requirements.

Modelica and Dymola

Modelica is a freely available, object-oriented language for modelling of large, complex, heterogeneous, hybrid, and multi-domain systems. It has been developed since 1996. Models are described mathematically by differential, algebraic, and discrete equations. From the user's point of view, models are described by schematics diagrams built by several components, also called blocks. A component has connectors, often called ports, which describe the possibilities of interaction. By drawing connection lines between connectors a physical system or block diagram model is constructed. Internally a block is defined by an equation based description of the model in Modelica syntax. The Modelica language is a textual description to define all parts of a model and to structure model components in libraries, called packages. An appropriate Modelica simulation environment, such as Dymola, is needed to graphically edit and browse a Modelica model and to perform model simulations [57].

Dymola is a commercial modelling and simulation environment based on the open Modelica modelling language. Dymola (Dynamic Modeling Laboratory) is suitable for modelling in various fields of physics. Model libraries are available in many engineering domains. Some advantageous highlights of Dymola are: handling of large and complex models, faster modelling by graphical model composition, open for user defined model components, open interface to other programs, 3D Animation, and real-time simulation [58].

Drying chamber

The drying chamber is implemented as a class of the type model to a user-defined library. A system of equations is embedded, visualised by a block. The most important equations are originated from the balances concerning the drying medium, in Chapter 2.3.1. Since it's assumed that the drying medium's and the shelf's temperature are the same, the shelf's thermal mass is also included in this block. Three different user-defined classes of the type connector are used to connect the model to other blocks, to provide the exchange of information. The HeatPort

that represents a heat flow characterised by $\dot{Q}$ and T, a SteamPort as mass flow characterised by $\dot{m}$, T, and p, and a MoistAirPort also as mass flow characterised by $\dot{m}$, T, p, and ξ. The information transferred via these connectors is of the type flow which follow Kirchhoff's first law and of the type effort or potential which appear, in case of conjoint connectors, with the same value. The connectors have properly been chosen with respect to the heat and enthalpy flows indicated in Fig. 2.20. As a result, the chamber can be connected to blocks which represent the ambient air, the stack of bricks or other models of interaction. The mask of the block is another important interface for the user. Parameters which characterise the object and the initial values for the differential equations can be set here. The most important parameters which have to be provided when instantiating a drying chamber are summarised in Tab. 2.4. These parameters remain constant by definition, during the simulation. It's also possible to specify initial values of iteration variables, helping the solver to find a solution for the first time step at the beginning of the simulation.

When creating an overall model, several chambers can be arranged and easily be linked as blocks in the graphical scheme. For example the energy supply can also be integrated if suitable models exist. Optimisation tasks in plant management are possible.

Drying kinetics

The drying kinetics is also defined as a class of the type model. The entire formalism hides behind a single block representing a brick or a stack of bricks. A set of parameters such as geometry, clay properties, and initial states have to be provided by the user to characterise the drying process. These parameters are summarised in Tab. 2.3. Communication and information exchange happens via four different connectors: the drying medium's conditions, the heat flow for energy input, the mass flow representing the drying rate, and the heat transfer coefficient using an additional connector class. The heat transfer coefficient can be specified as constant by the user, or originates from a calculation procedure depending, for example, on a process parameter. Arrays of variables and loops are useful tools to deal with the one-dimensional discretisation of the wall thickness. Modelica is fairly suitable for solving small fields. For the consideration of larger multi-dimensional fields, alternative simulation environments have to be used. One of the main reasons why using the Modelica language was the advantage that multi-domain simulations are rather easy to realise. Components of different user-defined, commercial, and standard libraries can be merged to a single model and the simulation can be performed using one and the same solver.

Optimisation of the models

A statistic concerning the system of equations is provided, when translating a model in Dymola. A variety of parameters is issued to assess the original and the translated model. For example, the number of standard variables, the number of differentiated variables, the number of parameters, number and sizes of linear systems, number and sizes of non-linear systems including the used

iteration variables, and many more are shown. The number and sizes of the non-linear systems are helpful optimisation indicators, concerning the system's runtime and complexity.

By evaluating this statistic it was found that, the supposedly simpler chamber model performed worse compared to the brick model. The main reasons were the prior used fluid property functions provided by the Modelica standard library [109]. The performance has been increased by linearising some of the fluid property functions, like the specific enthalpy and the specific internal energy of liquid water, vapour and dry air. The composition of these species leads to the specific quantities of wet air. As a result, a runtime reduction by the factor of 10 has been achieved under imperceptible change of the solution.

Stand-alone executable

Dymola is a commercial and very powerful environment for model development and simulation. Since the software is not available to the project partner Wienerberger AG, a license independent tool was created.

In the first step, a standard case model was built which main components are a drying chamber block and a brick block. The process boundary conditions such as feed flow or ambient conditions are provided by objects of the class CombiTimeTable. The CombiTimeTable is a table look-up with respect to time and linear or periodic extrapolation methods obtaining the processed data from a text file.

Based on the prepared standard model, the executable file was generated by the project partner AIT . From now on, no licence is needed, it can be used independently of the Dymola simulation environment. All process parameters can still be specified by the user. Just the number of nodes for the discretisation of the brick's wall thickness had to be chosen as fixed value in advance. Thus, the equation system's complexity depends on the number of nodes. Once the executable file has been compiled, it's no longer possible to interfere with the basic structure of the model. The user interface to provide the model parameters and process boundary conditions is given by the text files. After executing a simulation, the results are written to an output text file.

As final step, a suitable tool for convenient pre and post processing was developed by the project partner Wienerberger AG. In the future it can be used for designing new plants and for process optimisations on existing plants.

2.3.4 Validation and results

The experimental set-up as described in Chapter 2.3.1 was used to generate measurement data for the validation of the implemented models. The experiments were performed on the production site of Wienerberger AG in Haiding, using the small-scale laboratory drying container, which was equipped with a drying chamber, an air circulation system, and a compression heat pump [7].

About 35 drying tests were performed by the project partner Wienerberger AG and AIT.

The drying duration of each test was about 10 h. The chamber was loaded with 24 pieces of Wienerberger Porotherm 25-38 per drying test, hence, about 30 t of green bricks were dried in total. The moisture content of the freshly shaped green bricks was about $y = 0.28$ at the beginning of the drying process and was lowered to the allowed kiln-entrance moisture content of $y = 0.01$ to 0.04. Process parameters, namely the circulated drying air flow and the chamber temperature, were varied. The measured data from test V7 were selected to present the results of the validation.

The validation process is carried out in two main steps. First, the drying kinetics model is validated to determine the parameters related to the raw material and to investigate the heat transfer at the brick's surface. The simulation is decoupled from the effects of the drying chamber, since the measured climate is used as a boundary condition of the drying product. In the second step, the effects of the chamber are examined more closely and a descriptive set of parameters was found. The measured data were partly used as input variables for the simulation and for comparison to results from the simulation.

But before starting the validation process, the used measurement data should be assessed on their maximum possible errors of measurement.

Quality of measurement data used for the model validation

Different quantities were measured and logged on the experimental set-up, shown in Fig. 2.18. Some of the relevant variables are summarised in Tab. 2.2 with the error of measurement, including the error of the measurement section and the error of the measurement sensor, as declared by the manufacturer.

Table 2.2: Error of measurement, including the error of the measurement section and the error of the measurement sensor

Measured variable	Symbol	Value	Unit
Temperature of brick	ϑ_{brick}	± 1.7	K
Relative humidity of feed	φ_{in}	± 5.3	%rH
Feed temperature	ϑ_{in}	± 1.2	K
Relative humidity in chamber	φ_{ch}	± 1.5	%rH
Temperature in chamber	ϑ_{ch}	± 0.8	K
Mass of brick	m_{brick}	± 0.03	kg
Shrinkage	χ	± 0.65	%

The brick's temperature, the brick's mass, the relative humidity, and temperature in the chamber were measured at different locations. The values used for the validation are the means of the relevant measured variables.

The feed mass flow rate $\dot{m}_{in}$ wasn't measured directly. It's determined from the energy balance of the outer heater. The outcome determined on the basis of velocity measurement with

a hot-wire anemometer seemed less trustworthy. $\dot{Q}_{HE}$ was determined from the internal heater's energy balance (cf. Fig. 2.18).

Drying kinetics

As the first step, the model for the drying kinetics has been validated. Tab. 2.3 contains the established parameter set for the Wienerberger Porotherm 25-38 shaped of the clay from Haiding.

Table 2.3: Summary of the model parameter, initial values, and input variables, used for the model validation of the drying kinetics

Parameter concerning the product's body	Symbol	Value	Unit
Initial volume	V_{ini}	1.3241×10^{-2}	m^3
Initial wall thickness	s_{ini}	8×10^{-3}	m
Initial surface	A_{ini}	3.2616	m^2
Mass of dry product	m_{dry}	22.11	kg
Initial mass	m_{ini}		kg
Initial temperature	ϑ_{ini}		°C
Number of nodes for discretisation	n	30	1

Parameter concerning the product's material	Symbol	Value	Unit
Linear relative shrinkage at shrinking end	χ_{SE}	3.97×10^{-2}	$\frac{\mathrm{m}}{\mathrm{m}}$
Reference temperature	ϑ_{ref}	25	°C
Reference moisture diffusion coefficient	κ_{ref}	54×10^{-9}	$\frac{\mathrm{m}^2}{\mathrm{s}}$
Reference volumetric moisture content	ψ_{ref}	0.449	$\frac{\mathrm{m}^3}{\mathrm{m}^3}$
Exponent in Eq. 2.55	k_{psi}	9	1
Diffusion resistance	μ	25	1
Thermal conductivity of dry product	λ_{dry}	1	$\frac{\mathrm{W}}{\mathrm{m\,K}}$
Specific heat capacity of dry product	c_{dry}	850	$\frac{\mathrm{J}}{\mathrm{kg\,K}}$
Specific heat capacity of water	c_w	4182	$\frac{\mathrm{J}}{\mathrm{kg\,K}}$
Density of water	ρ_w	980	$\frac{\mathrm{kg}}{\mathrm{m}^3}$
Specific surface of clay	A_{spec}	10.8	$\frac{\mathrm{m}^2}{\mathrm{g}}$
Guess of drying air's final temperature	$\vartheta_{ch,final}$		°C
Guess of drying air's final relative humidity	$\varphi_{ch,final}$		1

Input variable	Symbol	Value	Unit
Mass fraction of water in drying air	ξ_{ch}		$\frac{\mathrm{kg}}{\mathrm{kg}}$
Temperature of drying air	ϑ_{ch}		°C
Pressure of drying air	p_{ch}		Pa
Heat transfer coefficient	α		$\frac{\mathrm{W}}{\mathrm{m}^2\,\mathrm{K}}$

The individual parameters originate from different sources. Some parameters were determined from CAD files and some were measured or weighed directly from the green or dried brick (V_{ini}, s_{ini}, A_{ini}, and m_{dry}). The values of the diffusion resistance μ and the parameter k_ψ are the results of parameter variations in the course of the validation process. It's difficult to detect them under the usage of measuring techniques. The heat transfer coefficient α at a given constant ACU rotational speed was also determined by parameter variation. Further, a correlation for α could be found and will be discussed later in detail. The initial conditions and simulation inputs like ξ_{ch}, ϑ_{ch}, ϑ_{ini}, χ_{SE}, ϑ_{final}, and φ_{final} are mainly based on the logged data at the beginning and during the drying tests. Some material properties like λ_{dry}, c_{dry}, c_w, and ρ_w are chosen as common empirical values or from fluid property tables. Others, especially which characterise the raw material's drying properties like the specific surface A_{spec}, the equilibrium moisture isotherm, and the moisture diffusion coefficient κ_{ref}, were determined using special testing frames. The clay from Haiding was analysed more closely by the project partner IZF in Essen. The used measurement techniques and the obtained results will briefly be introduced.

The standardised moisture diffusion coefficient κ_{ref} at the reference temperature $\vartheta_{ref} = 25\,°C$ and the reference moisture content $y_{ref} = 0.25$ was determined by a transient method.

Therefore, a cylindrical shaped sample with a diameter of $33\,mm$ is packed as diffusion resistant and thermally insulated. Just the abutting surface is in contact to the drying air flow ($\vartheta = 50\,°C$, $\varphi = 0.55$, and $u = 2\,m/s$). The sample's mass and temperature are measured during the test. After a test duration of $1\,h$, so that the drying process is still situated in the shrinkage afflicted period, the sample is cut in slices. The mass and volume of each slice are measured. After that, the slices are dried at $105\,°C$ and weighted again. According to Eq. 2.48 the moisture diffusion coefficient can be determined under the usage of the measured quantities.

The described method is highly error-prone. The cutting of the sample with the resulting cut losses and the incomplete homogeneity of the treated clay material have to be mentioned. The maximum error of measurement is estimated as approximately $\pm 10\,\%$ [75].

For the analysed raw material, a standardised moisture diffusion coefficient was found as $\kappa_{ref} = 54 \times 10^{-9}\,m^2/s$. Common values range from $\kappa_{ref} = 8 \times 10^{-9}\,m^2/s$ for clays with bad drying behaviour to $\kappa_{ref} = 100 \times 10^{-9}\,m^2/s$ for clays with good drying behaviour [75].

To investigate the raw materials behaviour concerning the residual water content y_{eq} after drying, the equilibrium moisture isotherm at $\vartheta = 25\,°C$ and $\vartheta = 40\,°C$ shown in Fig. 2.27 have been developed. The sample of wet clay was exposed to a climate with constant temperature $\vartheta =$ const. and falling humidity, starting at almost saturated conditions. After reaching $\varphi = 0$, the humidification process follows. Measuring the trend of the sample's mass over the prevailing relative humidity provides the isotherms as shown in Fig. 2.27. The equilibrium moisture content reached while drying, is higher than the equilibrium moisture content found while humidification, under the same surrounding air conditions (cf. Chapter 2.2.2).

The black plotted trend in Fig. 2.27 is implemented to the drying kinetics model, to provide the final moisture content depending on the chamber air's relative humidity. It's the mean of
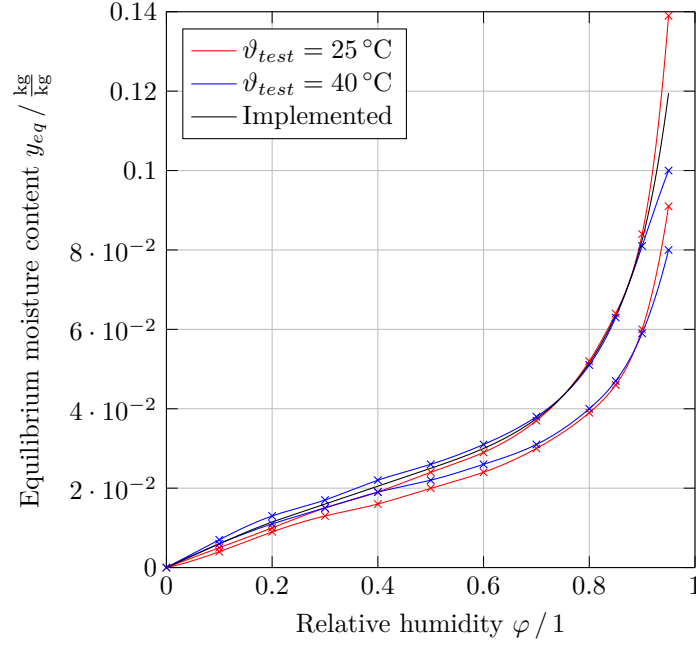
Figure 2.27: The equilibrium moisture isotherms of the Wienerberger Porotherm's raw material processed in Haiding

the isotherms part during the drying phase. Since there is no measurably dependency on the present temperature, its implementation is omitted.

The mercury porosimetry is an experimental method to determine various quantities of a porous material, such as the pore size distribution, the total pore volume, and the internal surface area which expresses the specific surface A_{spec}. Mercury is pressed into the pores of the completely dry material. The smaller the pores the more pressure is needed. The specific surface was found as $A_{spec} = 10.8\,\mathrm{m^2/g}$, which equates a common value.

The implemented models as described in Chapter 2.3.3 are the central part of the validation process. The model's boundary conditions like the measured chamber temperature ϑ_{ch} and chamber relative humidity φ_{ch} are provided by objects of the Modelica class CombiTimeTable. A CombiTimeTable is a table look-up with respect to time and linear extrapolation methods obtaining the drying test's measurement data from a text file. The heat transfer coefficient α is provided as a constant value for each drying test, as a result of a parameter variation.

The results of the drying test V7 and the corresponding simulation results are presented in course of the validation process. The ACU's rotational speed was kept as constant at maximum speed during the whole drying test.

Fig. 2.28 shows the drying chamber's measured climate during the drying test in the h_{1+X},X-chart. At the beginning the chamber's air is saturated at ambient temperature. This behaviour was observed in most of the drying tests. The chamber temperature increases during the entire
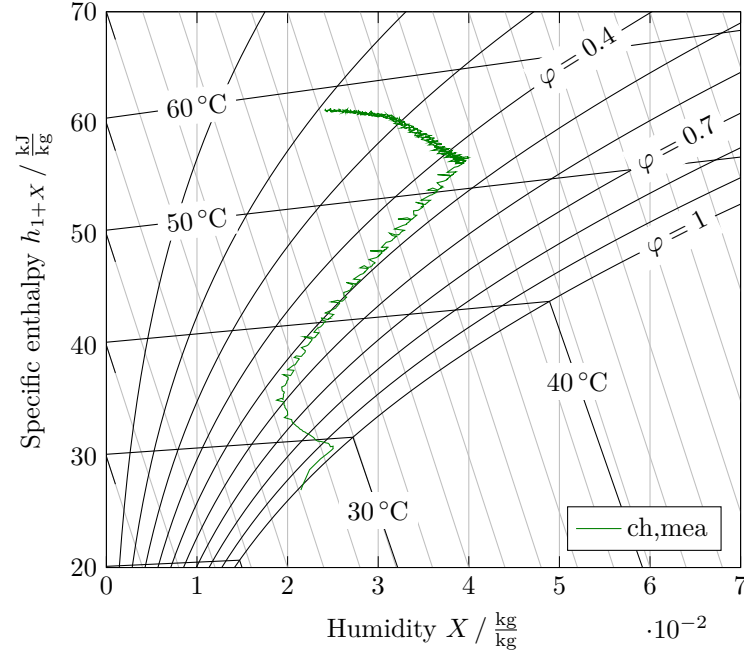
Figure 2.28: Measured chamber climate during the drying test, shown in the h_{1+X},X-chart

test period. The humidity X in the chamber rises after the system's short initial phase. But, the relative humidity φ_{ch} decreases, as it also depends on the rising temperature. After a duration of $t \approx 3.1\,\text{h}$, there is a kink in the trend and the humidity X falls until the end of the experiment. A clear distinction between the first and second drying period isn't possible regarding to the logged chamber climate data. The climate is mainly influenced by the conditions of the incoming drying air, thus by the control behaviour of the system. In the first validation step, the chamber climate only serves as input for the simulation. A more detailed interpretation will be performed in step two.

Fig. 2.29 shows the time evolution of the corresponding relative humidity φ_{ch}. The relative humidity starts at saturation with $\varphi = 1$ and decreases during the whole testing time, in particular during the initial phase.

The time evolution of the measured chamber temperature $\vartheta_{ch,mea}$ and the brick's temperature $\vartheta_{brick,mea}$ are shown in Fig. 2.30. The trend of the brick's temperature $\vartheta_{brick,mea}$ is the averaged trend of 8 sensors. The appreciable oscillation arises due to the movement of the supporting shelf. It's placed on rails and moves periodically, thus reversing the direction of the air flow through the bricks, to ensure fast and uniform drying. The position is changing every 6 minutes.

The brick's simulated core temperature $\vartheta_{C,sim}$ and its surface temperature $\vartheta_{surf,sim}$ are equal during the first drying period and take course close to the wet-bulb temperature $\vartheta_{WB,mea}$. The second drying period starts after $t \approx 4\,\text{h}$, when the brick's temperature begins to depart from
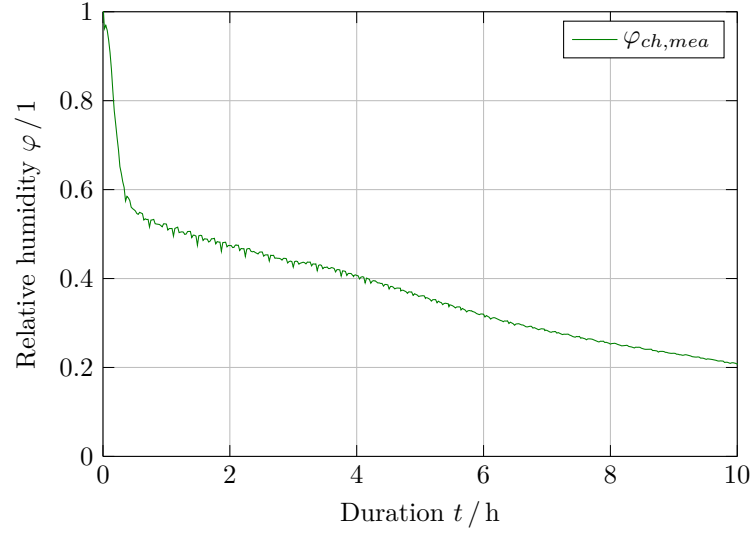
Figure 2.29: Time evolution of the measured relative humidity in the drying chamber
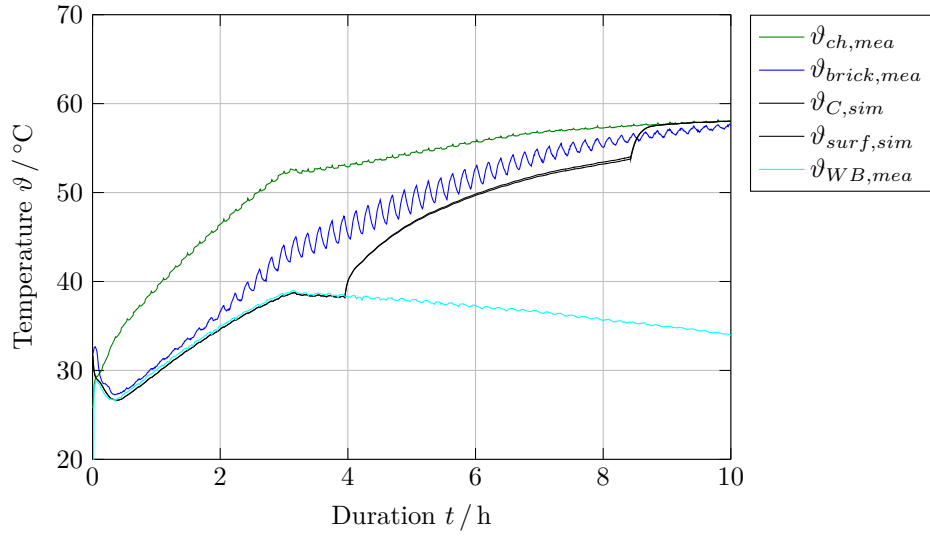
Figure 2.30: Time evolution of the arising temperatures: comparison of the simulated brick surface and core temperature with the measured brick mean temperature

$\vartheta_{WB,mea}$. The last kink in the trend indicates the end of the drying process and the brick's temperature rises until it's equal to the chamber temperature.

To discuss the differences between the measured and simulated brick temperature, Fig. 2.31 should be considered. As already mentioned, the trend of the brick's temperature $\vartheta_{brick,mea}$ is the average trend of 8 sensors. The sensors were distributed over several of the 24 bricks. The
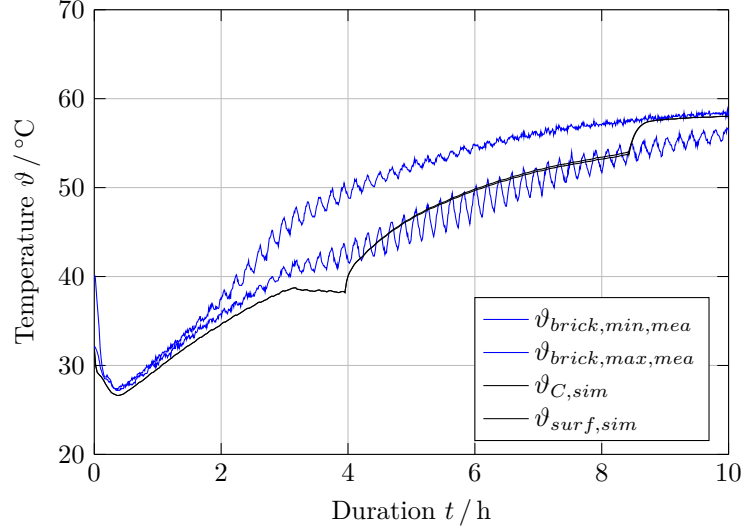
Figure 2.31: Time evolution and comparison of the simulated brick surface and core temperature with the measured brick minimum and maximum temperature

chart shows the minimum and maximum measured temperature. The graphs suggest that the second drying period, for the individual bricks or different positions at one and the same brick, starts and also ends at different points in time. Averaged over the whole drying chamber this results in a creeping transition from the first to the second drying period and from the second drying period to the drying end as well, in contrast to the simulation results.

The maximum difference between the simulation results and the minimum measured temperature is about $4\,\mathrm{K}$. At this point, it's also important to take a critical look at the measured data. The brick temperature in the simulation highly depends on the relative humidity and the temperature of the chamber air. Both are measured quantities and afflicted by an error of measurement (cf. Tab. 2.2). Especially when measuring the relative humidity, high errors occur. The measured brick temperature is also afflicted by a measurement error. In addition, the temperatures were sensed by Pt100 sensors, which are associated with an elevated thermal inertia.

One of the main and most important results is illustrated in Fig. 2.32. The time evolution of the brick's simulated mass is compared with the mean measured mass $m_{brick,mea}$ of two scales. The drying process starts at a mass of about $28\,\mathrm{kg}$ per brick. Higher drying rates are typical for the first drying period. The mass decreases stronger than in the second drying period. The trend of the measured mass is very smooth at the end of the drying process. Again, the trend is an averaged graph. Another reason could be due to light sorption effects at low moisture contents. According to the simulation results, the first drying period ends after approximately $4\,\mathrm{h}$. A discontinuity can be observed at this point in time, since the equation system has changed
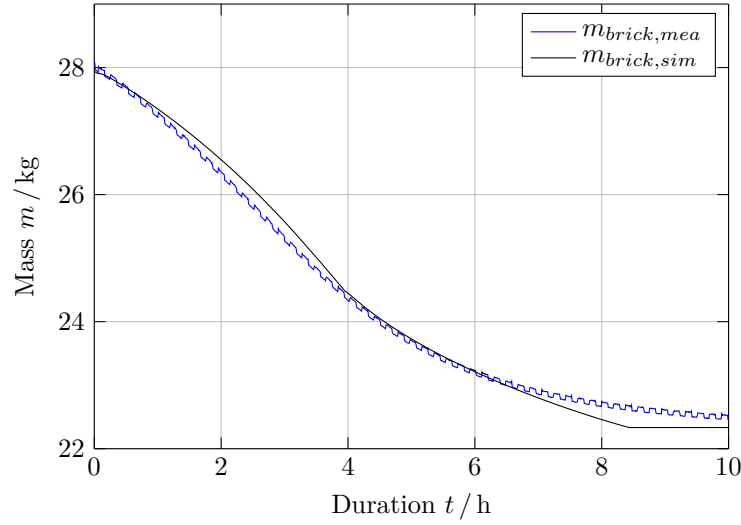
Figure 2.32: Time evolution and comparison of the simulated brick mass with the measured brick mean mass

within the simulation. With continuing drying the brick's mass and drying rate decrease further and after 8.5 h the drying process has finished, indicated by another kink of the curve. Again, the equation system has changed.

The measured values are obviously influenced by the forces due to the air flow, since discontinuities can be identified appearing with the same frequency like the temperature oscillations do.

Fig. 2.33 compares the measured relative linear shrinkage, with the relative linear shrinkages at the surface and at the wall's centre provided as a simulation result. There's a small difference in the simulated curves, hence there's just a light moisture gradient between the brick's surface and wall centre. The small moisture gradients during the shrinkage afflicted period suggest that the drying process was performed slowly and an insensitive product with regard to susceptibility to cracking was dried. Due to the assumption of ideal, unhindered shrinkage, the shrinking process stops abruptly when χ has reached χ_{SE}. The model parameter χ_{SE} has to be provided by the user. In the drying experiment the transition is smooth.

The curves in Fig. 2.34 are results of the simulation. The moisture distributions over half of the wall's cross section are illustrated. At the beginning $t = 0$ of the drying process it was assumed that the moisture is distributed evenly. After starting the drying process, the moisture content falls. The distributions during the first drying period, when the moisture content at the surface is greater than the equilibrium moisture content, are taken at equidistant time intervals. Humidity gradients aren't recognisable at the beginning. But when the moisture content in the near-surface layers further falls, the moisture diffusion coefficient drops massively (cf. Fig. 2.17) and moisture gradients are formed. The second drying period begins, after the equilibrium moisture content got reached at the surface. The drying interface begins to move towards the

127
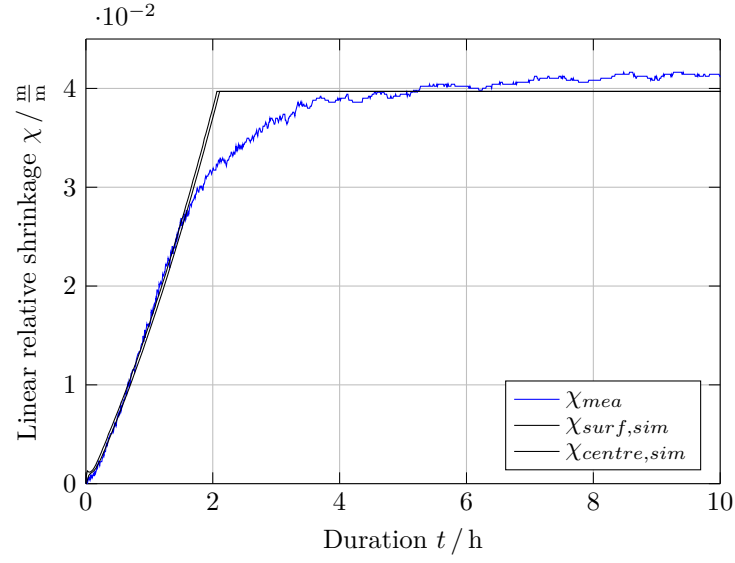
Figure 2.33: Time evolution and comparison of the simulated linear relative shrinkage at the surface and at the wall's centre with the measured linear relative shrinkage
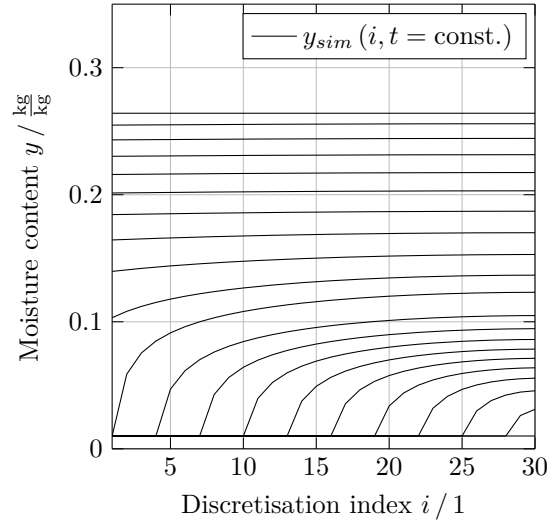
Figure 2.34: Moisture distribution over half of the wall's cross section at different points in time: simulation result

wall's centre. The drying is completed, when the moisture content again is distributed evenly with the equilibrium moisture content.

Fig. 2.35 shows a simulation result, the thickness of the dry layer $s_{dry,sim}$ or the position of the drying interface depending on the drying duration. If the surface is wet, the drying interface is also located there. At $t \approx 4\,\mathrm{h}$, the first discrete volume dries up and the second drying period
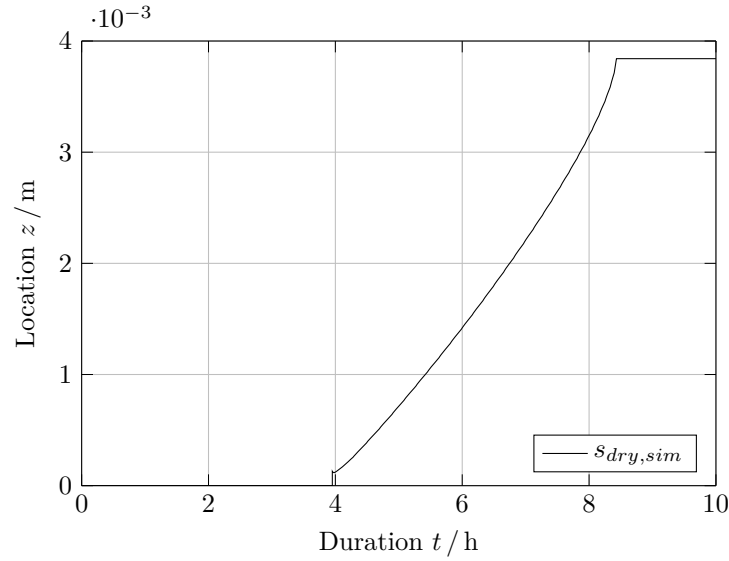
Figure 2.35: Time evolution of the dry layer's thickness, indication of the first drying period's and the drying process' end: simulation results

begins. Due to the finite dimension of the discrete volume, the extent of the dry layer abruptly jumps to its value. A smoothing algorithm is implemented for the continuing movement of the drying interface. After $t \approx 8.5\,\mathrm{h}$ the drying interface reaches the centre of the wall and the drying process has finished. The final position differs from $s_{ini}/2 = 4\,\mathrm{mm}$ due to the total shrinkage of the brick's wall.

As a result, the simulation outcome according to the drying test V7 is matching very well to the measured data. That's also the case for almost all of the 35 performed drying tests, which are all reproduced under usage of the parameter set summarised in Tab. 2.3.

Convective heat transfer

A parameter variation regarding the heat transfer was performed in the course of the validation process. During the first drying period, the drying rate and the brick's mass evolution primarily depend on the heat transfer and the coupled mass transfer at the brick's surface. The drying tests were performed at different but during a certain test constant ACU speed, hence, under constant convective heat transfer conditions. The heat transfer coefficients in Fig. 2.36 indicated by circles are found at the corresponding ACU speed by investigating the first drying period of each drying test.

The Nußelt number Nu is defined by Eq. 2.10. According to the theory of similarity the empiric, dimensionless correlation Eq. 2.11, depending on the Reynolds number Re and the Prandtl number Pr, often is used to describe convective heat transfer problems. Assuming $Re = Re(n)$ and constant fluid properties delivers a proper shape for the regression function.
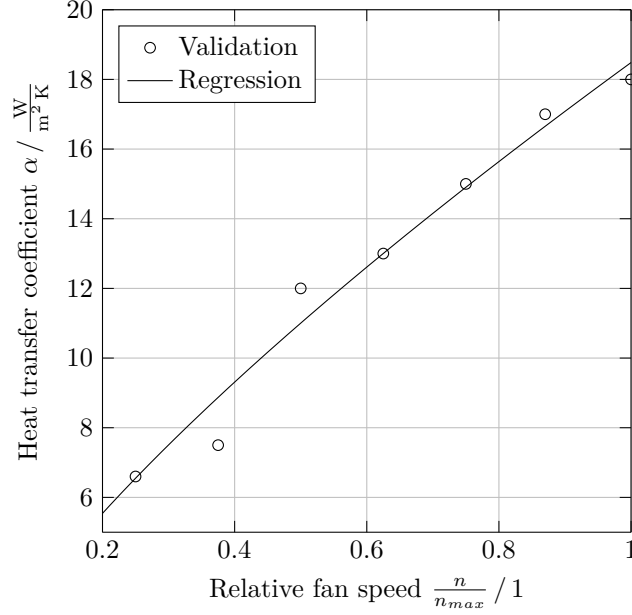
Figure 2.36: Convective heat transfer coefficient depending on the relative
ACU rotational speed

Using the data found through the parameter variation, the following correlation for the convective heat transfer coefficient depending on the relative ACU rotational speed can be found as the regression curve:

$$\alpha\left(n\right) = 18.484 \left(\frac{n}{n_{max}}\right)^{0.7484} \frac{\text{W}}{\text{m}^2\,\text{K}} \tag{2.124}$$

Where n is the prevailing rotational speed and n_{max} the maximum possible rotational speed of the ACU.

Drying chamber

The drying chamber model is treated as the validation's second step. Tab. 2.4 contains the parameter set that was found to characterise the laboratory container's drying chamber. Again, the parameters originate from different sources. Some like the chamber dimensions B_{ch}, H_{ch}, and L_{ch} were measured directly. The heat capacity C_{sh} was found by estimating the mass of the supporting steel shelf. The heat transmission coefficient of the chamber wall k_{wall} and the leakage mass flow rate $\dot{m}_{leak}$ are the results of parameter variations. The simulation inputs, the initial and ambient conditions are mainly based on the logged data at the beginning and during the drying tests.

In the following discussion, the results of the validation calculation concerning the drying chamber are presented. Again, the measurement data and simulation results from test V7 are used.

Table 2.4: Summary of the model parameter, initial values, and input variables, used for the model validation of the drying chamber

Parameter concerning the container	Symbol	Value	Unit
Initial relative humidity	$\varphi_{ch,ini}$		1
Initial temperature	$\vartheta_{ch,ini}$		°C
Width	B_{ch}	2.3	m
Height	H_{ch}	2.2	m
Length	L_{ch}	2	m
Heat transmission coefficient of wall	k_{wall}	1	$\frac{\text{W}}{\text{m}^2\,\text{K}}$
Heat capacity of shelf	C_{sh}	980	$\frac{\text{kJ}}{\text{K}}$
Input variable	**Symbol**	**Value**	**Unit**
Feed mass flow rate	$\dot{m}_{in}$		$\frac{\text{kg}}{\text{s}}$
Feed temperature	ϑ_{in}		°C
Mass fraction of water in feed air	ξ_{in}		$\frac{\text{kg}}{\text{kg}}$
Energy input by internal heater	$\dot{Q}_{HE}$		W
Leakage mass flow rate	$\dot{m}_{leak}$		$\frac{\text{kg}}{\text{s}}$
Ambient temperature	ϑ_{amb}		°C
Mass fraction of water in ambient air	ξ_{amb}		$\frac{\text{kg}}{\text{kg}}$
Ambient pressure	p_{amb}		Pa
Fan speed	n/n_{max}		1

Fig. 2.37 shows the time evolution of the determined feed mass flow rate $\dot{m}_{in,mea}$, used as an input boundary condition for the simulation. $\dot{m}_{in,mea}$ remains approximately constant, after a short initial phase.

Another quantity used as input variable is the heat flow rate $\dot{Q}_{HE,mea}$ supplied by the internal heat exchanger. The time evolution is shown in Fig. 2.38.

The most important criterion for assessing the chamber model's quality is the attendant chamber climate. Fig. 2.39 compares the trend of the measured climate (green) with the results from the simulation (black) in a h_{1+X},X-chart. The conditions of the feed air are plotted in red colour.

Fig. 2.40 illustrates the trends of the relevant relative humidities. The measured variable φ_{in} is used as a boundary condition for the simulation. $\varphi_{ch,mea}$ and $\varphi_{ch,sim}$ are representing the measured and the simulated relative humidity in the drying chamber. The simulated curve shows two kinks, due to the change of the equation system used in the simulation: the first when ending the first drying period and the second when ending the drying process. When the drying process has finished, $\varphi_{in,mea}$ and $\varphi_{ch,mea}$ end up at similar values, since there is no evaporation anymore. $\varphi_{ch,mea}$ illustrates the relative humidity of the ambient air, hence, the condition of the incoming leakage mass flow.
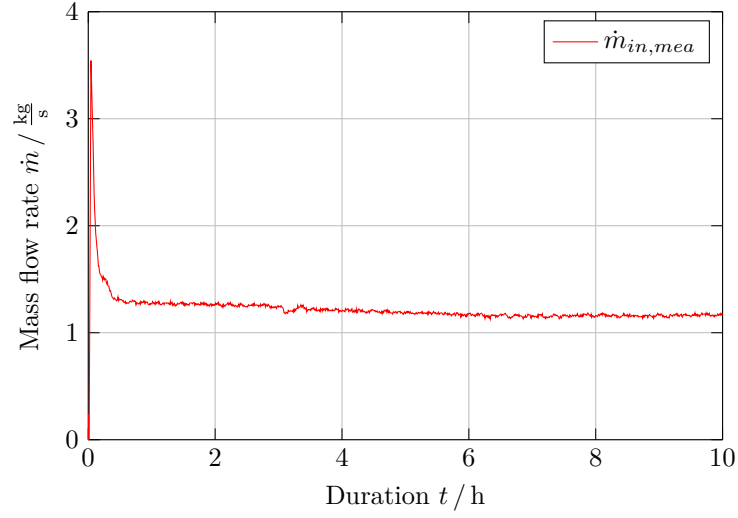
Figure 2.37: Time evolution of the determined feed mass flow rate into the drying chamber
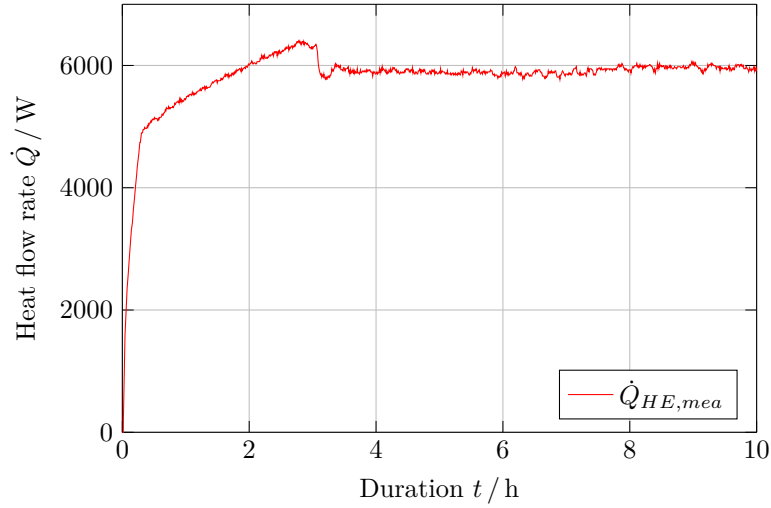
Figure 2.38: Time evolution of the determined heat flow rate supplied to the drying air by the internal heat exchanger

Fig. 2.41 summarises the prevailing temperatures during the test and the simulation. The feed air flow is heated by the external heater, where the hot intermediate circuit serves as the energy source, before it's entering the drying chamber. The hot intermediate circuit's temperature is a control variable of the complete system and can be adjusted by the external cooler. The long duration of the heating phase until $t \approx 3\,\mathrm{h}$, indicated by the kink of $\vartheta_{in,mea}$, suggests that the external cooler becomes active after this point in time. Before, the full thermal energy provided by the heat pump was needed for drying and heating the system.
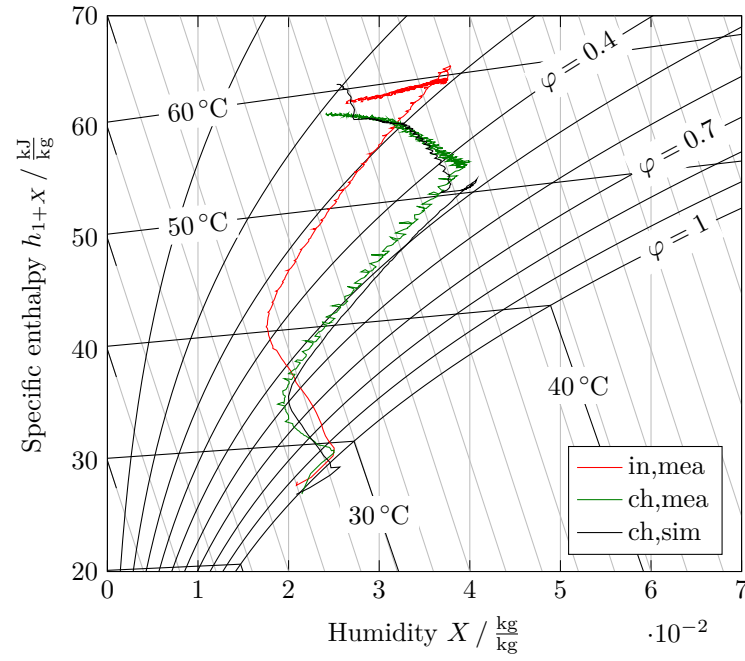
Figure 2.39: Comparison of the simulated with the measured chamber climate during the drying test, shown in the h_{1+X},X-chart
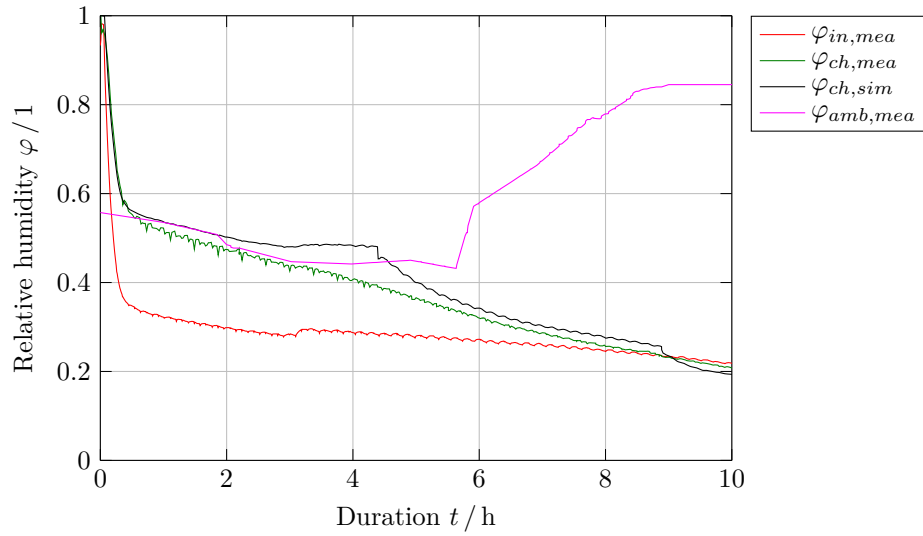
Figure 2.40: Time evolution and comparison of the arising simulated and measured relative humidities

The measured chamber temperature $\vartheta_{ch,mea}$ and the simulated chamber temperature $\vartheta_{ch,sim}$ are matching quite well. The trends are only differing between the end of the heating phase
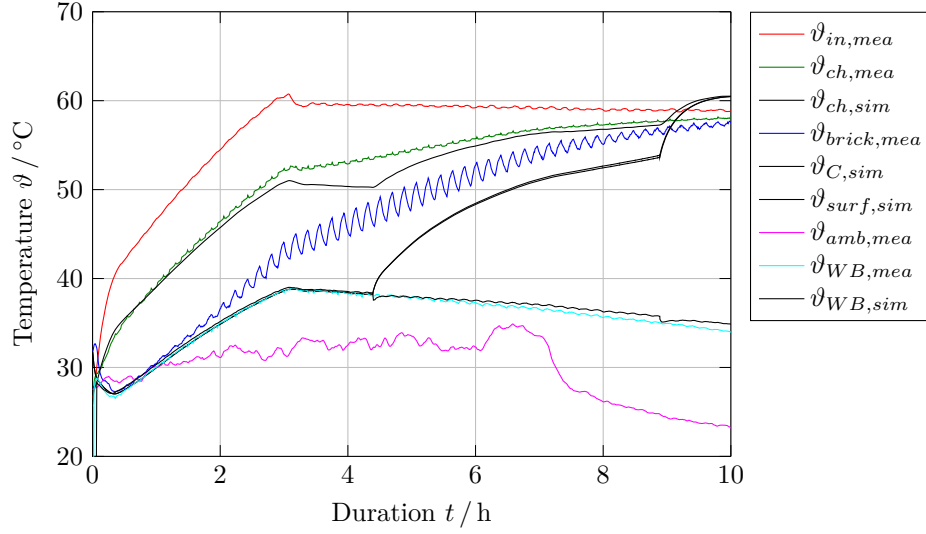
Figure 2.41: Time evolution and comparison of the arising simulated and measured temperatures

$t \approx 3\,\text{h}$ and the beginning of the second drying period $t \approx 4.25\,\text{h}$ according to the simulation results. The differing trend of $\vartheta_{ch,mea}$ can again be interpreted as the consequences of a smooth transition from the first to the second drying period, averaged over the whole chamber. Since the point in time, when the second drying period starts lightly depends on the location in the chamber. In the simulation that happens at all locations at the same point in time. After drying has finished, the feed air, the chamber air, and also the brick prevail at almost equal temperature.

The interpretation of the measured and simulated brick temperature has already been discussed in the course of the drying kinetics' validation process. The same argumentation applies here.

As a result, the simulation outcome according to the drying test V7 is matching very well to the measured data. That's also the case for almost all of the 35 performed drying tests, which are all reproduced under usage of the parameter sets summarised in Tab. 2.3 and Tab. 2.4.

To conclude, the brick temperature is less important for the investigation or optimisation of dryers. The mass profile is one of the most important results, as it dictates the drying time. Another important result is the chamber climate. In case of energy supply by heat pumps, the exhaust air with chamber conditions can be used as the heat pump's energy source. Thus, the specific energy and the resulting dew point are from interest.

Another interesting observation during the investigations has been made. The first chamber model did not contain any possibility to consider leakage flows. But, the first validation has shown, that in case of the laboratory container, the leaks do have a significant influence and cannot be neglected. The chamber model had to be extended. A parameter variation claimed a leakage mass flow rate of $\dot{m}_{leak} = 0.1\,\text{kg/s}$. Assuming the air density with $\rho = 1.1\,\text{kg/m}^3$ leads

to the volume flow rate $\dot{V}_{leak} = 327\,\text{m}^3/\text{h}$. That correlates to a ventilation number[3] of 32/h.

Based on these findings, a blower door test was performed. A gauge pressure of $\Delta p = 50\,\text{Pa}$ resulted in a leakage volume flow of $\dot{V}_{leak} = 425\,\text{m}^3/\text{h}$. And for a negative pressure of $\Delta p = 50\,\text{Pa}$ a leakage volume flow of $\dot{V}_{leak} = 325\,\text{m}^3/\text{h}$ was found. Identified leaks were the chamber door, passages of conduits, bore holes, etc. The measured leakage flows are of the same order of magnitude, as the claimed flow in the simulation. However, the pressure conditions at the leaks in the chamber are difficult to determine when the ACU is operating.

Leakage certainly has a bigger impact on the laboratory container than on real dryers. Thus, there is a large leakage compared to the chamber volume. Further, the container was placed outdoors, thus influenced by the environmental conditions. A real chamber dryer is usually placed in the production hall and isn't directly exposed to the weather conditions, which change strongly with the seasons.

2.4 Summary and outlook

The aim of this chapter was the development of an open and easily expandable drying library to investigate the drying behaviour of clay bricks in chamber dryers. Dryers are major energy consumers in the brick and tile industry, because of the requirement to provide the latent heat of evaporation for all the moisture that is removed. Fossil-fired, convective exhaust air dryers are mainly used. These systems dissipate the exhaust air including the water vapour to the environment. Hence, this type of dryers tends to have pretty low thermal efficiency, often below 50 %. There's a huge necessity and potential for improving efficiency and reducing energy consumption concerning industrial drying processes.

In the Fundamentals chapter, the commonly used dryer technologies in the brick and tile industry and the facilities for the drying energy supply were presented. The most important properties of the manufactured material in conjunction with drying were discussed. That's the basis to approach the thermodynamic transport mechanisms and to describe the heat and mass transfer processes, within the drying product and at the drying product's surface, during the first and second drying period. Practical and permissible modelling assumptions and the mathematical derivation and formulation were presented. The consideration of the chamber dryer as an ideal stirred tank reactor and the drying product as a one-dimensional symmetrical plate, were the most important modelling assumptions. Consequently, the effort in the model equations' numerical treatment and the computational complexity while solving transient problems could be kept manageably.

The next step was the model implementation of a chamber dryer in its general structure and the drying kinetics of the contained drying product. Therefore, the presented equation system was conveniently attributed to these two main classes of objects. The mathematical

---

[3]The ventilation number is defined as the hourly air volume flow, related to the considered room's volume. The ventilation number of a new detached house is about 2 [110].

formulations were given as discrete, differential, algebraic equation systems. Shrinkage, the first and the second drying period require different sets of model equations. The object-oriented modelling language Modelica and the modelling and simulation environment Dymola were used for the implementation process. A new library was developed, providing the described classes and other appropriate components and connectors.

Furthermore, a license independent tool for simulative investigations of chamber dryers was created. Dymola is a very powerful but commercial environment for model development and simulation. Since the software is not available to the project partner Wienerberger AG, a stand-alone executable file was generated. The tool will be used for designing new plants and for process optimisations on existing plants.

The final step was the model validation using measurement data of about 35 drying tests, performed on a small-scale laboratory container. Process parameters, namely the circulated drying air flow and the chamber temperature, were varied. The measured data from test V7 were selected to present the results of the validation. The validation process was carried out in two main steps. First, the parameters related to the raw material were determined and a correlation for the heat transfer at the brick's surface was found. Then, the effects of the chamber were examined more precisely. A descriptive set of parameters was found. The measurement data were partly used as input variables for the simulation and for comparison to results of the simulation.

All the substantial properties and processes were reproduced with sufficient accuracy under appropriate application of the discussed simplifications and modelling assumptions. The simulation outcome according to the drying test V7 was matching very well to the measured data. That's also the case for almost all of the 35 performed drying tests, which were all reproduced under usage of one and the same parameter set. Hence, the implemented models in conjunction with the determined parameter sets are forming a convenient tool for further investigations.

From now on, a general chamber dryer model and drying kinetics model of porous media for simulative investigations is available in Modelica language. The parameter sets found in the validation, characterise the clay from Haiding and the small-scale laboratory container. The set has to be adjusted, if different dryers are considered. Some parameters like the geometry are rather easy to change. Others, such as the quality of the heat transfer, the leakage mass flow, and the heat transfer through the dryer walls, have to be estimated based on experience or investigated more in detail. The same applies to the kinetics model. If the raw material, its mixture or the brick's shape is changed, the affected parameters have to be adjusted. Therefore, a lot of empirical data can be found in the literature.

The developed library contains the two main classes and other useful components. Appropriate connectors and important functions for fluid properties are already available. The library can easily be extended with other components. For example, a simplified tunnel dryer model has

already been implemented.

One of the main reasons why using the Modelica language was the advantage that transient multi-domain simulations are rather easy to realise. Components of different user-defined, commercial, and standard libraries can be merged to a single model and the simulation can be performed using one and the same solver. Therefore, the connectors or interfaces have to be chosen appropriately. Composite systems, creating an overall model could be investigated. For example, several chambers could be arranged and easily linked as blocks in a graphical schema. The energy supply could be provided by different technologies, if suitable models exist. Furthermore, considerations of the drying plants in conjunction with the kiln would be feasible. The kilns waste heat could be used as the energy source for the dryer. Optimisation tasks in plant or fabric management is be possible.

Summary and benefit

The aim of this work was to investigate and advance industrial HTHPs in order to increase the supply temperature and to expand the field of application, especially in concern of industrial drying processes.

Since the compressor and the working fluid play the central roles in this concern, the focus in Chapter 1 was placed on these two components as parts of HTHPs. General theoretical investigations on the use of water as a working fluid, and in particular, as an application under the usage of a reciprocating compressor with direct injection cooling were presented. Furthermore, experimental investigations were carried out to evaluate the hot gas cooling with liquid water injection. In the first experimental step, an injection system was developed and tested successfully. As a subsequent experimental step, an existing reciprocating compressor test bench was adapted and tests with the injection system were performed.

In Chapter 2 the development of an open and easily expandable drying library, for the investigation of the drying behaviour of clay bricks in a chamber dryer was described. The modelling approaches and the descriptive mathematical formulations were implemented in the modelling language Modelica and validated using measurement data from drying tests performed on a small-scale laboratory container, as a specific application. All the substantial properties and processes were reproduced with sufficient accuracy. With the developed tool multi-domain simulations, like optimisation tasks in plant management or performance studies, are rather easy to realise by combining components of the drying with a user-defined or a standard library. The models are forming the basis to investigate drying processes in conjunction with the energy supply by HTHPs, to assess the process quality, and to extend their application field.

In course of the DryPump project, components of the developed library have already successfully been applied by the protect partner AIT. Namely as load for performance studies of the heat pump driven small-scale laboratory drying container (cf. Fig. 2.18). The commercial TIL library of TLK-Thermo GmbH[4] was used to build up the heat pump and intermediate circuits. It's a library for the simulation of thermodynamic systems with the focus on applications in refrigeration technology. The resulting chamber climate was from importance. In case of energy supply by heat pumps, the exhaust air with chamber conditions is used as the heat

---

[4]https://www.tlk-thermo.com/

pump's energy source. Thus, the specific energy and the resulting dew point were from interest.

The tests performed on the laboratory container have shown SEC values ranging between 0.5 and 0.75 kWh/kg [7]. They are in good accordance with data measured in heat pump dryers for timber [19]. In addition, they are considerably low compared to most industrial dryers which typically show SEC values ranging from 1 to 2 kWh/kg [3]. The data from the drying test were further used to validate the mentioned overall model. Numerical simulations in conjunction with the validated overall model provided a mean SEC of about 0.5 kWh/kg. The average SEC in the simulation could be lowered to 0.355 kWh/kg by different acts of optimisation [2].

List of Figures

List of Tables

Bibliography

[1] Michael Hartl et al. *SteamUp: Wärmepumpensysteme bis 200 °C unter Verwendung von Wasser als Kältemittel zur Integration in industriellen Prozessen.* Publizierbarer Endbericht Projekt 843872, e!Mission.at 4. Ausschreibung, KliEn / FFG, Wien, 2015. URL: `https://www.energieforschung.at/assets/project/final-report/SteamUp-Endbericht-publizierbar.pdf` (visited on Nov. 24, 2018).

[2] Michael Hartl et al. *DryPump: Effiziente Trocknung mit Kompressionswärmepumpen.* Publizierbarer Endbericht Projekt 848912, Energieforschungsprogramm 1. Ausschreibung, KliEn / FFG, Wien, 2017.

[3] Michael Lauermann et al. "Industrielle Trocknung mit Kompressionswärmepumpen: Modellbildung und Simulation der konvektiven Ziegeltrocknung".
In: *Annual Meeting of the Deutscher Kaelte und Klimatechnischer Verein 2016.*
Ed. by Deutscher Kaelte- und Klimatechischer Verein. Vol. 2.
Red Hook, NY: Curran Associates, Inc., 2016, pp. 1353–1364. ISBN: 9781510836563.

[4] Michael Lauermann et al.
"Industrielle Trocknung mit Kompressionswärmepumpen: Ein numerischer Vergleich von zwei hydraulischen Einbindungsvarianten an einem konkreten Beispiel".
In: *Proceedings der 10. Internationalen Energiewirtschaftstagung (IEWT) 2017.*
Ed. by TU Wien. Wien, 2017.
URL: `http://eeg.tuwien.ac.at/eeg.tuwien.ac.at_pages/events/iewt/iewt2017/html//files/fullpapers/232_Lauermann_fullpaper_2017-02-17_09-46.pdf`
(visited on Nov. 24, 2018).

[5] Veronika Wilk et al. "Erhöhung der Energieeffizienz industrieller Trocknungsprozesse durch den Einsatz von Wärmepumpen". In: *14. Symposium Energieinnovation.*
Ed. by TU Graz. Graz: Verlag der Technischen Universität Graz, 2016.
ISBN: 9783851254495.

[6] Veronika Wilk et al. "Techno-ökonomische Analyse von Wärmepumpen für die industrielle Trocknung mit Monte-Carlo-Simulation".
In: *15. Symposium Energieinnovation.* Ed. by TU Graz.
Graz: Verlag der Technischen Universität Graz, 2018. ISBN: 9783851255850.

[7]   Michaela Fraubaum et al.
        "Experimental evaluation of brick drying using a compression heat pump".
        In: *Proceedings of the 6th European Drying Conference*. Ed. by University of Liege. 2017.

[8]   Statistik Austria, ed. *Energiedaten Österreich 2016: Änderung wichtiger Kennzahlen und*
        Einflussfaktoren im Vergleich zum Vorjahr.
        Wien: Bundesanstalt Statistik Österreich, 2017. URL:
        `https://www.statistik.at/web_de/statistiken/energie_umwelt_innovation_`
        `mobilitaet/energie_und_umwelt/energie/index.html` (visited on Nov. 24, 2018).

[9]   T. Kudra. "Energy Aspects in Drying". In: *Drying Technology* 22.5 (2004), pp. 917–932.
        ISSN: 0737-3937. DOI: `10.1081/DRT-120038572`.

[10]   Ian C. Kemp. "Reducing Dryer Energy Use by Process Integration and Pinch Analysis".
        In: *Drying Technology* 23.9-11 (2005), pp. 2089–2104. ISSN: 0737-3937.
        DOI: `10.1080/07373930500210572`.

[11]   Anne Tretau. "Einfluss der Prozessführung auf den thermischen Energiebedarf von
        Konvektionstrocknern in der Ziegelindustrie".
        Dissertation. Magdeburg: Otto-von-Guericke-Universität Magdeburg, 2008.

[12]   Cordin Arpagaus. *Hochtemperatur Wärmepumpen: Literaturstudie zum Stand der*
        Technik, der Forschung, des Anwendungspotenzials und der Kältemittel.
        Ed. by Förderverein Institut für Energiesysteme. Buchs, 2017.
        URL: `https://www.fv-ies.ch/fileadmin/NTB_Institute/IES/FV-`
        `IES/Literaturstudie_Hochtemperatur_Waermepumpen.pdf` (visited on Nov. 24, 2018).

[13]   Wolfgang Eifler et al.
        Küttner Kolbenmaschinen: Kolbenpumpen, Kolbenverdichter, Brennkraftmaschinen.
        7th ed. Wiesbaden: Vieweg+Teubner, 2009. ISBN: 9783834893024.

[14]   Heinz P. Bloch and John J. Hoefner.
        Reciprocating compressors: Operation & maintenance. 1st ed.
        Houston, TX: Gulf Pub. Co, 1996. ISBN: 0884155250.

[15]   Wolfgang Eder and Franz Moser. *Die Wärmepumpe in der Verfahrenstechnik*. 1st ed.
        Wien: Springer, 1979. ISBN: 9783709122518.

[16]   Hans Dieter Baehr and Stephan Kabelac.
        Thermodynamik: Grundlagen und technische Anwendungen. 14th ed.
        Berlin: Springer, 2009. ISBN: 9783642005565.

[17]   Anton A. Kiss and Carlos A. Infante Ferreira.
        Heat Pumps in Chemical Process Industry. 1st ed.
        Boca Raton: CRC Press Taylor & Francis Group, 2017. ISBN: 9781498718950.

[18] M. A.R. Eisa, R. Best, and F. A. Holland.
      "Working Fluids for High Temperature Heat Pumps".
      In: *Heat Recovery Systems* 6.4 (1986), pp. 305–311. ISSN: 01987593.
      DOI: 10.1016/0198-7593(86)90116-5.

[19] Vasile Minea, ed. *Advances in Heat Pump-Assisted Drying Technology*. 1st ed.
      Advances in Drying Science and Technology.
      Boca Raton, London, and New York: CRC Press Taylor & Francis Group, 2016.
      ISBN: 9781498734998.

[20] Walter Grassi. *Heat Pumps: Fundamentals and Applications*. 1st ed.
      Green Energy and Technology. Cham: Springer, 2018. ISBN: 9783319621982.

[21] Choyu Watanabe et al. "Pioneering Industrial Heat Pump Technology in Japan".
      In: *Proceedings of 11th IEA Heat Pump Conference 2014*. Ed. by IEA. 2014.
      URL: https://heatpumpingtechnologies.org/publications/pioneering-
      industrial-heat-pump-technology-in-japan/ (visited on Nov. 24, 2018).

[22] Fei Qin et al. "Experimental investigation and theoretical analysis of heat pump systems
      with two different injection portholes compressors for electric vehicles".
      In: *Applied Energy* 185 (2017), pp. 2085–2093. ISSN: 03062619.
      DOI: 10.1016/j.apenergy.2015.12.032.

[23] Dongwoo Kim et al. "Optimization of the injection-port geometries of a vapor injection
      scroll compressor based on SCOP under various climatic conditions".
      In: *Energy* 135 (2017), pp. 442–454. ISSN: 03605442.
      DOI: 10.1016/j.energy.2017.06.153.

[24] Yongseok Jeon et al. "Numerical study on the optimal design of injection-hole
      geometries of a twin rotary compressor in a liquid injection heat pump".
      In: *Applied Thermal Engineering* 113 (2017), pp. 1178–1188. ISSN: 13594311.
      DOI: 10.1016/j.applthermaleng.2016.11.115.

[25] Dongwoo Kim et al. "Performance comparison among two-phase, liquid, and vapor
      injection heat pumps with a scroll compressor using R410A".
      In: *Applied Thermal Engineering* 137 (2018), pp. 193–202. ISSN: 13594311.
      DOI: 10.1016/j.applthermaleng.2018.03.086.

[26] Shuaihui Sun et al. "Experimental Investigation on the Performance of Scroll
      Refrigeration Compressor With Suction Injection Cooling".
      In: *Proceedings of the ASME Fluids Engineering Division Summer Meeting 2014*.
      Ed. by ASME. New York: ASME, 2014. ISBN: 9780791846223.
      DOI: 10.1115/FEDSM2014-22200.

[27] Hyun Joon Chung et al. "Performance evaluation of a gas injection CO2 heat pump according to operating parameters in extreme heating and cooling conditions".
In: *Energy* 154 (2018), pp. 337–345. ISSN: 03605442.
DOI: `10.1016/j.energy.2018.04.132`.

[28] Cordin Arpagaus et al. "High temperature heat pumps: Market overview, state of the art, research status, refrigerants, and application potentials".
In: *Energy* 152 (2018), pp. 985–1010. ISSN: 03605442.
DOI: `10.1016/j.energy.2018.03.166`.

[29] Mattias Nilsson, Harald Nes Rislå, and Konstantinos Kontomaris.
"Measured performance of a novel high temperature heat pump with HFO-1336mzz(Z) as the working fluid". In: *Proceedings of 12th IEA Heat Pump Conference 2017*.
Ed. by IEA. 2017. ISBN: 9789090304120.
URL: `http://hpc2017.org/wp-content/uploads/2017/05/O.3.4.2-Measured-performance-of-a-novel-high-temperature-heat-pump-with-HFO-1336mzzZ-as-the-working-fluid.pdf` (visited on Nov. 24, 2018).

[30] Marwan Chamoun et al. "Experimental Investigation of a New High Temperature Heat Pump Using Water as Refrigerant for Industrial Heat Recovery".
In: *Proceedings of the International Refrigeration and Air Conditioning Conference 2012*.
Ed. by Purdue University. 2012.
URL: `https://docs.lib.purdue.edu/iracc/1165/` (visited on Nov. 24, 2018).

[31] Franz Helminger et al. "Hochtemperatur-Wärmepumpen-Messergebnisse einer Laboranlage mit HFO-1336mmz-Z bis 160 °C Kondensationstemperatur".
In: *14. Symposium Energieinnovation*. Ed. by TU Graz.
Graz: Verlag der Technischen Universität Graz, 2016. ISBN: 9783851254495.
URL: `https://www.tugraz.at/fileadmin/user_upload/Events/Eninnov2016/files/lf/Session_F2/LF_Helminger.pdf` (visited on Nov. 24, 2018).

[32] Europäische Union. *Verordnung (EU) Nr. 517/2014 des Europäischen Parlaments und des Rates vom 16. April 2014 über fluorierte Treibhausgase und zur Aufhebung der Verordnung (EG) Nr. 842/2006*. 2014. URL:
`https://eur-lex.europa.eu/legal-content/DE/TXT/PDF/?uri=CELEX:32014R0517`
(visited on Nov. 24, 2018).

[33] Choyu Watanabe et al.
"Industrial Heat Pumps and Their Application Examples in Japan".
In: *Proceedings of 12th IEA Heat Pump Conference 2017*. Ed. by IEA. 2017.
ISBN: 9789090304120. URL:
`http://hpc2017.org/wp-content/uploads/2017/05/P.3.7.5-Industrial-Heat-Pumps-and-Their-Application-Examples-in-Japan.pdf` (visited on Nov. 24, 2018).

[34] Konstantinos Kontomaris et al. "Combined Heat and Power From Low Temperature Heat: HFO-1336mzz(Z) as a Working Fluid for Organic Rankine Cycles". In: *Proceedings of the 16th International Refrigeration and Air Conditioning Conference 2016*. Ed. by Purdue University. New York: Curran Associates, Inc., 2016. ISBN: 9781510828735. URL: `https://docs.lib.purdue.edu/iracc/1815/` (visited on Nov. 24, 2018).

[35] Heinz P. Bloch. *A practical guide to compressor technology*. 2nd ed. Hoboken, NJ: John Wiley & Sons, 2006. ISBN: 9780471727934.

[36] Mahbod Heidari, Sylvain Lemofouet, and Alfred Rufer. "On The Strategies Towards Isothermal Gas Compression And Expansion". In: *Proceedings of the International Compressor Engineering Conference 2014*. Ed. by Purdue University. 2014. URL: `https://docs.lib.purdue.edu/cgi/viewcontent.cgi?article=3284&context=icec` (visited on Nov. 24, 2018).

[37] K. Klotsche, C. Thomas, and U. Hesse. "Thermal and Fluid Mechanical Investigation of an Internally Cooled Piston Rod". In: *Proceedings of the 10th International Conference on Compressors and their Systems*. Ed. by Institute of Physics IOP. Materials Science and Engineering. Red Hook, NY: Curran Associates, Inc., 2017. ISBN: 9781510847750. DOI: `10.1088/1757-899X/232/1/012002`.

[38] Tim Guilles. *Automotive engines: Diagnosis, repair and rebuilding*. 6th ed. Australia and United States: Delmar Cengage Learning, 2011. ISBN: 9781435486416.

[39] P. L. Stephenson et al. "Isothermal Compression by Dense Water Sprays in a Reciprocating Piston Compressor". In: *Proceedings of the 18th Annual Conference on Liquid Atomization & Spray Systems 2002*. Ed. by ILASS. Madrid: CSIC, 2002. ISBN: 9788495480705. URL: `http://www.ilasseurope.org/ICLASS/ilass2002/papers/026.pdf` (visited on Nov. 24, 2018).

[40] M. W. Coney et al. "Development Of A Reciprocating Compressor Using Water Injection To Achieve Quasi-Isothermal Compression". In: *Proceedings of the International Compressor Engineering Conference 2002*. Ed. by Purdue University. 2002. URL: `https://docs.lib.purdue.edu/icec/1508/` (visited on Nov. 24, 2018).

[41] Shao-kai Yang, Sen-quan Zhou, and Si-ying Sun. "Internal Water-Spray Cooling in the Reciprocating Compressor". In: *Proceedings of the International Compressor Engineering Conference 1988*. Ed. by Purdue University. 1988. URL:

`https://docs.lib.purdue.edu/cgi/viewcontent.cgi?article=1668&context=icec`
(visited on Nov. 24, 2018).

[42]   Markus Friedl et al. *Zweiphasenkompressor für Wärmepumpen: Phase 1: Konzept: Schlussbericht Projekt SI/500669-01.*
Ed. by Schweizerische Eidgenossenschaft, Bundesamt für Energie.
Bern and Rapperswil, 2012.
URL: `http://www.bfe.admin.ch/dokumentation/energieforschung/index.html?lang=de&publication=10930` (visited on Nov. 24, 2018).

[43]   Marcel Koller and Markus Friedl. *Zweiphasenkompressor für Wärmepumpen: Phase 2b: Funktionsmuster - Teil Kompressor: Schlussbericht Projekt SI/501019-02.*
Ed. by Schweizerische Eidgenossenschaft, Bundesamt für Energie.
Bern and Rapperswil, 2017.

[44]   Bruno Eckert.
Axialkompressoren und Radialkompressoren: Anwendung, Theorie, Berechnung. 1st ed.
Berlin, Göttingen, and Heidelberg: Springer, 1953. ISBN: 9783642527210.

[45]   Richard van Basshuysen and Fred Schäfer, eds.
Handbuch Verbrennungsmotor: Grundlagen, Komponenten, Systeme, Perspektiven.
7th ed. ATZ-MTZ-Fachbuch. Wiesbaden: Springer Vieweg, 2015. ISBN: 9783658046774.

[46]   Niranjan Miganakallu et al. "Experimental Investigation of Water Injection Technique in Gasoline Direct Injection Engine". In: *Proceedings of the ASME Internal Combustion Engine Fall Technical Conference - 2017*. Ed. by ASME. New York: ASME, 2017.
ISBN: 9780791858318. DOI: `10.1115/ICEF2017-3619`.

[47]   Koji Takasaki et al. "Direct Water Injection to Improve Diesel Spray Combustion".
In: *Proceedings of the 2003 spring technical conference of the ASME Internal Combustion Engine Division*. Ed. by ASME. New York: ASME, 2003, pp. 27–34.
ISBN: 0791836789. DOI: `10.1115/ICES2003-0554`.

[48]   R. K. Sullerey and Ankur Agarwal. "Effect of Water Injection on Emission Characteristics of a Turbocharged Diesel Engine". In: *Proceedings of the 2009 spring technical conference of the ASME Internal Combustion Engine Division*. Ed. by ASME.
New York: ASME, 2009, pp. 371–378. ISBN: 9780791843406.
DOI: `10.1115/ICES2009-76025`.

[49]   E. Amani, M. R. Akbari, and S. Shahpouri.
"Multi-objective CFD optimizations of water spray injection in gas-turbine combustors".
In: *Fuel* 227 (2018), pp. 267–278. ISSN: 00162361. DOI: `10.1016/j.fuel.2018.04.093`.

[50] David Alejandro Block Novelo and Uyioghosa Igie. "Aero engine compressor cooling by water injection - Part 1: Evaporative compressor model".
In: *Energy* 160 (2018), pp. 1224–1235. ISSN: 03605442.
DOI: `10.1016/j.energy.2018.05.170`.

[51] David Alejandro Block Novelo and Uyioghosa Igie. "Aero engine compressor cooling by water injection - Part 2: Performance and emission reductions".
In: *Energy* 160 (2018), pp. 1236–1243. ISSN: 03605442.
DOI: `10.1016/j.energy.2018.05.171`.

[52] Bernd Epple et al. *Simulation von Kraftwerken und wärmetechnischen Anlagen*. 1st ed.
Wien and New York: Springer, 2009. ISBN: 9783211296950.

[53] R. Meyer-Pittroff and Th. Hackensellner. "Experimental Development of a High Temperature Heat Pump Using a Liquid Ring Compressor".
In: *Heat Pumps: Solving Energy and Enviromental Challenges*.
Ed. by Takamoto Saito and Yoshio Igarashi. Oxford et al.: Pergamon Press, 1990,
pp. 615–625. ISBN: 0080401937. DOI: `10.1016/B978-0-08-040193-5.50071-7`.

[54] Heinz Moisi and Renè Rieberer. "Refrigerant Selection and Cycle Development for a High Temperature Vapor Compression Heat Pump".
In: *Proceedings of 12th IEA Heat Pump Conference 2017*. Ed. by IEA. 2017.
ISBN: 9789090304120.
URL: `http://hpc2017.org/wp-content/uploads/2017/05/O.3.4.3-Refrigerant-Selection-and-Cycle-Development-for-a-High-Temperature-Vapor-Compression-Heat-Pump.pdf` (visited on Nov. 24, 2018).

[55] Hans Dieter Baehr and Karl Stephan. *Wärme- und Stoffübertragung*. 8th ed.
Berlin: Springer Vieweg, 2013. ISBN: 9783642365584.

[56] Nasser Ashgriz, ed. *Handbook of Atomization and Sprays: Theory and Applications*.
1st ed. New York et al.: Springer, 2011. ISBN: 9781441972637.

[57] Modelica Association, ed. *Modelica: A Unified Object-Oriented Language for Systems Modeling: Language Specification Version 3.3 Revision 1*. 2014.
URL: `https://www.modelica.org/documents` (visited on Nov. 24, 2018).

[58] Dassault Systèmes, ed. *Dymola: Dynamic Modeling Laboratory: User Manual Volume 1*.
Lund, 2013.

[59] Otto Krischer and Werner Kast, eds.
Die wissenschaftlichen Grundlagen der Trocknungstechnik. 3rd ed. Vol. 1.
Trocknungstechnik. Berlin and Heidelberg: Springer, 1978. ISBN: 9783642618802.

[60] Günter Wozniak. *Zerstäubungstechnik: Prinzipien, Verfahren, Geräte*. 1st ed.
Berlin and Heidelberg: Springer, 2003. ISBN: 9783642625091.

[61] Robert Bosch GmbH, ed.
      Gasoline direct injection: Key technology for greater efficiency and dynamics.
      Stuttgart, 2013.
      URL: http://www.bosch.co.jp/tms2015/en/products/pdf/Bosch_di_folder.pdf
      (visited on Nov. 24, 2018).

[62] Hermann Breitbach et al. "Magere Schichtverbrennung beim Ottomotor".
      In: *MTZ - Motortechnische Zeitschrift* 74.5 (2013), pp. 370–377. ISSN: 0024-8525.
      DOI: 10.1007/s35146-013-0098-2.

[63] Karl Kröll and Werner Kast. *Trocknen und Trockner in der Produktion.* 2nd ed. Vol. 3.
      Trocknungstechnik. Berlin and Heidelberg: Springer, 1989. ISBN: 9783540184720.

[64] Verein Deutscher Ingenieure VDI-Gesellschaft Verfahrenstechnik und
      Chemieingenieurwesen, ed. *VDI-Wärmeatlas.* 11th ed.
      Berlin and Heidelberg: Springer-Verlag, 2013. ISBN: 9783642199813.

[65] R. B. Keey. *Drying: Principles and Practice.* Vol. 13.
      International series of monographs in chemical engineering.
      Oxford: Pergamon Press, 1972. ISBN: 9780080169033.

[66] Volker Gnielinski, Alfons Mersmann, and Franz Thurner.
      Verdampfung, Kristallisation, Trocknung. 1st ed. Berlin and Heidelberg: Springer, 1993.
      ISBN: 9783540670643.

[67] Arun S. Mujumdar, ed. *Handbook of Industrial Drying.* 4th ed.
      Advances in Drying Science and Technology. Boca Raton: CRC Taylor & Francis, 2014.
      ISBN: 9781466596658.

[68] Karl Kröll. *Trockner und Trocknungsverfahren.* 2nd ed. Vol. 2. Trocknungstechnik.
      Berlin and Heidelberg: Springer, 1978. ISBN: 0387081089.

[69] M. Beckmann et al. "Optimierung des Trocknungsprozesses von Dachziegeln in einem
      industriellen Kammertrockner durch mathematische Modellierung und experimentelle
      Untersuchungen". In: *Tagungsbericht Ibausil 16. Internationale Baustofftagung.*
      Ed. by Bauhaus-Univ. Weimar. Weimar: Bauhaus-Univ., 2006, pp. 0805–0812.
      ISBN: 3000182632.

[70] Friedrich Kneule. *Das Trocknen.* 1st ed. Vol. 6. Grundlagen der chemischen Technik.
      Aarau and Frankfurt a.M.: Sauerländer, 1959.

[71] Li Jin Goh et al. "Review of heat pump systems for drying application".
      In: *Renewable and Sustainable Energy Reviews* 15.9 (2011), pp. 4788–4796.
      ISSN: 13640321. DOI: 10.1016/j.rser.2011.07.072.

[72] Siva Achariyaviriya, Somchart Soponronnarit, and Apichit Terdyothin.
"Mathematical Model Development and Simulation of Heat Pump Fruit Dryer".
In: *Drying Technology* 18.1-2 (2000), pp. 479–491. ISSN: 0737-3937.
DOI: 10.1080/07373930008917718.

[73] Evangelos Tsotsas and Arun S. Mujumdar, eds. *Energy Savings.* 1st ed. Vol. 4.
Modern Drying Technology. Hoboken: John Wiley & Sons, 2011. ISBN: 9783527315598.

[74] Odilio Alves-Filho. *Heat pump dryers: Theory, design and industrial applications.* 1st ed.
Boca Raton, London, and New York: CRC Press Taylor & Francis Group, 2016.
ISBN: 9781498711333.

[75] Uta Telljohann. "Theoretische und experimentelle Untersuchungen der Trocknung
plastisch geformter Ziegelrohlinge".
Dissertation. Magdeburg: Otto-von-Guericke-Universität Magdeburg, 2004.

[76] Karl Jasmund and Gerhard Lagaly. *Tonminerale und Tone: Struktur, Eigenschaften,
Anwendungen und Einsatz in Industrie und Umwelt.*
Darmstadt: Steinkopff Verlag, 1993. ISBN: 9783642724886.

[77] Hermann Salmang and Horst Scholze. *Keramik.* 7th ed.
Berlin, Heidelberg, and New York: Springer, 2007. ISBN: 9783540632733.

[78] Wilhelm Hinz. *Die Silikate und ihre Untersuchungsmethoden.* Vol. 1.
Silikate: Grundlagen der Silikatwissenschaft und Silikattechnik.
Berlin: Verl. für Bauwesen, 1970.

[79] Dirk Deppe. "Mechanismus und Beeinflussung von Trockenausblühungen aus
Kalziumsulfat bei der Konvektionstrocknung von Ziegelrohlingen".
Dissertation. Magdeburg: Otto-von-Guericke-Universität Magdeburg, 2005.

[80] P. Balint et al. "Equilibrium Moisture Diagrams for the Drying of Clays".
In: *Ceramics International* 7.1 (1981), pp. 35–38.
DOI: 10.1016/0272-8842(81)90038-9.

[81] Aleksei Vasilevič Lykov and Ernst Pezold.
Experimentelle und theoretische Grundlagen der Trocknung.
Berlin: Verlag Technik, 1955.

[82] Aleksei Vasilevič Lykov. *Heat and mass Transfer in Capillary-porous Bodies.* 1st ed.
Oxford: Pergamon Press, 1966. ISBN: 9781483225685.

[83] G. Musielak and T. Śliwa.
"Modeling and Numerical Simulation of Clays Cracking During Drying".
In: *Drying Technology* 33.14 (2015), pp. 1758–1767. ISSN: 0737-3937.
DOI: 10.1080/07373937.2015.1036287.

[84] Evangelos Tsotsas and Arun S. Mujumdar, eds.
Computational Tools at Different ScalesModern. 1st ed. Vol. 1.
Modern Drying Technology. Hoboken: John Wiley & Sons, 2007. ISBN: 9783527315567.

[85] E.-U. Schlünder. "Drying of Porous Material During the Constant and the Falling Rate
Period: A Critical Review of Existing Hypotheses".
In: *Drying Technology* 22.6 (2004), pp. 1517–1532. ISSN: 0737-3937.
DOI: 10.1081/DRT-120038738.

[86] Frank P. Incropera et al. *Fundamentals of Heat and Mass Transfer*. 6th ed.
Hoboken: John Wiley & Sons, 2007. ISBN: 9780471457282.

[87] Massoud Kaviany. *Principles of Heat Transfer in Porous Media*. 2nd ed.
Mechanical engineering series. New York: Springer, 1995. ISBN: 0387945504.

[88] Alfons Mersmann. *Stoffübertragung*. Wärme- und Stoffübertragung.
Berlin et al.: Springer, 1986. ISBN: 0387159207.

[89] Martin Krus. "Feuchtetransport- und Speicherkoeffizienten poröser mineralischer
Baustoffe: Theoretische Grundlagen und neue Messtechniken".
Dissertation. Stuttgart: Universität Stuttgart, 1995.

[90] Thomas Metzger and Evangelos Tsotsas.
"Influence of Pore Size Distribution on Drying Kinetics: A Simple Capillary Model".
In: *Drying Technology* 23.9-11 (2005), pp. 1797–1809. ISSN: 0737-3937.
DOI: 10.1080/07373930500209830.

[91] Uta Telljohann, Karsten Junge, and Eckehard Specht. "Moisture Diffusion Coefficients
for Modeling the First and Second Drying Sections of Green Bricks".
In: *Drying Technology* 26.7 (2008), pp. 855–863. ISSN: 0737-3937.
DOI: 10.1080/07373930802136053.

[92] Erich Manegold. *Grundlagen*. Vol. 1. Kapillarsysteme.
Heidelberg: Straßenbau-, Chemie- u. Technik-Verl.-Ges., 1955.

[93] A. J. J. van der Zanden and M. H. de Wit. "A Procedure to Measure the Diffusion
Coefficient of Water in Brick as a Function of the Water Concentration".
In: *Drying Technology* 30.5 (2012), pp. 526–534. ISSN: 0737-3937.
DOI: 10.1080/07373937.2011.648782.

[94] G. H. A. van der Heijden et al.
"Non-isothermal drying of fired-clay brick, an NMR study".
In: *Chemical Engineering Science* 64.12 (2009), pp. 3010–3018. ISSN: 00092509.
DOI: 10.1016/j.ces.2009.03.012.

[95]   Alptug Yataganbaba and İrfan Kurtbaş. "A scientific approach with bibliometric analysis related to brick and tile drying: A review".
In: *Renewable and Sustainable Energy Reviews* 59 (2016), pp. 206–224. ISSN: 13640321.
DOI: `10.1016/j.rser.2015.12.357`.

[96]   Miloš Vasić, Željko Grbavčić, and Zagorka Radojević.
"Analysis of Moisture Transfer During the Drying of Clay Tiles with Particular Reference to an Estimation of the Time-Dependent Effective Diffusivity".
In: *Drying Technology* 32.7 (2014), pp. 829–840. ISSN: 0737-3937.
DOI: `10.1080/07373937.2013.870194`.

[97]   Miloš Vasić, Željko Grbavčić, and Zagorka Radojević. "Determination of the moisture diffusivity coefficient and mathematical modeling of drying".
In: *Chemical Engineering and Processing: Process Intensification* 76 (2014), pp. 33–44.
ISSN: 02552701. DOI: `10.1016/j.cep.2013.12.003`.

[98]   John Crank. *The mathematics of diffusion.* 2nd ed. Oxford: Clarendon Press, 1975.
ISBN: 0198533446.

[99]   Guerman I. Efremov. "Drying Kinetics Derived from Diffusion Equation with Flux-Type Boundary Conditions". In: *Drying Technology* 20.1 (2002), pp. 55–66. ISSN: 0737-3937.
DOI: `10.1081/DRT-120001366`.

[100] N. Boukadida, S. Ben Nasrallah, and P. Perre.
"Mechanism of two-dimensional heat and mass transfer during convective drying of porous media under different drying conditions".
In: *Drying Technology* 18.7 (2000), pp. 1367–1388. ISSN: 0737-3937.
DOI: `10.1080/07373930008917783`.

[101] V. K. Chaitanya Pakala and O. A. Plumb.
"Heat Transfer at an Evaporating Front in Porous Media".
In: *Proceedings of the ASME Summer Heat Transfer Conference 2009.*
Ed. by American Society of Mechanical Engineers. New York: ASME, 2009,
pp. 317–326. ISBN: 9780791843581. DOI: `10.1115/HT2009-88240`.

[102] H. Shokouhmand et al.
"Performance Optimization of a Brick Dryer Using Porous Simulation Approach".
In: *Drying Technology* 29.3 (2011), pp. 360–370. ISSN: 0737-3937.
DOI: `10.1080/07373937.2010.497954`.

[103] Genival da Silva Almeida et al. "Heat and mass transport in an industrial tunnel dryer: Modeling and simulation applied to hollow bricks".
In: *Applied Thermal Engineering* 55.1-2 (2013), pp. 78–86. ISSN: 13594311.
DOI: `10.1016/j.applthermaleng.2013.02.042`.

[104] Salah Ben Mabrouk, Besma Khiari, and Mohamed Sassi.
"Modelling of heat and mass transfer in a tunnel dryer".
In: *Applied Thermal Engineering* 26.17-18 (2006), pp. 2110–2118. ISSN: 13594311.
DOI: `10.1016/j.applthermaleng.2006.04.007`.

[105] B. Nait-Ali et al. "Thermal conductivity of ceramic green bodies during drying".
In: *Journal of the European Ceramic Society* 37.4 (2017), pp. 1839–1846. ISSN: 09552219.
DOI: `10.1016/j.jeurceramsoc.2016.12.011`.

[106] Schweizer, ed. *Formelsammlung und Berechnungsprogramme Anlagenbau.* URL: `https://www.schweizer-fn.de/stoff/wkapazitaet/wkapazitaet_baustoff_erde.php` (visited on Nov. 24, 2018).

[107] Joel H. Ferziger and Milovan Perić. *Numerische Strömungsmechanik.* 1st ed.
Berlin: Springer, 2008. ISBN: 9783540675860.

[108] Suhas V. Patankar. *Numerical heat transfer and fluid flow.*
Series in computational methods in mechanics and thermal sciences.
Bristol, PA: Taylor & Francis, 1980. ISBN: 0891165223.

[109] Modelica. *Standard Library - Version 3.2.1.*
URL: `https://doc.modelica.org/om/Modelica.html` (visited on Nov. 24, 2018).

[110] Deutsches Institut für Normen. *DIN 1946-6:2009-05, Raumlufttechnik - Teil 6: Lüftung von Wohnungen - Allgemeine Anforderungen, Anforderungen zur Bemessung, Ausführung und Kennzeichnung, Übergabe/Übernahme (Abnahme) und Instandhaltung.*
Berlin: Beuth Verlag, 2009.

Stefan Falkner

Curriculum Vitae

Personal Information

Date of birth	June 20, 1988
Place of birth	Linz, Austria
Citizenship	Austria
Email	st.falkner@gmail.com

Education

03/2015 - Present	**Doctoral programme in Engineering Sciences Mechanical Engineering**, *TU Wien*, Vienna.
Thesis	Experimental investigation of injection cooling for water as the working fluid of high temperature heat pumps and theoretical study of industrial drying processes
03/2012 - 09/2014	**Master programme Mechanical Engineering**, *TU Wien*, Vienna.
Thesis	Modellierung und Simulation von thermischen Speichern
Focused on	Advanced and Alternative Energy Systems, Hydraulic Machinery and Hydraulic Systems
	Master examination passed with distinction
10/2008 - 02/2012	**Bachelor programme Mechanical Engineering**, *TU Wien*, Vienna.
Thesis	Erstellen von Funktionen für die Berechnung der Stoffwerte von Gasen
2002 - 2007	**School Education**, *HTBLA Neufelden*, Neufelden.
Thesis	Rundholzfertigung - Mittels einer Maschine können Holzkanter rund gefräst und nachgeschliffen werden
Focused on	Automation Engineering
	Final exam passed with distinction

Professional Experience

04/2015 - 09/2018	**Research assistant**, *Institute for Energy Systems and Thermo-dynamics, TU Wien*, Vienna.
03/2015 - 04/2015	**Electrical fitter**, *PKE Electronics AG*, Vienna. Assembly of security and multimedia equipment at Baku Congress Centre, Baku, Azerbaijan
07/2013	**Trainee**, *R&D, ÖkoFEN Forschungs- und Entwicklungs GmbH*, Lembach i.M.
07/2012 & 09/2012	**Trainee**, *R&D, Global Hydro Energy GmbH*, Niederranna.
10/2011 - 02/2013	**Tutor**, *Institute of Engineering Design and Product Development, TU Wien*, Vienna.
10/2008 - 04/2015	**Marginally employed**, *Ihre Linie Musikagentur*, Kirchberg o.d.D.
02/2008 - 10/2008	**Ambulanceman**, *Red Cross*, Walding. Civilian service
07/2007 - 01/2008	**Production worker**, *Material testing, voestalpine Stahl GmbH*, Linz.
07/2005	**Trainee**, *Hauser GmbH*, St. Martin i.M.
07/2004	**Trainee**, *Boote Feichtner GmbH Nfg. KG*, Linz.

Skills

Languages	German, English
Software and Programming	MS Office, LaTeX, C/C++, Java, Python, Matlab, Simulink, Modelica, Dymola, OpenModelica, KED, IPSEpro, ANSYS Fluent, Catia, Solid Edge
Licences	A, B, C, E, F, Boat Master Licence - 10 m